



**Heat Transfer Enhancement on Jet Impinging Surface by Decreasing
Effect of Cross-flow**

Makatar Wae-hayee

**A Thesis Submitted in Partial Fulfillment of the Requirements for the Degree of
Doctor of Engineering in Mechanical Engineering**

Prince of Songkla University

2013

Copyright of Prince of Songkla University

Thesis Title Heat transfer enhancement on jet impinged surface by decreasing effect of cross-flow
Author Mr.Makatar Wae-hayee
Major Program Mechanical Engineering

Major Advisor :

.....
(Asst.Prof.Dr.Chayut Nuntadusit)

Examining Committee :

.....Chairperson
(Dr.Kittinan Maliwan)

.....
(Asst.Prof.Dr.Chayut Nuntadusit)

Co-advisor :

.....
(Assoc.Prof.Dr.Perapong Tekasakul)

.....
(Assoc.Prof.Dr.Perapong Tekasakul)

.....
(Dr.Thanansak Theppaya)

.....
(Assoc.Prof.Dr.Asi Bunyajitradulya)

The Graduate School, Prince of Songkla University, has approved this thesis as partial fulfillment of the requirements for the Doctor of Engineering Degree in Mechanical Engineering

.....
(Assoc.Prof.Dr.Teerapol Srichana)
Dean of Graduate School

This is to certify that the work here submitted is the result of the candidate's own investigations. Due acknowledgement has been made of any assistance received.

.....Signature
(Asst.Prof.Dr.Chayut Nuntadusit)
Major Advisor

.....Signature
(Mr.Makatar Wae-hayee)
Candidate

(4)

I hereby certify that this work has not been accepted in substance for any degree, and is not being currently submitted in candidature for any degree.

.....Signature

(Mr.Makatar Wae-hayee)

Candidate

ชื่อวิทยานิพนธ์	การเพิ่มความสามารถถ่ายเทความร้อนบนพื้นผิวที่เจ็ทพุ่งชน โดยลดผลกระทบจากกระแสไหลตัด
ผู้เขียน	นายมัถคาร์ แวหะยี
สาขาวิชา	วิศวกรรมเครื่องกล
ปีการศึกษา	2556

บทคัดย่อ

งานวิจัยนี้มีจุดประสงค์เพื่อเพิ่มการถ่ายเทความร้อนบนพื้นผิวที่เจ็ทพุ่งชน โดยลดผลกระทบจากกระแสไหลตัด ในงานวิจัยได้ใช้ออรัฟฟิสรูปร่างวงกลมยาวที่มีอัตราส่วนความยาวต่อความกว้าง (Aspect ratio) $AR=4$ และ 8 แทนออรัฟฟิสรูปร่างวงกลม ($AR=1$) โดยกำหนดให้พื้นที่หน้าตัดเท่ากัน ในกรณีของออรัฟฟิสแบบวงกลมยาวได้ศึกษาผลของมุมปะทะ (θ) คือมุมที่แกนหลักของออรัฟฟิสทำมุมกับทิศทางการไหลของกระแสไหลตัดที่ $\theta=0^\circ$, 15° , 30° และ 45° สำหรับระยะจากปากทางออกเจ็ทถึงพื้นผิวที่เจ็ทพุ่งชนกำหนดให้คงที่ที่ $H=2D_E$ โดย D_E คือเส้นผ่านศูนย์กลางออรัฟฟิสเทียบเท่าที่มีค่าเท่ากับ 13.2 mm งานวิจัยแบ่งการศึกษาออกเป็นสามส่วน ในส่วนแรกและส่วนที่สองศึกษากรณีของเจ็ทลำเดียวและเจ็ทแถวจำนวน 4 ลำ พุ่งชนพื้นผิวภายในอุโมงค์ลมที่มีกระแสไหลตัดที่ถูกสร้างขึ้น อัตราส่วนความเร็ว (ความเร็วเจ็ทต่อด้วยความเร็วกระแสไหลตัด) ได้ปรับให้อยู่ที่ $VR=3$, 5 และ 7 สำหรับกรณีของเจ็ทแถวได้ศึกษาผลของทิศทางการทำมุมของออรัฟฟิสวงกลมยาว 3 แบบคือ (1) เอียงในแนวเดียวกัน (2) เอียงสลับเข้าหากัน และ (3) เอียงสลับออกจากกัน ในส่วนที่สามได้ศึกษากรณีเจ็ทกลุ่มจำนวน 4×6 ลำ ที่มีการจัดเรียงแบบแถวตรง (Inline) และแบบแถวสลับ (Staggered) โดยกำหนดระยะห่างระหว่างเจ็ทคงที่ $S=3D_E$ นอกจากนี้ได้ทำการปรับค่าเรย์โนลด์ส์นัมเบอร์อยู่ที่ $Re=5,000$, 7,500 และ 13,400 สำหรับการวัดอุณหภูมิบนพื้นผิวได้ใช้แผ่นเทอร์โมลิกวิดคริสตัลและหาการกระจายของนัสเซิลด์นัมเบอร์บนพื้นผิวด้วยเทคนิคการวิเคราะห์ภาพ สำหรับการศึกษาลักษณะการไหลบนพื้นผิวที่เจ็ทพุ่งชนได้ใช้เทคนิคฟิล์มน้ำมัน นอกจากนี้ได้ศึกษาลักษณะการไหลโดยใช้โปรแกรมคำนวณทางพลศาสตร์ของไหลจำลองการไหลในคอมพิวเตอร์

จากผลการทดลองโดยภาพรวมพบว่า เจ็ทที่ไหลออกจากออรัฟฟิสแบบวงกลมยาว $AR=4$ และ 8 ที่ $\theta=0^\circ$ สามารถลดผลกระทบจากกระแสไหลตัด คือการโน้มเอียงของเจ็ทตามการไหลของกระแสไหลตัดน้อยกว่ากรณีของเจ็ทจากออรัฟฟิสหน้าตัดกลม ($AR=1$) ซึ่งมีผลทำให้การถ่ายเทความร้อนบนพื้นผิวของเจ็ทจากออรัฟฟิสแบบวงกลมยาวทั้งสองกรณีที่ $\theta=0^\circ$ สูงกว่ากรณีของ

เจ็ทจากออร์บิทัล $AR=1$ สำหรับผลของมุมปะทะที่ $\theta=15^\circ$ พบว่าลักษณะการไหลและการถ่ายเทความร้อนใกล้เคียงกับกรณีมุมปะทะ $\theta=0^\circ$ เมื่อมุมปะทะเพิ่มขึ้นเป็น $\theta=30^\circ$ และ 45° พบว่าเจ็ทมีการโน้มเอียงไปทางการไหลของกระแสไหลตัดมากขึ้นและทำให้เกิดการพุ่งชนพื้นผิวได้น้อย เนื่องจากการเพิ่มพื้นผิวปะทะระหว่างเจ็ทและกระแสไหลตัด ส่งผลทำให้การถ่ายเทความร้อนบนพื้นผิวลดลงตามการเพิ่มขึ้นของมุมปะทะ โดยเฉพาะอย่างยิ่งกรณีที่กระแสไหลตัดมีความเร็วสูง $VR=3$ สำหรับผลของรูปร่างออร์บิทัลพบว่ากรณี $AR=4$ แนวโน้มการถ่ายเทความร้อนสูงกว่ากรณี $AR=8$ เนื่องจากเจ็ทที่ไหลออกจากออร์บิทัล $AR=8$ มีพื้นที่สัมผัสระหว่างลำเจ็ทกับกระแสไหลตัดมากกว่ากรณี $AR=4$ ส่งผลทำให้เจ็ทจากออร์บิทัล $AR=8$ ได้รับผลกระทบจากกระแสไหลตัดมากกว่ากรณี $AR=4$

สำหรับผลการศึกษาคณิศเจ็ทแถวพบว่า บริเวณที่เจ็ทพุ่งชนซึ่งตรงกับบริเวณที่อัตราการถ่ายเทความร้อนสูงมีพื้นที่ลดลงเมื่อเทียบกับกรณีเจ็ทลำเดียว เนื่องจากเจ็ทแถวถูกจำกัดบริเวณโดยเจ็ทที่อยู่ด้านข้าง สำหรับผลของทิศทางการทำมุมของออร์บิทัลวงกลมยาวพบว่า กรณีมุมแบบ (3) เอียงสลับออกจากกัน ให้อัตราการถ่ายเทความร้อนสูงกว่าแบบ (1) เอียงในแนวเดียวกัน และ (2) เอียงสลับเข้าหากัน

สำหรับผลการศึกษาคณิศของเจ็ทกลุ่มพบว่า การจัดเรียงของเจ็ทแบบแถวตรงให้อัตราการถ่ายเทความร้อนสูงกว่ากรณีการจัดเรียงแบบแถวสลับ เนื่องจากกรณีแบบแถวตรง กระแสไหลตัดสามารถไหลผ่านช่องว่างระหว่างแถวของลำเจ็ทได้ตลอด ในขณะที่การจัดเรียงแบบแถวสลับ กระแสไหลตัดถูกกั้นโดยลำเจ็ทที่อยู่ด้านปลายทางการไหล สำหรับออร์บิทัลแบบวงกลมยาว $AR=4$, $\theta=0^\circ$ สามารถลดผลของกระแสไหลตัดและสามารถช่วยเพิ่มอัตราการถ่ายเทความร้อนให้สูงทั้งกรณีการจัดเรียงแบบแถวตรงและแถวสลับ ซึ่งเมื่อเทียบกับออร์บิทัลแบบวงกลมยาว $AR=8$, $\theta=0^\circ$ พบว่าสามารถลดผลของกระแสไหลตัดและช่วยให้อัตราการถ่ายเทความร้อนสูงเฉพาะกรณีการจัดเรียงแบบแถวตรง เมื่อพิจารณาผลของมุมปะทะในกรณีเจ็ทกลุ่มพบว่า การเพิ่มขึ้นของมุมปะทะช่วยเพิ่มอัตราการถ่ายเทความร้อนเล็กน้อยในบริเวณต้นทางการไหล สำหรับบริเวณปลายทางการไหล อัตราการถ่ายเทความร้อนลดลงอย่างมาก

Thesis Title	Heat Transfer Enhancement on Jet Impinged Surface by Decreasing Effect of Cross-flow
Author	Mr. Makatar Wae-hayee
Major Program	Mechanical Engineering
Academic Year	2013

ABSTRACT

The aim of this research is to enhance the heat transfer on the impinged surface by reducing the effect of cross-flow. The round orifice ($AR=1$) was replaced by elongated orifices with a ratio of orifice length to orifice width of $AR=4$ and 8 in based on identical an exit area. For the case of elongated orifice, an attacking angles, defined as the major axis of elongated orifice to the cross-flow direction, at $\theta=0^\circ$, 15° , 30° and 45° were studied. A jet-to-plate distance was fixed at $H=2D_E$, when D_E is an equivalent orifice diameter. The research was categorized with three parts. The first and second parts are focused on a single jet and a row of 4 jets that impinge on inner surface of wind tunnel under a simulated cross-flow. Velocity ratios (jet velocity/cross-flow velocity) were varied at $VR=3$, 5 and 7 for both these sections. For the case of jet row, effect of rotating directions of elongated orifices with 3 types, (1) parallel, (2) counter-convergent and (3) counter-divergent configurations were examined. For the third part, the impingement array of 4×6 jets arranged with inline and staggered nozzle configurations were studied, and jet-to-jet distances were fixed at $S=3D_E$. The Reynolds number was also varied at $Re=5,000$, $7,500$ and $13,400$. The local temperature distribution on the impinged surface was measured using Thermo-chromic Liquid Crystal sheet (TLCs), and the local heat transfer coefficient was evaluated using image processing method. The oil film technique was used to visualize the flow patterns on the impingement surface. The numerical simulation was employed to gain insight into the fluid flow.

The results show generally that the impinging jets discharging from both elongated orifices, $AR=4$ and 8 , at $\theta=0^\circ$ can minimize the cross-flow effect. The deflection of jets toward cross-flow direction for elongated orifices is smaller than those conventional orifice ($AR=1$). This affects directly to the heat transfer rate on the impingement surface that the impinging jets from both elongated orifices with $\theta=0^\circ$ can increase the heat transfer rate higher than those the case of $AR=1$. The effects of small attacking angle ($\theta=15^\circ$) found that the flow and heat transfer characteristics are rather similar to the case of attacking angle at $\theta=0^\circ$. However, the deflections of jets to the cross-flow streamwise become greater and

impingement on the target surface is weaker when the attacking angle becomes larger, $\theta=30^\circ$ and 45° . This is due to increase the attacking area between the jets and the cross-flow; the heat transfer was decreased by increasing the attacking angle, especially, for the case of high cross-flow velocity, $VR=3$. The effect of orifice shape shows that the heat transfer rate for the case of $AR=4$ is generally higher than those the case of $AR=8$. This reason is from that the perimeter of jet discharging from the orifice with $AR=8$ is larger than those the case of $AR=4$ casing to increase contact area between the jet and the cross-flow. This make the effect of cross-flow on jet impingements from $AR=8$ are prominent than those the case of $AR=4$.

For the case of jet row, it was found that the impingement regions corresponding to the areas of high heat transfer become smaller when compare with the case of single jet. This is due to the jet row is confined by adjacent jets. The effect of elongated orifice arrangement was found that the heat transfer rate of (3) counter-divergent configuration is higher than the others; (1) parallel and (2) counter-convergent configurations.

For the case of jet impingement array, it was found that the heat transfer rate of jet with inline arrangement is higher than those the staggered one. The cross-flow can easily pass through the gaps between the rows of inline jets, whereas it appears to be directly blocked by the downstream jet for the case of staggered arrangement. The jet impingement from elongated orifice with $AR=4$ at $\theta=0^\circ$ can minimize the effect of cross-flow and can increase the heat transfer rate for both inline and staggered arrangement. When compaire with those the case of $AR=8$ at $\theta=0^\circ$, it can decrease the effect of cross-flow and can enhance the heat transfer particularly for the inline arrangement. The effect of attacking angle for impingement array was found that the increasing of the attacking angle case to slightly increase the heat transfer rate particularly for the upstream region. For the downstream region, the heat transfer rate decreases greatly.

ACKNOWLEDGEMENT

This research was supported by grants from Thailand Energy Policy and Planning Office, Ministry of Energy, the Graduate School and Faculty of Engineering, Prince of Songkla University.

Contents

	Page
Abstract in Thai	(5)
Abstract in English	(7)
Acknowledgments	(9)
Contents	(10)
List of Figures	(12)
List of Abbreviations and Symbols	(14)
List of Publications	(16)
Reprints and Permissions	(19)
1. Introduction	1
2. Objectives	2
3. Experimental model, parameters, and apparatus	2
3.1 Experimental model	2
3.2 Experimental parameters	3
3.3 Experimental setup	4
4. Method	6
4.1 Heat transfer measurement	6
4.2 Flow visualization on the impinged surface	7
4.3 Numerical simulation	7
5. Results and discussion	8
5.1 A single impinging jet under simulated cross-flow	8
5.1.1 Flow and heat transfer characteristics for $AR=1$	8
5.1.2 Heat transfer characteristics for $AR=4$ and 8	11
5.1.3 The average Nusselt number	13
5.2 A row of Impinging jets under simulated cross-flow	13
5.2.1 Flow and heat transfer characteristics for $AR=1$	13
5.2.2 Flow and heat transfer characteristics for $AR=4$ and 8	15
5.2.3 The average Nusselt number	15
5.3 Jet impingement array	17
5.3.1 Flow and heat transfer characteristics for $AR=1, 4$ and 8 with $\theta=0^\circ$	18

Contents (Cont.)

	Page
5.3.2 Flow and heat transfer characteristics for AR=1, 4 and 8 with attacking angle	23
5.3.3 Spanwise average Nusselt number	27
5.3.4 The average Nusselt number	28
6. Concluding remarks	29
References	31
Appendix A	33
Appendix B	65
Appendix C	121
Vitae	179

List of Figures

	Page
Fig.1. Flow characteristics of jet impingement array in confined channel [6].	1
Fig.2. Interaction of cross-flow through round and elongated round geometries.	2
Fig.3. Experimental model for single impinging jet and row of impinging jets.	3
Fig.4. Experimental model for array of impinging jets.	3
Fig.5. The details of orifice geometries with identical cross-section area and attacking Angle.	4
Fig.6. Configuration of elongated orifice for row of impinging jets.	4
Fig.7. Schematic diagram of the experimental setup for single and row of impinging jets.	5
Fig.8. Schematic diagram of the experimental setup for array of impinging jets.	5
Fig.9. Test section of heat transfer measurement.	7
Fig.10. Velocity vectors and Y-component velocity contours on Z-X plane at 1.5-mm above the impinged surface (CFD result, the marked circles represent the position of the orifice).	9
Fig.11. Contours of turbulence kinetic energy on Z-X plane at 1.5-mm above the impinged surface (CFD result, the marked circles represent the position of the orifice).	9
Fig.12. Flow characteristics on the impinged surface (Experimental result)	9
Fig.13. Nusselt number distributions on the impinged surface (Experimental result, $T_j=27^\circ\text{C}$, $Re_j = 13,400$).	9
Fig.14. Nusselt number distribution along the crossflow direction ($Z/D=0$, $T_j=27^\circ\text{C}$ and $Re_j=13,400$).	10
Fig.15. (a) Y-component velocity contours and (b) turbulence kinetic energy at 1.5-mm above the impinged surface (CFD result).	10
Fig.16. Nusselt number distributions on the impinged surface for the single jet (Experimental result, $T_j=27^\circ\text{C}$, $Re_j = 13,400$).	12
Fig.17. Average Nusselt number on the impinged surface for the single jet (Experimental result, $T_j=27^\circ\text{C}$, $Re_j = 13,400$).	13
Fig.18. Flow patterns on the impinged surface for $AR=1$ (Experimental result).	14
Fig.19. Velocity vectors and Y-component velocity contours on X-Z plane for $AR=1$ (CFD result, above from target surface of 1.5-mm).	14
Fig.20. Nusselt distributions on the impinged surface for $AR=1$ (Experimental result).	14

List of Figures (Cont.)

	Page
Fig.21. Nusselt distributions on the impinged surface of row of impinging jets (Experimental result).	16
Fig.22. Vectors and contours of velocity in Y-Z plane at $X/D=0.25$ for $V/R=3$.	17
Fig.23. Average Nusselt number (Experimental result).	17
Fig.24. Flow patterns on the impingement surface with oil film technique for the inline arrangement and $Re=13,400$ (Experimental results).	19
Fig.25. Flow patterns on the impingement surface with oil film technique for the staggered arrangement and $Re=13,400$ (Experimental results).	19
Fig.26. Flow characteristic of impinging jets on Z-X plane above the impingement surface of 1 mm for the in-line arrangement and $Re=13,400$ (CFD results).	20
Fig.27. Flow characteristic of impinging jets on Z-X plane above the impingement surface of 1 mm for the staggered arrangement and $Re=13,400$ (CFD results).	20
Fig.28. Flow characteristic of impinging jets on X-Y plane at $Z=1.5D_E$ for the in-line arrangement and $Re=13,400$ (CFD results, Numbers in marked circle indicate the jet column order).	22
Fig.29. Flow characteristic of impinging jets on X-Y plane at $Z=-0.75D_E$ for the staggered arrangement and $Re=13,400$ (CFD results, Numbers in marked circle indicate the jet column order).	22
Fig.30. Flow characteristic of impinging jets on Y-Z plane for $AR=4$, $\theta=45^\circ$, and $Re=13,400$ (CFD results).	23
Fig.31. Sketch of the cross-flow through difference of attacking angle.	23
Fig.32. Nusselt number distributions on the impingement surface for the inline arrangement and $Re=13,400$ (Experimental results, $T_j=27^\circ\text{C}$).	25
Fig.33. Nusselt number distributions on the impingement surface for the staggered arrangement and $Re=13,400$ (Experimental results, $T_j=27^\circ\text{C}$).	25
Fig.34. Spanwise average Nusselt number distribution along the cross-flow direction (Experimental results, $T_j = 26.7^\circ\text{C}$ and numbers in marked circle indicate the jet column order).	27
Fig.35. Average Nusselt number (Experimental result).	29

List of Abbreviations and Symbols

List of Abbreviations

A	Area of stainless steel foil (m^2)
AR	Orifice aspect ratio, orifice length/orifice width (-)
D	Orifice diameter (mm)
D_E	Equivalent orifice diameter (mm)
H	Jet-to-plate distance (D)
h	Convective heat transfer coefficient ($\text{W}/\text{m}^2 \cdot ^\circ\text{C}$)
\bar{h}	Average convective heat transfer coefficient ($\text{W}/\text{m}^2 \cdot ^\circ\text{C}$)
\bar{h}_c	Average natural heat transfer coefficient ($\text{W}/\text{m}^2 \cdot ^\circ\text{C}$)
I	Electrical current (A)
k	Conductivity of jet ($\text{W}/\text{m} \cdot ^\circ\text{C}$)
L	Orifice length (mm)
Nu	Nusselt number (-)
\bar{Nu}	Average Nusselt number (-)
\dot{Q}_{input}	Heat transfer rate from power supply (W)
\dot{Q}_{losses}	Heat losses from heated wall to environment (W)
\dot{q}_{input}	Heat flux dissipated on stainless steel foil (W/m^2)
\dot{q}_r	Heat flux by radiation (W/m^2)
\dot{q}_c	Heat flux by natural convection (W/m^2)
R	Electrical resistance of stainless steel foil (Ω)
Re	Reynolds number (-)
S	Jet-to-jet distance (D)
T_j	Jet temperature ($^\circ\text{C}$)
T_s	Surrounding temperature ($^\circ\text{C}$)
T_w	Wall temperature ($^\circ\text{C}$)
\bar{T}_w	Average wall temperature ($^\circ\text{C}$)
VR	Velocity ratio, jet velocity/cross-flow velocity (-)
W	Orifice Width (mm)

List of Abbreviations and Symbols (Cont.)**List of Symbols**

ε_{TLC}	The emissive coefficient of the TLC sheet (-)
θ	Attacking angle, angle of the cross-flow streamwise to the major axis of the elongated orifice (°)
σ	The Stefan-Boltzman constant ($\text{W}/\text{m}^2 \cdot \text{K}^4$)

List of Publications

The list of publications was sorted in order of the study. The publications of the single jet, the row and the array of jet impingements were attached in Appendix A, Appendix B and Appendix C, respectively.

1. Publications of single impinging jet

1.1 Conference Paper

Makatar Wae-hayee, Chayut Nuntadusit and Perapong Tekasakul, Effect of velocity ratio on flow and heat transfer characteristics of an impinging jet in crossflow, The 5th PSU-UNS International Conference on Engineering and Technology (ICET-2011), May 2-3, 2011, Phuket, Thailand.

1.2 Conference Paper

Makatar Wae-hayee and Chayut Nuntadusit, Flow and heat transfer characteristics of non-circular impinging jet in crossflow, The 8th International Conference on Flow Dynamics (ICFD-2011), November 9-11, 2011, Miyagi, Japan.

1.3 Conference Paper

Makatar Wae-hayee, Perapong Tekasakul and Chayut Nuntadusit, Heat transfer enhancement of an impinging jet in crossflow by elongated round orifice, The 10th International Gas Turbine Congress (IGTC-2011), November 13-18, 2011, Osaka, Japan.

1.4 Journal Paper

M. Wae-hayee, P. Tekasakul, S. Eiamsa-ard and C. Nuntadusit, "Effect of Cross-flow Velocity on Flow and Heat Transfer Characteristics of Impinging Jet with Low Jet-to-Plate Distance" **This manuscript have been submitted in Journal of Mechanical Science and Technology.**

2. Publications of row of impinging jets

2.1 Conference Paper

C. Nuntadusit and M. Wae-hayee, "Flow and Heat Transfer Characteristics of Row of Jet Impingement from Elongated Orifice under Cross-flow" The 4th International Conference on Jets, Wakes and Separated Flows (ICJWSF2013), September 17-21, 2013, Nagoya, Japan.

List of Publications (Cont.)

2.2 Journal Paper

M. Wae-hayee, P. Tekasakul, S. Eiamsa-ard and C. Nuntadusit, “Flow and Heat Transfer Characteristics of In-line Impinging Jets with Cross-flow at Short Jet-to-plate Distance”, **This manuscript have been submitted in Journal of Mechanical Science and Technology.**

2.3 Journal Paper

Makatar Wae-hayee, Perapong Tekasakul and Chayut Nuntadusit, Heat Transfer Enhancement on a Surface of a Row of Jet Impingements by Elongated Orifice under Cross-flow, Part 1: Parallel Orifice Configuration, **This manuscript is being drafted.**

2.4 Journal Paper

Makatar Wae-hayee, Perapong Tekasakul and Chayut Nuntadusit, Heat Transfer Enhancement on a Surface of a Row of Jet Impingements by Elongated Orifice under Cross-flow, Part 2: Counter Orifice Configuration, **This manuscript is being drafted.**

3. Publications of array of impinging jets

3.1 Conference Paper

Makatar Wae-hayee, Chayut Nuntadusit and Perapong Tekasakul, Heat Transfer enhancement on a surface under arrays of impinging jets : effect of jet flow arrangement, The 5th PSU-UNS International Conference on Engineering and Technology (ICET-2011), May 2-3, 2011, Phuket, Thailand.

3.2 Conference Paper

Makatar Wae-hayee, Perapong Tekasakul, and Chayut Nuntadusit, Heat Transfer Enhancement on Surface with Jets Impingement from Some Arrays of Elongated Round Orifices, The Second TSME International Conference on Mechanical Engineering (TSME-IcoME-2011), 19-21 October, 2011, Krabi, Thailand.

3.3 Journal Paper

M. Wae-hayee, P. Tekasakul and C. Nuntadusit, “Influence of Nozzle Arrangement on Flow and Heat Transfer Characteristics for Arrays of Circular Impinging Jets” Songklanakarin Journal of Science and Technology, 2012, Vol. 35(2), pp.203-212.

List of Publications (Cont.)**3.4 Journal Paper**

Chayut Nuntadusit, Makatar Wae-hayee, Perapong Tekasakul and Smith Eiamsa-ard, Local heat transfer characteristics of array impinging jets from elongated orifices, International Communications in Heat and Mass Transfer, Volume 39, Issue 8, October 2012, Pages 1154-1164.

3.5 Journal Paper

M. Wae-hayee, P. Tekasakul, and C. Nuntadusit, "Effect of Attacking Angle of Elongated Orifice on the Flow and Heat Transfer Characteristics of Jet Impingement Array", **This manuscript is being drafted.**

List of Permissions

1. Journal Paper

M. Wae-hayee, P. Tekasakul and C. Nuntadusit, "Influence of Nozzle Arrangement on Flow and Heat Transfer Characteristics for Arrays of Circular Impinging Jets" Songklanakarin Journal of Science and Technology, 2012, Vol. 35(2), pp.203-212.



AGREEMENT IN RELATION TO REUSE AND REPRINT AN ARTICLE FOR SONGKLANAKARIN JOURNAL OF SCIENCE AND TECHNOLOGY (SJST)

This is an agreement between Songklanakarin Journal of Science and Technology (Publisher) and..... Mr. Makatar Wae-hayee.....(Author).

Author status

- I am the sole author of the article.
- I am one author on behalf of all co-author of the article.

Author contact

Energy Technology Research Center and Department of Mechanical Engineering,
Faculty of Engineering, Prince of Songkla University, Hat Yai, Songkhla, 90112
Thailand.

Publisher contact

Songklanakarin Journal of Science and Technology,
Research and Development Office, Prince of Songkla University,
Hat Yai, Songkhla, 90110 Thailand.

We (Songklanakarin Journal of Science and Technology) grant you a permission to reproduce an article published in our journal as mentioned below for your academic purpose (reuse and reprint in a thesis).

Authorized Article to Reuse and Reprint

Entitled:	Influence of nozzle arrangement on flow and heat transfer characteristics of arrays of circular impinging jets
Author (s):	Makatar Wae-hayee, Perapong Tekasakul, and Chayut Nuntadusi
Volume:	35
No.:	2 (March - April)
Year:	2013
Start Page:	203
End Page:	212
No. of pages:	10

.....

List of Permissions (Cont.)

2. Journal Paper

Chayut Nuntadusit, Makatar Wae-hayee, Perapong Tekasakul and Smith Eiamsa-ard, Local heat transfer characteristics of array impinging jets from elongated orifices, International Communications in Heat and Mass Transfer, Volume 39, Issue 8, October 2012, Pages 1154-1164.

ELSEVIER LICENSE TERMS AND CONDITIONS

Sep 27, 2013

This is a License Agreement between Chayut Nuntadusit ("You") and Elsevier ("Elsevier") provided by Copyright Clearance Center ("CCC"). The license consists of your order details, the terms and conditions provided by Elsevier, and the payment terms and conditions.

All payments must be made in full to CCC. For payment instructions, please see information listed at the bottom of this form.

Supplier	Elsevier Limited The Boulevard, Langford Lane Kidlington, Oxford, OX5 1GB, UK
Registered Company Number	1982084
Customer name	Chayut Nuntadusit
Customer address	Department of Mechanical Engineering, Hat yai, Songkhla 90112
License number	3236880624750
License date	Sep 27, 2013
Licensed content publisher	Elsevier
Licensed content publication	International Communications in Heat and Mass Transfer
Licensed content title	Local heat transfer characteristics of array impinging jets from elongated orifices
Licensed content author	C. Nuntadusit, M. Wae-hayee, P. Tekasakul, S. Eiamsa-ard
Licensed content date	October 2012
Licensed content volume number	39
Licensed content issue number	8
Number of pages	11
Start Page	1154
End Page	1164
Type of Use	reuse in a thesis/dissertation
Portion	full article
Format	both print and electronic
Are you the author of this Elsevier article?	Yes
Will you be translating?	No
Order reference number	
Title of your thesis/dissertation	Heat Transfer Enhancement on Jet Impinging Surface by Decreasing Effect of Cross-flow

List of Permissions (Cont.)

Expected completion date	Oct 2013
Estimated size (number of pages)	120
Elsevier VAT number	GB 494 6272 12
Permissions price	0.00 USD
VAT/Local Sales Tax	0.0 USD / 0.0 GBP
Total	0.00 USD
Terms and Conditions	

INTRODUCTION

1. The publisher for this copyrighted material is Elsevier. By clicking "accept" in connection with completing this licensing transaction, you agree that the following terms and conditions apply to this transaction (along with the Billing and Payment terms and conditions established by Copyright Clearance Center, Inc. ("CCC"), at the time that you opened your Rightslink account and that are available at any time at <http://myaccount.copyright.com>).

GENERAL TERMS

2. Elsevier hereby grants you permission to reproduce the aforementioned material subject to the terms and conditions indicated.
3. Acknowledgement: If any part of the material to be used (for example, figures) has appeared in our publication with credit or acknowledgement to another source, permission must also be sought from that source. If such permission is not obtained then that material may not be included in your publication/copies. Suitable acknowledgement to the source must be made, either as a footnote or in a reference list at the end of your publication, as follows:

 "Reprinted from Publication title, Vol /edition number, Author(s), Title of article / title of chapter, Pages No., Copyright (Year), with permission from Elsevier [OR APPLICABLE SOCIETY COPYRIGHT OWNER]." Also Lancet special credit - "Reprinted from The Lancet, Vol. number, Author(s), Title of article, Pages No., Copyright (Year), with permission from Elsevier."
4. Reproduction of this material is confined to the purpose and/or media for which permission is hereby given.
5. Altering/Modifying Material: Not Permitted. However figures and illustrations may be altered/adapted minimally to serve your work. Any other abbreviations, additions, deletions and/or any other alterations shall be made only with prior written authorization of Elsevier Ltd. (Please contact Elsevier at permissions@elsevier.com)
6. If the permission fee for the requested use of our material is waived in this instance, please be advised that your future requests for Elsevier materials may attract a fee.
7. Reservation of Rights: Publisher reserves all rights not specifically granted in the combination of (i) the license details provided by you and accepted in the course of this licensing transaction, (ii) these terms and conditions and (iii) CCC's Billing and Payment terms and conditions.
8. License Contingent Upon Payment: While you may exercise the rights licensed immediately upon issuance of the license at the end of the licensing process for the transaction, provided that you have

List of Permissions (Cont.)

disclosed complete and accurate details of your proposed use, no license is finally effective unless and until full payment is received from you (either by publisher or by CCC) as provided in CCC's Billing and Payment terms and conditions. If full payment is not received on a timely basis, then any license preliminarily granted shall be deemed automatically revoked and shall be void as if never granted. Further, in the event that you breach any of these terms and conditions or any of CCC's Billing and Payment terms and conditions, the license is automatically revoked and shall be void as if never granted. Use of materials as described in a revoked license, as well as any use of the materials beyond the scope of an unrevoked license, may constitute copyright infringement and publisher reserves the right to take any and all action to protect its copyright in the materials.

9. Warranties: Publisher makes no representations or warranties with respect to the licensed material.

10. Indemnity: You hereby indemnify and agree to hold harmless publisher and CCC, and their respective officers, directors, employees and agents, from and against any and all claims arising out of your use of the licensed material other than as specifically authorized pursuant to this license.

11. No Transfer of License: This license is personal to you and may not be sublicensed, assigned, or transferred by you to any other person without publisher's written permission.

12. No Amendment Except in Writing: This license may not be amended except in a writing signed by both parties (or, in the case of publisher, by CCC on publisher's behalf).

13. Objection to Contrary Terms: Publisher hereby objects to any terms contained in any purchase order, acknowledgment, check endorsement or other writing prepared by you, which terms are inconsistent with these terms and conditions or CCC's Billing and Payment terms and conditions. These terms and conditions, together with CCC's Billing and Payment terms and conditions (which are incorporated herein), comprise the entire agreement between you and publisher (and CCC) concerning this licensing transaction. In the event of any conflict between your obligations established by these terms and conditions and those established by CCC's Billing and Payment terms and conditions, these terms and conditions shall control.

14. Revocation: Elsevier or Copyright Clearance Center may deny the permissions described in this License at their sole discretion, for any reason or no reason, with a full refund payable to you. Notice of such denial will be made using the contact information provided by you. Failure to receive such notice will not alter or invalidate the denial. In no event will Elsevier or Copyright Clearance Center be responsible or liable for any costs, expenses or damage incurred by you as a result of a denial of your permission request, other than a refund of the amount(s) paid by you to Elsevier and/or Copyright Clearance Center for denied permissions.

LIMITED LICENSE

The following terms and conditions apply only to specific license types:

15. **Translation:** This permission is granted for non-exclusive world **English** rights only unless your license was granted for translation rights. If you licensed translation rights you may only translate this content into the languages you requested. A professional translator must perform all translations and reproduce the content word for word preserving the integrity of the article. If this license is to re-use 1 or 2 figures then permission is granted for non-exclusive world rights in all languages.

List of Permissions (Cont.)

16. **Website:** The following terms and conditions apply to electronic reserve and author websites:

Electronic reserve: If licensed material is to be posted to website, the web site is to be password-protected and made available only to bona fide students registered on a relevant course if:

This license was made in connection with a course,

This permission is granted for 1 year only. You may obtain a license for future website posting,

All content posted to the web site must maintain the copyright information line on the bottom of each image,

A hyper-text must be included to the Homepage of the journal from which you are licensing at <http://www.sciencedirect.com/science/journal/xxxxx> or the Elsevier homepage for books at <http://www.elsevier.com> , and

Central Storage: This license does not include permission for a scanned version of the material to be stored in a central repository such as that provided by Heron/XanEdu.

17. **Author website** for journals with the following additional clauses:

All content posted to the web site must maintain the copyright information line on the bottom of each image, and the permission granted is limited to the personal version of your paper. You are not allowed to download and post the published electronic version of your article (whether PDF or HTML, proof or final version), nor may you scan the printed edition to create an electronic version.

A hyper-text must be included to the Homepage of the journal from which you are licensing at <http://www.sciencedirect.com/science/journal/xxxxx> . As part of our normal production process, you will receive an e-mail notice when your article appears on Elsevier's online service ScienceDirect (www.sciencedirect.com). That e-mail will include the article's Digital Object Identifier (DOI). This number provides the electronic link to the published article and should be included in the posting of your personal version. We ask that you wait until you receive this e-mail and have the DOI to do any posting.

Central Storage: This license does not include permission for a scanned version of the material to be stored in a central repository such as that provided by Heron/XanEdu.

18. **Author website** for books with the following additional clauses:

Authors are permitted to place a brief summary of their work online only.

A hyper-text must be included to the Elsevier homepage at <http://www.elsevier.com> . All content posted to the web site must maintain the copyright information line on the bottom of each image. You are not allowed to download and post the published electronic version of your chapter, nor may you scan the printed edition to create an electronic version.

Central Storage: This license does not include permission for a scanned version of the material to be stored in a central repository such as that provided by Heron/XanEdu.

19. **Website** (regular and for author): A hyper-text must be included to the Homepage of the journal from which you are licensing at <http://www.sciencedirect.com/science/journal/xxxxx> . or for books to the Elsevier homepage at <http://www.elsevier.com>

20. **Thesis/Dissertation:** If your license is for use in a thesis/dissertation your thesis may be submitted to your institution in either print or electronic form. Should your thesis be published commercially, please reapply for permission. These requirements include permission for the Library and Archives of Canada to supply single copies, on demand, of the complete thesis and include permission for UMI to supply single copies, on demand, of the complete thesis. Should your thesis

List of Permissions (Cont.)

be published commercially, please reapply for permission.

21. Other Conditions:

v1.6

If you would like to pay for this license now, please remit this license along with your payment made payable to "COPYRIGHT CLEARANCE CENTER" otherwise you will be invoiced within 48 hours of the license date. Payment should be in the form of a check or money order referencing your account number and this invoice number RLNK501122459. Once you receive your invoice for this order, you may pay your invoice by credit card. Please follow instructions provided at that time.

**Make Payment To:
Copyright Clearance Center
Dept 001
P.O. Box 843006
Boston, MA 02284-3006**

For suggestions or comments regarding this order, contact RightsLink Customer Support: customercare@copyright.com or +1-877-622-5543 (toll free in the US) or +1-978-646-2777.

Gratis licenses (referencing \$0 in the Total field) are free. Please retain this printable license for your reference. No payment is required.

1. Introduction

Jet impingement is a high-performance technique for heat transfer enhancement in thermal equipment. It has also been used in industrial processes for heating, cooling and drying. Since the heat transfer rate is very high at the area where the jet directly impinges on, it provides rapid cooling or heating on the local heat transfer area. However, many thermal industrial applications have large surface area of heat transfer such as combustor chamber wall and gas turbine blade cooling, steel and glass quenching, and textile and paper drying. When high and uniform heat transfer rate is required over the entire surfaces, multiple impinging jets or array of impinging jets are applied [1-5].

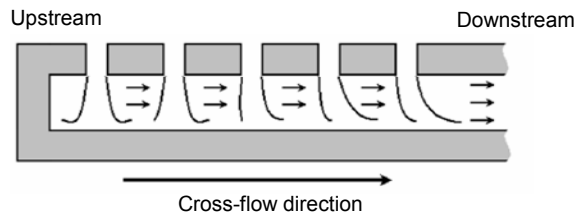


Fig.1. Flow characteristics of jet impingement array in confined channel [6]

An important factor affecting on flow and heat transfer characteristics of multiple impinging jets in a confined space is the cross-flow. Cross-flow is defined as fluid flow in the perpendicular direction to the jet impingement flow. In the case of multiple impinging jets in a confined space, the spent jet is accumulated from upstream to the downstream end of the channel as shown in Fig.1. The flow rate or velocity of the cross-flow is thus increased from upstream to the downstream of the channel. Consequently, downstream jets tend to deflect to cross-flow direction and impinge weakly on impinged surface due to significant cross-flow effect, and their heat transfers are significantly reduced by the cross-flow [6].

To enhance the heat transfer by reducing effect of cross-flow on jet impingement flow is very important. In more recent works, drilling of effusion holes, on the upper surface (nozzle plate) [7, 8], and at the lower surface (impingement surface) [9], in confined channel to eliminate the cross-flow has been attempted. In this work, to reduce the interaction area between impingement flow and cross-flow by modified orifice geometry from conventional round to elongated orifices as shown in Fig.2.

In addition, another approach to enhance the heat transfer rate is to produce longitudinal vortices near the inclined rectangular blocks mounted on a smooth surface [10, 11]. To apply the inclination interaction between the cross-flow and the jet issuing from the

elongated orifice, the attacking angle, defined as the major axis of the elongated orifice to the cross-flow direction, should be examined.

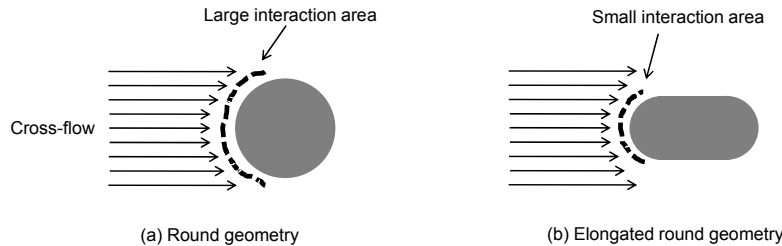


Fig.2. Interaction of cross-flow through round and elongated round geometries

2. Objectives

The aim of this research is to enhance the heat transfer on the impinging surface by reducing the effect of cross-flow. The round orifice ($AR=1$) was replaced by elongated orifices with a ratio of orifice length to orifice width, $AR=4$ and 8 in based on identical exit area. Attacking angles, defined as the major axis of elongated orifice to the cross-flow direction, at $\theta=0^\circ$, 15° , 30° and 45° were also studied experimentally and numerically. A jet-to-plate distance is two times of the round orifice diameter. The research was categorized by three parts; the first and second parts are focused on a single and a row of impinging jet(s) under simulated cross-flow. Velocity ratios (cross-flow velocity/jet velocity) were varied at $VR=3$, 5 and 7 in these sections. For the third one, the elongated orifices were applied under impingement array that arrange with inline and staggered nozzle configurations. The Reynolds number was also varied in this section at $Re=5,000$, $7,500$ and $13,400$.

3. Experimental model, parameters and apparatus

3.1 Experimental model

Experimental models are categorized with three parts; the single jet and the row of jets impinging on the inner side of rectangular wind tunnel under simulated crossflow as shown in Fig.3, and array of impinging jets with inline and staggered arrangement as shown in Fig.4. The jets discharging from round orifices impinge on target surface. For the single impinging jet and the row of impinging jets, the cross-flow was simulated by introducing air through the test section. For the case of impingement array, the crossflow is generated by accumulation of spent jet (jet after impingement) at the upstream side that flows

out to the exit at the other end of the duct as shown in Fig.4(a). The arrays of jet configuration, both for the inline and staggered arrangements, consist of 24 jet holes distributed in 6 columns and 4 rows as shown in Fig.4(b) and (c).

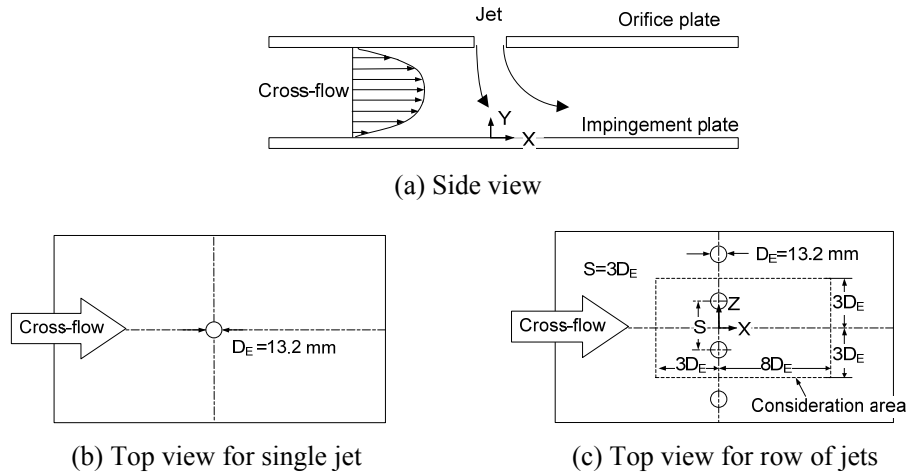


Fig.3. Experimental model for single impinging jet and row of impinging jets

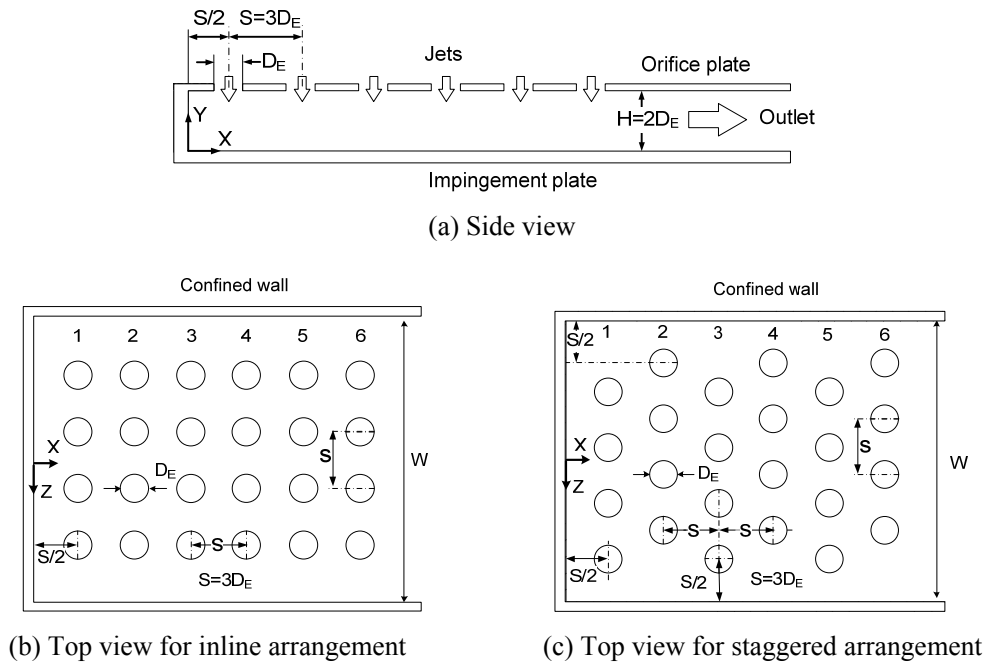


Fig.4. Experimental model for array of impinging jets

3.2 Experimental parameters

All orifices having $AR=1, 4$ and 8 have the same exit area of 136.8 mm^2 , and each round orifice has an equivalent diameter (D_E) of 13.2 mm , as shown in Fig.5. The

attacking angle, defined as the angle between the major axis of the elongated orifice to the cross-flow direction (X-axis), was varied at $\theta=0^\circ, 15^\circ, 30^\circ$ and 45° , as shown also in Fig.5. The jet-to-plate distance was fixed at $H=2D_E$. For the single and the row of impinging jets, the jet velocity was fixed corresponding to $Re=13,400$, and cross-flow velocity was varied corresponding to velocity ratios (jet velocity/cross-flow velocity) $VR=3, 5$ and 7 . In the case of impingement array, both arrangements have constant jet-to-jet distance of $S=3D_E$. The experiments were carried out at jet Reynolds number of $Re=5,000, 7,500$ and $13,400$. In addition, for the case of row of impinging jets, elongated orifices were arranged with parallel, counter-convergent and counter-divergent configurations as shown in Fig.6.

AR=1	$D_E=13.2$ mm	
AR=4	L= 24 mm	W = 6 mm
AR=4	L= 33.6 mm	W = 4.2 mm
Attacking angle	$\theta=0^\circ, 15^\circ, 30^\circ$ and 45°	

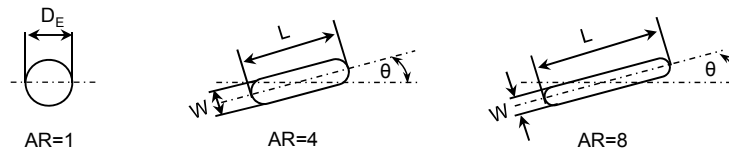


Fig.5. The details of orifice geometries with identical cross-section area and attacking angle

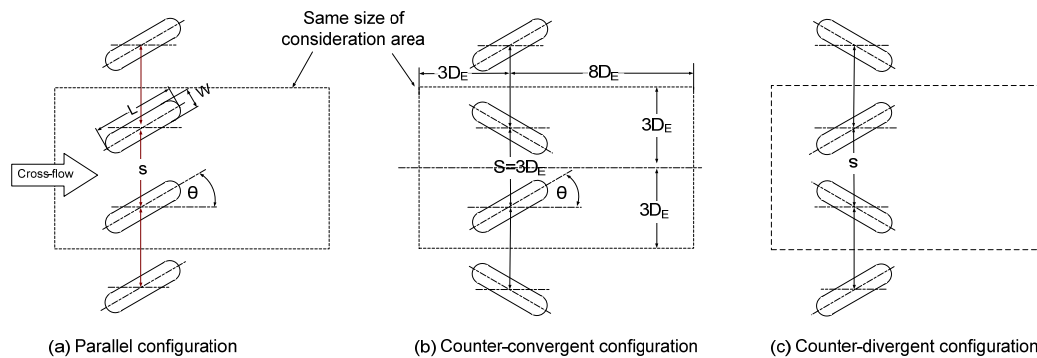


Fig.6. Configuration of elongated orifice for row of impinging jets

3.3 Experimental setup

A schematic diagram of the experimental apparatus is shown in Fig.7 and 8. For the single and the row of impinging jets as shown in Fig.7, air was introduced through the inlet chamber of wind tunnel, flow straightener, two layers of mesh plates, the test section and a chamber outlet by using a 3-HP blower. The cross-section of wind tunnel was with height of 26.4 mm ($2D$) and width of 300 mm. The length of calming section of wind tunnel was 200

cm which is sufficient to achieve fully developed flow in the test section. A Pitot-static tube was located upstream of the test section to measure a cross-flow velocity at the center of channel. The inlet temperatures of jets and cross-flow were kept constant by a temperature and power controller.

For jet supplier, the apparatus of single, row and array of impinging jets can be used together. The 3-HP blower was used to introduce air through a temperature controlled chamber equipped with 2-kW heater, a calibrated orifice flow meter, a jet chamber (constant cross-section of 360-mm \times 360-mm and a height of 850-mm), and a jet orifice before entering the test section. The jet chamber is equipped with two layers of perforated plates and two layers of mesh plates to achieve uniform flow field approaching the orifice plate.

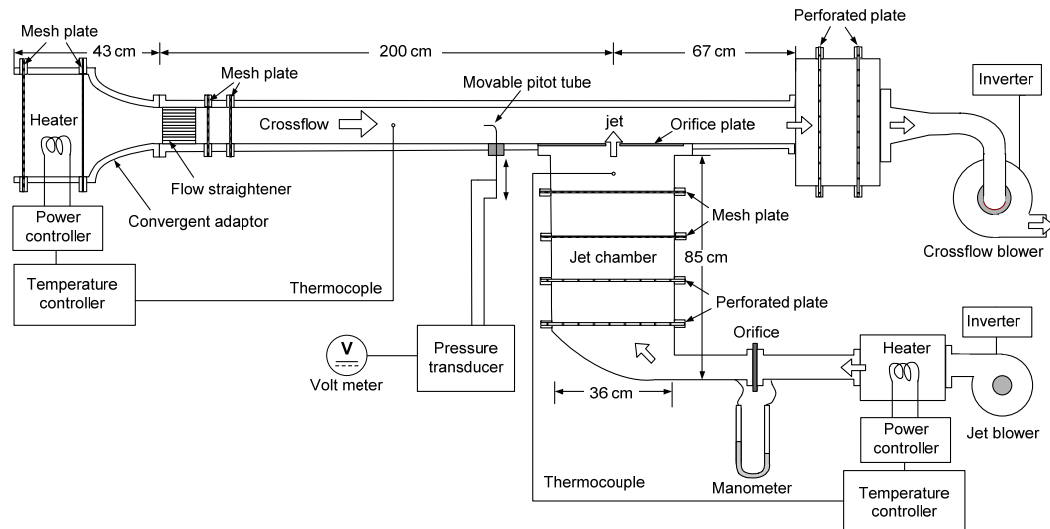


Fig.7. Schematic diagram of the experimental setup for single impinging jet and row of impinging jets

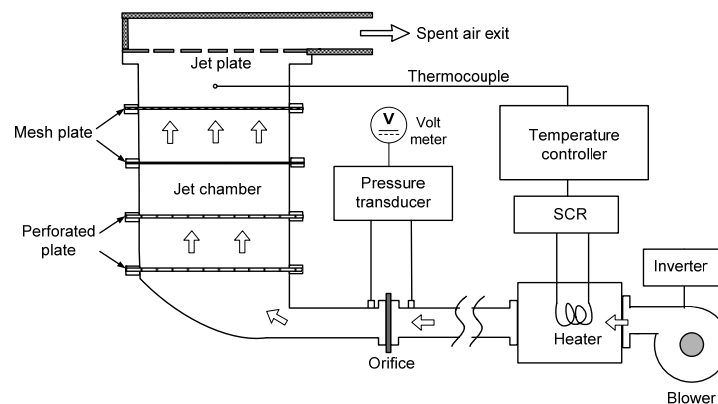


Fig.8. Schematic diagram of the experimental setup for array of impinging jets

4. Method

4.1 Heat transfer measurement

The test section was directly mounted to the jet chamber as shown in Fig.9. Air with constant temperature is discharged through the orifice plate and impinges upon the heat transfer surface. The heat transfer surface, made of stainless steel foil (30 μm thick), is attached with the Thermochromic Liquid Crystal sheet (TLCs, Omega, LCS-95, U.S.A.) on the rear side of the impingement surface. The stainless steel foil is stretched between couple of copper bus bars. The heat transfer surface is heated by a DC power supply that can supply electrical current up to 50 A through the copper bus bars. Electrical energy dissipated in the stainless steel foil can be calculated from:

$$\dot{Q}_{input} = I^2 \cdot R \quad (1)$$

where I is the electrical current, and R is the electrical resistance of the stainless steel foil.

The local heat transfer coefficient by forced convection of the jet, h , can be evaluated from:

$$h = \frac{\dot{Q}_{input} - \dot{Q}_{losses}}{A(T_w - T_j)} = \frac{\dot{q}_{input} - \dot{q}_r - \dot{q}_c}{T_w - T_j} \quad (2)$$

where A is area of stainless steel foil, $\dot{q}_r = \sigma \varepsilon_{TLC} (\overline{T_w}^4 - T_s^4)$ and $\dot{q}_c = \overline{h_c} (\overline{T_w} - T_s)$ are the heat losses to the environment by radiation and free convection, respectively, $\overline{T_w}$ and T_j are the average wall temperature and jet temperature, σ is the Stefan-Boltzman constant ($=5.670 \times 10^{-8}$ J/K), ε_{TLC} is the emissive coefficient of the TLC sheet ($=0.9$), T_s is the surrounding temperature, and $\overline{h_c}$ is the average natural heat transfer coefficient calculated from natural convective heat transfer from the heat transfer surface to the surrounding.

The wall temperature (T_w) on the impingement surface was measured using the TLCs attached at the rear side of the jet impingement surface. A digital camera was used to capture color on the TLCs under manual brightness mode. Images of color pattern on the TLCs were converted from RGB (Red, Green and Blue) system to HSI (Hue, Saturation, and Intensity) system. The Hue (H) value was provided to correlate color of the TLCs to the temperature. The TLCs was calibrated under the same conditions of the experimental runs.

The local Nusselt number can be calculated from:

$$Nu = \frac{hD}{k} \quad (3)$$

where D is the round orifice diameter, and k is the jet thermal conductivity.

The average Nusselt number can be calculated from:

$$\overline{Nu} = \frac{\overline{h}D}{k} \quad (4)$$

where \overline{h} is the average heat transfer coefficient, calculated from Equation (2) by replacing T_w with the average temperature on the impingement surface, $\overline{T_w}$.

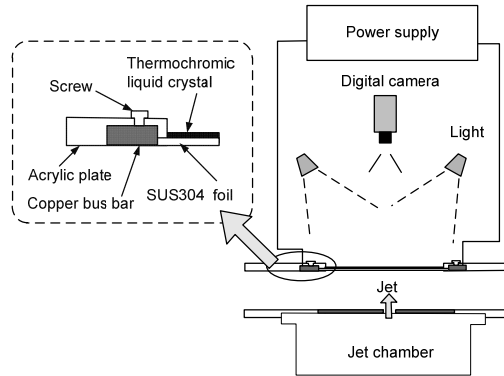


Fig.9. Test section of heat transfer measurement

4.2 Flow visualization on the impinged surface

The flow pattern on the impinged surface was visualized by using oil film technique. The oil was mixed with 7 g of liquid paraffin, 3.5 g of titanium dioxide and 1.8 g of oleic acid. The transparent plastic plate was uniformly painted with the oil under the same film thickness was employed to represent the impinged surface. During the experiment, the oil film pattern on the impinged surface was recorded using video camera.

4.3 Numerical simulation

A 3-D numerical simulation with the ANSYS Fluent 13.0 was employed to investigate the flow characteristics of the jets and the cross-flow. The calculation based on finite volume method was adopted to solve governing differential equations with boundary conditions. A numerical model was identically created to the experimental model. A turbulence model with SST was applied due to high accurate prediction in impingement problems and moderate computational cost [12-14]. This turbulent model has also been employed to accurately predict a flow and heat transfer characteristics of impinging jet under the cross-flow [14 and 15].

The generated grid system was even rectangular, and the elements were concentrated near the wall of wind tunnel and mixing region. The boundary conditions were identically specified to experimental conditions. A solution method was based on SIMPLE algorithm with second order upwind for all spatial discretization. The solution was considered

to be converged when the normalized residual of the algebraic equation was less than a prescribed value of $1.0E-5$ [15 and 16].

5. Results and discussion

5.1 A single impinging jet under simulated cross-flow

In the beginning of this section, flow and heat transfer characteristics for the case of single jet with $AR=1$ will be explained, and heat transfer characteristic for $AR=4$ and 8 will be briefly discussed. More details of this section have been written in publication as attached in **Appendix A**.

5.1.1 Flow and heat transfer characteristics for $AR=1$

Flow and heat transfer characteristics of single impinging jet with $AR=1$ under simulated cross-flow are shown in Fig.10-13. The velocity vectors and velocity contours in Y-component on Z-X plane at 1.5-mm above the impinging surface are shown in Fig.10. The Y-component velocity represents the velocity in direction normal to the impinging surface. The positive velocity of the downstream jet, indicates that the jet impinges on the wall. When the cross-flow velocity increases, the impingement region shifts downstream, especially, at the highest cross-flow velocity (Fig.10(c)). This is due to the significant jet deflection caused by the cross-flow.

The turbulence kinetic energy contours on Z-X plane at 1.5-mm above the impinging surface are shown in Fig.11. At low cross-flow velocity ($VR=7$) as shown in Fig.11(a), the regions with high turbulence kinetic energy are detected in both upstream and downstream wall jets, and the high intensity region of the upstream wall jet is larger than that of the downstream one. In addition, the turbulence kinetic energy at stagnation region is very low which is similar to that found in a common impinging jet without cross-flow. As the cross-flow velocity increases, the region with high turbulence kinetic energy of upstream wall jet shifts downstream, and the region with low turbulence kinetic energy at stagnation region becomes smaller.

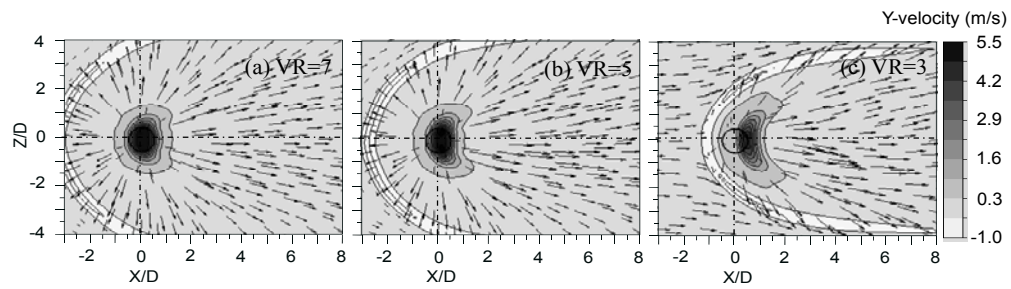


Fig.10. Velocity vectors and Y-component velocity contours on Z-X plane at 1.5-mm above the impinging surface (CFD result, the marked circles represent the position of the orifice)

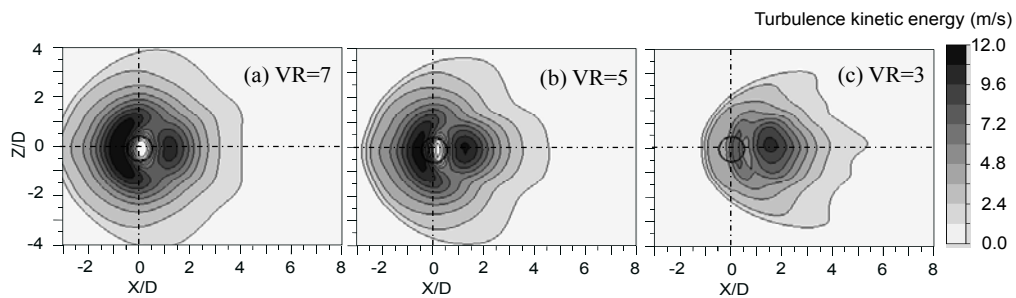


Fig.11. Contours of turbulence kinetic energy on Z-X plane at 1.5-mm above the impinging surface (CFD result, the marked circles represent the position of the orifice)

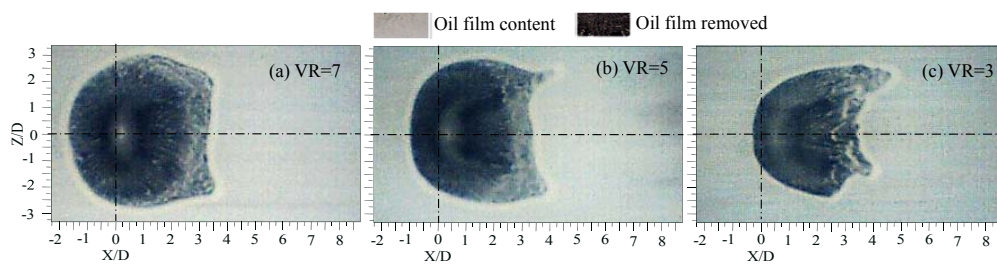


Fig.12. Flow characteristics on the impinging surface (Experimental result)

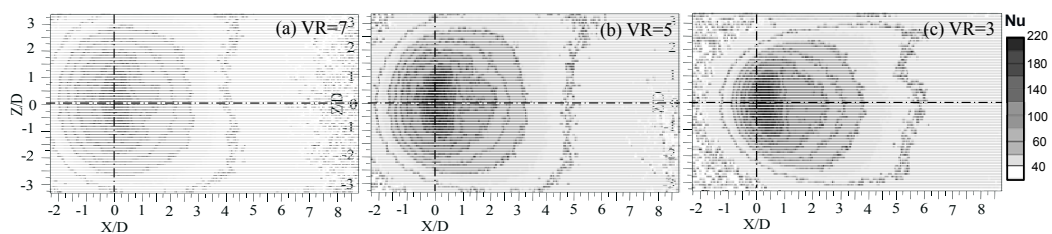


Fig.13. Nusselt number distributions on the impinging surface (Experimental result,

$$T_f=27\text{ }^\circ\text{C}, Re_j=13,400).$$

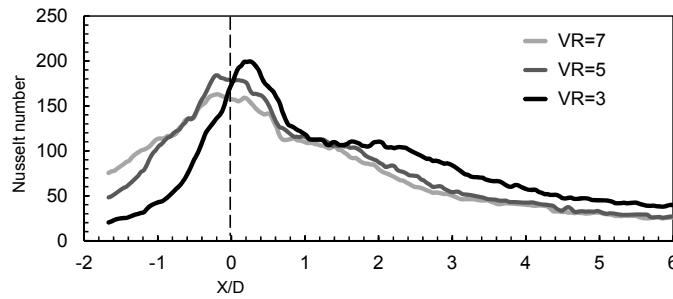


Fig.14. Nusselt number distribution along the crossflow direction ($Z/D=0$, $T_f=27^\circ\text{C}$ and $Re_f=13,400$)

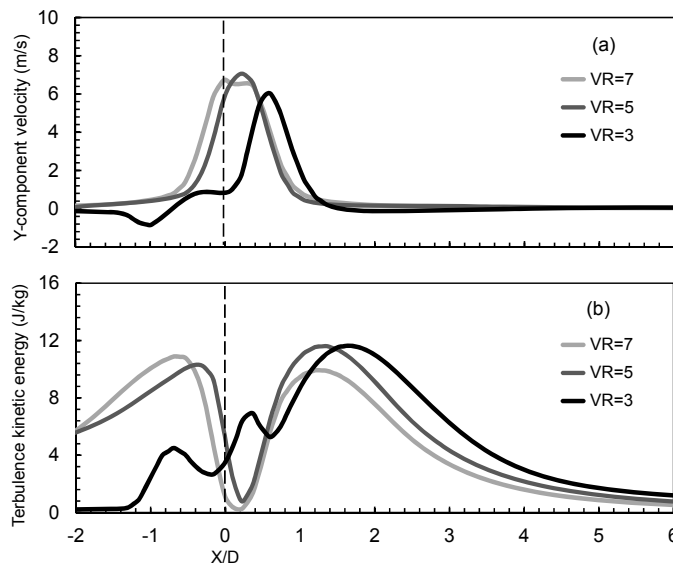


Fig.15. (a) Y-component velocity contours and (b) turbulence kinetic energy at 1.5-mm above the impinged surface (CFD result)

The flow visualization on the impinged surface by oil film technique is shown in Fig.12(a-c). The black area is an impinged surface where an oil film removed while the white area is a remaining oil film. A white point surrounded by black areas represents the stagnation point of the impinging jet bounded by the impingement region. The visualization shows that the upstream impingement region ($X/D < 0$) and both lateral sides ($\pm Z/D$) are contracted while the downstream impingement area is elongated as cross-flow velocity increases.

The Nusselt number distribution along the cross-flow direction at $Z/D=0$, is shown in Fig.14. The upstream Nusselt number ($X/D < 0$) becomes lower when cross-flow velocity increases. This corresponds to the contraction of the upstream impinged area as

shown in Fig.12. In contrast, the downstream Nusselt number ($X/D > 0$) becomes higher when the cross-flow velocity increases. At $VR=3$, the downstream Nusselt number for $2 < X/D < 3$ is conspicuously enhanced, due to the high turbulence kinetic energy of the range as revealed in Fig.15(b). In addition, the Nusselt number peak of the stagnation region increases with increasing cross-flow velocity. The highest Nusselt number peak takes place at $VR=3$ and $X/D=0.2$, as a result of the optimum synergy between the Y-component velocity and the turbulence kinetic energy. As shown in Fig.15, at $X/D=0.2$, the jet and cross-flow with $VR=3$ offer the peak of turbulence kinetic energy coupled with the moderate Y-component velocity. However, for $VR=3$, at $X/D=-0.8$ or 1.8 , the peak of turbulence kinetic energy takes place with a low Y-component velocity, resulting in a low Nusselt number. The lower Nusselt number peak at $VR=5$ and 7 as compared to that at $VR=3$ can be explained by the same fact.

The results in the present work reveal that at the low jet-to-plate distance ($2D$), the increase of cross-flow velocity corresponding to the decrease of VR from 7 to 3 , result in the increase of Nusselt number peak of the stagnation area. This is different from that found at large jet-to-plate distance ($\geq 3D$). In the latter case, Nusselt number peak of the stagnation area decreases as cross-flow velocity increases due to the large colliding area between cross-flow and jet impingement [4, 17].

5.1.2 Heat transfer characteristics for $AR=4$ and 8

The effects of orifice geometry, attacking angle and cross-flow velocity on local heat transfer distribution on impingement surface of single jet are shown in Fig.16. Generally, the Nusselt number is high at impingement regions and low at upstream regions. These areas of high Nusselt number are more contracted along upstream direction ($-X$ axis) and more extended along downstream one (X axis) when the cross-flow velocity increases. The areas of high Nusselt number, in addition, are more obliquely extended along $+Z$ axis when the attacking angle is larger.

The Nusselt number at stagnation region of $AR=4$ and 8 at $\theta=0^\circ$ (Fig.16(d)-(f) and (m)-(o)) are higher than those $AR=1$ (Fig.16(a)-(c)) under the same VR . These results show that the jet discharging from elongated orifice with $\theta=0^\circ$ can minimize the cross-flow effect. However, for the case of $\theta > 0^\circ$, these area of high Nusselt number along upstream direction are contracted, especially, for the case of large attacking angle ($\theta=30^\circ$) and high cross-flow velocity ($VR=3$) and longer orifice shape ($AR=8$) as shown in Fig.16(u).

The areas of high Nusselt number are extended in the X -axis and obliquely extended in the $+Z$ -axis when the attacking angle becomes larger. The extension of impingement regions in the X -axis is from the effect of cross-flow, and the oblique extension of these

regions in the +Z-axis is from the effect of attacking angle. More the detail of flow and heat transfer characteristics of this section will be concisely discussed in the row jet section.

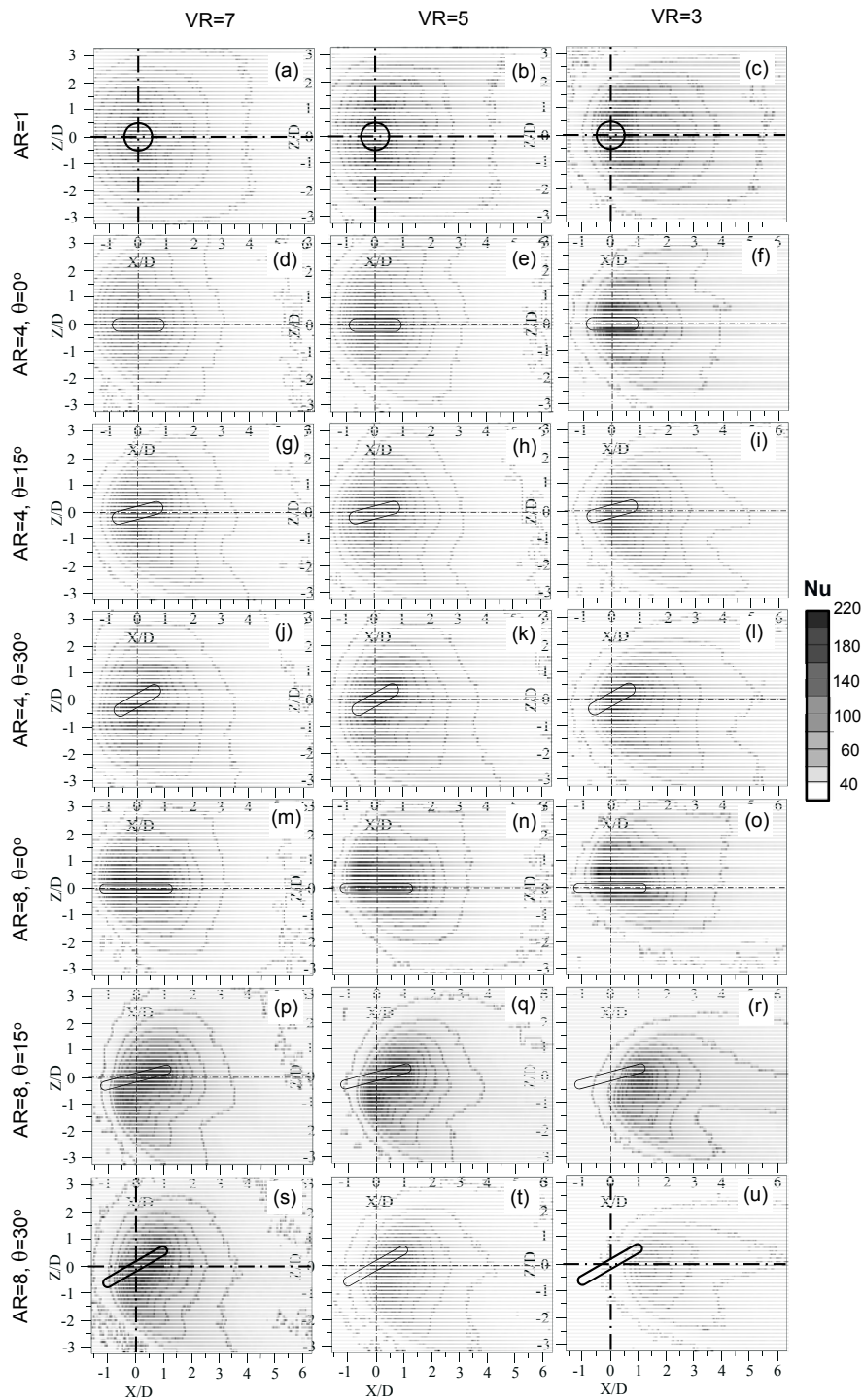
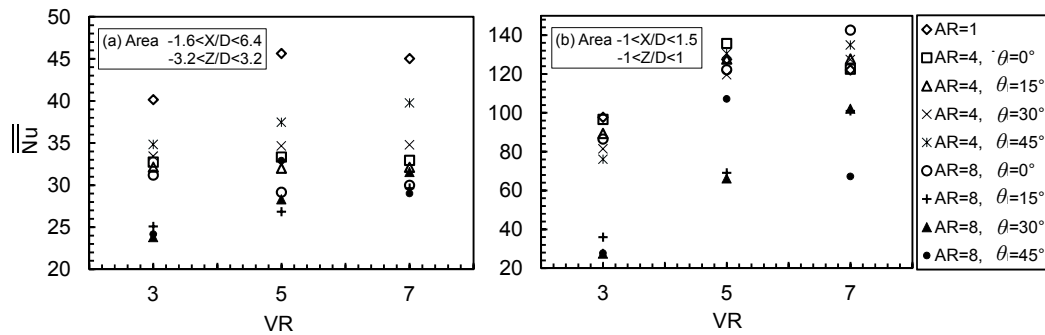


Fig.16. Nusselt number distributions on the impinged surface for the single jet (Experimental result, $T_f=27^\circ\text{C}$, $Re_j=13,400$).



(a) Area in region $-1.6 < X/D < 6.4$, $-3.2 < Z/D < 3.2$ (b) Area in region $-1 < X/D < 1.5$, $-1 < Z/D < 1$

Fig.17. Average Nusselt number on the impinging surface for the single jet (Experimental result, $T_f=27^\circ\text{C}$, $Re_j=13,400$).

5.1.3 The average Nusselt number

The variations of average Nusselt number calculated from the large heat transfer area, $-1.6 < X/D < 6.4$, $-3.2 < Z/D < 3.2$, and the small one, $-1 < X/D < 1.5$, $-1 < Z/D < 1$, are shown in Fig.17(a) and Fig.17(b), respectively. For the large heat transfer area (Fig.17(a)), the average Nusselt number in the case of $AR=1$ is higher than the others at any VR . When consider the small heat transfer area as shown in Fig.17(b), it was found that the average values of some parameters of the elongated orifice are higher than those the case of round orifice. This was shown that the jet from the elongated orifice can increase heat transfer rate particularly in the stagnation region; the heat transfer at around stagnation region can not be increased. However, when elongated orifice is applied on multiple of impinging jets, the area around stagnation is confined by nearby jet. The heat transfer surface will be concentrated by the enhancement heat transfer area in stagnation region corresponding to number of the impinging jet. This matter will be shown in the section of multiple impingement.

5.2 A row of Impinging jets under simulated cross-flow

In this section, flow and heat transfer characteristics for the case of row of jets with $AR=1$ will be initially explained, and the ones with $AR=4$ and 8 will be latterly discussed. More details of this section have been written in publication as attached in **Appendix B**.

5.2.1 Flow and heat transfer characteristics for $AR=1$

The effect of cross-flow velocity on flow and heat transfer characteristics of $AR=1$ are shown in Fig.18-20. The Nusselt number distributions on impinged surface as shown in Fig.20 coincide with flow patterns and Y-component velocity contours on the impinged surface as shown in Fig.18 and 19. As cross-flow velocity increased (VR decreased),

the area with high Nusselt number (corresponding to black area of oil film pattern and high Y-component velocity) shifted downstream. It should be mentioned that Nusselt number was also high in the middle between the adjacent impingement regions. This location corresponds to the area in which oil film was removed in Fig.18, where Y-component velocity was negative in Fig.19. The flow and heat transfer characteristics of this row of impinging jet are similar to those single impinging jet, but the areas of high Nusselt number (corresponding to black area of oil film pattern and high Y-component velocity) are getting smaller due to confinement of adjacent jets.

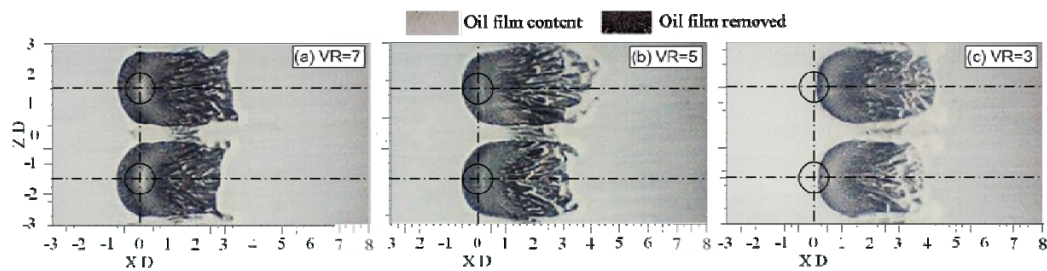


Fig.18. Flow patterns on the impinged surface for $AR=1$ (Experimental result)

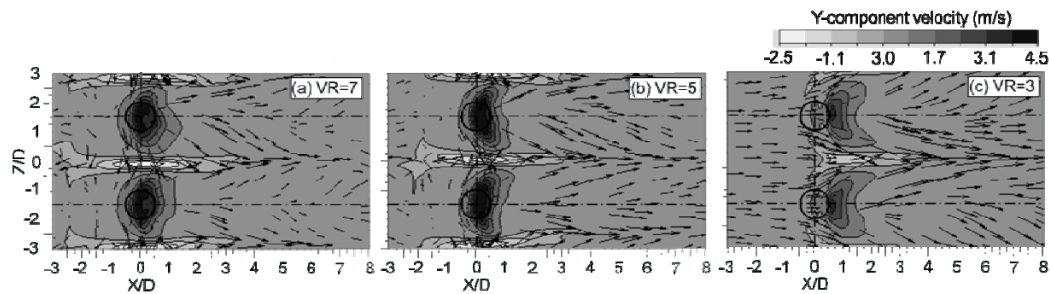


Fig.19. Velocity vectors and Y-component velocity contours on X-Z plane for $AR=1$ (CFD result, above from target surface of 1.5-mm)

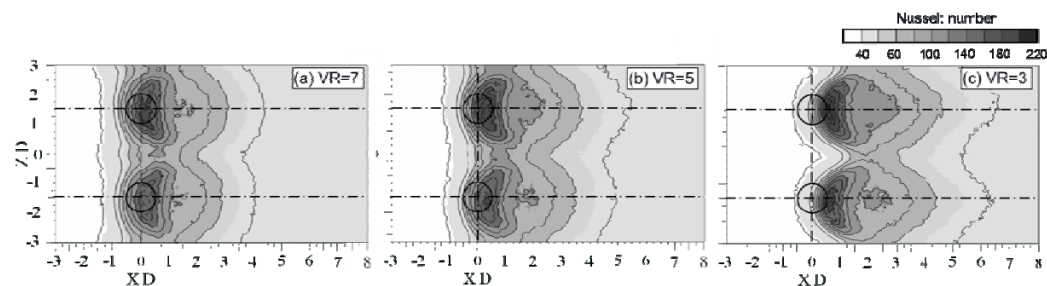


Fig.20. Nusselt distributions on the impinged surface for $AR=1$ (Experimental result)

5.2.2 Flow and heat transfer characteristics for $AR=4$ and 8

The effect of orifice geometry and arrangement on local Nusselt number distributions on the impingement surface are shown in Fig.21. Areas of high Nusselt number of $AR=1$ are more shifted to downstream directions when cross-flow velocity increases as shown in Fig.21(a)-(c). For the case of $AR=4$ and 8 with $\theta=0^\circ$ as shown in Fig.21(d)-(f) and (p)-(r), the shifting of areas of high Nusselt number to downstream direction at high cross-flow velocity are minimized when compare with the case of $AR=1$. This is due to jets from elongated orifices can more penetrate into the cross-flow.

When compare the effect of orifice arrangement, it is found that the area of high Nusselt number are obliquely shifted in spanwise direction ($\pm Z$ -axis) depending on the direction of orifice arrangement. In the case of parallel orifice configuration as shown in Fig.21(g)-(i) and (s)-(u), the area of high Nusselt number are obliquely shifted in $+Z$ -axis. For the case of counter-convergent orifice configuration as shown in Fig.21(j)-(l) and (v)-(x), the areas of high Nusselt number shift separately in Z -axis while they shift combinely in Z -axis for the case of counter-divergent orifice configuration as shown in Fig.21(m)-(o) and (y)-(a1). These characteristics of Nusselt number distributions are corresponding to the deflections of impinging jets in Z -axis as shown in Fig.22. In addition, the shifting of these areas along X - and Z -axes are larger when the the cross-flow velocity increases.

5.2.3 The average Nusselt number

The average Nusselt numbers on the impingement surface versus the attacking angle are shown in Fig.23. Almost all average values for $AR=4$ is higher than those the case of $AR=8$. For the case of high cross-flow velocity, $VR=3$, the average Nusselt number is decreased when the attacking angle increases. This average values of $AR=4$ with counter-divergent orifice configuration for $VR=5$ and 7 are slightly increased when attacking angle increases from $\theta=15^\circ$ to $\theta=30^\circ$. For the other cases, the average values are decreased when attacking angle increase.

When compare the effect of orifice configurations, almost all average values of counter-divergent orifice configuration is higher than those the others. This can be noted that the higher heat transfer for the case of counter-divergent orifice configuration is from enhancement local heat transfer along orifice interval due to inclination interaction of both adjacent wall jets.

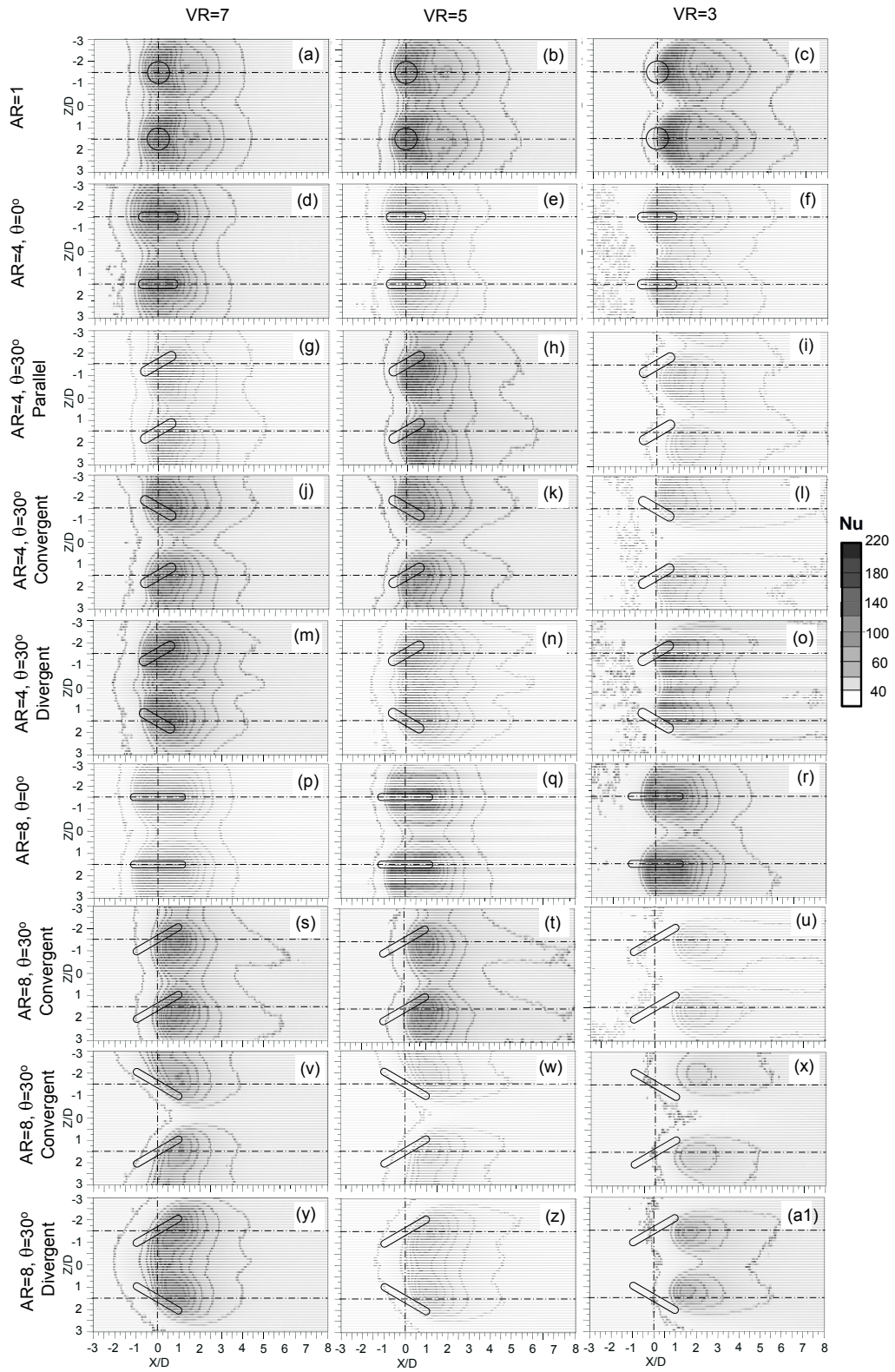


Fig.21. Nusselt distributions on the impinging surface of row of impinging jets (Experimental result)

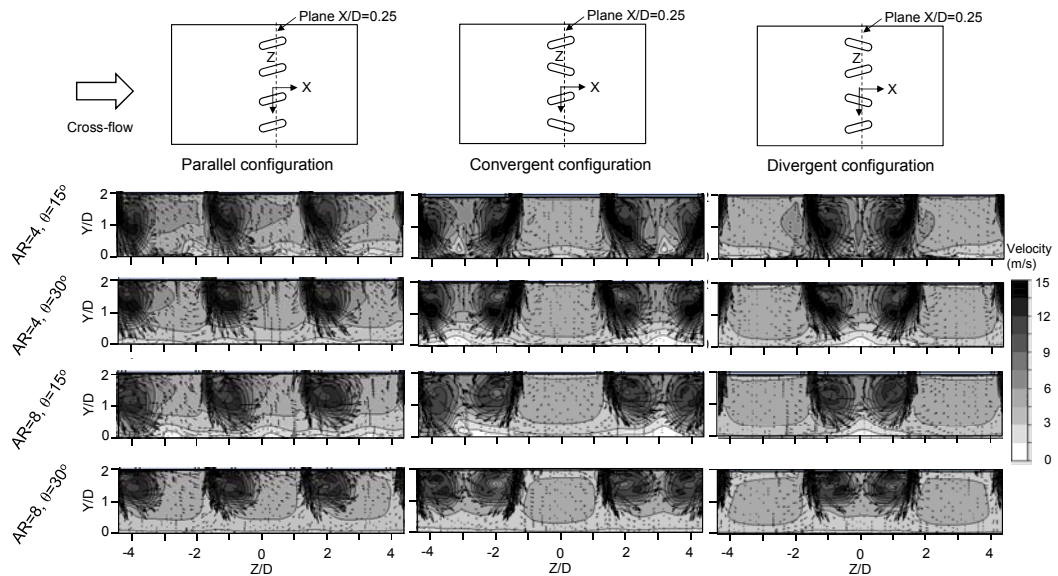


Fig.22. Vectors and contours of velocity in Y-Z plane at $X/D=0.25$ for $VR=3$.

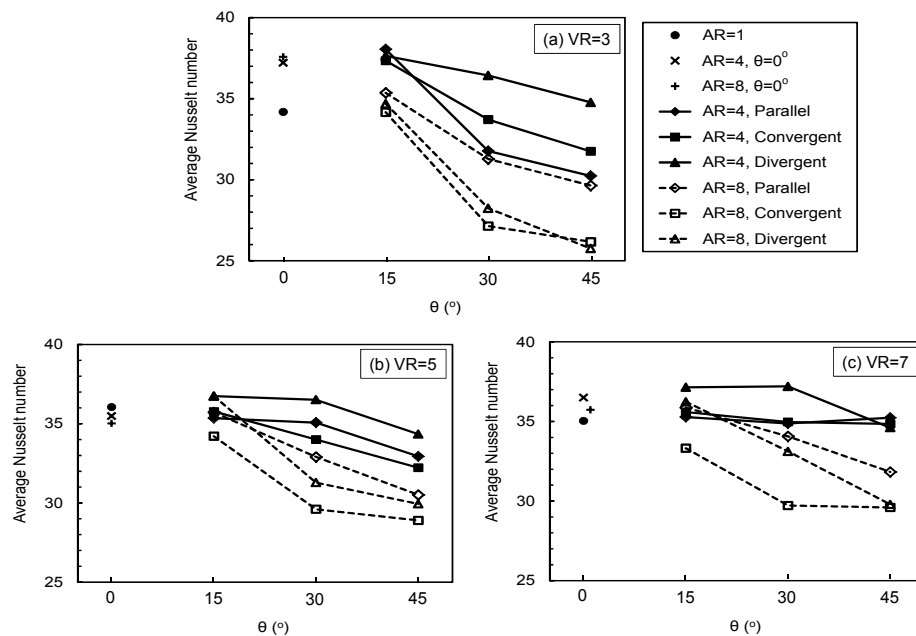


Fig.23. Average Nusselt number (Experimental result).

5.3 Jet impingement array

In this section, flow and heat transfer characteristics for the case of array of impinging jet will be briefly discussed. To easily understand, the results of $AR=1, 4$ and 8 at $\theta=0^\circ$ for both inline and staggered arrangement will be firstly explained, and the results with

the same parameters at $\theta > 0^\circ$ will be secondly clarified. More discussion of this section has been written in publication as attached in **Appendix C**.

Flow patterns on the impingement surface are shown in Fig.24 and 25, and velocity vector and contour in the Y-axis on Z-X plane near the impingement surface (1 mm above the surface) are shown in Fig.26 and 27. The Nusselt number distributions on the impingement surface are shown in Fig.32 and 33. These contours of Nusselt number agree well with the oil film patterns on the impingement surface, as well as the contours of Y-component velocity near the impingement surface. Areas of high Nusselt number ($Nu > 180$) are impingement regions that relate to the black area of flow patterns and high Y-component velocity in flow fields. This good agreement can be correspondingly used to explain the characteristics of jets flow from the CFD results on the flow and heat transfer behavior from the experiment.

5.3.1 Flow and heat transfer characteristics for $AR=1, 4$ and 8 with $\theta=0^\circ$

To preliminarily discuss in this sub-section at $\theta=0^\circ$, Fig.24(a)-(c), Fig.25(a)-(c), Fig.26(a)-(c) and Fig.27(a)-(c) will be presented for flow patterns, and the Fig.32(a)-(c) and Fig.33(a)-(c) will be presented for heat transfer characteristics.

Flow characteristics; for both inline and staggered arrangements of $AR=1$ as shown in Fig.24(a) and Fig.25(a), the impingement area of each cell are shifted to downstream direction due to the effect of cross-flow. This cross-flow effect on jet impingements with inline arrangement is less significant than on the ones with the staggered arrangement by notifying cancellation of the impingements at downstream region ($13 < X/D < 20$). This flow characteristic can be explained that the cross-flow can easily pass through space between rows of inline jets, whereas it was blocked by downstream jets in the case of staggered arrangement (more discussion in **Appendix C3**). It can be seen that there are no impingement regions (Black areas) at the last jet column in Fig.24(a) and no areas of high Y-component velocity contour at the same jet column as shown in Fig.26(a). It can also be observed that the deflection of downstream impinging jets with staggered arrangement as shown in Fig.29(a) is stronger than those with the inline one as shown in Fig.28(a).

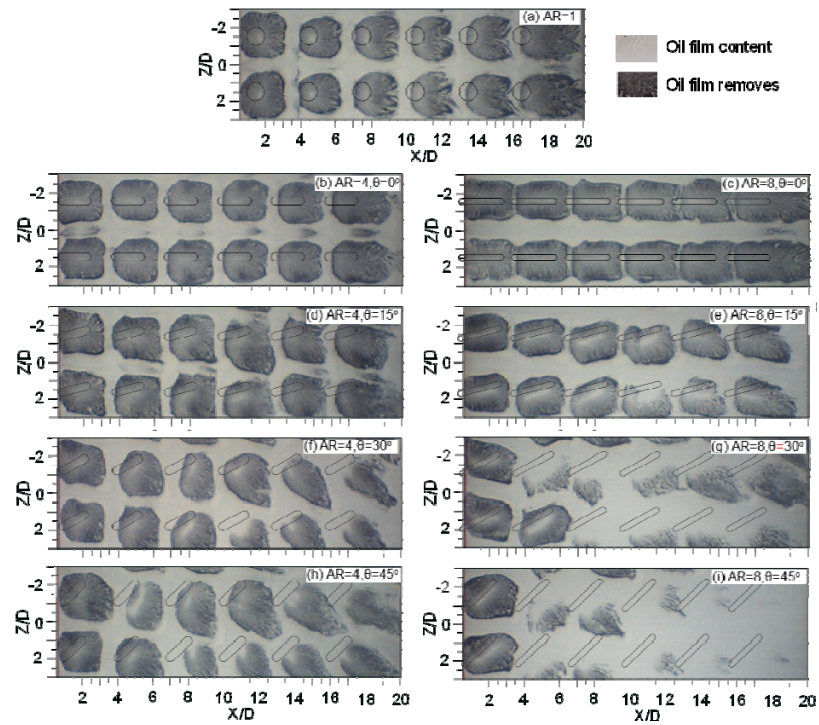


Fig.24. Flow patterns on the impingement surface with oil film technique for the inline arrangement and $Re=13,400$ (Experimental results).

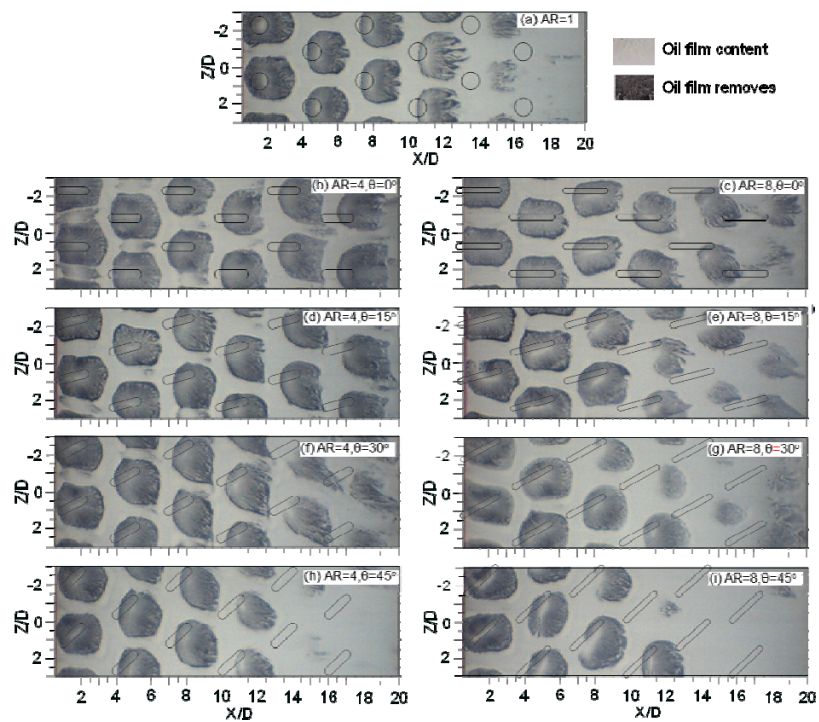


Fig.25. Flow patterns on the impingement surface with oil film technique for the staggered arrangement and $Re=13,400$ (Experimental results).

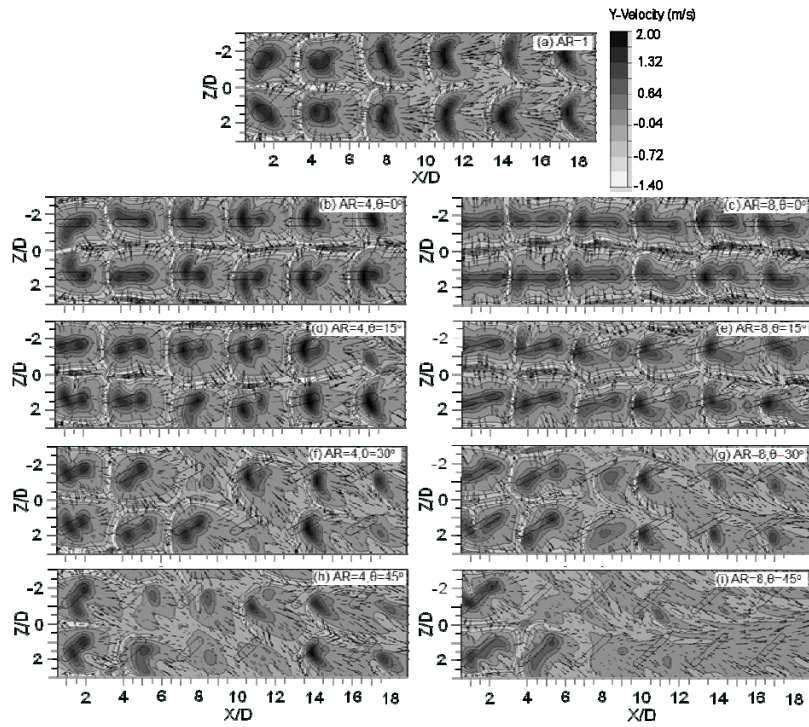


Fig.26. Flow characteristic of impinging jets on Z-X plane above the impingement surface of 1 mm for the in-line arrangement and $Re=13,400$ (CFD results).

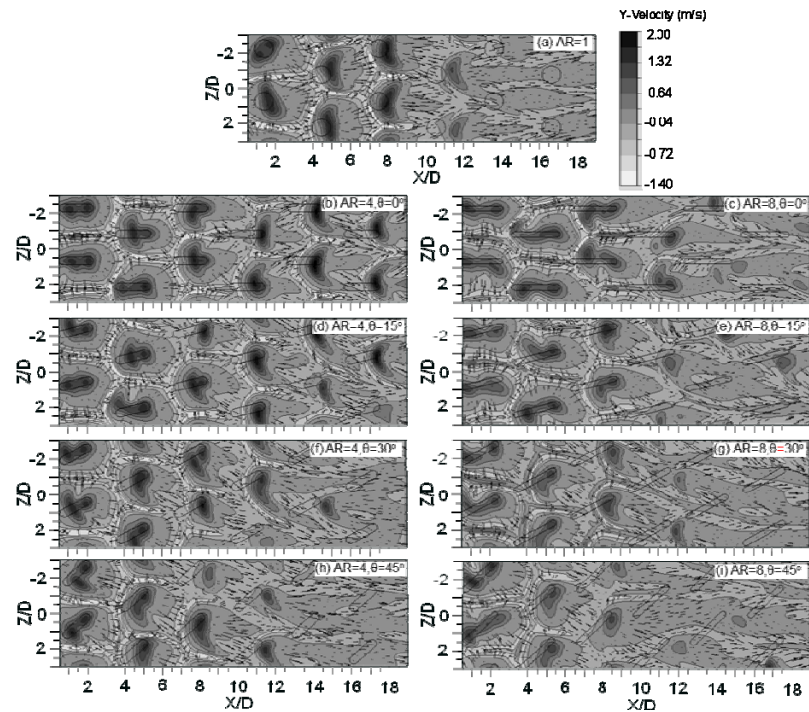


Fig.27. Flow characteristic of impinging jets on Z-X plane above the impingement surface of 1 mm for the staggered arrangement and $Re=13,400$ (CFD results).

In the case of orifice with $AR=4$ and 8 at $\theta=0^\circ$, it is found that the cross-flow effect can be minimized by these elongated orifices for the inline arrangement, notified by getting the larger impingement region of $AR=4$ and 8 (black region in Fig.24(b) and (c)) than those the $AR=1$ (Fig.24(a)). For the case of staggered arrangement, the impingement region (Black region) at downstream region ($10 < X/D < 20$) of $AR=8$ (Fig.25(c)) is larger than that $AR=1$ (Fig.25(a)), but it seem to be smaller comparing to those $AR=4$ (Fig.25(b)). This is due to the jet issuing from elongated orifice with $AR=8$ producing the longer circumference as well as increasing contact area to mix with the cross-flow. It can also be observed that the Y-component velocity areas at the downstream direction of $AR=8$ (Fig.27(c)) are smaller than that the $AR=4$ (Fig.27(b)) and larger than those $AR=1$ (Fig.27(a)). Corresponding to preceding paragraph, with the case of $\theta=0^\circ$, the use of jet with $AR=4$ and inline arrangement can be minimized the cross-flow effect. More details of this section have been intensely discussed in **Appendix C4**.

Heat transfer characteristics; The Nusselt number distribution on the impingement surface for $AR=1, 4$ and 8 at $\theta=0^\circ$ with $Re=13,400$ for both jet arrangements are shown in Fig.32(a)-(c) and Fig.33(a)-(c). Generally, the heat transfer rates of impinging jets for $AR=4$ and 8 at $\theta=0^\circ$ are higher than those for $AR=1$, and the areas of high heat transfer are shifted further downstream. Apparently, Nusselt number associated by the jets with an inline arrangement are less significantly affected by the cross-flow than those with staggered arrangement indicated by a more uniform Nusselt number distribution on the impinged surface. For the inline jet arrays at all AR, Nusselt number of downstream jets is just slightly decreased compared to those of the upstream ones. On the other hand, for the staggered jet arrays with $AR=1$ and 8 , Nusselt number is dramatically changed with increasing axial distance (X/D). Only at $AR=4$, Nusselt number is gradually decreased along the axial direction.

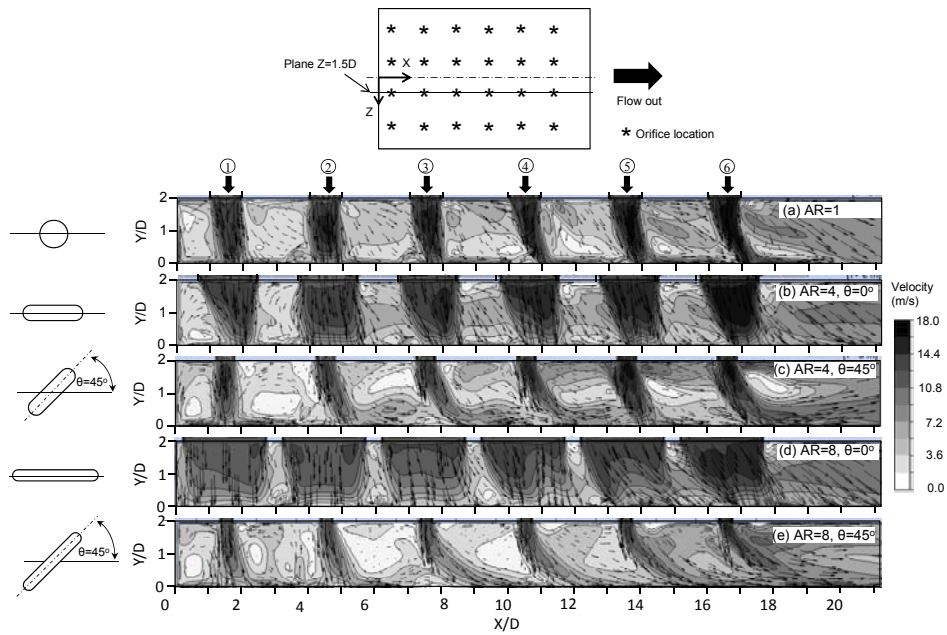


Fig.28. Flow characteristic of impinging jets on X-Y plane at $Z=1.5D_E$ for the in-line arrangement and $Re=13,400$ (CFD results, Numbers in marked circle indicate the jet column order).

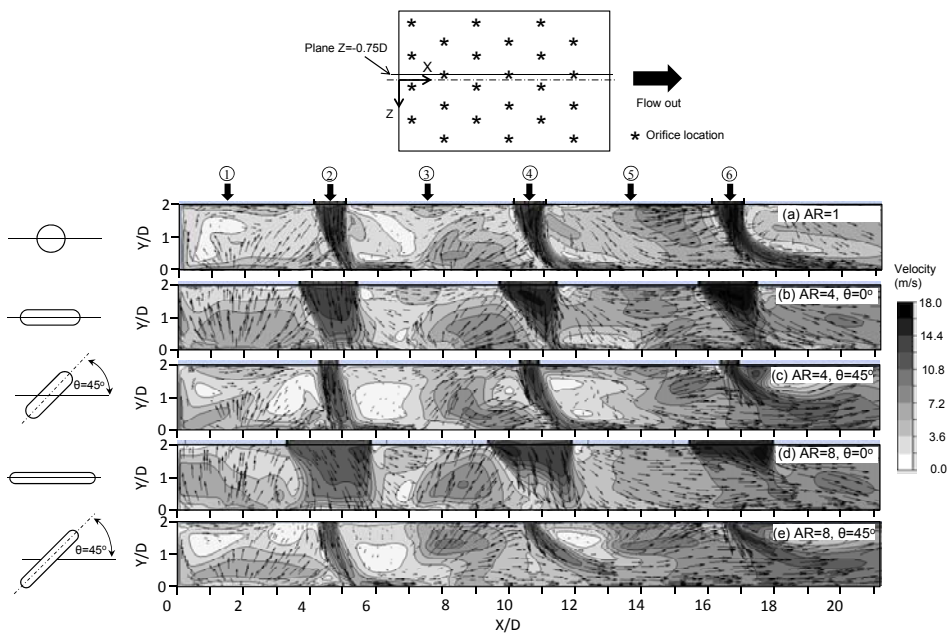


Fig.29. Flow characteristic of impinging jets on X-Y plane at $Z=-0.75D_E$ for the staggered arrangement and $Re=13,400$ (CFD results, Numbers in marked circle indicate the jet column order).

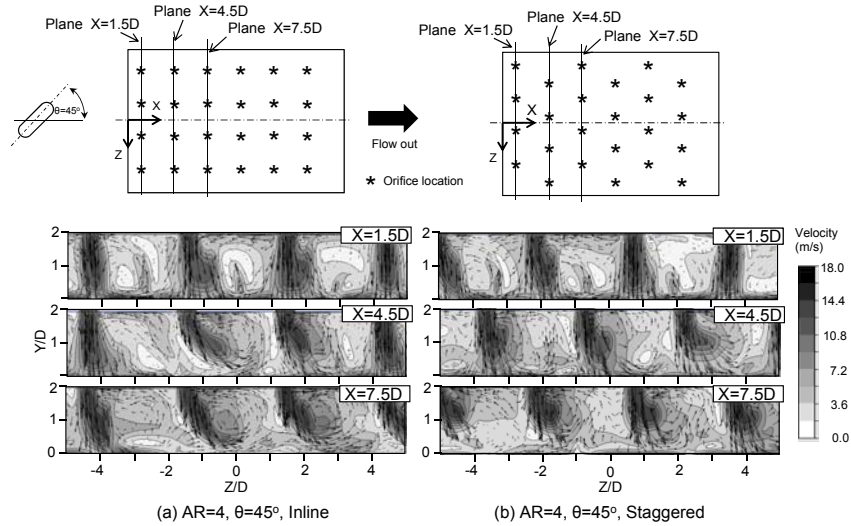


Fig.30. Flow characteristic of impinging jets on Y-Z plane for $AR=4$, $\theta=45^\circ$, and $Re=13,400$ (CFD results).

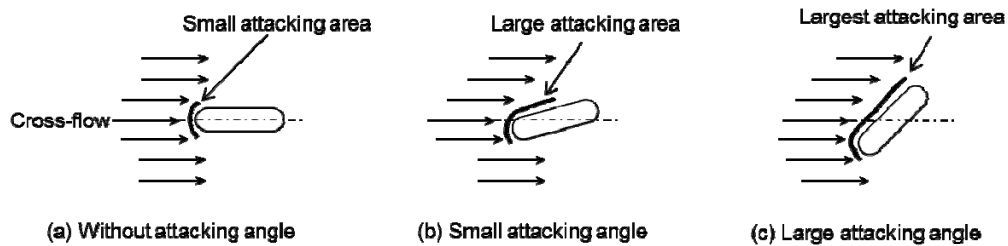


Fig.31. Sketch of the cross-flow through difference of attacking angle.

5.3.2 Flow and heat transfer characteristics for $AR=1$, 4 and 8 with attacking angle

Flow characteristics; flow characteristics for the case of $AR=4$ with $\theta=15^\circ$ for the inline arrangement as shown in Fig.24(d), the impingement region of each cell is directly extended in the X-axis and obliquely extended in the Z-axis. In addition, each impingement cell is more obliquely extended in the +Z-axis and contracted in the -Z-axis when the attacking angle becomes larger, at $\theta=30^\circ$ and 45° as shown in Fig.24(f) and (h). This is different from those with $AR=4$ at $\theta=0^\circ$, that the impingement regions are particularly extended in the X-axis (without extending into the +Z-axis) as shown in Fig.24(b).

The extension of the impingement regions to the downstream direction is from the cross-flow effect. It can be observed from Fig.28 and 29 that the downstream impinging jets (jet columns No.4 to 6) are more deflect to cross-flow part line than that the

upstream jets (jet columns No.1 to 3). The oblique extension of impingement region to the +Z direction is from the attacking angle effect as shown in Fig.30. The jets are deflected in the +Z direction along the orifice configurations. This deflection is stronger when location of jets is far from the first jet column. Moreover, the deflection of jets with staggered arrangement is larger than the one with inline that will be discussed in the next section.

For the case with $AR=8$ at $\theta=15^\circ$ with the inline arrangement as shown in Fig. 24(e), the characteristics of flow patterns of the jets is similar to the case with $AR=4$ under the same attacking angle mentioned above. However, when the attacking angle becomes $\theta=30^\circ$ and 45° , the impingement regions at $4 < X/D < 20$ seem to be getting smaller as shown in Fig. 24(g) and (i). For the case of the largest attacking angle, $\theta=45^\circ$, particularly, there is no impingement area in the downstream region ($13 < X/D < 20$) because the high cross-flow velocity strikes on the jet flow with the large attacking area. This can be observed in Fig.28(e) for the case of $AR=8$ at $\theta=45^\circ$ that the downstream impinging jets (columns 5 and 6) tend to deflect to cross-flow part line with slightly impinging on the target surface.

When the inline and staggered arrangements are compared, it is found that the impingement regions for the inline arrangement can be seen throughout the streamwise direction (except for the case of $AR=8$ at $\theta=30^\circ$ and 45°). This flow characteristics are similar to the case of staggered arrangement for $AR=4$ at $\theta=0^\circ$, $\theta=15^\circ$, $\theta=30^\circ$ (Fig.25(b), (d) and (f)) and $AR=8$ at $\theta=0^\circ$ (Fig.25(c)). However, for the others, they are unclearly expressed at the downstream area ($10 < X/D < 20$). The absence of the impingement regions corresponds to the stronger deflection of the downstream jet with staggered arrangement as compared at the same conditions between Fig.28 and 29.

Results show that the attacking angle has significant effects on the impinging jet array of the elongated orifice as schematically sketched in Fig.31. For the case of attacking angle $\theta=0^\circ$, the cross-flow strikes on the jet issuing from the elongated orifice with the small attacking area as depicted in Fig.31(a). This attacking area becomes larger when the attacking angle is increased, as shown in Fig.31(b) and (c). Moreover, the attacking angle effect for the case of $AR=8$ is more prominent than for the case of $AR=4$ due to the longer perimeter of $AR=8$. Consequently, the deflection of jet from the orifice with $AR=8$ is larger than the case of $AR=4$ as mentioned above.

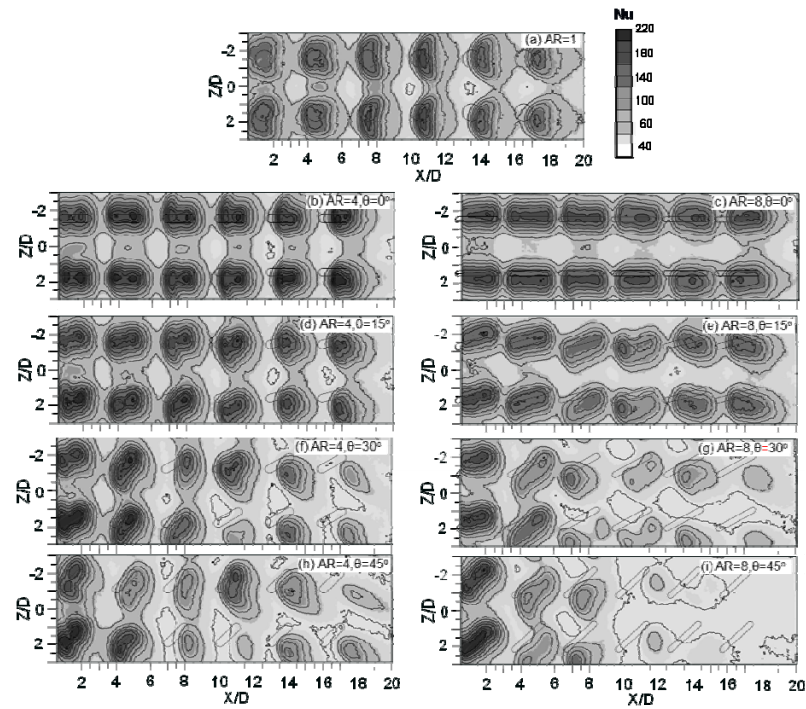


Fig.32. Nusselt number distributions on the impingement surface for the inline arrangement and $Re=13,400$ (Experimental results, $T_f=27^\circ\text{C}$).

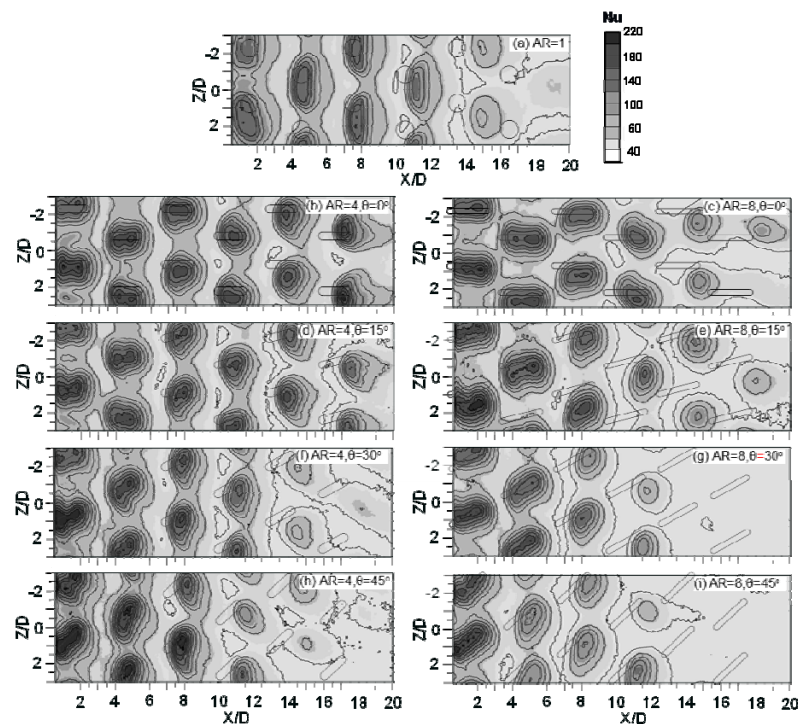


Fig.33. Nusselt number distributions on the impingement surface for the staggered arrangement and $Re=13,400$ (Experimental results, $T_f=27^\circ\text{C}$).

Heat transfer characteristics; the characteristics of Nusselt number distributions for the case of a small attacking angle, $\theta=15^\circ$ (Fig.32(d), (e) and Fig.33(d), (e)), is comparable to those with the attacking angle of $\theta=0^\circ$ (Fig.32(b), (c) and Fig.33(b), (c)), but the heat transfer characteristic is quite different from the case of large attacking angles at $\theta=30^\circ$ and 45° (Fig.32(f)-(i) and Fig.33(f)-(i)). The Nusselt number in the downstream region ($10 < X/D < 20$) of both jet arrangements abruptly decreases when the attacking angle is larger due to increasing attacking area between the cross-flow and the impinging jets, as discussed earlier on the jet flow characteristics.

Indeed, the areas of high Nusselt number ($Nu > 180$) in each impingement cell are extended in the X-axis and obliquely extended in the +Z-axis when the attacking angle is larger. This corresponds well to those impingement regions on the surface as shown before in Fig.24 and 25 by oil film technique, and in Fig.26 and 27 by CFD. The extension of these high value areas in the X-axis is from the effect of cross-flow shown earlier in Fig.28 and 29, and the oblique extension of these areas in the +Z-axis is from the effect of attacking angle as previously illustrated in Fig.30.

From Fig.33, the area of high Nusselt number (corresponding to impingement regions) of each impingement cell for inline arrangement with $AR=4$ and 8 at $\theta=0^\circ$ and 15° is rather uniformly distributed from upstream to downstream direction. These areas become smaller when the attacking angle become larger to be $\theta=30^\circ$ and 45° . Especially for the case of $AR=8$ and $\theta=45^\circ$, there are no impingement region for the last jet column as shown in Fig.33(i). This is due to large blocked area from the long circumference of orifice with $AR=8$ and the large attacking angle at significant cross-flow effect at downstream direction as earlier discussion in flow characteristics. These area becoming smaller at downstream direction is clearly seen for the case of staggered arrangement as shown in Fig.33 accept for $AR=4$ with $\theta=0^\circ$ and 15° as shown in Fig.33(b) and (d). The distribution of area of high Nusselt number is rather consistent from upstream to downstream direction. This is shown that the jet from $AR=4$ can be minimized the effect of cross-flow batter than that $AR=8$.

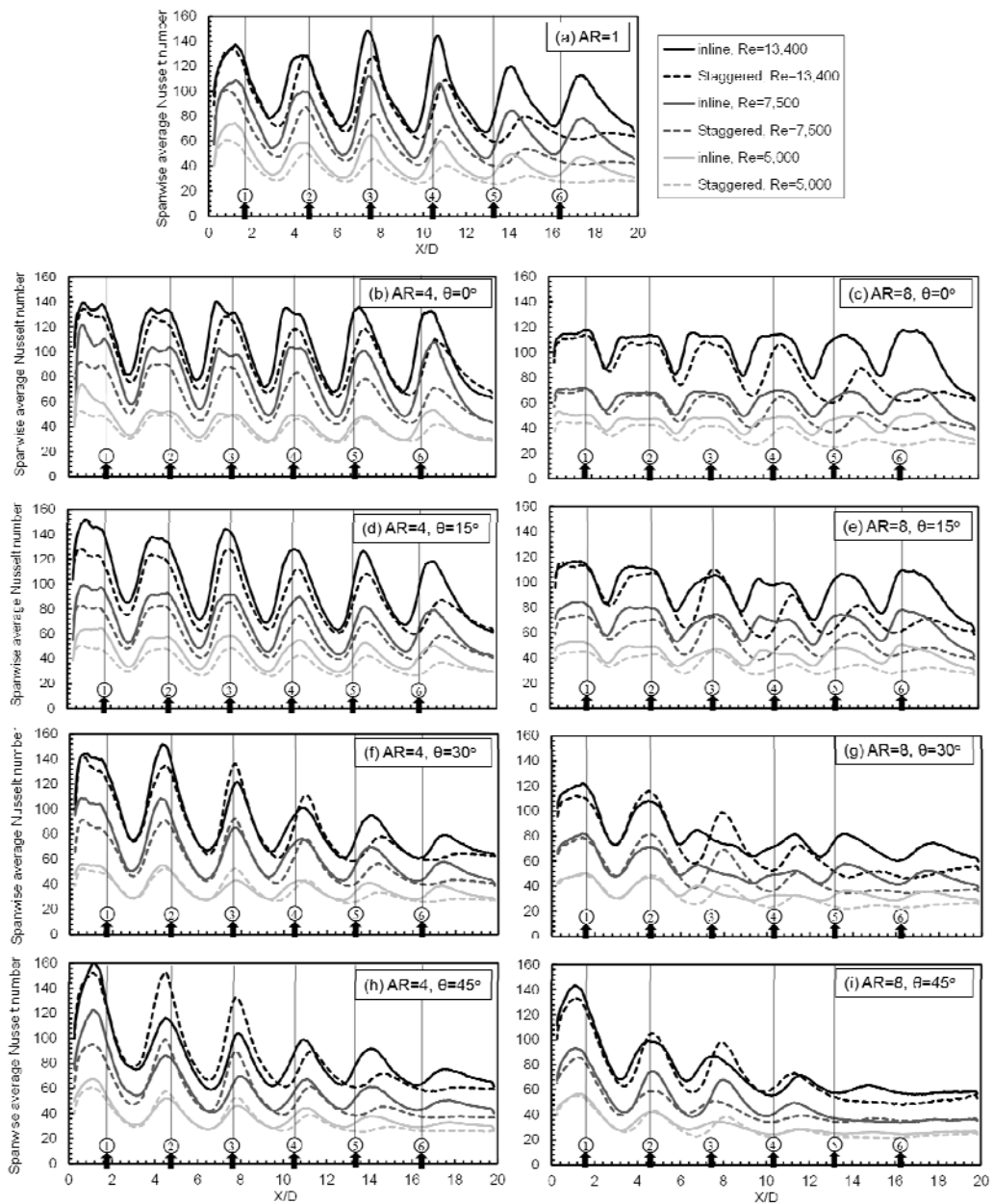


Fig.34. Spanwise average Nusselt number distribution along the cross-flow direction (Experimental results, $T_j = 26.7^\circ\text{C}$ and numbers in marked circle indicate the jet column order).

5.3.3 Spanwise average Nusselt number

Distributions of the spanwise average Nusselt number along the downstream direction for the case of $Re=5,000$, $7,500$ and $13,400$ are shown in Fig.34. Each value in this case is calculated from the local heat transfer coefficient, which in turn is dependent on the

average local wall temperatures taken in the range of $-3 < Z/D < 3$. Generally, decreasing Reynolds number, the value gets smaller while its distribution characteristics slightly change. Each distribution and its peak value at a particular X/D location for the case of attacking angle at $\theta=0^\circ$ and $\theta=15^\circ$ is quite similar and consistent compared to other spanwise locations, as shown in Fig.34(b)-(e). But, the peak value seems to be dramatically decreased when the attacking angle becomes larger at $\theta=30^\circ$ and 45° towards the downstream region ($10 < X/D < 20$), as shown in Fig.34(f)-(i). In the particular case of $AR=8$ at $\theta=45^\circ$ (Fig.34(i)), the distributions in this region become rather flat, especially for $Re=7,500$ and $5,000$ for both jet arrangements. This relates to those the cancelation of impingement of downstream jets as early shown in Fig.30(e).

Almost all of the spanwise average Nusselt number for the inline arrangement is higher than those of the staggered arrangement except their peak values at jet column 3 and 4 for $AR=4$ at $\theta=30^\circ$ (Fig.34(f)), and jet column 2 and 3 for $AR=8$ at $\theta=30^\circ$ (Fig. 34(g)), and $AR=4$ and 8 at $\theta=45^\circ$ (Fig.34(h) and (i)). This is due to the high local Nusselt number at their impingement regions resulting from the effects of jet arrangement and attacking angle at upstream region that the cross-flow effect is low.

5.3.4 The average Nusselt number

The average Nusselt number on the impingement surface calculated from the average local wall temperature in area of $0.5 < X/D < 20$ and $-3 < Z/D < 3$ versus the attacking angle are shown in Fig.35. Almost all of the average Nusselt number tend to decrease when the attacking angle is increased. However, as shown in Fig.35(b), for the case of $AR=8$ with $Re=7,500$ in both jet arrangements, the average value at $\theta=15^\circ$ is higher than that at $\theta=0^\circ$, but is still lower than that for the case of $AR=1$.

For the case of $AR=4$, $Re=13,400$ with the inline arrangement (Fig.35(c)), and $AR=8$, $Re=5,000$ with the staggered arrangement (Fig.35(a)), the corresponding average Nusselt number in the case of $\theta=15^\circ$ is slightly higher than that for $AR=1$, but is still lower than that at $\theta=0^\circ$. From these results, the effect of attacking angle is not very significant in increasing the heat transfer on the overall impingement surface. It can, however, increase local heat transfer in the upstream region, the area with minor cross-flow effect.

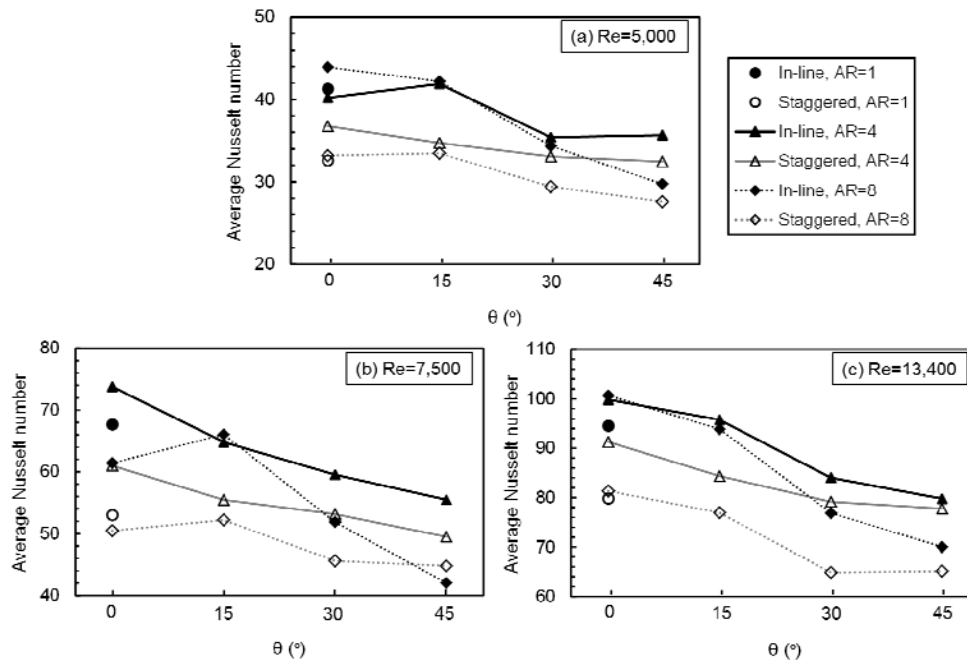


Fig.35. Average Nusselt number (Experimental result)

6. Concluding remarks

The main focus of this research is to enhance a heat transfer rate on surface of jet impingement by minimizing a cross-flow effect using elongated orifice. The matters were categorized by three parts; the first and second parts for a single and a row of impinging jet(s), respectively, under simulated cross-flow. The final one provides for impingement array with inline and staggered nozzle configurations. The main results can be concluded as follow;

1. Impinging jets discharging from both elongated orifice, $AR=4$ and 8 with $\theta=0^\circ$ can minimize the cross-flow effect. The deflections of jets with $AR=4$ and 8 with $\theta=0^\circ$ toward the cross-flow direction are smaller than those conventional orifice, $AR=1$. This affects directly to enhance heat transfer rate on the impingement surface by getting a higher when compare with those conventional orifice.

2. The effects of small attacking angle ($\theta=15^\circ$) of elongated orifices on the flow and heat transfer characteristics of impinging jets are rather similar to the case of attacking angle at $\theta=0^\circ$. It is, however, quite different when the attacking angles become larger at $\theta=30^\circ$ and 45° . Deflections of impinging jets with larger attacking angles are more deflect to the cross-flow directions. The heat transfer rate on the impingement surface decreases greater when the attacking angle becomes larger.

3. For the single impinging jet and the row of impinging jets, the local heat transfer at impingement regions for the high cross-flow velocity are higher than that the low one. This result attributes the good matching between high Y-component velocity that impinge on target surface and high turbulence intensity distribution. This heat transfer behaviour was found for the case of low jet-to-plate distance.

4. The effects of elongated orifice configurations for the row of impinging jets with parallel, counter-convergent and counter-divergent configurations on the heat transfer characteristics show that the average values for the counter-divergent configuration are higher than those the others.

5. For the array of impinging jets, the effects of cross-flow on the flow and heat transfer characteristics in the staggered arrangement is stronger than those inline arrangement. The cross-flow can easily pass through the gaps between the rows of inline jets, whereas it appears to be directly blocked by the downstream jet in the case of staggered arrangement. This affects directly on the heat transfer that the average value of inline arrangement is higher than those the staggered one. When apply the elongated orifices to this impingement array system, it was found that the jets discharging from these elongated orifices with $AR=4$ can minimize the cross-flow effect despite for the case of staggered arrangement.

6. The effect of attacking angle for impinging jet array show that heat transfer on the impingement surface decreases greater when the attacking angle becomes larger. However, when specific area on this surface is considered, local heat transfer at the upstream region for large attacking angles $\theta=30^\circ$ and 45° is found to be higher than those for attacking angles $\theta=0^\circ$ and 15° , especially in the case of staggered arrangement. These results are also confirmed by flow visualization on the region with larger impingement area.

References

- [1] R. Viskanta, Heat transfer to impinging isothermal gas and flame jets, *Exp. Therm. Fluid Sci.* 6 (1993) 111-134.
- [2] L.-E. Brizzi, A. Bernard, J.-L. Bousgarbies, E. Dorignac, J.-J. Vullierme, Study of several impinging jets, *J. Thermal Science* 9 (2000) 217-223.
- [3] B.P.E. Dano, J.A. Liburdy, Structure detection and analysis of non-circular impinging jets in a semi-confined array configuration, *Exp. Therm. Fluid Sci.* 31 (2007) 991-1003.
- [4] L.W. Florschuetz, C.R. Truman, D.E. Metzger, Streamwise flow and heat transfer distributions for jet array impingement with crossflow, *J. Heat Transfer-Trans. ASME.* 103 (1981) 337-342.
- [5] V. Katti, S.V. Prabhu, Influence of spanwise pitch local heat transfer distribution for in-line arrays of circular jets with air flow in two opposite, *Exp. Therm. Fluid Sci.* 14 (2008) 84-95.
- [6] E.I. Esposito, Jet impingement cooling configurations for gas turbine combustion, Thesis of Master in Mechanical Engineering, Louisiana State University (2006).
- [7] D.-H. Rhee, P.-H. Yoon, H.H. Cho, Local heat/mass transfer and flow characteristics of array impinging jets with effusion holes ejecting spent air, *Int. J. Heat Mass Transfer* 46 (2003) 1049-1061.
- [8] T.B. Hoberg, A.J. Onstad, J.K. Eaton, Heat transfer measurements for jet impingement arrays with local extraction, *Int. J. Heat Fluid Flow* 31 (2010) 406-467.
- [9] H.-C. Chiu, J.-H. Jang, W.-M. Yan, Experimental study on the heat transfer under impinging elliptic jet array along a film hole surface using liquid crystal thermograph, *Int. J. Heat Mass Transfer* 52 (2009) 4435-4448.
- [10] G. Biswas, K. Torii, D. Fujii, K. Nishino, Numerical and experimental determination of flow structure and heat transfer effects of longitudinal vortices in a channel flow, *Int. J. Heat Mass Transfer* 39 (1996) 3441-3451.
- [11] L.-T. Tian, Y.-L. He, Y.-G. Lei, W.-Q. Tao, Numerical study of fluid flow and heat transfer in a flat-plate channel with longitudinal vortex generators by applying field synergy principle analysis. *Int. Commun. Heat Mass Transfer* 36 (2009) 111-120.
- [12] Y. Shi, M.B. Ray, A.S. Mujumdar, Numerical study on the effect of cross-flow on turbulent flow and heat transfer characteristics under normal and oblique semi-confined impinging slot jets, *Drying Technology* 21 (2003) 1923-1939.
- [13] N. Zuckerman, N. Lion, Jet impingement heat transfer: physics, correlations, Numerical modeling, *Advances Heat Transfer* 39 (2006) 565-631.

- [14] T.T. Chandratilleke, D. Jagannatha, R. Narayanaswamy, Heat transfer enhancement in microchannels with cross-flow synthetic jets, *Int. J. Therm. Sci.* 49 (2010) 504-513.
- [15] M-W. Heo, K.-D. Lee, K.-Y. Kim, Optimization of an inclined elliptic impinging jet with cross flow for enhancing heat transfer, *Heat Mass Transfer* 47 (2011) 731-742.
- [16] Y.-T. Yang, Y.-X. Wang, Three-dimensional numerical simulations of an inclined jet with cross-flow, *Int. J. Heat Mass Transfer* 48 (2005) 4019-4027.
- [17] S. Ashforth-Frost and K. Jambunathan, Effect of nozzle geometry and semi-confinement on the potential core of a turbulent axisymmetric free jet, *Int. Comm. Heat Mass Transfer* 23, (1996) 155-162.

Appendix A

The publications of single impinging jet under simulated cross-flow

Appendix A1

Conference Paper 1

M. Wae-hayee, C. Nuntadusit, and P. Tekasakul “Effect of velocity ratio on flow and heat transfer characteristics of an impinging jet in crossflow”, The 5th PSU-UNS International Conference on Engineering and Technology (ICET-2011), Phuket, May 2-3,



The 5th PSU-UNS International Conference on Engineering and Technology (ICET-2011), Phuket, May 2-3, 2011
 Prince of Songkla University, Faculty of Engineering
 Hat Yai, Songkhla, Thailand 90112

EFFECT OF VELOCITY RATIO ON FLOW AND HEAT TRANSFER CHARACTERISTICS OF AN IMPINGING JET IN CROSSFLOW

M. Wae-hayee¹, C. Nuntadusit^{1*}, P. Tekasakul¹

1. Department of Mechanical Engineering, Faculty of Engineering,
 Prince of Songkla University, Hatyai, Songkhla, Thailand

*Authors to correspondence should be addressed via email: chayut@me.psu.ac.th

Abstract: The effect of velocity ratio (VR , ratio of jet velocity to crossflow velocity) on flow and heat transfer characteristics on an impinging jet with crossflow was investigated. The air jet issued from circular orifice and then impinged normal to heated surface in wind tunnel. The jet-to-plate distance (H , wind tunnel height) was fixed at $2D$ (D is orifice diameter). The velocity ratios were varied from $VR=3, 5$ and 7 . The temperature distribution on an impinged surface was visualized by using thermochromic liquid crystal sheet (TLCs) and Nusselt number distribution was evaluated with image processing technique. The flow patterns on impinged surface were visualized by using oil film technique. The numerical simulation was also employed to gain insight into the fluid flow of jet impingement in the crossflow. The results show that the averaged Nusselt number was highest in case of $VR=5$. The heat transfer in jet impingement region was enhanced when increasing VR from 0 to 5 and the heat transfer was decreased again when increasing VR from 5 to 7 . The locations of maximum Nusselt number were shifted to downstream direction due to crossflow and the interaction between impinged jet and cross flow near the wall was revealed.

Key Words: Impinging jet, Crossflow, Thermochromic liquid crystal sheet, CFDs

1. INTRODUCTION

Jet impingement is a high-performance technique for heat transfer enhancement in thermal equipment. It has been also used in industrial process for a heating, cooling or drying. It provides for rapid cooling or heating on local heat transfer area. However, the heat transfer rate is very high on jet directly impinged area. Many of thermal industrial applications have large heat transfer area such as, a combustor wall chamber and gas turbine blade cooling, steel and glass quenching, textile and paper drying. A high and uniform heat transfer rate is required over entire that areas. Hence, multiple of impinging jets are applied.

Multiple of impinging jets are formed by number of individual jet impingements. The flow and heat transfer characteristics of multiple impinging jets are influenced by two interactions. First is an interaction between adjacent before impingement wall and secondly, the wall jets formed by the adjacent jets collide on the target surface [1]. Another parameter that influences multiple jet impingements in a confined space is the crossflow. The crossflow is defined as the fluid flow in the direction perpendicular to the jet impingement flow. The crossflow can be either due to external flow resource or due to accumulated spent jet fluid flow. The crossflow has been found to significantly reduce the heat transfer of impinging jet in downstream [2, 3].

Goldstein and Behbahani [4] studied the single jet impingement from a circular pipe orifice for case of with and without crossflow. The results show that a maximum Nusselt number decreases with increasing flux momentum of crossflow for jet-to-plate distance $H=12D$ (D is orifice diameter) and the maximum Nusselt number increases, when decreased the jet-to-plate distance to $H=6D$ with moderate flux momentum of crossflow. Bouchez and Goldstein [5] experimentally studied the local heat transfer on the impinged surface and flow visualization of the jet in the crossflow, the experiment carried out of the single jet impingement from a circular pipe orifice normal to a surface, the results show that the low velocity of crossflow can created a recirculation zone upstream of the stagnation point and the heat transfer coefficient for jet-to-plate distance $H=6D$ has higher than $H=12D$ for all flux momentum ratios.

Barata and Durao [6] investigated the flow characteristic of an impinging jet in crossflow. They found that the upstream side of wall jet interacted with the crossflow and formed a vertex close to the ground target plate which flow was similar to the horseshoe structure. Nakabe et al. [7] experimentally studied a single inclined impinging jet in the crossflow with jet to crossflow velocity $VR=3, 5$ and 7 and showed the increasing heat transfer on the target surface in case of

high crossflow velocity $VR=7$. Yang and Wang [8] conducted the numerical simulation of an inclined impinging jet in crossflow with same experimental condition of Nakabe et al. [7]. The results indicated that for the case of the low velocity ratio ($VR=3$), there appeared very strong circulation flow near the stagnation region when compare with other velocity ratio ($VR=5$ and 7).

All literature reviews have been briefly discussed in above. It was found that the crossflow significantly reduced or enhanced the heat transfer of impinging jet according to the ratio of jet to crossflow velocity and jet-to-plate distance. Most of the previous works on impingement heat transfer under the crossflow are concerned with jet from a pipe nozzle [4, 5, and 6]. In practical industrial applications, the heat transfer surface is large and the multiple impinging jets were must applied with orifice type nozzle. Hence, the interacted characteristic between the jet and the crossflow are unlike for case of single and multiple impingements. Also, the flow and heat transfer characteristics in case of jet impingement from the pipe and orifice nozzle are difference.

In case of multiple of jet impingements, the maximum heat transfer on the target surface was 2D-3D of jet-to-plate spacing (according on the jet-to-jet spacing) [2, 3 and 9]. While, the maximum heat transfer on the target surface in case of single jet impingement was 5D-8D of the jet-to-plate distance, according on the nozzle type and confined or unconfined of the test section [10, 11 and 12]. From these reasons, the effect of crossflow on jet impingement from orifice nozzle with low jet-to-plate distance ($H=2D-3D$) should be concerned than the jet impingement from the pipe nozzle with high jet-to-plate distance ($H>6D$).

The aim of this research was to study the effect of velocity ratio on flow and heat transfer in case of impinging jet from orifice nozzle with low jet-to-plate distance $H=2D$. The experimental investigation was carried out of the jet to the crossflow velocity ratios $VR=v_j/v_\infty=3, 5$ and 7 . The temperature distribution on the impinged surface was investigated by using TLCs and Nusselt number distribution was evaluated by using image processing technique. The flow characteristics on the impinged surface were visualized by using oil film technique. The numerical simulation was employed to gain insight into the fluid flow of jet impingement in the crossflow by using commercial CFD software (ANSYS ver. 12.0).

2. EXPERIMENTAL MODEL AND PARAMETERS

The experimental model in this study, the jet was discharged from a circular orifice and then impinged normal to opposite heated surface in wind tunnel with rectangular cross section as show in Fig.1. The crossflow was generated by sucking air pass through the test section with centrifugal blower located downstream of wind tunnel. To consider the effect of jet to crossflow velocity (VR) on flow and heat transfer characteristic on the impinged surface, the jet flow was fixed at a constant flow rate and the crossflow velocity was varied. An origin of the Cartesian coordinates was located on the

impinged surface as shows in Fig.1. The X-axis, Y-axis and Z-axis are the streamwise of crossflow, normal to streamwise and spanwise direction of wind tunnel, respectively.

The experiment was carried out at orifice diameter $D=13.2$ mm and jet-to-plate distance $H=2D$. The comparisons for flow and heat transfer characteristics on the impinged surface were based on the constant jet velocity (at $Re=v_j D/\nu=12,700$) and varied crossflow velocity, corresponding to velocity ratio between the jet and the crossflow $VR=3, 5$ and 7 .

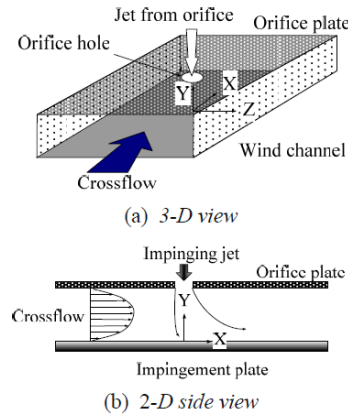


Fig. 1. Experimental model of an impinging jet in a crossflow

3. EXPERIMENTAL SETUP AND METHOD

3.1. Experimental setup

Fig.3. shows a schematic view of the experimental apparatus. The experimental apparatus composed of two parts: jet flow supplied part and crossflow supplied part. For the jet flow supplied part, the centrifugal blower (3HP) accelerates the air which then flows through a temperature controlled chamber and towards the orifice flow meter. The air subsequently passes through a jet chamber with constant cross-section 360-mm-wide, 360-mm-long and 850-mm-high. The jet chamber was equipped with two layers of perforated plates and two layers of mesh plates to ensure that a uniform flow field approaches to the orifice plate.

The crossflow in the wind tunnel was sucked through the inlet chamber, a flow straightener, two of mesh plates, the test section and an outlet chamber with centrifugal blower (3HP) located at downstream of wind tunnel. The wind tunnel has rectangular cross-section 300-mm-width and the height is $2D$ (Aspect ratio is 11.4). The wind tunnel has sufficient length to ensure that the flow passes through the test section with a fully developed velocity profile. In addition, the inlet chamber and wind tunnel was assembled by convergent connection to reduce the effect from wind tunnel inlet.

The test section was mounted upon the jet chamber and its dimension was 139-mm-wide and 26.4-mm-high.

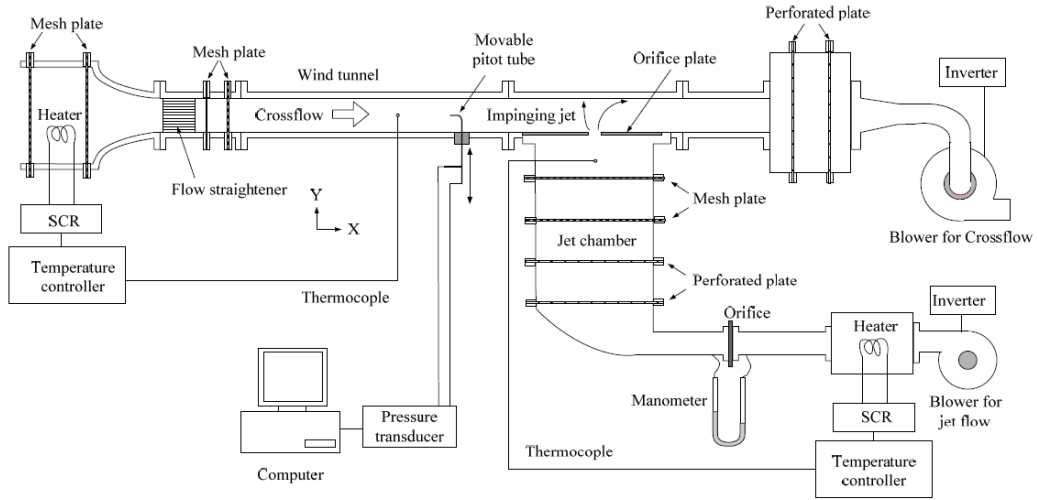


Fig.2. Schematic of the experimental apparatus

The surface of heat transfer measurement (Opposite site of jet plate) of test section was designed for replaceable with transparent acrylic plate for the flow visualization technique. As well as, the Pitot-static tube was mounted before test section for the crossflow velocity profile measurement. For all experimental conditions, the jet and crossflow were controlled with constant temperature at 27°C and temperature variation of the jet and the crossflow was controlled within 0.2°C.

3.2. Heat transfer measurement

Fig. 3 shows the detail of test section for heat transfer measurement. The air with constant temperature discharged from an orifice plate and impinged upon the heat transfer surface. The heat transfer surface was made of stainless steel foil (30- μm -thicknesses) which attached with TLC sheet on the rear side of jet impinged surface. The stainless steel foil was stretched between couple of copper bus bars. The heat transfer surface was heated by DC power supply that can supply current up to 40A passes through copper bus bars. An amount of electrical energy was dissipated in the stainless steel foil and it can be calculated from equation

$$\dot{Q}_{input} = I^2 \cdot R \quad (1)$$

where here, I is the electrical current and R is the electric resistance of stainless steel foil.

The heated impinged surface was cooled with impinging jet. Hence, the local values of heat transfer coefficient (h) by force convection of jet can be evaluated from equation

$$h = \frac{\dot{Q}_{input} - \dot{Q}_{losses}}{A(T_w - T_j)} = \frac{\dot{q}_{input} - \dot{q}_r - \dot{q}_c}{T_w - T_j} \quad (2)$$

where $\dot{q}_r = \sigma \varepsilon_{TLC} (T_w - T_s)$ and $\dot{q}_c = h_c (T_w - T_s)$ are the heat loss transferred to the environment by radiation and convection, respectively. The T_w and T_j are the wall and jet temperature, the σ is a Stefan-Boltzman constant, the ε_{TLC} is a emissive coefficient of the black background

paint and the TLCs that has been given in [9], T_s is a surrounding temperature and h_c is a natural heat transfer coefficient that was calculated from natural convective heat transfer from the horizontal plate orientation to the surrounding.

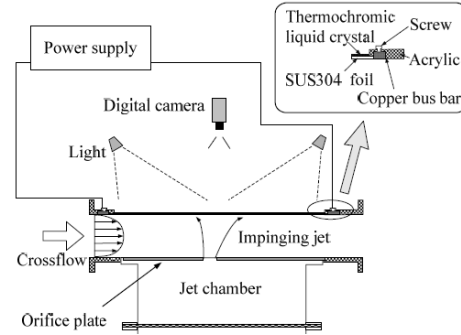


Fig.3. Detail of heat transfer measurement

The wall temperature (T_w) on the impinging surface was measured by using TLCs that attached on the rear side of jet impinged surface. The CCD camera was used to capture colour on TLCs. The images of colour pattern on TLCs were then converted from the RGB (Red, Green and Blue) colour system to the HSI (Hue, Saturation and Intensity) colour system. The Hue (H) value provides a convenient way to correlate the colour of TLCs to their temperature in range of 28-40°C. The TLCs was calibrated with same location on the test section to keep all external factors same with the heat transfer experiment. The local Nusselt number was calculated from

$$Nu = \frac{hD}{k} \quad (3)$$

where D is the diameter of orifice and k is a conductivity of air jet. An average Nusselt number was calculated from

$$\overline{Nu} = \frac{\overline{h}D}{k} \quad (4)$$

where here, the average heat transfer coefficient \overline{h} was calculated from Eq.(2) by replacing T_w to $\overline{T_w}$ that is a averaged temperature on the impinging surface.

3.3. Flow visualization on the impinging surface

The flow visualization on the impinging surface was illustrated by using oil film technique. The oil film was prepared by liquid paraffin, titanium dioxide and oleic acid. A transparent plastic plate was replaced to the impinging surface and oil film was painted uniformly on jet impinging surface. The CCD camera was captured the oil film flow on the impinging surface at each different time (30 second/frame).

4. NUMERICAL SIMULATION (CFD)

The flow characteristic was illustrated by using 3-D numerical simulation (ANSYS ver.12.0). The model of numerical simulation is same with the experimental model; dimension, mass flow rate of jet and crossflow, boundary and experimental condition. The standard k-ε turbulent model with general wall-function mode was used for solving numerical simulation problems.

5. RESULTS AND DISCUSSION

5.1 Velocity profile of crossflow

Fig.4 shows the velocity profile of crossflow in Y-axis pass the center of wind tunnel(Y is wind tunnel height). The velocity profile shows a good agreement between the CFD and experimental data. The trend of both data illustrate that the flow before enter to the test section with fully developed flow. From this result, the flow characteristic of crossflow before enter to the test section of both experiment and CFD are almost matched.

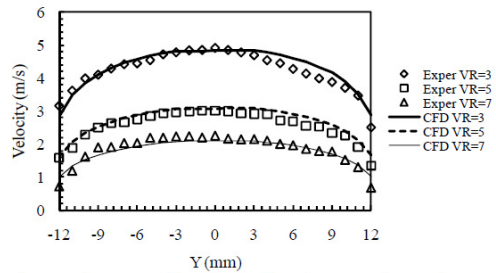


Fig.4. Velocity profile of crossflow (Y is wind tunnel height)

5.2 Flow characteristic of jet and crossflow

Fig.5 shows the velocity distribution in ZX-plane through the center of jet (Y=0). The jet discharged from the nozzle and impinged upon the target surface. Before jet impinging on the wall, the crossflow deflected the jet to downstream side of crossflow. The tendency of deflection of jet depends on the crossflow velocity or

VR. The jet was more deflected to the downstream of crossflow when the VR decreases.

In case of VR=5 and 7, the wall jet was appeared on both side of upstream and downstream of jet impingement region. This condition was different from the VR=3 which the wall jet was appeared only downstream.

Fig. 5 (b) and (c) show the point of velocity approach to zero which nearly located to the target surface in middle of jet impingement region for VR=5 and 7. This represented the stagnation point. It was found that the stagnation point was shifted to the downstream when the crossflow velocity was increased. However, the stagnation point in case of VR=3 was obscured.

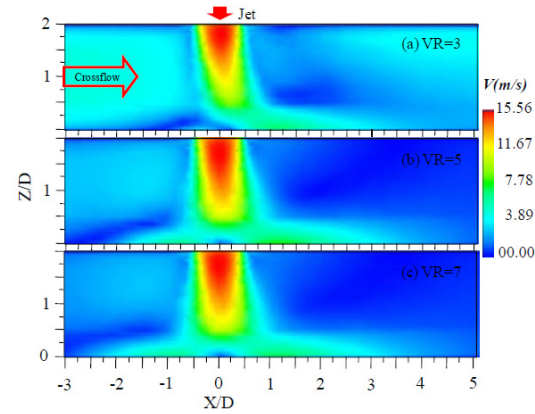


Fig. 5. Velocity contour in ZX-plane (Y=0) at different VR

Fig.6 shows streamline in ZX-plane at Y=0. The results obviously illustrated the interaction between jet and crossflow. In case of VR=5 and 7 shows the ground vortex in the upstream of jet impingement region. The ground vortex of VR=7 is larger than VR=3, because of the wall jet can be penetrated in the upstream of crossflow about 3.3D then the wall jet collided with crossflow and turn to downstream as shows in Fig. 6 (c). Difference from in case of VR=5, the wall jet can penetrate in the crossflow about 2.5D as shows in Fig. 6 (b). The dimension of ground vortex depends on the distance of wall jet that can be penetrated as much as in the upstream direction.

In case of higher velocity of crossflow VR=3 (Fig. 6 (a)), the ground vortex was disappeared. But, the wall jet can be penetrated in the crossflow about 1.2D in the upstream and then rapidly turn to the downstream. In this case, the velocity of crossflow dominated the velocity of wall jet.

Fig. 7 shows the streamline in ZX-plane at Y=-6 mm from the jet exit. The result shows that the crossflow passed through the jet flow with difference flow characteristics according to the VR. In case of VR=3, the circulation flow was appeared in downstream side of jet. This circulation flow can be promoted the turbulent flow inside the jet before impingement.

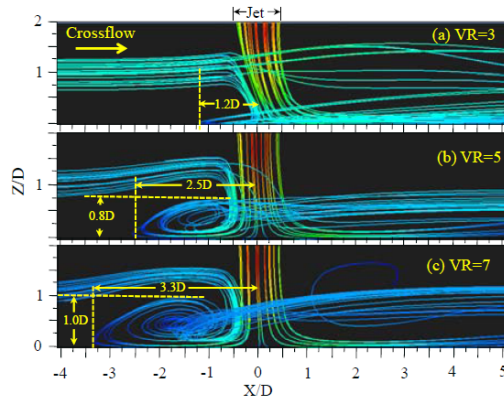


Fig.6. Streamline in ZX-plane ($Y=0$) at different VR

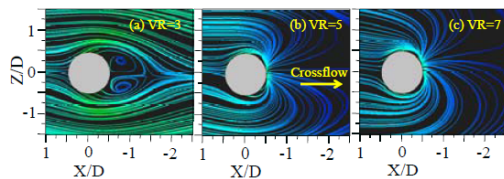


Fig.7. Streamline in ZX-plane at $Y=-6$ mm from the jet exit (Solid circle are the position of orifice).

5.3 Flow and heat transfer on the impinged surface

Fig. 8 shows the flow visualization on the impinged surface by using Oil film technique. The black area represented oil film completely removed wall region and white area represented area of oil film. The impingement region has black area due to high shear stress on the surface. The oil film was removed from this region. Small white area in the middle of black area represents the stagnation point of jet with velocity almost zero. In case of without crossflow and case of $VR=7$ with lowest crossflow velocity (Fig. 8 (a) and (d)), the stagnation point was clearly expressed. For case of $VR=3$, the stagnation point unclearly expressed as shown in Fig. 8 (b), because of highest velocity of crossflow (jet impinged on surface weakly).

From the Fig.8, the distance of stagnation point shifted far away from the center of orifice $0.15D$, $0.25D$ and $0.5D$ for $VR=7$, 5 and 3 , respectively. The distance from the stagnation point to the central orifice increased with decreasing the VR, corresponding to the numerical simulation model that shows in Fig.5 as has been discussed in above.

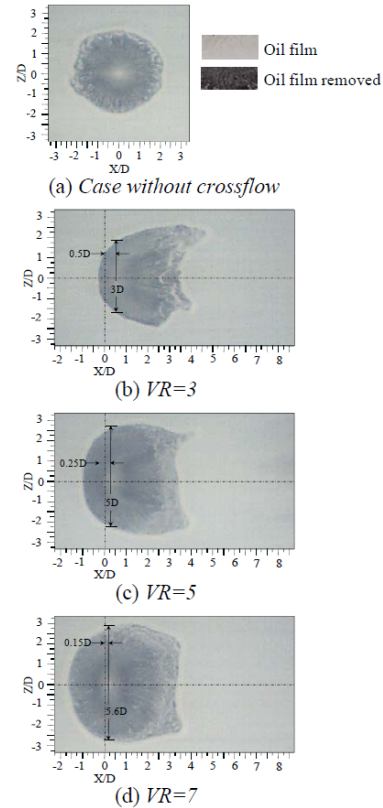


Fig. 8. Oil film patterns on an impinged surface at different VR

Fig. 9 shows the local Nusselt number distribution on the impinged surface. The area of high heat transfer in jet impingement region became smaller in spanwise direction for $VR=3$ and become larger for $VR=5$ and 7 . This result is consistent with the area of stagnation region that has been shown in Fig. 8. The distance of stagnation region in centerline in spanwise are $3D$, $5D$, and $5.6D$ for $VR=3$, 5 and 7 , respectively. This result illustrates the area of stagnation region become smaller as the crossflow velocity increasing.

The heat transfer peak in stagnation region for case jet without crossflow is lower than other case of jet with crossflow. For case jet with crossflow, the peak of heat transfer increased with increasing velocity of crossflow. The variation of heat transfer peak was obviously as shown in Fig.10. This heat transfer enhancement is attributed to the interaction between the jet and the crossflow which increased turbulent intensity in the jet before impingement, corresponding to the numerical simulation model that shows in Fig.7.

Table 1 shows the variation of averaged Nusselt number on the impinged surface that calculated from the equation (4). The $VR=5$ has highest averaged Nusselt number, because of the high local Nusselt number are appropriated between stagnation region and around it. So, difference from the $VR=5$ that shows the peak of heat transfer only at stagnation point.

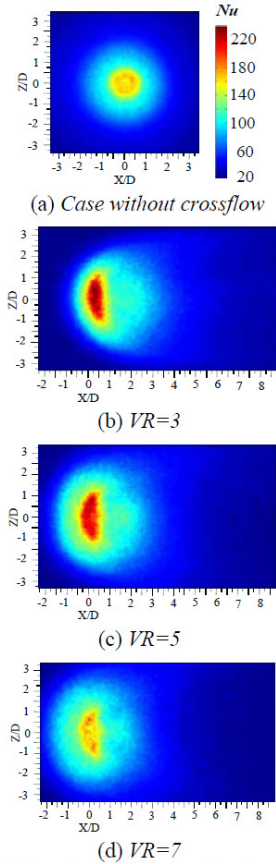


Fig. 9. Local Nusselt number on an impinged surface at different VR ($T_j=27^\circ\text{C}$)

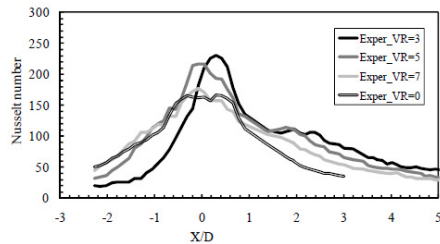


Fig. 10. Local Nusselt number distribution on impinged surface at different VR ($T_j=27^\circ\text{C}$, $Re_j=12,700$, $Z/D=0$)

Table 1. Averaged Nusselt number

VR	3	5	7
Averaged Nusselt number	72.7	78.1	72.9

5. CONCLUSION

The main results are shown as follows;

(1) The jet was more deflected to the downstream of crossflow when the crossflow velocity increasing and the ground vortex in upstream of $VR=7$ larger than in case of $VR=3$.

(2) The higher velocity crossflow can increase the peak of heat transfer in stagnation region. This is attributed to the interaction between the jet and the crossflow which increased turbulent intensity in jet before impingement.

ACKNOWLEDGEMENT

This research was sponsored by Faculty of Engineering, Prince of Songkla University through grant No. ENG-53-2-7-02-0070-S.

REFERENCES

- [1] J. Y., San, and M. D., Lai, "Optimum jet-to-jet spacing of heat transfer for staggered arrays of impinging air jets", *Heat Mass Transfer Int. J.*, Vol. 44, 2001, pp. 3997–4007.
- [2] R. Viskanta, "Heat transfer to impinging isothermal gas and flame jets", *Experimental Thermal and Fluid Science J.*, 1993, Vol.68, pp.111-134.
- [3] V. Katti and S. V. Prabhu, "Influence of spanwise pitch local heat transfer distribution for in-line arrays of circular jets with air flow in two opposite", *Experimental Thermal and Fluid Science. J.*, 2008, Vol. 33, pp 84-95.
- [4] R. J. Goldstein and I. Behbahan, "Impingement of a circular jet with and without cross flow", *Heat Mass Transfer Int. J.*, Vol. 25, 1982, pp. 1377–1382.
- [5] J.-P. Bouchez and R. J. Goldstein "Impingement cooling from a circular jet in a cross flow", *Heat Mass Transfer Int. J.*, Vol. 18, 1975, pp. 719–730.
- [6] J. M. M. Barata, and D. F. G. Durao, "Laser-Dropller measurements of impinging jet flows through a crossflow", *Experimental in Fluids J.*, 2004, Vol. 36, pp. 665-674.
- [7] K. Nakabe, K. Suzuki, K. Inaoka, A. Higashio, J.S. Acton, and W. Chen, "Generation of longitudinal vortices in internal flows with an inclined impinging jet and enhancement of target plate heat transfer", *Heat and Fluid Flow Int J.*, 1998, Vol. 19, pp. 573-581.
- [8] Y.-T. Yang and Y.-X. Wang "Three-Dimensional Numerical Simulation of an Inclined Jet with Cross-Flow", *Heat and Mass Transfer Int. J.*, 2005, Vol.48, pp.4019-402.
- [9] L.F.G. Geers, M.J. Tummers, T.J. Bueninck and K. Hanjalic, "Heat transfer correlation for hexagonal and in-line arrays of impinging jets", *Heat and Mass Transfer Int. J.*, 2008, Vol. 51, pp 5389-5399.
- [10] S. Ashforth-Frost and K. Jambunathan "Effect of nozzle geometry and semi-confinement on the potential core of a turbulent axisymmetric free jet", *Heat Mass Transfer Int. J.*, 1996, Vol.23, pp.155-162.
- [11] D. W. Colucci and R. Viskanta, "Effect of nozzle geometry on local convective heat transfer to a confined impinging air jet", *Experimental Thermal and Fluid Science J.*, 1996, Vol.13, pp.71-80.
- [12] K. Jambunathan, E. Lai, M. A. Moss and B. L. Button, "A review of heat transfer data for single circular jet impingement", *Heat and Fluid flow Int. J.*, 1996, Vol.13, pp.106-115.

Appendix A2

Conference Paper 2

M. Wae-hayee and C. Nuntadusit, "Flow and Heat transfer Characteristics of Non-circular Impinging jet in Crossflow" The 8th International Conference on Flow Dynamics (ICFD2011), November 9-11, 2011, Sendai, Miyagi, Japan.

Flow and Heat Transfer Characteristics of Non-Circular Impinging Jet in Crossflow

M. Wae-hayee, C. Nuntadusit

Energy Technology Research Center and Department of Mechanical Engineering, Faculty of Engineering,
Prince of Songkla University, Hat Yai, Songkhla 90112, Thailand
chayut@me.psu.ac.th

ABSTRACT

The aim of this research is to enhance the heat transfer rate on surface of impinging jet in crossflow. The round orifice ($AR=1$) was replaced by elongated round orifices with aspect ratio $AR=4$ in based on identical exit area. Effect of attacking angle ($\theta=0^\circ, 45^\circ$) and jet to crossflow velocity ratio $VR=3$ and 7 were studied. The numerical simulation was employed to gain insight into the fluid flow, and thermochromic liquid crystal was used to visualize heat transfer characteristic on a target surface. Results show that the orifice with $AR=4$ and $\theta=45^\circ$ can increase the heat transfer rate at stagnation region under the low crossflow velocity ($VR=7$).

1. Introduction

A jet impingement is a high performance technique for heating, cooling or drying process. When high and uniform heat transfer rate on surface are required over a large area, multiple of impinging jets are applied. An important factor that influences on the multiple jet impingements in a confined space is crossflow. The crossflow is produced by accumulating spent jets from upstream to downstream of the confined space. The crossflow has been found to significantly reduce the heat transfer of impinging jet [1].

The aim of this research is to enhance the heat transfer rate on the impinged surface with crossflow. The conventional round orifice was replaced by elongated round orifices with identical exit area. The effect of velocity ratio and attacking angle were also studied.

2. Model and parameters

The model is the jet discharging from orifice and impinging normal to opposite surface in rectangular duct as shown in Fig. 1. The crossflow is generated by introducing air through the rectangular duct, flow normal perpendicular to the impinging jet. An origin of coordinate is located on the impinged surface as shows in Fig.1. The X-, Y- and Z-axes are along the crossflow streamwise, normal to the streamwise, and along the spanwise directions, respectively.

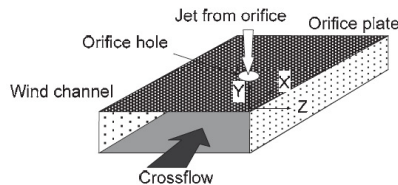


Fig. 1. The model of the impinging jet in the crossflow

The investigation was conducted for orifice aspect ratios (ratio of orifice length to orifice width) $AR=4$ (Fig.2) for compare the results with the round orifice ($AR=1$). The comparisons of flow and heat transfer characteristics are based on the constant jet velocity and varied crossflow velocity according to the velocity ration (jet to crossflow velocity) $VR=3$ and 7 . The

orifice diameter of round jet was $D=13.2$ mm, and jet-to-plate distance was $H=2D$. The attacking angle of major axis of elongated round orifice to the crossflow direction ($\theta=45^\circ$) also studied. During the elongated round orifice test run, the jet mass flow rate was set based on the exit area identical with the conventional round orifice for the required Reynolds number ($Re_E=13,400$).



Fig. 2. Orifice geometry with identical area cross-section (AR is length over width of orifice)

3. Method

The flow characteristic was illustrated by using 3-D numerical simulation (ANSYS ver.12.0). The standard $k-\epsilon$ turbulent model with general wall-function mode was used for solving numerical simulation problems. A non-uniform grid was finely generated in orifice hole and impingement regions. A solution method is based on SIMPLE algorithm with second order upwind for all spatial discretization. The experimental investigation was carried out the heat transfer characteristic by using thermochromic liquid crystal (TLC) sheet, and Nusselt number distribution was evaluated by using image processing method. The details of both numerical and experimental method were explained in ref. [2].

4. Results and Discussion

The velocity vectors and contours of Y-component velocity (direction from orifice plate to target surface is positive velocity) in XZ-plane at 1.0-mm-height from the target surface were shown in Fig. 3. The area of highest Y-component velocity represent the region of stagnation point. Due to high crossflow velocity, the stagnation point of $VR=3$ is shifted to downstream of crossflow ($X/D>0$) when compare with each identical experimental condition for $VR=7$.

The area of high Y-component velocity expands in $-Z$ -axis (pressure side) slightly larger than in $+Z$ -axis (suction side) in the case of $\theta=45^\circ$ under low crossflow velocity (Fig. 3 (e)). Moreover, due to the high velocity crossflow, the area of high Y-velocity expands in $+Z$ -axis and contracts in $-Z$ -axis (Fig. 3 (f)). The expansion area of high Y-velocity in $+Z$ -axis can be

explained that the wall jet flows in same direction with crossflow. In contrast to the contraction area of high Y-velocity in -Z-axis, the wall jet collide with the counter direction of crossflow, and wall jet in -Z-axis rapidly turn to downstream direction of crossflow.

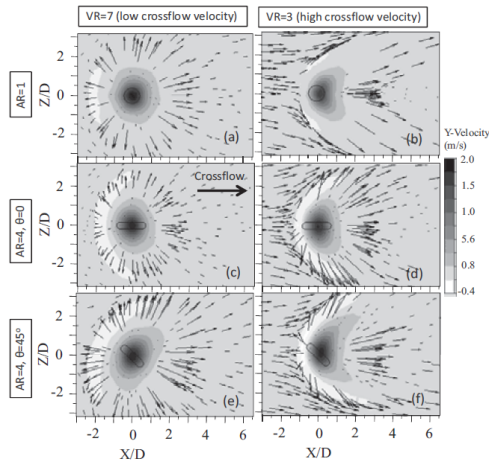


Fig.3. Velocity vectors and Y-velocity contours in XZ-plane at 1.0-mm-height from the target surface

Vectors and contours of velocity in YZ-plane for the case of AR=4, $\theta=45^\circ$ and VR=7 is shown in Fig. 4. The circulation flow was appeared in +Z-axis, and the size of circulation flow become larger at far X/D to downstream. The circulation flow in +Z-axis turn to the jet flow; consequently, the jet is more entrain in +Z-axis than in -Z-axis.

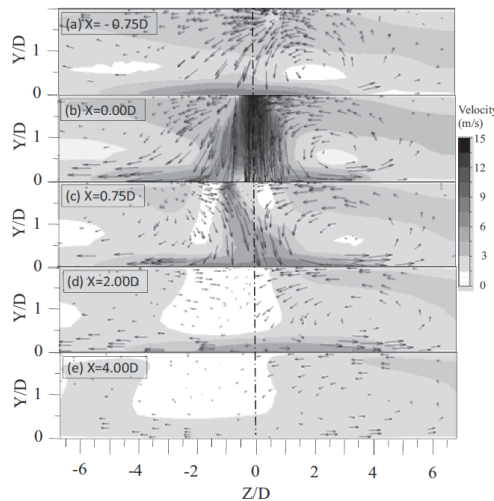


Fig.4 Vector and contour of velocity in YZ-plane for AR=4, $\theta=45^\circ$ and VR=7 at different X/D

The distributions of Nusselt number on target surface are shown in Fig. 5. The results show that the area of high Nusselt number ($Nu>180$) appears in

stagnation region for the case of low crossflow velocity. In the case of high crossflow velocity, the areas of high Nusselt number are shifted to downstream of crossflow due to the higher crossflow velocity. The location of high Nusselt number coincide the locations of high Y-component velocity that illustrated in Fig.3.

The peak of Nusselt number is highest for AR=4, $\theta=0$ with VR=3 (Fig.5(d)), because the jet can penetrate into the crossflow and strongly impinges on target surface despite high crossflow velocity. In the case of AR=4, $\theta=45^\circ$ with VR=7 (Fig.5(e)), the area of high Nusselt number expand in +Z-axis and contracts in -Z-axis coincide with the results illustrated in Fig. 3(e). Moreover, the area of high Nusselt number in -Z-axis is smaller when crossflow velocity increases (Fig.5(f)). Finally, the area of high Nusselt number is largest in the case of AR=4, $\theta=45^\circ$ and VR=7 (Fig.5(e)) corresponding to largest area of high Y-velocity as shown in Fig. 3(e).

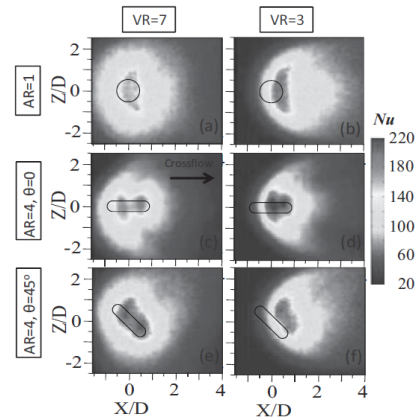


Fig.5. The Nusselt number distribution (experimental results) on the impinging surface

5. Concluding remarks

The jet from orifice with AR=4 can increases heat transfer on stagnation region when compare with the AR=1. In the case of AR=4 with $\theta=45^\circ$ under low crossflow velocity (VR=7), the area of high Nusselt number is largest corresponding to the large area of high velocity that impinges on target surface, and the areas of high Nusselt number expands in +Z-axis and contracts in -Z-axis when crossflow velocity increases to VR=3.

Acknowledgements

This research was supported by grants from Thailand Energy Policy and Planning Office, Ministry of Energy, the Graduate School and Faculty of Engineering, Prince of Songkla University.

References

[1] R. J. Goldstein, Int. J. Heat Mass Transfer, 25 (1982), pp. 1377-1382.
 [2] M. Wae-hayee, ICET5th Int. Conf., MME-P77, (2011). pp. 783-788.

Appendix A3

Conference Paper 3

M. Wae-hayee C. Nuntadusit, and P. Tekasakul, "Heat Transfer Enhancement of an Impinging Jet in Crossflow by Elongated Round Orifice" The 10th International Gas Turbine Congress 2011 Osaka (IGTC'11), November 13-18, 2011, Osaka, Japan.

Heat Transfer Enhancement of an Impinging Jet in Crossflow by Elongated Round Orifice

M. Wae-hayee¹, P. Tekasakul¹, C. Nuntadusit¹

¹Energy Technology Research Center and Department of Mechanical Engineering, Faculty of Engineering, Prince of Songkla University, Hat Yai, Songkhla 90112, Thailand

Corresponding author: C. Nuntadusit
chayut@me.psu.ac.th

ABSTRACT

The aim of this research is to enhance the heat transfer on the impinging surface by reducing the effect of crossflow. The round orifice (AR=1) was replaced by elongated round orifices with a ratio of orifice length to orifice width AR=4 in based on identical exit area. A jet-to-surface distance is two times of the round orifice diameter. A ratio of jet to crossflow velocity are varied from VR=3, 5 and 7. The experiment was also studied the effect of attacking angle $\theta=0^\circ$, 15° , 30° and 45° . The experimental investigation was carried out the heat transfer characteristic by using thermochromic liquid crystal (TLC) sheet and Nusselt number distribution was evaluated by using image processing method. The numerical simulation was employed to gain insight into the fluid flow of impinging jet in crossflow by using computational fluid dynamic (CFD). The results show that the jet impingement from the elongated round orifice can increase heat transfer rate in stagnation region for some of experimental condition. For moderate velocity crossflow VR=5, the heat transfer rate of AR=4 are higher 6% and 4% for $\theta=0^\circ$ and 45° than of AR=1, respectively. In case of low velocity crossflow VR=7, the heat transfer rate are higher 4%, 4% and 10% for $\theta=15^\circ$, 30° and 45° than of AR=1, respectively. The flow visualizations show that the location of jet impingement is shifted to downstream direction due to crossflow effect. The jet of AR=4 with $\theta=0^\circ$ can penetrated into the crossflow better than of the AR=1. The impingement region expands in +Z-axis and contracts in -Z-axis due to large attacking angle and high crossflow velocity.

INTRODUCTION

Jet impingement is a high-performance technique for heat transfer enhancement in thermal equipment. It has also been used in industrial processes for heating, cooling and drying. Since the heat transfer rate is very high at the area where the jet directly impinges on, it provides rapid cooling or heating on local heat transfer area. However, many thermal industrial applications have large heat transfer surface area such as combustor chamber wall and gas turbine blade cooling, steel and glass quenching, and textile and paper drying. When a high and uniform heat transfer is required over the entire surfaces, multiple impinging jets are applied.

An important factor on flow and heat transfer characteristics of multiple impinging jets in a confined space is the crossflow. The crossflow is defined as the fluid flow in the perpendicular direction to the jet impingement flow. It can be formed by either external flow or accumulating spent jet flow. In case of multiple impinging

jets in the confined space, the spent jet is accumulated from the upstream to the downstream of channel. The flow rate or velocity of crossflow is increased in the downstream of the channel, and crossflow velocity in downstream is higher than in the upstream of channel. Consequently, the flow and heat transfer of jet located in the downstream is significantly influenced by the crossflow.

Only a few works have studied the effects of crossflow on flow and heat transfer characteristics of multiple impinging jets. It is difficult to identify the interaction between crossflow and jet under multiple impingement flow. To interpret how much crossflow velocity that influences jet impingement flow; therefore, a single impinging jet under simulated crossflow is conducted. The crossflow velocity and the jet-to-plate distance were found to directly influence flow and heat transfer characteristics of single impinging jet [1, 2]. The Nusselt number decreases when the crossflow velocity and the jet-to-jet distance increase [3, 4].

To illustrate the interaction between the jet and the crossflow, flow visualisation has been employed. A recirculation zone at upstream of the stagnation point is generated by high jet velocity and low crossflow velocity [4]. Under identical condition, when the upstream wall jet was interacted with the crossflow, it was separated laterally into two streams [1]. This interaction formed a vortex along lateral side of impingement flow close to the ground target plate, and the flow pattern is similar to the horseshoe structure. The recirculation zone at upstream of the stagnation point and the horseshoe structure at lateral side of impingement flow were influenced the heat transfer enhancement on surface of both that regions.

Recently, various flow control techniques have been employed to enhance the heat transfer rate on impingement surface. Some examples are the modification of the jet orifice configuration from round to elliptic geometry [5], addition of mesh screens [6], and generation of a swirling jet [7, 8] and a pulsating jet [9, 10]. Examples given above employed a jet impingement without the crossflow. However, a few works studied a heat transfer enhancement of jet impingement under the crossflow in the form an inclined jet [2, 11] and a pulsating jet [12].

A main concept to enhance the heat transfer that has been discussed in above is to increase a turbulent intensity into the jet flow. In a case of jet impingement under crossflow, however, the effect of crossflow is very important to reduce the heat transfer on a target surface. A previous literature reported that the jet issuing from an elongated round nozzle can decrease the effect of crossflow [13]. The jet issuing from the elongated round nozzle can greatly penetrate to the crossflow while it is yet to employ for an impingement heat transfer under crossflow. To reduce the effect of crossflow by using the elongated round nozzle is a concept to increase the impingement heat transfer under crossflow.

The aim of this research is to enhance the heat transfer on the impinging surface by reducing the effect of crossflow in case of low jet-to-plate distance. The conventional round orifice was replaced by elongated round orifices with identical exit area. The effects of jet to crossflow velocity ratios and the attacking angle of major axis of orifice to the crossflow direction also studied. The flow visualization and heat transfer characteristics on the impinging surface were investigated experimentally and numerically.

EXPERIMENTAL MODEL AND PARAMETERS

The experimental model displaying the jet discharging from the round orifice and impinging normal to opposite surface of confined rectangular duct is shown in Fig. 1. The crossflow was generated by introducing air through the test section from the surface perpendicular to the impinging jet. An origin of the Cartesian coordinates was located on the impinging surface as shows in Fig.1 (a). The X-, Y- and Z-axes are along the crossflow streamwise, normal to the streamwise, and along the spanwise directions, respectively.

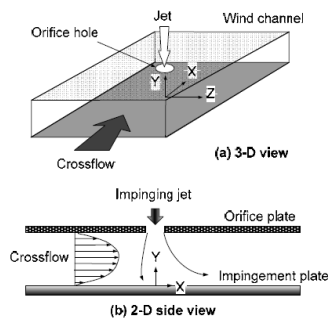


Fig.1 Experimental model of an impinging jet in a crossflow

The experiment was conducted for orifice aspect ratios (ratio of orifice length to orifice width) $AR=4$ to compare the results of the round orifice ($AR=1$) and the attacking angle of major axis of orifice to the crossflow direction $\theta=0^\circ, 15^\circ, 30^\circ$ and 45° as shows in Fig.2. The comparisons of flow and heat transfer characteristics on the impinging surface are based on the constant jet velocity and varied crossflow velocity according to the velocity ratio (jet to crossflow velocity) $VR=3, 5$ and 7 . The equivalent diameter of round jet and elongated round orifice was same at $D=13.2$ mm and jet-to-plate distance was $H=2D$. During the elongated round orifice test run, the jet mass flow rate was set based on the identical with of the round orifice for Reynolds number (base on equivalent diameter) of $Re_E=13,400$.



Fig.2 Orifice geometry with identical exit area (AR is ratio of length over width of orifice)

EXPERIMENTAL SETUP AND METHOD

Experimental Setup

A schematic diagram of the experimental apparatus is shown in Fig. 3. The experimental apparatus is composed of two parts: jet flow and crossflow supplies. For the jet flow supply, a 3-HP blower (Arith Machinery, Av-D1216) accelerates the air which then flows through a temperature controlled chamber equipped with 2-kW heater, an calibrated orifice flow meter, a jet chamber (constant cross-section of 360-mm x 360-mm and a height of 850-mm), and a jet orifice before entering the test section. The jet chamber is equipped with two layers of perforated plates and two layers of mesh plates to ensure a uniform flow field approaching the orifice plate.

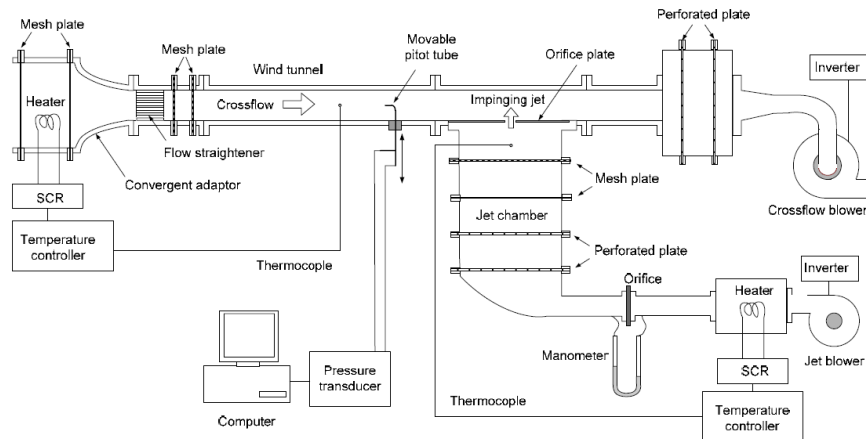


Fig.3 Schematic of the experimental apparatus

The crossflow in the wind tunnel was introduced through the inlet chamber, a flow straightener, two of mesh plates, the test section and a chamber outlet by another identical blower. The constant rectangular cross-section of the wind tunnel has a width of 300 mm and a height twice of the round orifice diameter. The wind tunnel has a sufficient length to ensure that the flow passing through the test section is fully developed. In addition, the chamber inlet and wind tunnel was assembled by a convergent adaptor to

reduce the effect of flow from wind tunnel inlet as shows in Fig. 3. The test section was directly mounted upon a jet chamber. Heat transfer measurement surface (opposite site of the jet plate) of the test section was replaceable by a transparent plate for the flow visualization technique. A Pitot-static tube was mounted before test section for the crossflow velocity measurement. Under all experimental conditions, the jet and crossflow were controlled at $27.0^\circ C$ by a temperature controller (Shinko, JCS-33A) and a power con-

troller (Sangi Electric, SCR-1A030). Temperature variation of the jet and the crossflow was controlled within 0.2°C. A couple of inverters (LS Industrial System, SV022iG5-4) were used to control both blowers for jet and crossflow supplies.

Heat Transfer Measurement

Fig. 4 shows details of the test section for heat transfer measurement. Air with constant temperature was discharged from an orifice plate and impinged upon the heat transfer surface. The heat transfer surface made of a stainless steel foil (30- μ m-thicknesses) attached with the TLC sheet (Omega, LCS-95) on the rear side of an impinging surface. The stainless steel foil was stretched between a couple of copper bus bars. The heat transfer surface was heated by a DC power supply (Silicon, WYK-15V50A-H) that can supply current up to 50 A through the copper bus bars. Electrical energy dissipated in the stainless steel foil can be calculated from

$$\dot{Q}_{input} = I^2 \cdot R \quad (1)$$

where, I is the electrical current and R is the electrical resistance of the stainless steel foil.

Hence, the local heat transfer coefficient by forced convection of jet can be evaluated from

$$h = \frac{\dot{Q}_{input} - \dot{Q}_{losses}}{A(T_w - T_j)} = \frac{\dot{q}_{input} - \dot{q}_r - \dot{q}_c}{T_w - T_j} \quad (2)$$

where $\dot{q}_r = \sigma \varepsilon_{TLC} (T_w - T_s)$ and $\dot{q}_c = h_c (T_w - T_s)$ are the heat loss to the environment by radiation and convection, respectively. T_w and T_j are the wall and jet temperatures, σ is the Stefan-Boltzman constant, ε_{TLC} is the emissive coefficient of the TLC sheet (=0.9) [14], T_s is the surrounding temperature, and h_c is the natural heat transfer coefficient calculated from natural convective heat transfer from the heat transfer surface to the surrounding.

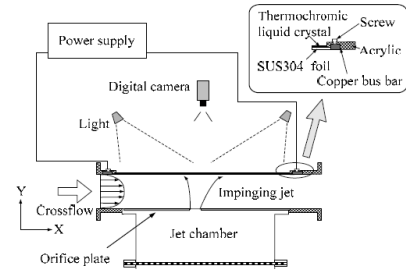


Fig. 4 A detail of heat transfer measurement

The wall temperature (T_w) on the impinging surface was measured by using the TLC sheet attached on the rear side of jet impinging surface. The CCD camera was used to capture colour on the TLC sheet. Images of the colour pattern on the TLC were converted from the RGB (Red, Green and Blue) system to the HSI (Hue, Saturation and Intensity) system. The Hue (H) value was used to correlate the colour of the TLC to the temperature. The TLC sheet was calibrated using the digital image processing system under the same conditions of the experimental runs to keep all external factors constant.

The local Nusselt number was calculated from

$$Nu = \frac{hD}{k} \quad (3)$$

where D is the round orifice diameter and k is a jet thermal conductivity.

An average Nusselt number was calculated from

$$\overline{Nu} = \frac{\overline{h}D}{k} \quad (4)$$

where the average heat transfer coefficient \overline{h} was calculated from Eq.(2) by replacing T_w by an average temperature on the impinging surface, $\overline{T_w}$.

NUMERICAL SIMULATION (CFD)

The flow characteristic was illustrated by using 3-D numerical simulation (ANSYS ver.12.0). The model of numerical simulation is same with the experimental model; dimension, mass flow rate of jet and crossflow, boundary and experimental condition. The numerical computation was carried out by solving the governing equations with boundary condition. The standard k- ε turbulent model with general wall-function mode was used for solving numerical simulation problems. A non-uniform grid system was finely generated in orifice hole and impingement region. A wall inflation function was used for 7 layers with smooth transition option before contacting a surface grid. A solution method was based on SIMPLE algorithm with second order upwind for all spatial discretization. The solution was considered to be converged when the normalized residual of the algebraic equation was less than a prescribed value of 1×10^{-4} .

RESULTS AND DISCUSSION

Experimental Verification

To verify the test section of this experiment, the stagnation Nusselt number (Nu_0) with varied Reynolds number of impingement jet without crossflow was compared with correlation from Lee and Lee [15]. Both experiment were square-edged shape of orifice outlet and slightly difference in the ratio of orifice plate thickness to the jet outlet diameter: 0.2 and 0.15 for those and this experiment, respectively. Comparison of the results is presented in the Fig.5, the solid line represents their correlation. The current data are slightly lower than their correlation. The lower discrepancy of current data are attributed on the heat transfer of confined jet impingement of this experiment are lower than of the unconfined jet impingement for those experiment [16].

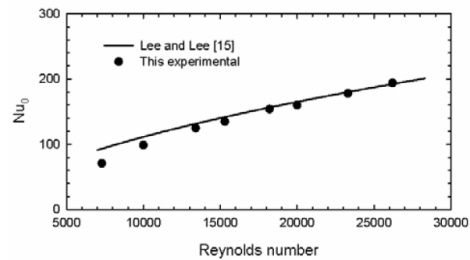


Fig.5 Comparison of stagnation point Nusselt number with Lee and Lee's correlation [15] in the case of without crossflow

Velocity Profile of the Crossflow

The velocity profile of the crossflow in Y-axis pass the center of the wind tunnel (Y is wind tunnel height) is shown in Fig.6. Both experimental and CFD results are compared. The result shows good agreement between CFD and experiments. The trend of both data illustrate that the flow enter to the test section with fully developed flow. From this result, the flow characteristic of the crossflow before enter to the test section of both experiment and

CFD are almost matched.

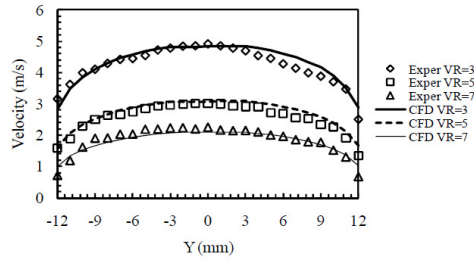


Fig.6 Velocity profile of crossflow before enter to the test section

Flow Characteristic of the Jet and the Crossflow

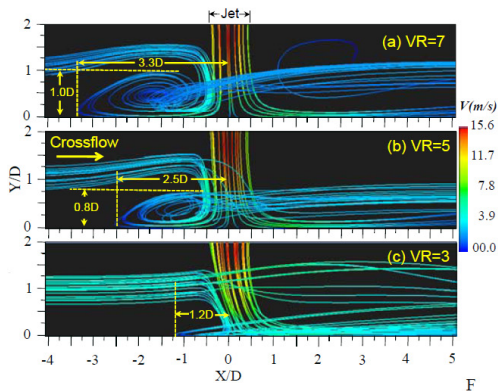


Fig.7 The streamline of jet and crossflow in YX-plane along centerline of jet (Y=0) for AR=1

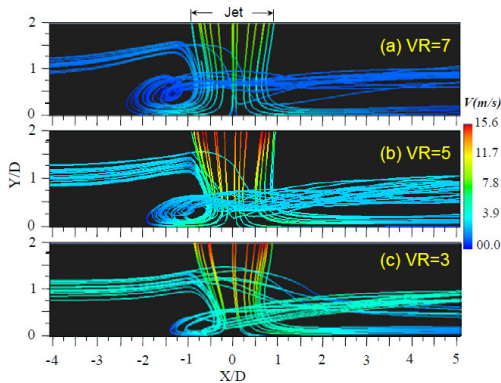


Fig.8 The streamline of jet and crossflow in YX-plane along centerline of jet (Y=0) for AR=4, $\theta=0^\circ$

The streamline of jet and crossflow in YX-plane through center of jet exit (Y=0) is shown in Fig. 7 and Fig. 8 for AR=1 and 4 with $\theta=0^\circ$, respectively. The results obviously illustrate the interaction between jet and crossflow. In the case of AR=1, the jet was deflected by the crossflow to downstream of it due to the high cross-

flow velocity. The jet was more deflected to the downstream when the VR decreases (crossflow velocity increases). When compare the streamline of case of AR=1 to case of AR=4, $\theta=0^\circ$ with identical VR, the deflection of jet for case of AR=4, $\theta=0^\circ$ is smaller than case of AR=1. The deflection of jet for case of AR=4, $\theta=0^\circ$ is smaller despite in the case of high crossflow velocity (consider between Fig.7 (c) and Fig.8 (c)).

In the case of VR=5 and 7 for AR=1 (Fig. 7 (a) and (b)), it appears ground vortex in the upstream side of jet impingement region. This ground vortex is produced by collision between wall jet in upstream of impingement region and the crossflow. The wall jet collides with crossflow and turns to downstream again. So, the size of the ground vortex corresponds to the crossflow velocity. The ground vortex for case of VR=7 is larger than case of VR=5 due to lower crossflow velocity. Moreover, in the case of highest crossflow velocity (Fig. 7 (c)), the ground vortex disappears because the crossflow velocity dominates the wall jet velocity in upstream. The wall jet rapidly turns to the downstream without producing the ground vortex. This is different from case of AR=4 with $\theta=0^\circ$ (Fig. 8), the ground vortex is produced in the upstream although crossflow velocity is high.

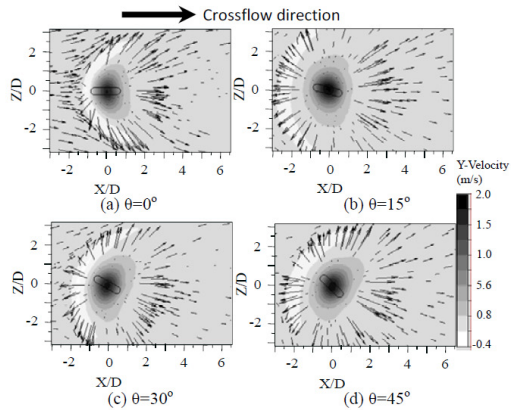


Fig.9 Velocity contour in XZ-plane at 1 mm above impingement surface for case of AR=4 with VR=7 (low velocity crossflow)

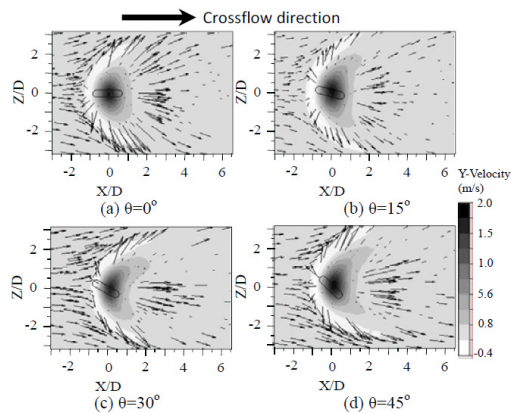


Fig.10 Velocity contour in XZ-plane at 1 mm above impingement surface for case of AR=4 with VR=3 (high velocity crossflow)

The velocity vectors and Y-velocity contours (direction is normal to target surface) in XZ-plane at 1 mm above impingement surface of AR=4 with VR=7 and 3 are shown in Fig.9 and Fig. 10, respectively. The region of high velocity in Y direction represent the location of stagnation point. The region where velocity in Y direction is minus represents the upward flow from target surface or areas of circulation flow in upstream that illustrated in Fig.8.

The stagnation point is shifted far to downstream of crossflow (X/D>0) due to higher crossflow velocity. The areas of circulation flow also shift to downstream of crossflow when crossflow velocity increases. The area of high Y-velocity expands in +Z-axis and contracts in -Z-axis due to attacking angle, especially in the case of AR=4 with $\theta=45^\circ$ and VR=3 (Fig.10 (d)). The expansion of Y-velocity in + Z-axis can be attributed that the jet was entrained by crossflow velocity with same directions.

Local Heat Transfer Distributions

The Nusselt number distributions on the impinging surface for the case of round orifice (AR=1) are shown in Fig. 11. The area of high heat transfer in the stagnation region for without crossflow is smaller than case with crossflow. For the case under crossflow (Fig.11 (b)-(c)), the area of high heat transfer along spanwise and upstream of impingement region became smaller when VR decreases.

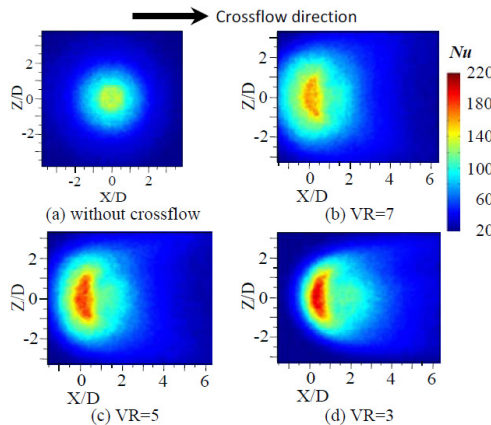


Fig.11 Nusselt number distribution on impinging surface in case of AR=1 ($Re_E=13,400$, $T_j=27.0^\circ\text{C}$)

From the case under crossflow in Fig. 11, the peak of Nusselt number enhance when crossflow velocity increase. The heat transfer enhancement at the stagnation region attributes the interaction between the jet and the crossflow increasing turbulent intensity into fluid flow. Corresponding to results of Katti and prabhu [17] indicating the crossflow can increase heat transfer in stagnation region in confined channel for low jet-to-plate distance.

The variation of Nusselt number for the case of AR=1, the peaks of Nusselt number increasing relate the increasing of crossflow velocity. This relation of heat transfer and crossflow velocity is contrast with results of Goldstein and Behbahani [3] and Bouchez and Goldstein [4]. Those results have been found that the peak of heat transfer was decreased by increasing of crossflow velocity. However, those and this experimental conditions are different. The jet-to-plate distance is 2D with orifice nozzle and $\leq 4D$ with pipe nozzle for this and those experiments, respectively. The differences of jet-to-plate distance and nozzle configuration importantly influence the heat transfer characteristic [18, 19]. Another effect is an experimental operation. The crossflow velocity was fixed and jet velocity was varied for those experiments whereas this experiment

is based on fixed for jet velocity and varied for crossflow velocity. Typically, the heat transfer on the surface from jet impingement is higher than the heat transfer from crossflow. Hence, to consider the effect of crossflow velocity on flow and heat transfer of jet impingement, the jet velocity should be fixed and varied for crossflow velocity that was employed as in this experiment.

In the case of low and intermediate crossflow velocity, VR=7 and 5 (Fig.11 (b) and (c)), the heat transfer at wall jet regions are higher than the case of without crossflow (Fig.11 (a)). The heat transfer increasing attributes that the interaction between the wall jet and the crossflow increase turbulent intensity into the fluid flow. This interaction produces a ground vortex in upstream (4) and both lateral sides of impingement region (1) for case of low and intermediate crossflow velocity.

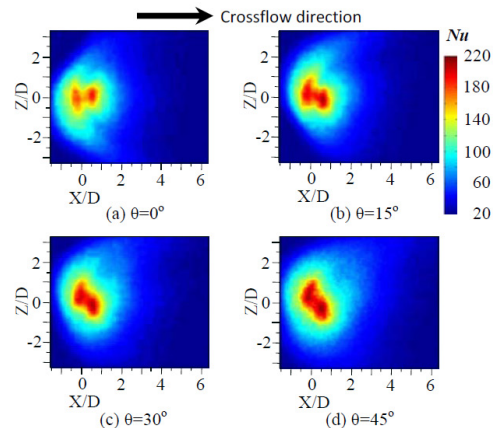


Fig.12 Nusselt number distribution on impinging surface in case of AR=4 with VR=7 (low velocity crossflow, $Re_E=13,400$ and $T_j=27.0^\circ\text{C}$)

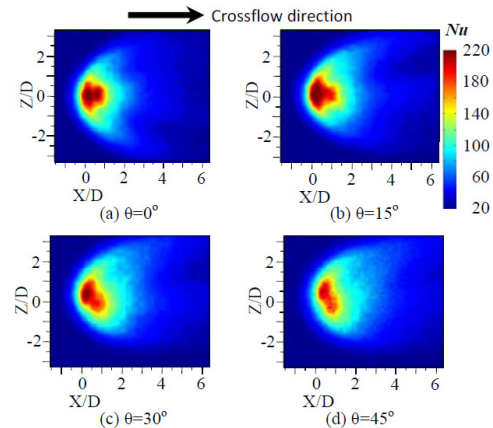


Fig.13 Nusselt number distribution on impinging surface in case of AR=4 with VR=3 (high velocity crossflow, $Re_E=13,400$ and $T_j=27.0^\circ\text{C}$)

The Nusselt number distributions on the impingement surface of AR=4 is shown in Fig. 12 and 13 for VR=7 and 3, respectively. The heat transfer characteristics for AR=4 are obviously different from the AR=1 depending on AR, attacking angle and VR. For the case of AR=4, $\theta=0^\circ$ and VR=7 (Fig. 12 (a)), the area of high

Nusselt number ($Nu > 90$) are rather symmetry in Z-axis. When the attacking angle was increased, the areas of high Nusselt number extend in +Z-axis and contract in -Z-axis. The heat transfer characteristics coincide with the flow visualization that has discussed in above. The area of high Nusselt number correspond the areas of high Y-velocity that has been illustrated in Fig. 9 and Fig. 10: the area of high Nusselt number are rather symmetry in Z-axis when attacking angle is zero, the area of high Nusselt number extend in +Z-axis when attacking angle was increased, and the area of high Nusselt number extend in downstream ($X/D > 0$) and contract in upstream ($X/D < 0$) when VR was decreased.

The attacking angle directly affects the heat transfer characteristic at stagnation region depending on variations of crossflow velocity. In the case of $AR=4$ for the large attacking angle, the Nusselt number at stagnation region enhance according to the low crossflow velocity (Fig.12) whereas it reduce according to high crossflow velocity (Fig.13). The relationship between AR and attacking angle swept by crossflow is schematically illustrated in Fig. 14.

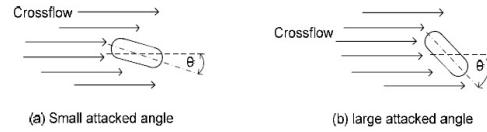


Fig.14 Illustrate the interaction area between jet and crossflow for $AR=4$ with variation of attacking angle

From the Fig. 12 (d), the area of high Nusselt number ($Nu > 180$) is large due to the largest attacked angle and low crossflow velocity. In this experimental condition, the large interactive area between jet and crossflow that illustrated in Fig.14 (b) increases turbulent intensity under low crossflow velocity. Ashforth-Frost and Jambunathan [16] and Ashforth-Frost et al. [17] have reported that the main parameters to enhance the heat transfer on target surface of impinging jet is an appropriated between momentum and turbulent intensity of jet before impingement.

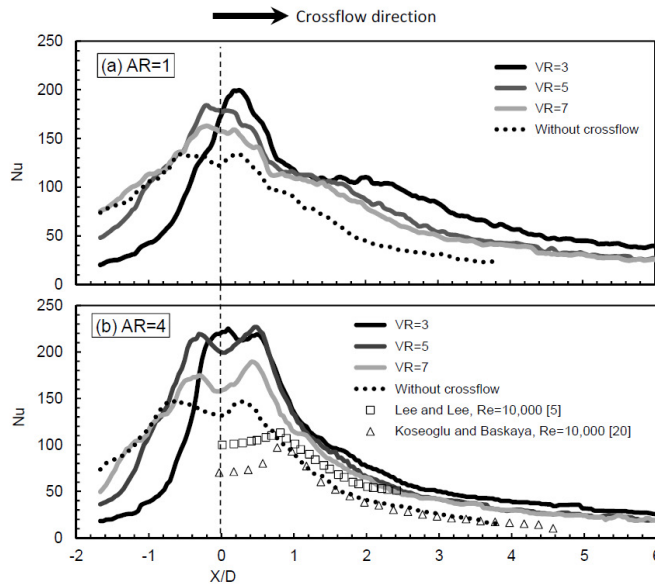


Fig.15 Nusselt number distribution along centerline of jet in X-axis ($Re_E=13,400$, $T_f=27.0$ °C and dash lines are centerline of orifice)

Local Nusselt number distributions along centerline of the orifice in X-axis are respectively shown in Fig. 15: (a) $AR=1$ and (b) $AR=4$ with $\theta=0^\circ$. The Fig. 15 (b) also shows the experimental result of Lee and Lee [15] and CFD result of Koseoglu and Baskaya [20], and both those investigations using the elliptic orifice with $AR=4$ without crossflow and keep constant Reynolds number for 10,000 (based on constant mass flow rate of round orifice). In the case of without crossflow (Fig. 15 (b)), the Nusselt number distribution at stagnation region of this experiment is higher than of those Lee and Lee [5] and Koseoglu and Baskaya [20] referring the higher Reynolds number of this experiment. However, the Nusselt number distribution at $X/D > 0.8$ of both investigations are slightly different. The discrepancy of Nusselt number attribute to almost similarity in orifice geometry for elongated round orifice of this and elliptic orifice of those investigations.

In the case of jet without crossflow as show in Fig.15, the area

of high Nusselt number ($Nu > 120$) for the case of $AR=1$ and 4 are $-0.5 < X/D < 0.5$ and $-0.8 < X/D < 0.7$, respectively. The area of high Nusselt number of $AR=4$ is larger than $AR=1$. The variations of high Nusselt number according to AR are similar with the case of the jet under crossflow. The enhancement of peaks of Nusselt number in stagnation regions corroborate that the jet from the elongated round orifice with $\theta=0^\circ$ more penetrate into the crossflow than the jet from the round orifice. This results corresponding to the flow visualization of jet in a crossflow of New et al. [21], theirs results illustrated that the elliptic jet penetrate into the crossflow more than the round jet.

In the case of under crossflow of both $AR=1$ and 4 in Fig.15, the Nusselt number distribution along upstream ($X/D < 0$) is obviously lower when crossflow velocity was increased. Different from the Nusselt number distribution along downstream ($X/D > 0$), it is higher when crossflow velocity was increased. The variation of Nusselt number in upstream can be illustrated that the wall jet

in upstream was minimized by counter crossflow direction. On the other hand, the wall jet in downstream was extended by entrainment of parallel crossflow direction. These results correspond to the flow visualization that has been discussed above.

Average Heat Transfer

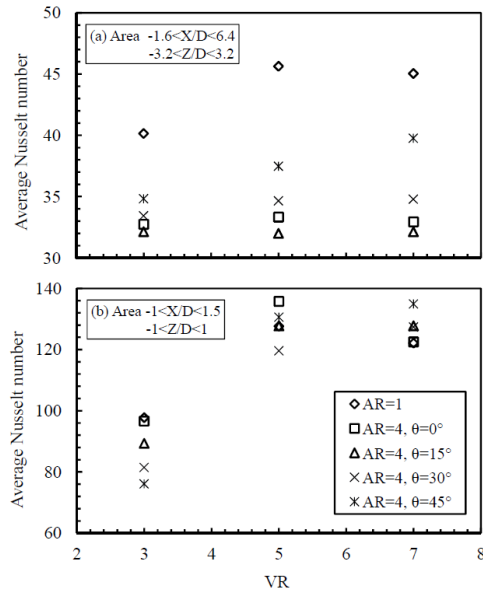


Fig.16 Average Nusselt number for (a) large and (b) small heat transfer area

The average Nusselt number was considered in two areas: $-1.6 < X/D < 6.4$ and $-3.2 < Z/D < 3.2$ (Fig. 17 (a)) for large heat transfer area and $-1 < X/D < 1.5$ and $-1 < Z/D < 1$ (Fig. 17 (b)) for small heat transfer area. In the case of the large heat transfer area, the heat transfer rate for case of AR=1 is highest, and the maximum value takes place at VR=5. The average Nusselt number of AR=1 is dominated in of AR=4 and 8 for any VR because the local Nusselt number at around stagnation region of AR=4 and 8 is low. For AR=1 with VR=5, the local Nusselt number is appropriately high between stagnation region and it's around, so this reason give highest average Nusselt number for large heat transfer area.

In contrast, for the small heat transfer area (Fig.16 (b)), the highest average Nusselt number occurs at VR=5, AR=4 with $\theta=0^\circ$. For the case of VR=5, the average Nusselt number for AR=4 with $\theta=0^\circ$ and 45° are higher than of AR=1 for 6 % and 2%, respectively. In the case of VR=7 also shows that the average Nusselt number for AR=4 with $\theta=15^\circ$, 30° and 45° are higher than of AR=1 for 4 %, 4% and 10%, respectively.

CONCLUSION

In the present study, effects of orifice geometry, velocity ratio and attacking angle on flow and heat transfer characteristics on the impinged surface under crossflow were investigated. The main results show that:

1. The jet more deflected to the downstream of crossflow when the crossflow velocity increases. The jet AR=1 is more deflect than of AR=4 because the jet AR=4 with $\theta=0^\circ$ can be penetrated into the crossflow better than of the AR=1.

2. The impingement region of jet from elongated round orifice are symmetry in Z-axis for $\theta=0^\circ$. When the attacking angle in-

creases, the impingement region is larger in +Z-axis and smaller in -Z-axis.

3. The effect of attacking angle for case of AR=4 can increase or decrease heat transfer at stagnation region depends on a variation of crossflow velocity. For the low crossflow velocity, the heat transfer increases when attacking angle increases. In contrast to the high crossflow velocity, the heat transfer decreases when attacking angle increases.

4. The average heat transfers at stagnation regions of AR=4 with $\theta=0^\circ$ and 45° are higher 6 % and 2% than of AR=1 for VR=5 and of AR=4 with $\theta=15^\circ$, 30° and 45° are higher 4 %, 4% and 10% than of AR=1 for VR=7, respectively.

5. The highest average heat transfer at stagnation region occurs at AR=4 with $\theta=0^\circ$ for VR=5, while in the case of VR=3, AR=4, $\theta=45^\circ$, the heat transfer rate is lowest due to the highest crossflow velocity and the largest attacking angle. The jet is more deflected to the downstream; consequently, the momentum impinging on a target surface was decreased.

ACKNOWLEDGEMENT

This research was supported by grants from the Thailand Energy Policy and Planning Office (EPPPO), Ministry of Energy, and the Graduate School and the Faculty of Engineering, Prince of Songkla University (PSU).

REFERENCES

- [1] Barata, J. M. M., and Durao, D. F. G., 2004, "Laser-Dropper measurements of impinging jet flows through a crossflow", *J. Experimental in Fluids*, Vol. 36, pp. 665-674.
- [2] Nakabe, K., Suzuki, K., Inaoka, K., Higashio, A., Acton, J.S., and Chen, W., 1998, "Generation of longitudinal vortices in internal flows with an inclined impinging jet and enhancement of target plate heat transfer", *Int. J. Heat and Fluid Flow*, Vol. 19, pp. 573-581.
- [3] Goldstein, R. J., and Behbahan, I., 1982, "Impingement of a circular jet with and without cross flow", *Int. J. Heat Mass Transfer*, Vol. 25, pp. 1377-1382.
- [4] Bouchez, J.-P., and Goldstein, R. J., 1975, "Impingement cooling from a circular jet in a cross flow", *Int. J. Heat Mass Transfer*, Vol. 18, pp. 719-730.
- [5] Lee, J., and Lee, S.-J., 2000, "The effect of nozzle aspect ratio on stagnation region heat transfer characteristics of elliptic impinging jet", *Int. J. Heat and Mass Transfer*, Vol.43, pp. 555-575.
- [6] Zhou, D. W., and Lee, S.-J., 2004, "Heat transfer enhancement of impinging jets using mesh screens", *Int. J. Heat and Mass Transfer*, Vol.47, pp.2097-2108.
- [7] Wen, M.Y., and Jang, K.J., 2003, "An impingement cooling on a flat surface by using circular jet with longitudinal swirling strips", *Int. J. Heat Mass Transfer*, Vol. 46, pp. 4657-4667.
- [8] Lee, D.H., Won, S.Y., Kim, Y.T., and Chung, Y.S., 2002, "Turbulent heat transfer from a flat surface to a swirling round impinging jet", *Int. J. Heat Mass Transfer*, Vol. 45, pp.223-227.
- [9] Mladin, E.C., and Zumbrunnen, D.A., 1997, "Local convective heat transfer to submerged pulsating jets", *Int. J. Heat Mass Transfer*, Vol. 46, No.14, pp. 3305-3321.
- [10] Hofmann, H. M., Movable, D. L., Kind, M., and Martin, H., 2007, "Influence of a pulsation on heat transfer and flow structure in submerged impinging jets", *Int. J. Heat and Mass Transfer*, Vol. 50, pp. 3638-3648.
- [11] Yang, Y.-T., and Wang, Y.-X., 2005, "Three-Dimensional Numerical Simulation of an Inclined Jet with Cross-Flow", *Int. J. Heat and Mass Transfer*, Vol.48, pp.4019-402.
- [12] Chandratilleke, T.T., Jagannatha, D., and Narayanaswamy, R., 2010, "Heat transfer enhancement in microchannels with cross-flow synthetic jets", *Int. J. Thermal Sciences*, Vol. 49, pp. 504-513.
- [13] Seifert, A., and Shemer, L., 1995, "Plume rise from a chimney

- with an elongated exit cross section". *J. Atmospheric Environment*, Vol. 29, pp. 709-713.
- [14] Geers, L.F.G., Tummers, M.J., Bueninck, T.J., and Hanjalic, K., 2008, "Heat transfer correlation for hexagonal and in-line arrays of impinging jets". *Int. J. Heat and Mass Transfer*, Vol. 51, pp. 5389-5399.
- [15] Lee, J., and Lee, S.-J., 2000, "The effect of nozzle configuration on stagnation region heat transfer enhancement of axisymmetric jet impingement," *Int. J. Heat and Mass Transfer*, Vol.43, pp.3497-3509.
- [16] Obot, N. Y., Mujumdar A. S., and Douglas, W. J. M., 1982, "Effect of semi-confinement on impingement heat transfer," *Proceedings, 7th Int. Heat Transfer Conf.*, Munchen, Germany, September 6-10, pp. 395-400.
- [17] Katti, V., and Prabhu, S. V., 2008, "Influence of spanwise pitch local heat transfer distribution for in-line arrays of circular jets with air flow in two opposite," *J. Experimental Thermal and Fluid Science*, Vol. 33, pp. 84-95.
- [18] Viskanta, R., 1993, "Heat transfer to impinging isothermal gas and flame jets," *J. Experimental Thermal and Fluid Science*, Vol.68, pp.111-134.
- [19] Ashforth-Frost, S., Jambumathan, K., and Whitney, C.F., 1997, "Velocity and turbulence characteristics of a semiconfined orthogonally impinging slot jet," *J. Experimental Thermal and Fluid Science*, Vol. 14, pp. 60-67.
- [20] Koseoglu, M. F., and Baskaya, S., 2008, "The effect of flow field and turbulence on heat transfer characteristics of confined circular and elliptic impinging jets," *Int. J. Thermal Sciences*, Vol. 47, pp. 1332-1346.
- [21] New, T. H., Lim, T. T., and Luo, S. C., 2004, "A flow field study of an elliptic jet in cross flow using PDIV technique," *J. Experiments in Fluids*, Vol. 36, pp. 604-618.

Appendix A4

Journal Paper 4

M. Wae-hayee, P. Tekasakul, S. Eiamsa-ard and C. Nuntadusit, "Effect of Cross-flow Velocity on Flow and Heat Transfer Characteristics of Impinging Jet with Low Jet-to-Plate Distance" **This manuscript have been submitted in Journal of Mechanical Science and Technology.**

Journal of Mechanical Science and Technology
Effect of Cross-flow Velocity on Flow and Heat Transfer Characteristics of Impinging Jet with Low Jet-to-Plate Distance
 --Manuscript Draft--

Manuscript Number:	MEST-D-13-01023
Full Title:	Effect of Cross-flow Velocity on Flow and Heat Transfer Characteristics of Impinging Jet with Low Jet-to-Plate Distance
Article Type:	Original Paper
Keywords:	Impinging jet; Cross-flow; Heat transfer; Thermochromic Liquid crystal
Corresponding Author:	C. Nuntadusit Prince of Songkla University Hat Yai, Songkhla THAILAND
Corresponding Author Secondary Information:	
Corresponding Author's Institution:	Prince of Songkla University
Corresponding Author's Secondary Institution:	
First Author:	M. Wae-hayee
First Author Secondary Information:	
Order of Authors:	M. Wae-hayee P. Tekasakul smith eiamsa-ard, D.Eng (Mechanical Eng.) C. Nuntadusit
Order of Authors Secondary Information:	
Abstract:	An effect of cross-flow velocity on flow and heat transfer characteristics of impinging jet in a case of low jet-to-plate distance at $H=2D$ was experimentally and numerically investigated. In the experiments, the air jet perpendicularly impinged on the wall of wind tunnel while a cross-flow was simultaneously induced. The jet velocity was fixed while the cross-flow velocity was varied corresponding to velocity ratios (jet velocity/cross-flow velocity) $VR=3, 5$ and 7 . The temperature distribution on an impinged surface was visualized by using Thermochromic Liquid Crystal sheet (TLCs), and Nusselt number distribution was evaluated by using image processing method. The flow pattern on impinged surface was visualized by using oil film technique. The numerical simulation was carried out for a better understanding of the jet flow in the cross-flow. The results show that Nusselt number peak shifts downstream and the peak intensity increases with increasing cross-flow velocity.
Suggested Reviewers:	Wei-Mon Yan wmyan@cc.hfu.edu.tw Relating work

Effect of Cross-flow Velocity on Flow and Heat Transfer Characteristics of Impinging Jet with Low Jet-to-Plate Distance

M. Wae-hayee¹, P. Tekasakul¹, S. Eiamsa-ard² and C. Nuntadusit^{1}*

¹Department of Mechanical Engineering, Faculty of Engineering
Prince of Songkla University, Hat Yai, Songkhla 90112, Thailand

²Department of Mechanical Engineering, Faculty of Engineering
Mahanakorn University of Technology, Bangkok 10530, Thailand

*Corresponding author, E-mail: chayut@me.psu.ac.th, chayut.n@gmail.com

ABSTRACT

An effect of cross-flow velocity on flow and heat transfer characteristics of impinging jet in a case of low jet-to-plate distance at $H=2D$ was experimentally and numerically investigated. In the experiments, the air jet perpendicularly impinged on the wall of wind tunnel while a cross-flow was simultaneously induced. The jet velocity was fixed while the cross-flow velocity was varied corresponding to velocity ratios (jet velocity/cross-flow velocity) $VR=3, 5$ and 7 . The temperature distribution on an impinged surface was visualized by using Thermochromic Liquid Crystal sheet (TLCs), and Nusselt number distribution was evaluated by using image processing method. The flow pattern on impinged surface was visualized by using oil film technique. The numerical simulation was carried out for a better understanding of the jet flow in the cross-flow. The results show that Nusselt number peak shifts downstream and the peak intensity increases with increasing cross-flow velocity.

Keywords: Impinging jet, Cross-flow, Heat transfer, Thermochromic Liquid crystal

1. INTRODUCTION

Jet impingement is widely used in various industrial applications because it offers high localized heating and cooling rates. The applications include tempering of glass, drying of paper, chemical vapour deposition, cooling turbine blade and electronic component. Heat transfer on an impinged surface is governed by two key factors: (1) an axial velocity of a jet which impinges on a target surface and (2) a turbulence intensity of a jet just before impingement. In general, after the end of a potential core, a jet begins to spread resulting in the reduction of the axial velocity and the increase of the

turbulence intensity in the direction parallel to the impinged surface. Therefore the maximum heat transfer is found at the optimum jet-to-plate distance [1-3].

Usually, the multiple impinging jets are applied on large heat transfer surface to attain high and uniform heat transfer rate on a large surface. In case of multiple impinging jets under a confined space, a cross-flow is generated by the spent air of the impinging jet. Consequently, the flow and heat transfer of neighboring jets are significantly influenced by the cross-flow [4, 5]. To clarify the effect of cross-flow velocity on jet flow, several researches were performed by

introducing a single impinging jet in cross-flow. Barata and Durao visualized the flow characteristic of impinging jet and cross-flow [6]. Goldstein and Behbahani [7] and Bouchez and Goldstein [8] conducted a jet impingement under cross-flow in the case of a high jet-to-plate distance ($H \geq 4D$) where D is nozzle diameter. Heo *et al.* [9] and Shi *et al.* [10] used numerical technique to predict a flow and heat transfer of inclined impinging jet within cross-flow. The general results found are the cross-flow velocity and the jet-to-plate distance play important roles on flow and heat transfer characteristics and a high cross-flow velocity tends to decrease a heat transfer rate of impinging jet at stagnation region.

The published works mentioned above were carried out at high jet-to-plate distance ($H \geq 4D$), using pipe nozzles. Theoretically, a maximum heat transfer on a target surface of multiple impinging jets takes place at low jet-to-plate distance ($H \leq 2D$) [4, 11 and 12]. In addition, an orifice nozzle is easier to design and manufacture than a pipe nozzle for industrial applications. According to the facts mentioned above, the present work aims to study the effect of cross-flow on jet impingement at low jet-to-plate distance ($H=2D$) by using an orifice nozzle. To consider the effect of cross-flow on flow and heat transfer of impinging jet, the jet velocity was kept constant, while the cross-flow velocity was varied. Temperature distribution on the impinged surface was acquired by using Thermochromic Liquid Crystal sheet (TLCs), and the Nusselt number distribution was evaluated by using image processing method. The flow characteristic on the impinged surface was visualized by using oil film technique. The numerical simulation was also carried out to examine the fluid flow.

2. EXPERIMENTAL MODEL AND PARAMETERS

Figure 1 shows the experimental model in the present work. The jet issuing from the round orifice impinges on the impinged surface (normal to the flow) of the rectangular channel. A cross-flow was generated by introducing air through the test section from the surface perpendicular to the impinging jet. An origin of the Cartesian coordinates was located on the impinged surface. The X- and Y-directions are the cross-flow and axial jet flow directions, respectively. The effect of cross-flow velocity on flow and heat transfer characteristics was investigated by varying cross-flow velocity corresponding to three different velocity ratios (jet velocity to cross-flow velocity at the centre of channel) $VR=3, 5$ and 7 while the jet velocity was kept corresponding to $Re=13,400$. The orifice diameter was $D=13.2$ mm and jet-to-plate distance was $H=2D$.

3. EXPERIMENTAL MODEL AND PARAMETERS

A schematic diagram of the experimental apparatus is shown in Fig. 2. The experimental apparatus consisted of two parts; jet flow and cross-flow supplies. For the jet flow supply, a 3-hp blower was employed to accelerate air through a temperature controlled chamber equipped with 2-kW heater, an calibrated orifice flow meter, a jet chamber (with a constant cross-section area of $360\text{-mm} \times 360\text{-mm}$ and a height of 850-mm), and a jet orifice before entering the test section. The jet chamber was equipped with two layers of perforated plates and two layers of mesh plates to ensure a uniform flow field approaching the orifice plate. Another 3-hp blower was used to introduce the cross-flow through the inlet chamber, a flow straightener, two layers of

mesh plates and the test section. The wind tunnel with a width of 300 mm had a sufficient length to provide a fully developed flow through the test section. In addition, the chamber inlet and wind tunnel was assembled by a convergent adaptor to reduce the effect of wind tunnel inlet as shown in Fig. 2. The test section was directly mounted

upon a jet chamber. Pitot-static tube was mounted upstream of the test section to measure the cross-flow velocity. For all experiments, the temperature of inlet jet and cross-flow was kept constant at 27°C by the temperature and power controllers. The temperature variation of the jet and cross-flow was controlled within $\pm 0.2^\circ\text{C}$.

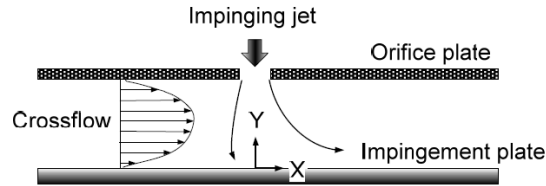


Fig. 1. The experimental model.

3.1 Heat transfer measurement

The test section for heat transfer measurement is shown in Fig. 2. The heat transfer surface made of a stainless steel foil with the thickness of 30- μm was attached to the TLC sheet (Omega, LCS-95). The stainless steel foil was stretched between the couple of copper bus bars. The heat transfer surface was heated by a DC power supply that can supply current up to 50 A through the copper bus bars. The local heat transfer coefficient by forced convection of the impinging jet on the heated surface can be evaluated from

$$\dot{q}_{input} = \frac{I^2 \cdot R}{A}$$

$$h = \frac{\dot{q}_{input} - \dot{q}_r - \dot{q}_c}{T_w - T_j}$$

where, I and R are the electrical current and the thermal resistance of the stainless steel foil, \dot{q}_r and \dot{q}_c are the heat loss to the environment by radiation and convection, T_w and T_j are the wall and jet temperatures, respectively. The wall temperature (T_w) on the impinging surface was measured by using the TLC sheet attached on the rear of the impinging surface. The TLC sheet was calibrated using the digital image processing

system under the same conditions for all experimental runs. The local Nusselt number can be calculated from

$$Nu = hD/k$$

where k is a jet thermal conductivity. The detail of heat transfer measurement was described in the previous works [5, 13].

3.2 Flow visualization on the impinged surface

The flow visualization on the impinged surface was illustrated by using oil film technique. The oil film was prepared by mixing liquid paraffin with titanium dioxide and oleic acid and then uniformly applied on the transparent plastic plate. During the experiment, the oil film behavior on the impinged surface was recorded using a CCD camera every 30 seconds.

4. NUMERICAL SIMULATION

The 3-D numerical simulation was used to visualize the flow characteristic of jet and cross-flow (ANSYS Fluent ver.12.0). The numerical model is same with the experimental one in dimension, mass flow rate of jet and cross-flow. The numerical

computation was carried out by solving the governing equations with boundary condition. The Shear-Stress-Transport (SST) $k-\omega$ turbulent model was selected for solving numerical simulation problems due to its high accurate prediction in impingement problems and moderate computational cost [14]. This turbulent model has also been employed to predict a flow and heat transfer characteristics of impinging jet under cross-

flow [9, 15]. A non-uniform grid system was finely generated at mixing region and wall. A solution method was based on SIMPLE algorithm with second order upwind for all spatial discretization. The solution was considered to be converged when the normalized residual of the algebraic equation was less than a prescribed value of 1×10^{-4} [9].

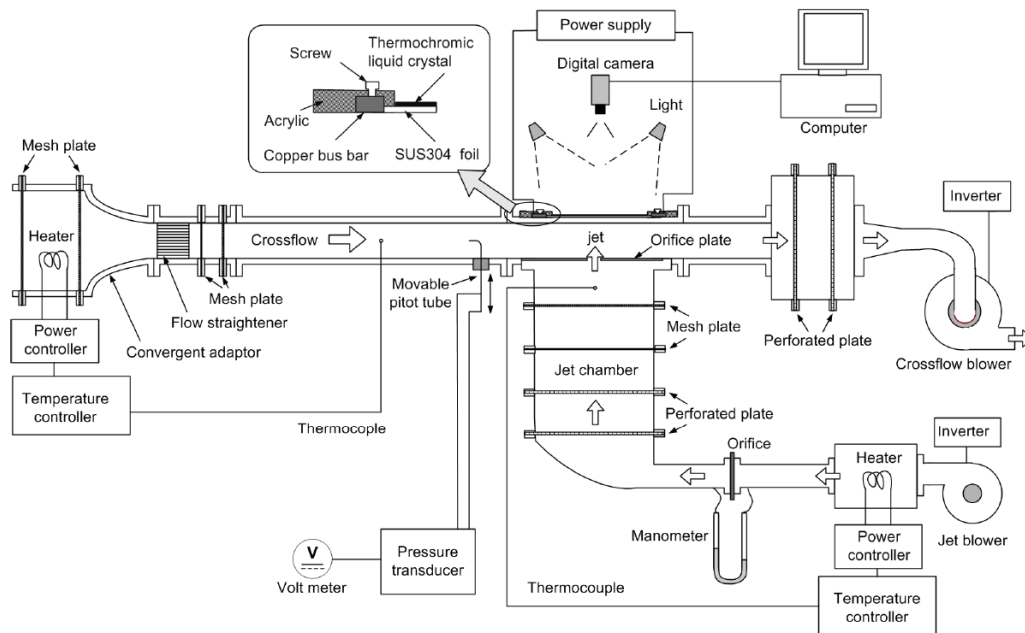


Fig. 2. Schematic diagram of the experimental setup.

5. RESULTS AND DISCUSSION

5.1 Experimental setup verification

To verify the test section of this experiment, stagnation point Nusselt numbers at various Reynolds numbers of impingement jet without cross-flow were compared with those from the previous work [16]. Comparison of the results is presented in the Fig. 3. The current data agree well with those in the previous work.

5.2 Flow characteristic of jet and cross-flow

Velocity vectors and velocity contours of jet and cross-flow through centerline of orifice in X-Y plane are shown in Fig. 4. The results reveal the jet is more deflected to downward from the stagnation point when the cross-flow velocity increases (or VR decreases). It is also can be observed that the wall jet (the jet which spreads radially on the target surface, after the impingement) located upstream of the stagnation point is suppressed as the cross-flow velocity increases. The suppression is significant at $VR=3$ as shown in Fig. 4(c) because the cross-flow with high velocity sweeps the jet downstream.

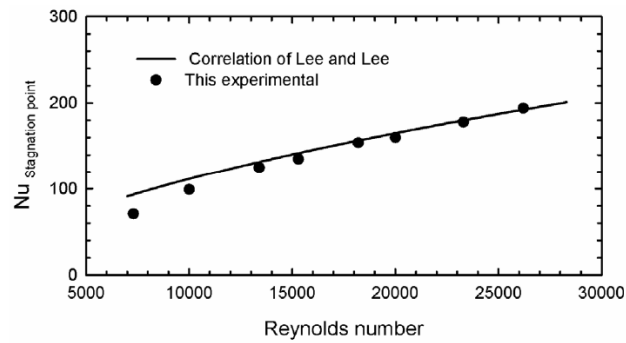


Fig. 3. Comparison of Nusselt numbers at the stagnation point in present work with those in the previous work [16].

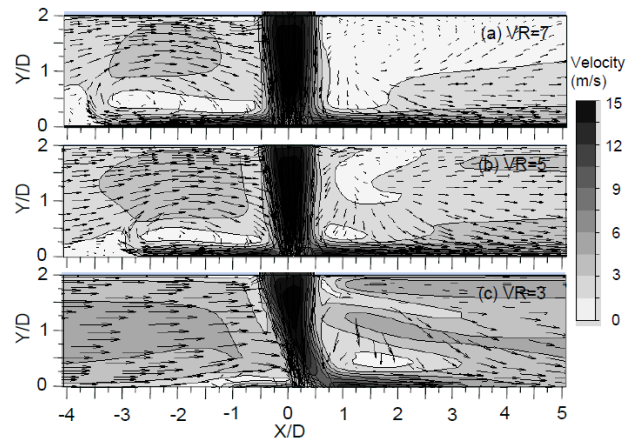


Fig. 4. Vectors and contours of velocity of the jet flow and cross-flow in X-Y plane.

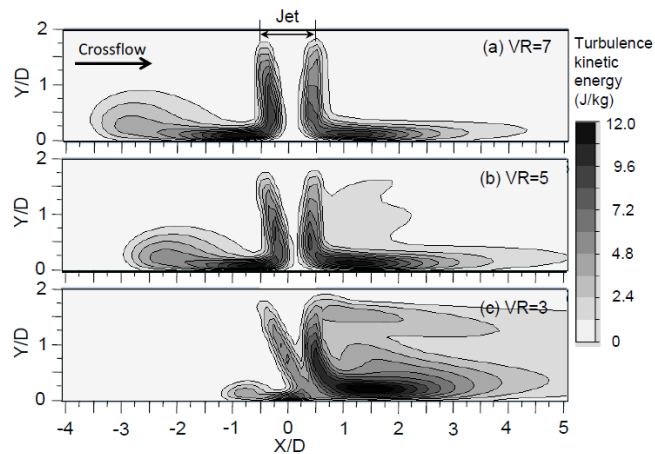


Fig. 5. Contours of turbulence kinetic energy of the jet flow and cross-flow in X-Y plane.

The contours of turbulence kinetic energy of the jet flow and cross-flow in X-Y plane are shown in Fig. 5. The turbulence kinetic energy at external jet region is higher than

that along the axial jet due to the mixing between outer jets and surrounding air. At $VR=7$ (Fig. 5(a)), the turbulence kinetic energy of upstream and downstream wall jets are comparable. The size of recirculation flow of the upstream wall jet is slightly higher than that of the downstream one, this is the result of the interaction between the upstream wall jet and the cross-flow with low velocity. However, when the cross-flow

velocity increases ($VR=5$ and 3), the turbulence kinetic energy of the downstream wall jet becomes higher than that of the upstream one. For $VR=3$ The turbulence kinetic energy is significantly enhanced at $1 < X/D < 2.5$ as shown in Fig. 5(c). This is responsible by the sweeping of the upstream wall jet by the cross-flow as mentioned above.

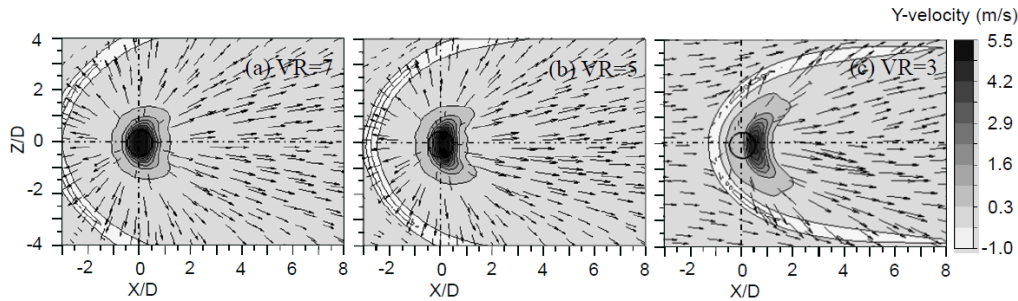


Fig. 6. Velocity vectors and Y-component velocity contours on X-Z plane (at 1.5-mm above the impinging surface and the circles represent the position of the orifice).

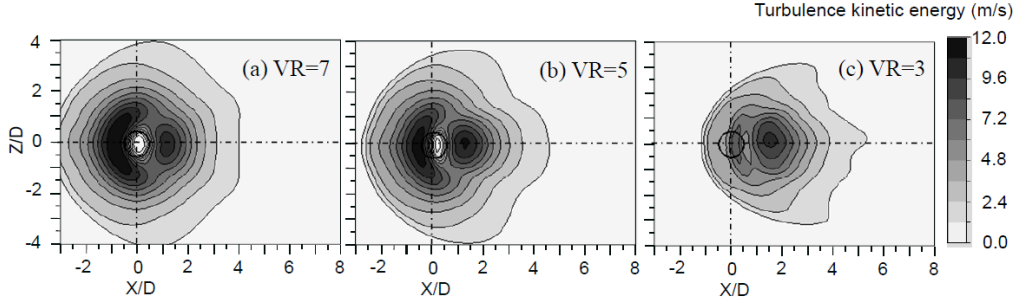


Fig. 7. Contours of turbulence kinetic energy on X-Z plane (at 1.5-mm above the impinging surface and the circles represent the position of the orifice).

The velocity vectors and velocity contours in Y-component on X-Z plane at 1.5-mm above the impinging surface are shown in Fig. 6. The Y-component velocity represents the velocity in direction normal to the impinging surface. The positive velocity of the downstream jet, indicates that the jet impinges on the wall. When the cross-flow velocity increases, the impingement region shifts downstream, especially, at the highest cross-flow velocity (Fig. 6(c)). This is due to the significant jet deflection caused by the of cross-flow as shown in Fig. 4(c).

The turbulence kinetic energy contours on X-Z plane at 1.5-mm above the impinging surface are shown in Fig. 7. At low cross-flow velocity ($VR=7$) as shown in Fig. 7(a), the regions with high turbulence kinetic energy are detected in both upstream and downstream wall jets, and the high intensity region of the upstream wall jet is larger than that of the downstream one. In addition, the turbulence kinetic energy at stagnation region is very low which is similar to that found in a common impinging jet without a cross-flow. As the cross-flow velocity

increases, the region with high turbulence kinetic energy of upstream wall jet shifts downstream, and the region with low turbulence kinetic energy at stagnation region becomes smaller due to the shear effect of the cross-flow.

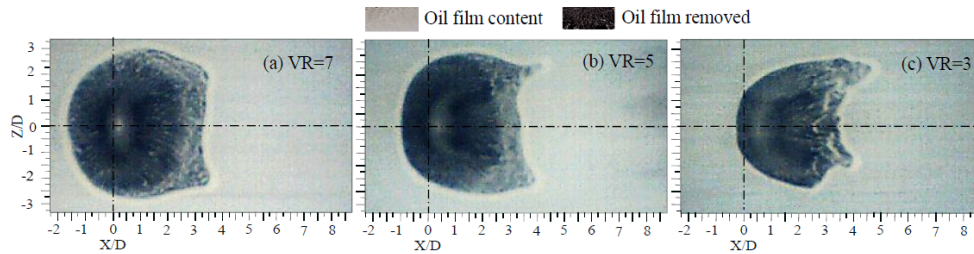


Fig. 8. Flow characteristics on the impinged surface ($Re_j = 13,400$).

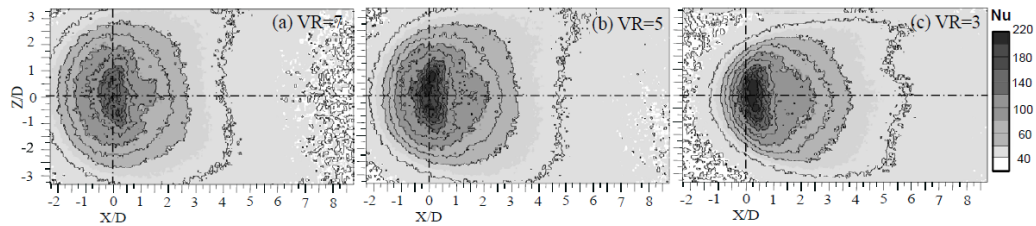


Fig. 9. Nusselt number distributions on the impinged surface ($T_j = 27\text{ }^\circ\text{C}$, $Re_j = 13,400$).

5.3 Flow patterns on the impinged surface

The flow visualization on the impinged surface by oil film technique is shown in Fig. 8(a-c). The black area is an impinged surface where an oil film removed while the white area is a remaining oil film. A white point surrounded by black areas represents the stagnation point of the impinging jet bounded by the impingement region. The visualization shows that the upstream impingement region ($X/D < 0$) and both lateral sides ($\pm Z/D$) are contracted while the downstream impingement area is elongated as cross-flow velocity increases.

5.4 Local Nusselt number on the impinged surface

The Nusselt number distributions on the impinged surface are shown in Fig. 9. The distributions coincide with the flow patterns on the impinged surface as shown in Fig. 8. According to the flow visualization, the

Nusselt numbers can be divided into three ranges for three different regions; $Nu > 140$, $40 < Nu < 140$ and $Nu < 40$ for the impingement region, the wall jet region and the cross-flow region, respectively. As cross-flow velocity increases, the high Nusselt number ($Nu > 140$) and wall jet region ($40 < Nu < 140$) shifted downstream. The Nusselt number distribution along the cross-flow direction at $Z/D = 0$, is shown in Fig. 10. The upstream Nusselt number ($X/D < 0$) becomes lower when cross-flow velocity increases. This corresponds to the contraction of the upstream impinged area as shown in Fig. 8. In contrast, the downstream Nusselt number ($X/D > 0$) becomes higher when the cross-flow velocity increases. At $VR = 3$, the downstream Nusselt number for $2 < X/D < 3$ is conspicuously enhanced, due to the high turbulence kinetic energy of the range as revealed in Fig. 11(b). In addition, the Nusselt number peak of the stagnation region increases with increasing cross-flow velocity. The highest Nusselt number peak

takes place at $VR=3$ and $X/D=0.2$, as a result of the optimum synergy between the Y-component velocity and the turbulence kinetic energy. As shown in Fig.11, at $X/D=0.2$, the jet and cross-flow with $VR=3$ offer the peak of turbulence kinetic energy coupled with the moderate Y-component velocity. However, for $VR=3$, at $X/D=-0.8$ or 1.8 , the peak of turbulence kinetic energy takes place with a low Y-component velocity, resulting in a low Nusselt number. The lower Nusselt number peak at $VR=5$ and 7 as compared to that at $VR=3$ can be

explained by the same fact. The results in the present work reveal that at the low jet-to-plate distance ($2D$), the increase of cross-flow velocity corresponding to the decrease of VR from 7 to 3 , results in the increase of Nusselt number peak of the stagnation area. This is different from that found at large jet-to-plate distance ($\geq 3D$). In the latter case, Nusselt number peak of the stagnation area decreases as cross-flow velocity increases due to the large colliding area between cross-flow and jet impingement [2, 3].

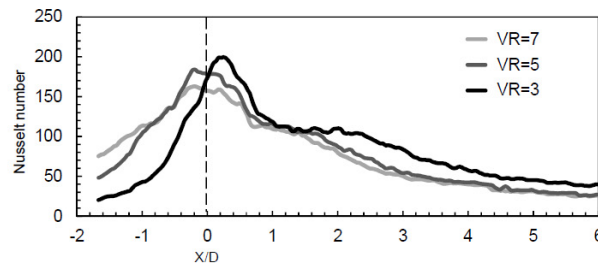


Fig. 10. Nusselt number distribution along the crossflow direction ($Z/D=0$, $T_j=27^\circ\text{C}$ and $Re_j=13,400$).

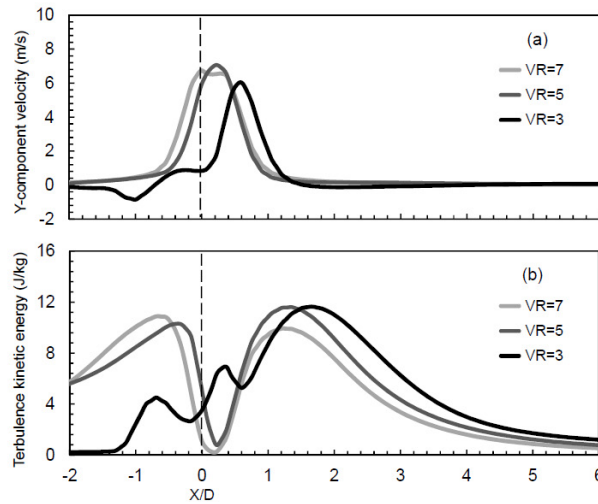


Fig. 11. CFD results of (a) Y-component velocity contours and (b) turbulence kinetic energy (at 1.5-mm above the impinged surface).

6. CONCLUSIONS

The present work has been carried out to investigate the effect of cross flow velocity

on heat transfer characteristics of impinging jet with low jet-to-plate distance at $H=2D$. The major findings can be drawn as follows:

1. The impingement region shifts downstream direction as cross-flow velocity increases, coinciding with the shifting of the high Nusselt number area.
2. When the cross-flow velocity increases, the upstream impingement region is contracted while the downstream one is extended, resulting in the decrease of the upstream Nusselt number and increase of the downstream one.
3. The Nusselt number peak of the stagnation region increases with increasing cross-flow velocity.

ACKNOWLEDGEMENTS

This research was supported by grants from Thailand Energy Policy and Planning Office, Ministry of Energy, the Graduate School and Faculty of Engineering, Prince of Songkla University (PSU).

REFERENCES

- [1] R. Viskanta, Heat transfer to impinging isothermal gas and flame jets, *Experimental Thermal and Fluid Science* 68 (1993) 111-134.
- [2] S. Ashforth-Frost, K. Jambunathan, Effect of nozzle geometry and semi-confinement on the potential core of a turbulent axisymmetric free jet, *International Communication in Heat Mass Transfer* 23 (1996) 155-162.
- [3] S. Ashforth-Frost, K. Jambunathan, C.F. Whitney, Velocity and turbulence characteristics of a semiconfined orthogonally impinging slot jet, *Experimental Thermal and Fluid Science* 14 (1997) 60-67.
- [4] V. Katti, S.V. Prabhu, Influence of spanwise pitch local heat transfer distribution for in-line arrays of circular jets with air flow in two opposite, *Experimental Thermal and Fluid Science* 33 (2008) 84-95.
- [5] C. Nuntadusit, M. Wae-hayee, P. Tekasakul, S. Eiamsa-ard, Local heat transfer characteristics of array impinging jets from elongated orifices, *International Communication in Heat Mass Transfer* 39 (2012) 1154-1164.
- [6] J.M.M Barata, D.F.G. Durao, Laser-Dropller measurements of impinging jet flows through a crossflow, *Experimental in Fluids* 36 (2004) 665-674.
- [7] R.J. Goldstein, I. Behbahan, Impingement of a circular jet with and without cross flow, *International Journal Heat and Mass Transfer* 25 (1982) 1377-1382.
- [8] J.P. Bouchez, R.J. Goldstein, Impingement cooling from a circular jet in a cross flow, *International Journal Heat and Mass Transfer* 18 (1975) 719-730.
- [9] M.W. Heo, K. D. Lee, K.Y. Kim, Optimization of an inclined elliptic impinging jet with cross flow for enhancing heat transfer, *Heat Mass Transfer* 47 (2011) 731-742.
- [10] Y. Shi, M.B. Ray, A.S. Mujumdar, Numerical study on the effect of cross-flow on turbulent flow and heat transfer characteristics under normal and oblique semi-confined impinging slot jets, *Drying Technology* 21 (2003) 1923-1939.
- [11] J.Y. San, Y.M. Tsou, Z.C. Chen, Impingement heat transfer of staggered arrays of air jets confined in a channel, *International Journal Heat and Mass Transfer* 50 (2007) 3718-3727.
- [12] J.Y. San, M.D. Lai, Optimum jet-to-jet spacing of heat transfer for staggered arrays of impinging air jets, *International Journal Heat and Mass Transfer* 44 (2001) 3997-4007.
- [13] C. Nuntadusit, A. Bunyajitradulya, S. Eiamsa-ard, Heat transfer enhancement by multiple swirling

- impinging jets with twisted-tape swirl generators, *International Communication in Heat Mass Transfer* 39 (2012) 102-107.
- [14] N. Zuckerman, N. Lion, Jet impingement heat transfer: physics, correlations, Numerical modeling, *Advances in Heat Transfer* 39 (2006) 565-631.
- [15] T.T. Chandratilleke, D. Jagannatha, R. Narayanaswamy, Heat transfer enhancement in microchannels with cross-flow synthetic jets, *International Journal Thermal Sciences* 49 (2010) 504-513.
- [16] J. Lee, S.J. Lee, The effect of nozzle configuration on stagnation region heat transfer enhancement of axisymmetric jet impingement, *International Journal Heat and Mass Transfer* 43 (2000) 3497-3509.

Appendix B

The publications of row of impinging jets under simulated cross-flow

Appendix B1

Conference Paper

C. Nuntadusit and M. Wae-hayee, "Flow and Heat Transfer Characteristics of Row of Jet Impingement from Elongated Orifice under Cross-flow" The 4th International Conference on Jets, Wakes and Separated Flows (ICJWSF2013), September 17-21, 2013, Nagoya, Japan.

FLOW AND HEAT TRANSFER CHARACTERISTICS OF ROW OF JET IMPINGEMENTS FROM ELONGATED ORIFICES UNDER CROSS-FLOW

*¹Chayut Nuntadusit and ¹Makatar Wae-hayee

¹Department of Mechanical Engineering, Faculty of Engineering,
Prince of Songkla University, Hatyai, Songkhla, Thailand
chayut@me.psu.ac.th

ABSTRACT

The aim of this article is to study the flow and heat transfer characteristics of row of jet impingements with simulated cross-flow. Elongated orifices with an aspect ratio of orifice length to orifice width at $AR=4$ was studied and compared with the case of circular orifices ($AR=1$) under the same cross-section area. Four of impinging jets with inline arrangement impinge on inner surface of wind tunnel with rectangular cross-section having height of two times of equivalent diameter of orifice. Two differences of cross-flow velocities corresponding to velocity ratios (jet velocity/cross-flow velocity), $VR=3$ and 7 , and attacking angle defined as angle of major axis of elongated orifice to cross-flow direction at $\theta=0^\circ$, 15° and 45° were examined. In order to measure the heat transfer on the impinged surface, temperature distributions were monitored using Thermochromic Liquid Crystal sheet (TLCs), and heat transfer coefficient distributions were evaluated using an image processing method. The flow characteristics on the impingement surface were visualized using the oil film technique. The numerical simulation was also employed to gain insight into the fluid flow. Results show that the impinging jets discharging from the elongated orifice with $\theta=0^\circ$ can minimize the cross-flow effect, and the area of high heat transfer is extended in upstream region of jet impingement.

1. INTRODUCTION

Impinging jet is widely employed in many thermal industrial applications and gas turbine components because the heat transfer rate under impingement region is high. To suffice heat transfer rate at a large heat transfer area, multiple impinging jets or jet impingement array, generally, are applied. Flow characteristics of jet impingement array under confined channel, an accumulation of jets after impingement, called a cross-flow, moves toward channel exit. Downstream jets, subsequently, tend to cross-flow path line resulting decreasing its momentum before impingement on a target surface and its heat transfer rate [1-3].

Some techniques to eliminate the cross-flow in confined channel of impingement array by drilling of effusion holes, on the upper surface (nozzle plate) [4, 5], and at the lower surface (impingement surface) [6] have been attempted. Elongated orifices, which were replaced to conventional round orifices to reduce the effect of cross-flow on the jet impingement array, have been investigated [7]. It was found that the heat transfer rate of impinging jets issuing from

these substituted orifices is more uniform and higher than those from conventional orifices.

Generally, to identify the interactions between multiple impinging jets and an inherent cross-flow are a difficult task. To clarify these interactions, the investigations are usually performed by introducing cross-flow through the impinging jet in wind tunnel [8 and 9]. In this work, the interactions between multiple impinging jets discharging from a row of elongated orifices [7] and cross-flow effect is concerned.

The aim of this research is to experimentally and numerically study the effect of cross-flow velocity on flow and heat transfer characteristics of a jet impingement row with elongated orifices. Two differences of high and low cross-flow velocities, and attacking angle, defined as the major axis of elongated orifice to the cross-flow direction, were examined. The local temperature distribution on the impinged surface was measured using Thermochromic Liquid Crystal sheet (TLCs). The oil film technique was used to visualize the flow patterns on the impingement surface. The numerical simulation was employed to gain insight into the fluid flow.

2. EXPERIMENTAL MODEL AND PARAMETERS

A row of 4 jets discharging from upper side of wind tunnel with rectangular cross-section impinges on the lower surface under a simulated cross-flow as shown in Fig.1. An origin of the Cartesian coordinates was located on the impinged surface. The X-, Y- and Z-axes are cross-flow streamwise, vertical, and spanwise coordinates, respectively.

Round orifices ($AR=1$) were replaced by elongated orifices with aspect ratio of its length to its width, $AR=4$. Both orifices have the same exit area of 136.8 mm^2 , and each orifice has an equivalent diameter (D_E) of 13.2 mm as shown in Fig.2 [7]. The attacking angle defined an angle between the major axis of the elongated orifice to the cross-flow direction (X-axis) was varied from $\theta=0^\circ$, 15° and 45° as also shown in Fig.2. The jet-to-plate (wind tunnel height) and jet-to-jet distances were fixed at $H=2D_E$ and $S=3D_E$, respectively. The jet velocity was fixed corresponding to $Re_E=13,400$ (based on velocity at center of orifice and equivalent diameter), and cross-flow velocity (velocity at wind tunnel center) was varied corresponding to velocity ratios (jet velocity/cross-flow velocity) $VR=3$ and 7 .

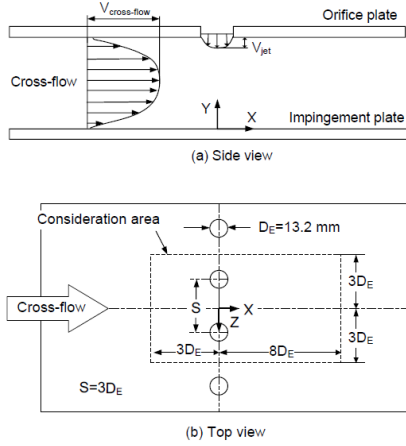


Fig. 1 Experimental model of row of impinging jets

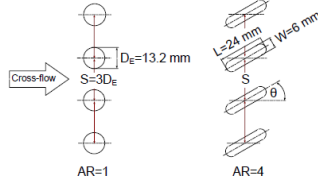


Fig. 2 Configuration of orifice arrangement

3. EXPERIMENTAL SETUP AND METHOD

3.1 Experimental apparatus

The experimental setup was assembled in two parts: jet and cross-flow supplies as shown in Fig.3. The impinging jets were generated by introducing air through a temperature controlled chamber equipped with air heater, calibrated orifice flow meter, jet chamber and jet orifice before entering the test section. The jet chamber having constant cross-section of 360 mm × 360 mm and a height of 850 mm was equipped with two layers of perforated plates and two layers of mesh plates to achieve a uniform flow field approaching the jet orifice plate.

The simulated cross-flow was produced by introducing air through the inlet chamber, flow straightener, two layers of mesh plates, the test section and a chamber outlet by using another blower. The cross-section of wind tunnel was rectangular with height of 26.4 mm ($2D_E$) and width of 300 mm. The length of calming section of wind tunnel was 200 cm which is sufficient to achieve fully developed flow before entering to the test section.

A Pitot-static tube was located upstream of the test section to measure a cross-flow velocity at the center of cross section of wind tunnel. For all experiments, the inlet temperatures of impinging jets and cross-flow were kept constant at 27.6 °C by a temperature and power controller.

3.2 Heat transfer measurement

The test section for heat transfer measurement was directly mounted to the wind tunnel as shown in Fig.3. The air jets with constant temperature discharging from the orifice plate were impinging on the heated surface for cooling. The wall temperature (T_w) on the impingement surface was measured by using TLC sheet (Omega, LCS-95, USA) that attached on the rear of this surface as shown particularly in Fig.3. The heat transfer surface was made of stainless steel foil which having thickness of 30 μ m was installed between a pair of copper bus bars. The heat transfer surface was heated by DC power supply through copper bus bars. An electrical energy dissipated in the stainless steel foil can be determined from

$$\dot{q}_{input} = \frac{I^2 \cdot R}{A} \quad (1)$$

where I is the electrical current, R and A are the electrical resistance and the area of the stainless steel foil.

The local heat transfer coefficient by forced convection of the impinging jets, h , can be evaluated from

$$h = \frac{\dot{q}_{input} - \dot{q}_r - \dot{q}_c}{T_w - T_j} \quad (2)$$

where $\dot{q}_r = \epsilon_{TLC}(\bar{T}_w^4 - T_s^4)$ and $\dot{q}_c = h_c(\bar{T}_w - T_s)$ are the heat losses to the environment by radiation and natural convection from rear side of TLC sheet, respectively; T_w and T_j are the wall and jet temperatures; σ is the Stefan-Boltzman constant; ϵ_{TLC} is the emissive coefficient of the TLC sheet; T_s is the surrounding temperature; and h_c is the natural heat transfer coefficient calculated from natural convective heat transfer from the heat transfer surface to the surrounding.

The digital camera was used to capture color patterns on TLC sheet. The images of color pattern were subsequently converted from the RGB (red, green and blue) color system to the HSI (Hue, Saturation and Intensity) color system. The Hue (H) value was used to correlate the color of TLCs to their temperature in range of 28-40°C via a calibration. The local Nusselt number was calculated

$$Nu = \frac{hD_E}{k} \quad (3)$$

here, D_E is the equivalent diameter of the orifice and k is a thermal conductivity of an air jet [7 and 10].

3.3 Flow visualizations on the impinged surface

The flow patterns on the impinged surface was visualized by using oil film technique. The oil was mixed with liquid paraffin, titanium dioxide and oleic acid. The transparent plastic plate, uniformly coated with the oil film, was employed to represent the impinged surface. During the experiment, the flow pattern of oil film on the impinged surface was recorded using video camera [7 and 10].

3.4 Numerical simulation

A 3-D numerical simulation with the ANSYS Fluent 13.0 was employed to visualize the flow characteristics of the jets and the cross-flow. The calculation based on finite volume method was adopted to solve governing differential equations with boundary conditions. A numerical model was identically created to the experimental model. SST turbulence model was applied due to high accurate prediction in impingement problems and moderate computational cost [11]. This turbulence model has also been employed to accurately predict a flow and heat transfer

characteristics of impinging jet under the cross-flow [9 and 12].

Majority of generated grid was even rectangular. The elements were concentrated near the wall of wind tunnel and mixing region. The boundary conditions were identically specified to experimental conditions. The outlet pressure was kept constant at 1 atm. A solution method was based on SIMPLE algorithm with second order upwind for all spatial discretization. The solution was considered to be converged when the normalized residual of the algebraic equation was less than a prescribed value of $1.0E-4$ [7].

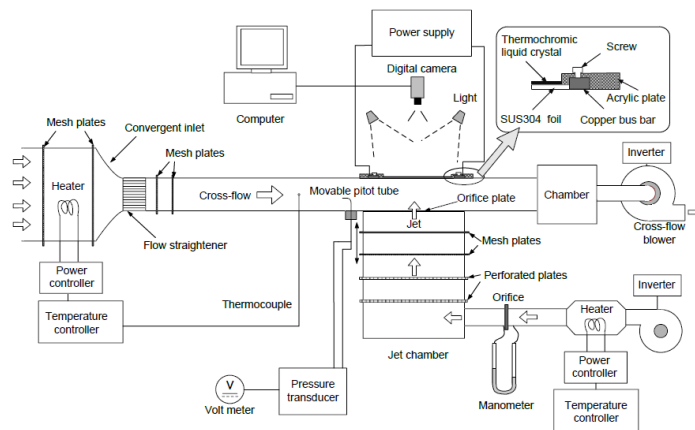


Fig. 3 Schematic diagram of the experimental setup

4. RESULTS AND DISCUSSIONS

4.1 Flow characteristics of jets and cross-flow

Velocity vectors and velocity contours in X-Y plane at $Z/D=1.5$ (jet centerline) are shown in Fig.4. In the case of low cross-flow velocity, $VR=7$, as shown in Fig.4 (left side), the impinging jet is slightly deflected to downstream direction (X-axis). The deflection of jet from the elongated orifice seem to be larger when the attacking angle becomes larger, $\theta=45^\circ$, as shown in Fig.4(g). In the case of high cross-flow velocity, $VR=3$, as shown in Fig.4 (right side), the deflection of jet is larger than those low cross-flow velocity, $VR=7$, due to higher cross-flow velocity. The deflection of jet is prominently large for the case of $AR=4$ at $\theta=45^\circ$ with $VR=3$ as shown in Fig.4(h). The greatest deflection of jet for this case is from two factors; strong momentum of cross-flow striking on the jet flow due to the high cross-flow velocity; and larger interaction area between the cross-flow and the jet flow due to the increasing of attacking angle.

When compare the flow characteristics in the case of $AR=4$ at $\theta=0^\circ$ with $VR=3$ (Fig.4(d)) to the case of $AR=1$ under the same VR (Fig.4(b)), it is found that the deflection of jet from elongated orifice is smaller than that conventional orifice. This can be explained that the jet discharge from elongated orifice with $\theta=0^\circ$ can more penetrate into the cross-flow than those the conventional orifices. This flow characteristic shows that the jet from

elongated orifice can decrease the effect of cross-flow when compare with the case of jet from conventional orifice.

A comparison of flow characteristics in Y-Z plane at $X/D=0.25$ are shown Fig.5. The jets of $AR=4$ with $\theta=15^\circ$ and 45° (Fig.5(e)-(h)) deflect to +Z-axis due to attacking angle effect. These deflections of jets for the case of $VR=3$ (Fig.5(f) and (h)) are larger than those $VR=7$ (Fig.5(e) and (g)) due to higher cross-flow velocity. The jets are more deflect to +X-axis when cross-flow velocity becomes higher as mentioned in previous. In the same way, the deflections of jets are more tend to +Z-axis when the attacking angle becomes larger. In additions, association of deflection of jets to +X-axis (downstream direction) and +Z-axis produces one circulation flow for one impinging jet. It is different for the case of $AR=1$ and $AR=4$ with $\theta=0^\circ$ that the circulation flow of one impinging jet is separated into two parts as shown in Fig.5(a)-(d).

The circulation flows along downstream direction for $AR=4$, $\theta=15^\circ$ with $VR=3$ at each cutting plane are shown in Fig.6. The circulation flows growth up and its center (pivot points) are more shift to +Z-axis for further downstream direction (+X-axis). This characteristic of circulation flow affects directly on heat transfer characteristics on the impingement surface that will be discussed in the next section.

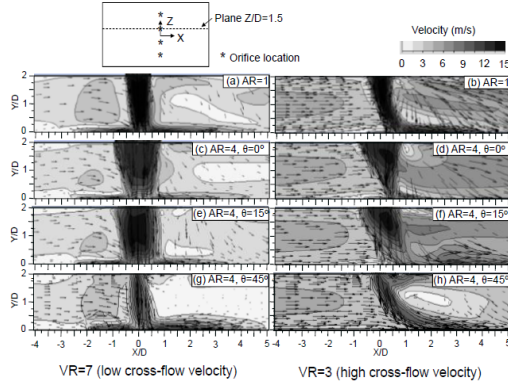


Fig. 4 Vectors and contours of velocity in X-Y plane at $Z/D=1.5$ (CFD results)

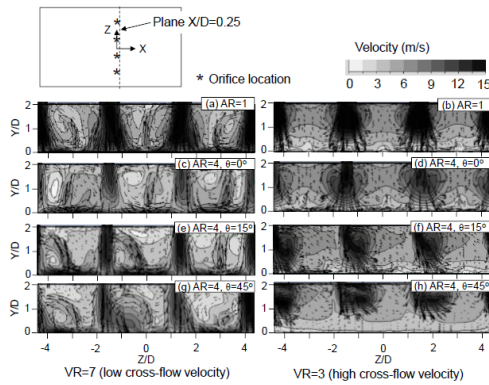


Fig. 5 Vectors and contours of velocity in Y-Z plane at $X/D=0.25$ (CFD results)

4.2 Flow characteristics above the impingement surface

Flow patterns of impinging jets on the impingement surface using the oil film technique are shown in Fig.7. The black and white regions represent the areas where the oil film is completely removed called impingement region and the area with original oil film coating, respectively. The impingement regions of $AR=1$ are more shifted to downstream directions when cross-flow velocity increases. This flow patterns correspond to those flow characteristics of downstream impinging jets in impingement array that have been discussed in Wae-hayee et al. [10]. For the case of $AR=4$ at $\theta=0^\circ$ with $VR=3$ as shown in Fig.7(d), the shifting of impingement regions to downstream direction are minimized when compare with the case of $AR=1$ under the same VR (Fig.7(b)). This is due to the jets from elongated orifices can more penetrate into the cross-flow as discussed previously in CFD results. This flow characteristics also correspond to those impingement array that employ

elongated orifices in Nuntadusit et al [7]. In addition, the impingement regions are obliquely shifted to $+Z$ -axis provided by the larger attacking angle. This is due to inclination interaction between the cross-flow and the jet flow corresponding to direction of orifice arrangement as shown previously in Fig.5.

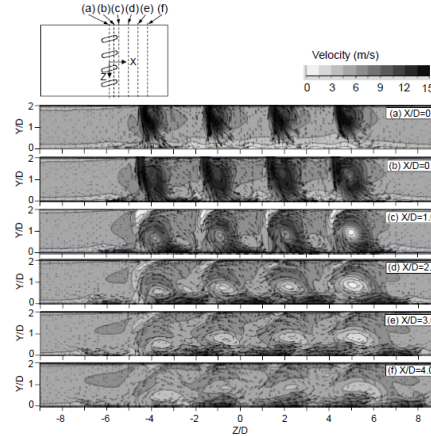


Fig. 6 Vectors and contours of velocity in Y-Z plane at $AR=4$, $\theta=15^\circ$ at $VR=3$ (CFD results)

The velocity vector and contour in the Y-axis on Z-X plane near the impingement surface (1 mm above the surface) from CFD results are shown in Fig.8. This position above from surface is chosen to represent the plane sufficiently near the surface due to the condition at the surface is no-slip. The Y-component velocity represents the velocity in the direction normal to the impingement surface. The positive direction is towards the direction of the jet that impinges on the target surface. Area of high Y-component velocity contour indicates the impingement region corresponding to removed oil film region as shown earlier in Fig. 7, and this CFD results agree very well with the flow patterns of oil film technique. With the good agreement, clarification of heat transfer behavior in the next section can refer to the flow characteristics from this CFD results.

4.3 Local Nusselt number on the impinged surface

Nusselt number distributions on impingement surface from experiments are shown in Fig.9. These contours of Nusselt number correspond to the oil film patterns on the impingement surface as shown in Fig.7 as well as the contours of Y-component velocity near the impingement surface as shown in Fig.8. Generally, the Nusselt number is high in impingement regions and low in upstream regions. These areas of high Nusselt number are more contracted along upstream direction ($-X$ -axis) and more extended along downstream one (X -axis) when the cross-flow velocity increases. The areas of high Nusselt number, in addition, are more obliquely extended along $+Z$ -axis when the attacking

angle becomes larger. For the case of $AR=4$, $\theta=15^\circ$ with $VR=3$ as shown in Fig.9(f), the area of high Nusselt number is extended along +Z-axis corresponding to the shifting of circulation flow as earlier shown in Fig.6.

The extension area of high Nusselt number along upstream direction of $AR=4$ at $\theta=0^\circ$ (Fig.9(c) and (d)) are larger than those $AR=1$ (Fig.9(a) and (b)) under the same VR . These results show that the jet discharging from elongated orifice with $\theta=0^\circ$ can minimize the cross-flow effect. This corresponds to the higher heat transfer of impingement array using elongated orifices that has been reported by Nuntadusit et al. [7]. However, for the case of $\theta=15^\circ$ and 45° , these area of high Nusselt number along upstream direction are contracted, especially, for the case of large attacking angle and high cross-flow velocity as shown in Fig.9(h).

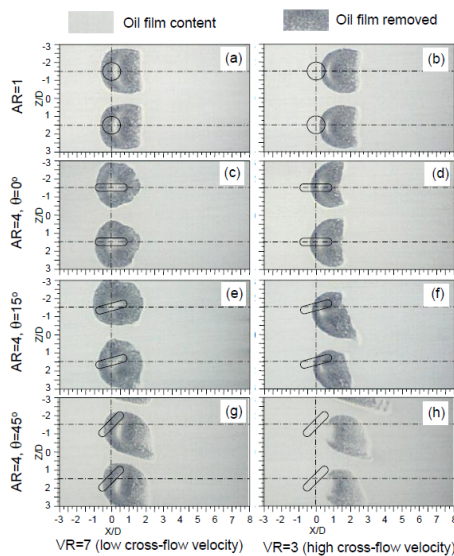


Fig. 7 Flow patterns on the impinging surface (experimental results)

Nusselt number distributions along downstream direction at orifice centerline ($Z/D=1.5$) are shown in Fig.10. The results show that the Nusselt number distribution of $AR=4$ at $\theta=0^\circ$ along upstream direction (+X-axis) is higher than those $AR=1$ throughout VR . The Nusselt number distribution of $AR=4$ along upstream direction, however, is lower when the attacking angle becomes larger.

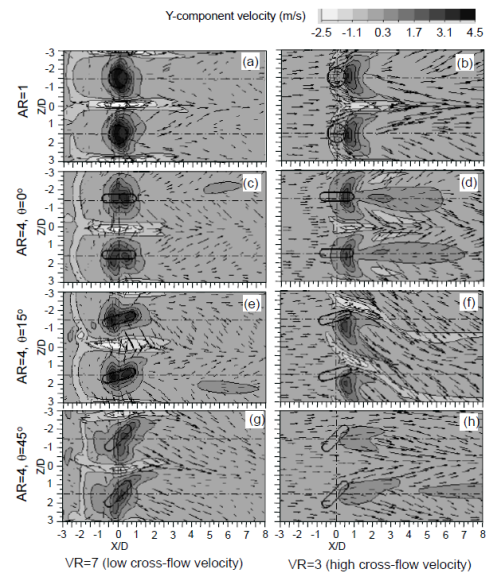


Fig. 8 Velocity vectors and Y-component velocity contours on Z-X plane (CFD results, The plane above from target surface of 1 mm)

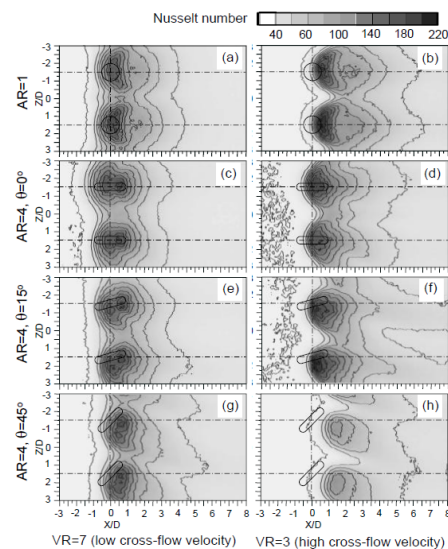


Fig. 9 Nusselt number distributions on the impinging surface (experimental results, $T_f=27^\circ\text{C}$)

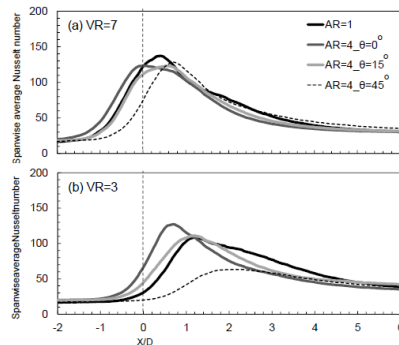


Fig. 10 Spanwise average Nusselt number distributions along downstream direction (experimental results)

Spanwise average Nusselt number that calculate from the average temperature in the rage of $-3 < Z/D < 3$ is shown in Fig.10. For $VR=7$ (Fig.10(a)), distributions of these average value for the case of $AR=4$, $\theta=0^\circ$ at upstream region ($X/D < 0$) is higher than of the others. When the attacking angle becomes $\theta=45^\circ$ at the same conditions, the distributions of average values become the lowest. Peak of spanwise average Nusselt number for the case of $AR=1$ is the highest, and all of distributions of this values at downstream direction ($X/D > 1$) are comparable. Due to the low cross-flow velocity effect, the distributions of these average values are slightly different. It is except for the case of $AR=4$, $\theta=45^\circ$ that the distributions of these values at upstream region ($X/D < 0$) is very low and different from the others due to very large attacking area between the jets and the cross-flow.

For the case of $VR=3$ as shown in Fig. (Fig.10(b)), the distributions of these values at upstream direction are quite different by getting the highest for the case of $AR=4$, $\theta=0^\circ$. However, in the downstream direction at $2 < X/D < 4$, the distributions of these values of $AR=1$ seem to be higher than the others.

5. CONCLUSIONS

The effect of cross-flow velocity on flow and heat transfer characteristics of jet impingement row discharging through elongated orifice with different attacking angle was experimentally and numerically studied. The main results can be summarized as follows;

1. Impinging jets discharging from the elongated orifices with $\theta=0^\circ$ can minimize the cross-flow effect. The deflections of jets toward cross-flow direction for elongated orifices with $\theta=0^\circ$ are smaller when compare with the case of conventional orifices under the same cross-flow velocity. This affects directly to the local heat transfer distributions on impingement surface that the impinging jets from elongated orifice with $\theta=0^\circ$ can extend the area of high heat transfer at impingement region, especially at upstream region.

2. The impingement regions (or areas of high Nusselt number) are extended in the X-axis and obliquely extended in the +Z-axis when the attacking angle becomes larger. The extension of impingement regions in the X-axis is from the

effect of cross-flow, and the oblique extension of these regions in the +Z-axis is from the effect of attacking angle.

ACKNOWLEDGMENTS

This research was supported by grants from Thailand Energy Policy and Planning Office, Ministry of Energy, the Graduate School and Faculty of Engineering, Prince of Songkla University.

REFERENCES

- [1] Viskanta, R., Heat Transfer to Impinging Isothermal Gas and Flame Jets, *Exp. Therm. Fluid Sci.*, Vol. 6, pp. 111-134 (1993).
- [2] Brizzi, L.-E., Bernard, A., Bousgarbies, J.-L., Dorignac, E., and Vullierme, J.-J., Study of Several Impinging Jets, *J. Thermal Science*, Vol. 9, pp. 217-223 (2000).
- [3] Katti, V., and Prabhu, S.V., Influence of Spanwise Pitch Local Heat Transfer Distribution for In-line Arrays of Circular Jets with Air Flow in Two Opposite, *Exp. Therm. Fluid Sci.*, Vol.14, pp. 84-95 (2008).
- [4] Rhee, D.-H., Yoon, P.-H., and Cho, H.H., Local Heat/Mass Transfer and Flow Characteristics of Array Impinging Jets with Effusion Holes Ejecting Spent Air, *Int. J. Heat Mass Transfer*, Vol.46, pp. 1049-1061 (2003).
- [5] Hoberg, T.B., Onstad, A.J., and Eaton, J.K., Heat Transfer Measurements for Jet Impingement Arrays with Local Extraction, *Int. J. Heat Fluid Flow*, Vol.31, pp. 406-467 (2010).
- [6] Chiu, H.-C., Jang, J.-H., and Yan, W.-M., Experimental Study on the Heat Transfer Under Impinging Elliptic Jet Array Along a Film Hole Surface Using Liquid Crystal Thermograph, *Int. J. Heat Mass Transfer*, Vol.52, pp. 4435-4448 (2009).
- [7] Nuntadusit, C., Wae-hayee, M., Tekasakul, P., and Eiamsa-ard, S., Local Heat Transfer Characteristics of Array Impinging Jets from Elongated Orifices, *Int. Commun. Heat Mass Transfer*, Vol.39, pp. 1154-1164 (2012).
- [8] Goldstein, R. J., and Behbahan, I., Impingement of a Circular Jet with and without Cross Flow, *Int. J. Heat Mass Transfer*, Vol.25, pp. 1377-1382 (1982).
- [9] Heo, M.-W., Lee, K.-D., and Kim, K.-Y., Optimization of an Inclined Elliptic Impinging Jet with Cross flow for Enhancing Heat Transfer, *Heat Mass Transfer*, Vol.47, pp. 731-742 (2011).
- [10] Wae-hayee, M., Tekasakul, P., and Nuntadusit, C., Influence of Nozzle Arrangement on Flow and Heat Transfer Characteristics of Arrays of Circular Impinging Jets, *Songklanakarin J. Sci. Technol.*, Vol. 35, pp. 203-212 (2013).
- [11] Zuckerman, N., and Lion, N., Jet Impingement Heat Transfer: Physics, Correlations, Numerical Modeling, *Advances Heat Transfer*, Vol.39, pp. 565-631 (2006).
- [12] Chandratilleke, T.T., Jagannatha, D., and Narayanaswamy, R., Heat Transfer Enhancement in Microchannels with Cross-flow Synthetic Jets, *Int. J. Therm. Scie.*, Vol.49, pp. 504-513 (2010).

Appendix B2

Journal Paper

M. Wae-hayee, P. Tekasakul, S. Eiamsa-ard and C. Nuntadusit, “Flow and Heat Transfer Characteristics of In-line Impinging Jets with Cross-flow at Short Jet-to-plate Distance”, **This manuscript have been submitted in Journal of Mechanical Science and Technology.**

Experimental Heat Transfer



FLOW AND HEAT TRANSFER CHARACTERISTICS OF IN-LINE IMPINGING JETS WITH CROSS-FLOW AT SHORT JET-TO-PLATE DISTANCE

Journal:	<i>Experimental Heat Transfer</i>
Manuscript ID:	Draft
Manuscript Type:	Original Articles
Date Submitted by the Author:	n/a
Complete List of Authors:	Wae-hayeea, M.; Prince of Songkla University, Tekasakula, P.; Prince of Songkla University, Eiamsa-ard, Smith; Mahanakorn University of Technology, Department of Mechanical Engineering Nuntadusit, C.; Prince of Songkla University,
Keywords:	heat transfer, heat exchangers, convection

SCHOLARONE™
Manuscripts

Only

Flow and Heat Transfer Characteristics of In-line Impinging Jets with Cross-flow at Short Jet-to-plate Distance

M. Wae-hayee¹, P. Tekasakul¹, S. Eiamsa-ard² and C. Nuntadusit^{1}*

¹Department of Mechanical Engineering, Faculty of Engineering
Prince of Songkla University, Hat Yai, Songkhla 90112, Thailand

²Department of Mechanical Engineering, Faculty of Engineering
Mahanakorn University of Technology, Bangkok 10530, Thailand

*Corresponding author, E-mail: chayut@me.psu.ac.th, chayut.n@gmail.com

ABSTRACT

The aim of this research is to numerically and experimentally study the flow and heat transfer characteristics of in-line impinging jets in cross-flow. The jets from round orifices perpendicularly impinged on inner surface of rectangular wind tunnel at a short distance between orifice plate and impinged surface (H) of $2D$, where D is a diameter of the orifice. The experiments were performed at three different velocity ratios (VR , jet velocity/cross-flow velocity) of 3, 5 and 7. The heat transfer characteristic was visualized using thermochromic liquid crystal sheet (TLCs) and the Nusselt number distribution was evaluated by an image processing technique. The flow pattern on the impinged surface was also visualized by oil film technique. The numerical simulation was used to explore a flow interaction between impinging jets and cross-flow. The results showed that Nusselt number peak increased by the increasing cross-flow velocity. For the range determined, the maximum Nusselt number peak was obtained at $VR=3$ as a consequence of the good matching between high Y-component velocity and high turbulence kinetic energy distributions.

Keywords: Impinging jets, Cross-flow, Heat transfer, TLC, CFD

1. INTRODUCTION

Impinging jets are applied in many thermal engineering applications where high heat and mass transfer rates are required. Applications include cooling of gas turbine blade, electronic device or wall of combustion chamber, drying of textile or paper and tempering of steel or glass sheets. To suffice high heat transfer rate in those areas, multiple impinging jets are usually applied. For multiple jets in a confined space, the jet impingement involves a cross-flow defined as a fluid flow in the perpendicular direction

to the jet impingement flow [1]. A cross-flow occurs from spent fluid from upstream jets in an array.

The effects of cross-flow on flow and heat transfer characteristics of multiple impinging jets were extensively investigated. Katti and Prabhu [1] experimentally investigated the influence of jet-to-jet distance and jet-to-plate distance on heat transfer characteristics of impingement jets array with in-line arrangement in confined duct. Their results suggested that a cross-flow significantly affected the heat transfer of the downstream

impingement jets. Florschuetz et al. [2] developed the Nusselt number correlation for both inline and staggered arrangement in case of jet-to-jet distance $S > 4D$ (D is nozzle diameter). Brizzi et al. [3] showed the flow and temperature patterns on the impinged surface of array of jets with an inline arrangement. Their finding indicated that flow patterns corresponded to the temperature distributions.

In general, identifying the interaction between multiple impinging jets and an inherent cross-flow is a difficult task, therefore only few works were reported [3, 4]. To clarify the interaction, the investigations are usually performed by applying simulated cross-flow by introducing fluid flow through a single impinging jet. Barata and Durao studied impinging flow through a cross-flow using Laser-Droplet measurement [5]. Goldstein and Behbahani [6] and Bouchez and Goldstein [7] examined impinging jet in simulated cross-flow at high jet-to-plate distances ($\geq 4D$). They found that heat transfer by impinging jet at stagnation region decreased with increasing cross-flow velocity. Heo et al. [8] and Shi et al. [9] used CFD to predict a flow and heat transfer of inclined impinging jet in cross-flow. According to the previous works [6-7], the behaviors of impinging jets in cross-flow were studied at long jet-to-plate distances ($\geq 4D$). Theoretically, a maximum heat transfer on a target surface of multiple impinging jets takes place at short jet-to-plate distances ($\leq 2D$) [1, 10, 11]. Therefore, the effect of cross-flow on multiple jet impingements at short jet-to-plate distances should be concerned.

The aim of this research is to experimentally and numerically study the effect of velocity ratio (VR) on flow and heat transfer of in-line impinging jets at a short jet-to-plate distance

(H) of $2D$. The studied parameters include three different cross-flow velocities and one impinging jet velocity. Temperature distributions on the impinged surface were investigated by using thermochromic liquid crystal sheet (TLCs), and the Nusselt number distribution was evaluated by using image processing method. The flow characteristic the impinged surface was visualized by using oil film technique. The numerical simulation was used to examine the fluid flow.

2. EXPERIMENTAL MODEL AND PARAMETERS

The experimental model is shown in Fig. 1. The impinging jets from round orifices impinged on the impinged surface in a rectangular wind tunnel. A cross-flow was simulated by introducing air through the test section, perpendicular to the impinging jets. The jet-to-plate and jet-to-jet distances were fixed at $H=2D$ and $S=3D$, respectively, where D is orifice diameter (13.2 mm). An origin of the Cartesian coordinates was located on the impinged surface. The X-, Y- and Z-axes are cross-flow streamwise, vertical, and spanwise coordinates, respectively. The impinging jet velocity was fixed corresponding to $Re=13,400$ and cross-flow velocity was varied corresponding to velocity ratios (jet to cross-flow velocities) $VR=3, 5$ and 7 .

3. EXPERIMENTAL MODEL AND PARAMETERS

3.1 Experimental apparatus

A schematic diagram of the experimental apparatus is shown in Fig.2. To stimulate cross-flow, air was introduced through the inlet chamber, flow straightener, two layers of mesh plates, the test section and a chamber outlet by using a 3-HP blower. The cross section of wind tunnel was with height

of 26.4 mm ($2D$) and width of 300 mm. The length of calming section of wind tunnel was 1500 mm, which is sufficient to achieve fully developed flow in the test section. To generate impinging jets, another 3-HP blower was used to introduce air through a temperature controlled chamber equipped with 2-kW heater, an calibrated orifice flow meter, a jet chamber (constant cross-section of 360-mm \times 360-mm and a height of 850-mm), and a jet orifice before entering the test section. The jet chamber is equipped with

two layers of perforated plates and two layers of mesh plates to achieve a uniform flow field approaching the orifice plate. The test section was directly mounted to the jet chamber. A Pitot-static tube was located upstream of the test section to measure a cross-flow velocity. For all experiments, the inlet temperatures of impinging jets and cross-flow were kept constant at 27.6 °C by a temperature and power controller. The temperature variation of the jet and cross-flow was controlled within $\pm 0.2^\circ\text{C}$.

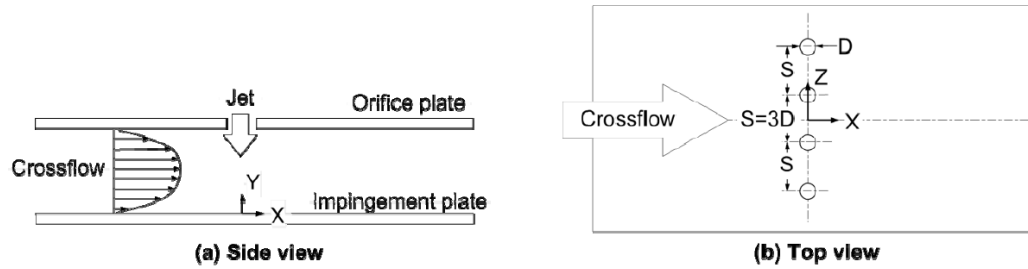


Fig. 1. The experimental model.

3.2 Heat transfer measurement

The test section for heat transfer measurement is shown in Fig. 2. The heat transfer surface made of a stainless steel foil with thickness of 30-Nm. The foil rear was attached to the TLC sheet (Omega, LCS-95). The stainless steel foil was stretched between couple of copper bus bars. The heat transfer surface was heated by a DC power source that can supply current up to 50 A through the copper bus bars. During jet impingement, the local heat transfer coefficient by forced convection from the impinged surface can be evaluated from

$$\dot{Q}_{input} = I^2 \cdot R \quad (1)$$

$$h = \frac{\dot{Q}_{input} - \dot{Q}_{losses}}{A(T_w - T_j)} = \frac{\dot{q}_{input} - \dot{q}_r - \dot{q}_c}{T_w - T_j} \quad (2)$$

where, I and R are the electrical current and the thermal resistance of the stainless steel foil, \dot{q}_r and \dot{q}_c are the heat loss to the environment by radiation and convection, T_w and T_j are the wall and jet temperatures,

respectively. The wall temperature (T_w) of the impinged surface was measured by using the TLC sheet attached to the rear of the impinged surface. The TLC sheet was calibrated using the digital image processing system under the same condition for all experiments to keep all external factors constant. The local Nusselt number can be calculated from

$$Nu = \frac{hD}{k} \quad (3)$$

where k is a jet thermal conductivity. The details of heat transfer measurement were described in the previous works [12, 13].

3.3 Flow visualization on the impinged surface

The flow pattern on the impinged surface was visualized by using oil film technique. The oil film was prepared by mixing liquid paraffin with titanium dioxide and oleic acid. The transparent plastic plate uniformly

Painted with oil film was employed to represent the impinging surface. During the experiment, the oil film behavior on the impinging surface was recorded using a CCD camera every 30 seconds [13].

4. NUMERICAL SIMULATION

The ANSYS Fluent 12.0 was used to visualize the flow characteristics. A 3-D numerical model based on finite volume method was adopted to solve governing differential equations with boundary conditions. A dimension of numerical model was same as that of experimental model. A shear stress transport (SST) turbulence model based on combination between a $k-\omega$ model at the wall and $k-\epsilon$ model in the main flow was applied due to high accurate prediction in impingement problems and

moderate computational cost [14]. This turbulent model has also been employed to accurately predict a flow and heat transfer characteristics of impinging jet under cross-flow [8, 15]. The computation domain was resolved by rectangular elements as shown in Fig.3. The majority of elements were even rectangular. The elements were concentrated near the wall of wind tunnel and mixing region. The boundary conditions were identically specified to experimental conditions. The outlet pressure was kept constant at 1 atm. A solution method was based on SIMPLE algorithm with second order upwind for all spatial discretization. The solution was considered to be converged when the normalized residual of the algebraic equation was less than a prescribed value of $1.0E-5$ [8].

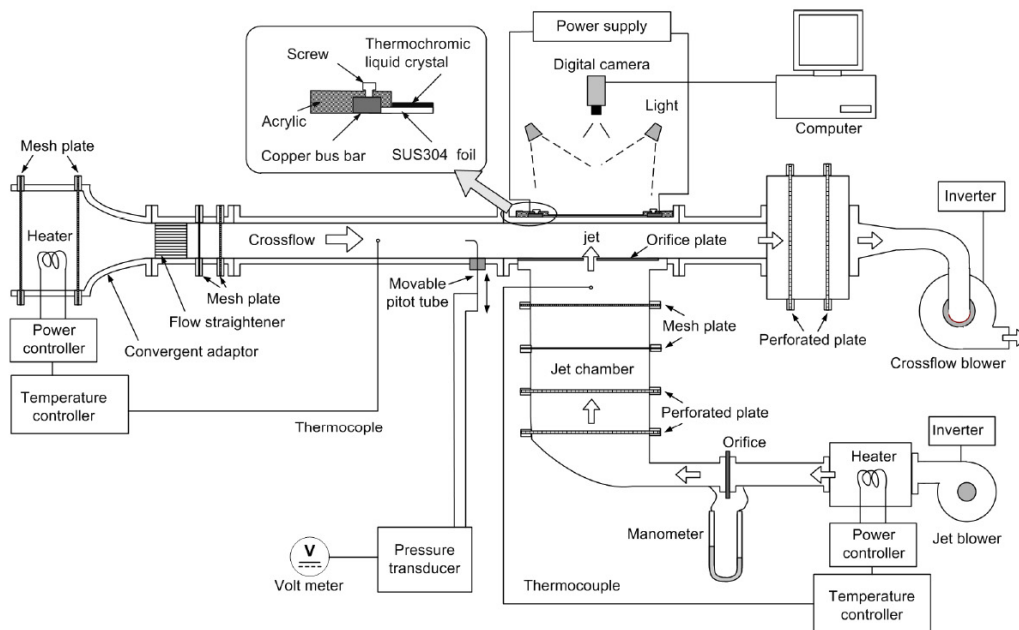


Fig. 2. Schematic diagram of the experimental setup.

5. RESULTS AND DISCUSSION

5.1 Experimental setup verification

Velocity vectors and velocity contours of jets and cross-flow in X-Y plane at $Z/D=1.5$ and 0 are shown in Fig.4 and 5. As shown in Fig.4(a), at low cross-flow velocity ($VR=7$) the upstream wall jet was slightly swept by

cross-flow and a circulation flow was generated upstream of the jet. A size of the circulation flow became smaller when the cross-flow velocity increased ($VR=5$) as shown in Fig.4(b). At high cross-flow velocity ($VR=3$) the upstream wall jet was completely swept and an upstream circulation flow was not found (Fig.4(c))

At $Z/D=0$, for low cross-flow velocity ($VR=5$ and 7), it was found that velocity vectors were mainly directed upward after the collision of two adjacent spanwise wall jets, and commencement position of the upward flow was shifted downstream (from $X/D=-3$ to -1) as cross-flow velocity increased, as shown in Fig.5 (a-b). However, at the highest cross-flow velocity ($VR=3$) the influence of cross-flow almost completely concealed the effect of jet impingement as velocity vectors tended to follow streamwise direction (Fig.5(c)). The contours of turbulence kinetic energy in X-Y plane at $Z/D=1.5$ and 0 are shown in Figs.6 and 7. At $Z/D=1.5$, turbulence kinetic energy was high at a wall jet region and low along a jet core. At $VR=5$ and 7 (Fig. 6(a) and (b)), the upstream and downstream turbulence kinetic energies were comparable. However, $VR=3$ (Fig. 6(c)) high turbulence kinetic energy was detected only around downstream wall jet region due to the jet sweeping by the strong cross-flow.

The turbulence kinetic energy contour at $Z/D=0$ (Fig.7) was found to be corresponded

to the velocity contour and velocity vector (Fig.5), as the upstream turbulence kinetic energy significantly decreased with increasing cross-flow velocity, especially for $VR=3$ as shown in Fig.7(c). The velocity vectors and velocity contours on X-Z plane are presented in Fig.8. The Y-component velocity represents the velocity in direction normal to the impinged surface (or vertical direction). The positive Y-component velocity was found around downstream of jet was (jets impinging on the wall) and high Y-component velocity was appeared around impingement region. Jet impingement was shifted downstream direction as cross-flow velocity increased or VR decreased. The shift was significant when VR decreased from 5 to 3. This agrees well with the vectors and contours of velocities shown in Fig.4. The areas of negative Y-component velocity were detected in the middle between impingement regions (white area). This is due to the collision between spanwise wall jet, resulting in upward flow. The white area became smaller as cross-flow velocity increased, because the collision between spanwise wall jets became weaker as suggested in Fig.5.

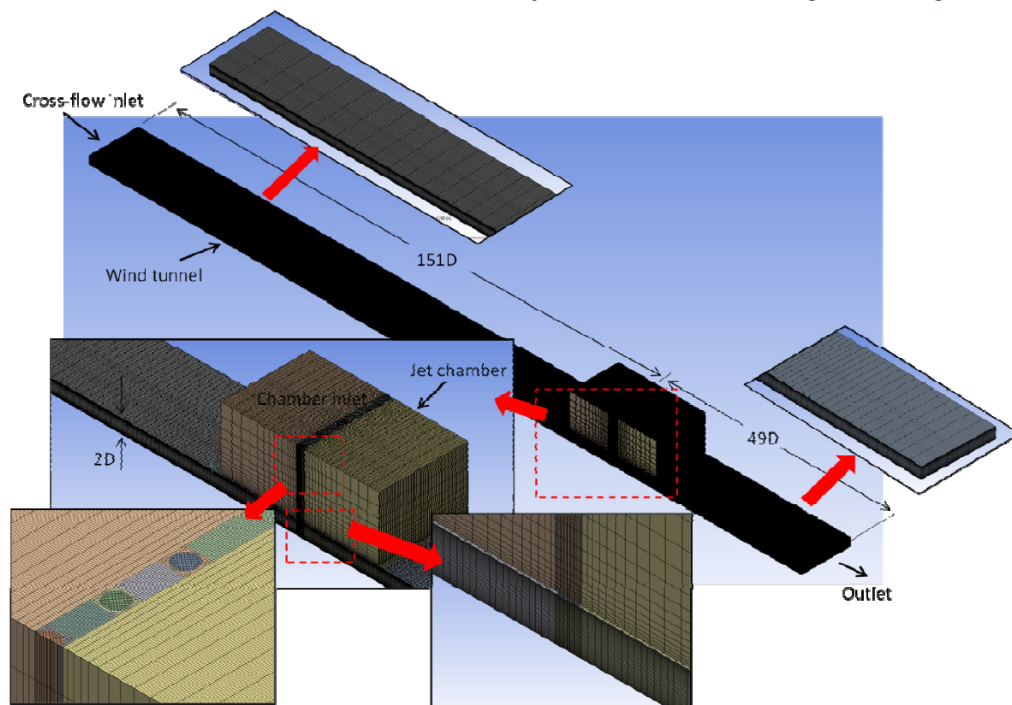


Fig. 3. Numerical model and generated grid.

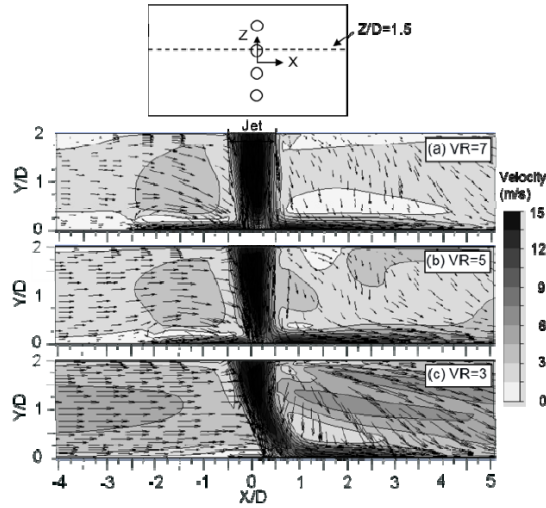


Fig.4. Vectors and contours of velocity in X-Y plane at $Z/D=1.5$.

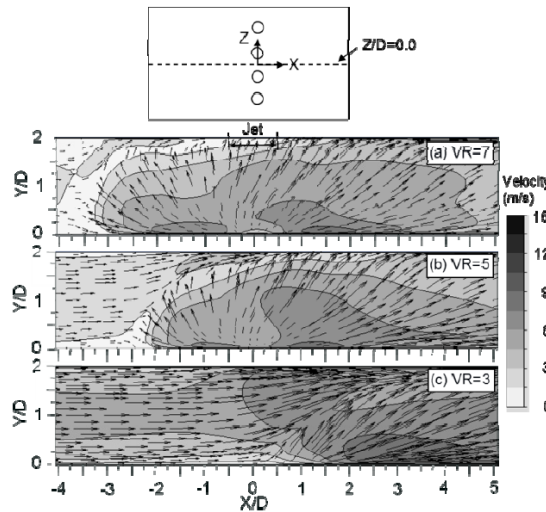


Fig.5. Vectors and contours of velocity in X-Y plane at $Z/D=0$.

5.2 Flow patterns on the impinged surface

The flow visualizations on the impinged surface by oil film technique are shown in Fig.9(a-c). The black area is an impinged surface where an oil film is removed while the white area corresponds to remaining oil film. The circles marked on the impinged plate are the positions of the orifices. As cross-flow velocity increased (VR decreased), the commencement of jet impingement was shifted downstream, resulting in the contraction of the upstream impingement region ($X/D < 0$) and expansion of the downstream impingement region ($X/D > 0$). The effects of cross flow were very

obvious when VR decreased from 5 to 3, as comparison shown in Fig.9(b and c). This flow characteristic coincides with the Y -component velocity shown in Fig.8(c). This behavior agrees well with that of the multiple impingement jets in the previous work [3].

In addition, oil film was apparently removed in the middle between the adjacent impingement regions because the interaction between spanwise wall jets. This effect was least significant at $VR=3$ because cross-flow with high velocity swept spanwise wall jets downstream as shown in Fig.5(c)

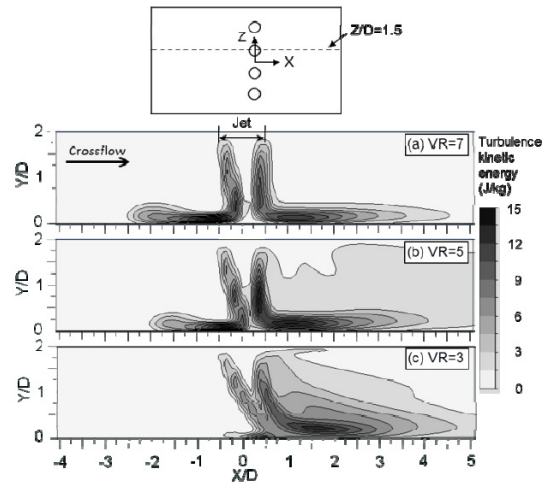


Fig. 6. Contours of turbulence kinetic energy in X-Y plane at $Z/D=1.5$.

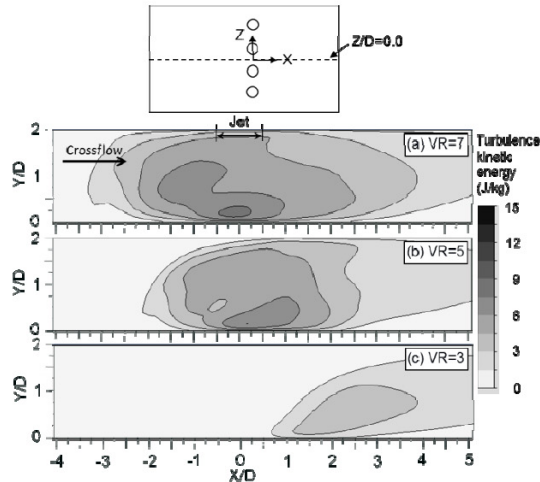


Fig. 7. Contours of turbulence kinetic energy in X-Y plane at $Z/D=0$.

5.3 Local Nusselt number on the impinged surface

The Nusselt number distributions on impinged surface are shown in Fig.10. Their characteristics coincide with Y-component velocity contours and flow patterns on the impinged surface shown in Figs. 8 and 9. As cross-flow velocity increased (VR decreased), the area with high Nusselt number shifted downstream. It should be mentioned that Nusselt number was also high in the middle between the adjacent impingement regions (at $Z/D=0$, $0.5 < X/D < 1.5$ in Figs.10 and 11). This location corresponds to the area in which Y-component velocity was negative in Fig.8, where oil film was removed in Fig.9. The

enhancement of Nusselt number in the area attributes to a high turbulence intensity near the surface as revealed in Fig.7.

At $Z/D=1.5$, the peaks of Nusselt number, Y-component velocity and turbulent kinetic energy were shifted downstream as cross-flow velocity increased (VR decreased) as shown in Fig.11(a) and 12(a-b). However, peak of Nusselt number at $VR=3$ was found to be highest while those of Y-component velocity and turbulent kinetic energy at $VR=3$ were found to be lowest as compared to those at $VR=5$ and 7.

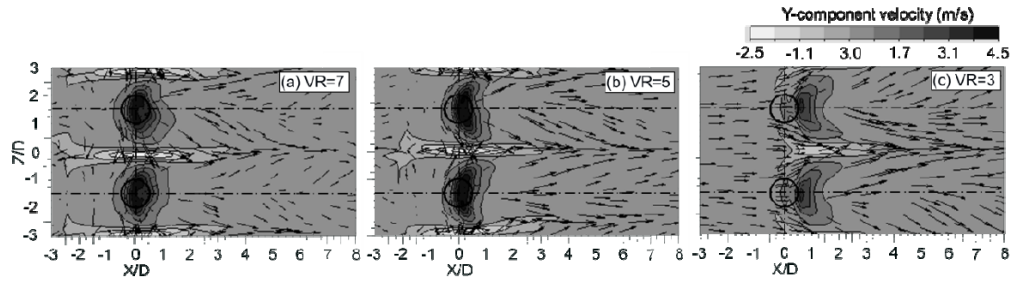


Fig. 8. Velocity vectors and Y-component velocity contours on X-Z plane (above from target surface of 1.5-mm and circular shape is a position of orifice).

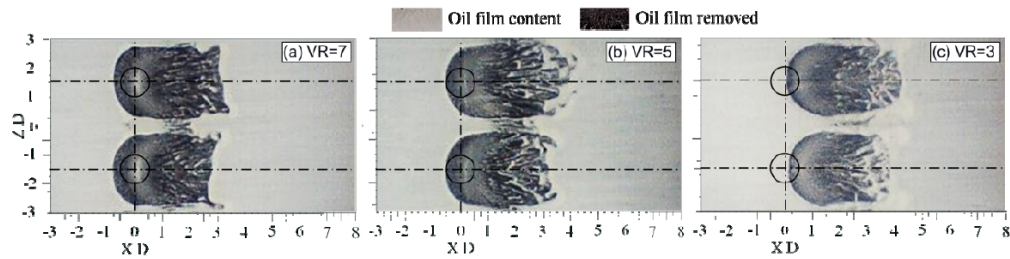


Fig. 9. Flow patterns on the impinging surface ($Re = 13,400$).

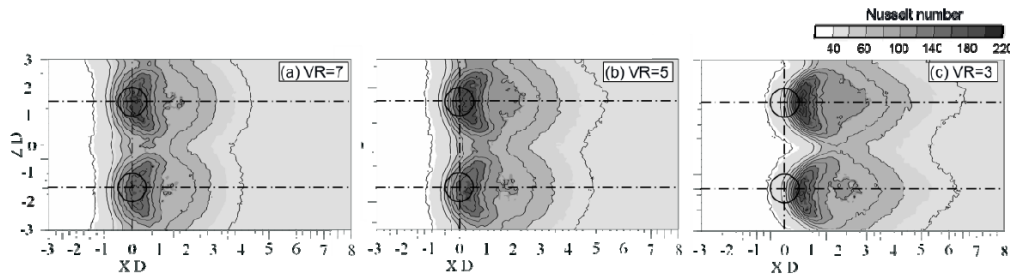


Fig. 10. Nusselt distributions on the impinging surface ($T_j=27^\circ\text{C}$, $Re_j=13,400$).

The apparently high Nusselt number peak at $VR=3$ is achieved because the peaks of Y-component velocity and turbulence kinetic energy take place at the identical streamwise location, indicated as point A and B in Fig.12. The good matching between high Y-component velocity and high turbulence kinetic energy distribution resulted in excellent heat transfer was also mentioned in the previous work [16]. On the other hand, the good matching between Y-component velocity and turbulence kinetic energy was not found at between at $VR=5$ and 7, thus the resultant Nusselt number peaks at these conditions were lower than that at $VR=3$. This behavior agrees with those reported by

Katti and prabhu [1] and Nuntadusit et al. [13] for the heat transfer associated by the multiple jet impingement in confined channel at short jet-to-plate distances ($\leq 2D$).

The important finding in the present work is that at a short jet-to-plate distance ($2D$), Nusselt number peak increased as cross-flow velocity increased or VR decreased. This effect is opposite to that found at long jet-to-plate distances ($\geq 3D$). The difference can be caused by the different sizes of space between jets to impinging surface in which collision between cross-flow and jet impingement takes place [17 and 18].

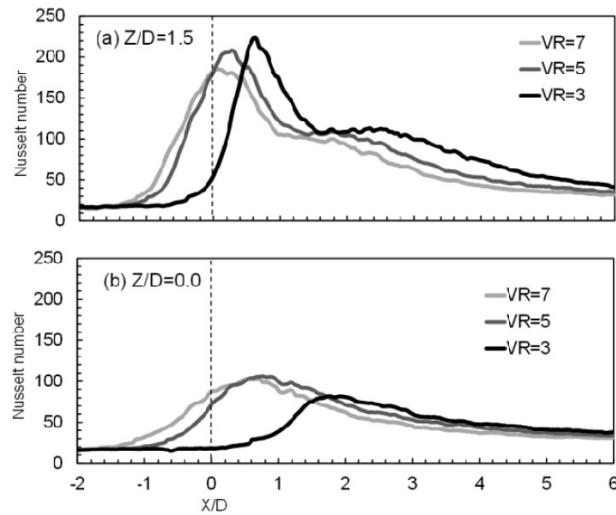


Fig. 13. Nusselt number distribution (a) $Z/D=1.5$ and (b) $Z/D=0$ ($T_j=27^\circ\text{C}$ and $Re_j=13,400$).

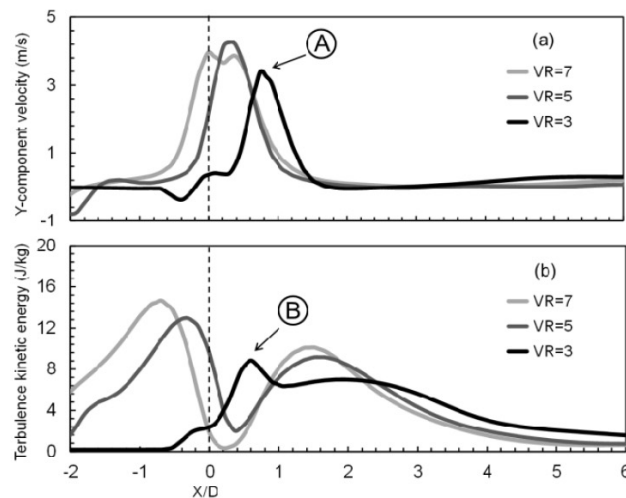


Fig. 14. (a) Y-component velocity contours and (b) turbulence kinetic energy along centerline of orifice (CFD results, above from target surface of 1.5-mm).

6. CONCLUSIONS

In this work, the effect of cross-flow velocity on the flow and heat transfer behaviors associated by in-line impinging jets was studied experimentally and numerically. The main results can be concluded as follows;

1. The jet impingement shifted downstream as cross-flow velocity increased. This behavior coincided with the shifting of high Nusselt number area.
2. The increased cross-flow velocity resulted in the contraction of the upstream impingement region ($X/D < 0$) and

expansion of the downstream impingement region ($X/D > 0$).

3. At a short jet-to-plate distance ($2D$), Nusselt number peak increased as crossflow velocity increased or VR decreased

ACKNOWLEDGEMENTS

This research was supported by grants from Thailand Energy Policy and Planning Office, Ministry of Energy, the Graduate School and

Faculty of Engineering, Prince of Songkla University (PSU).

REFERENCES

- [1] V. Katti and S. V. Prabhu, Influence of Spanwise Pitch Local Heat Transfer Distribution for In-Line Arrays of Circular Jets with Air Flow in Two Opposite, *Experimental Thermal and Fluid Science*, vol. 14, pp. 84-95, 2008.
- [2] L. W. Florschuetz, C. R. Truman and D. E. Metzger, Streamwise Flow and Heat Transfer Distributions for Jet Array Impingement with Crossflow, *Transaction of ASME: Journal of Heat Transfer*, vol. 103, pp. 337-342, 1981.
- [3] L. E. Brizzi, A. Bernard, J. L. Bousgarbies, E. Dorignac, and J. J. Vullierme, Study of Several Impinging Jet, *Journal Thermal Science*, vol. 9, pp. 217-223, 2000.
- [4] C. Carcasci, An Experimental Investigation on Air Impinging Jets Using Visualization Methods, *International Journal of Thermal Sciences*, vol. 38, pp. 808-818, 1999.
- [5] J. M. M. Barata and D. F. G. Durao, Laser-Dropller Measurements of Impinging Jet Flows through a Crossflow, *Experiments in Fluids*, vol. 36, pp. 665-674, 2004.
- [6] R. J. Goldstein and I. Behbahan, Impingement of a Circular Jet with and without Cross Flow, *International Journal of Heat and Mass Transfer*, vol. 25, pp. 1377-1382, 1982.
- [7] J. P. Bouchez and R. J. Goldstein, Impingement Cooling from a Circular Jet in a Cross Flow, *International Journal of Heat and Mass Transfer*, vol. 18, pp. 719- 730, 1975.
- [8] M. W. Heo, K. D. Lee, and K. Y. Kim, Optimization of an Inclined Elliptic Impinging Jet with Cross Flow for Enhancing Heat Transfer, *International Journal of Heat and Mass Transfer*, vol. 47, pp. 731-742, 2011.
- [9] Y., Shi, M. B. Ray, and A. S. Mujumdar, Numerical Study on the Effect of Cross-Flow on Turbulent Flow and Heat Transfer Characteristics under Normal and Oblique Semi-Confined Impinging Slot Jets, *Drying Technology*, vol. 21, pp. 1923-1939, 2003.
- [10] J. Y. San, Y. M. Tsou, and Z. C. Chen, Impingement Heat Transfer of Staggered Arrays of Air Jets Confined in a Channel, *International Journal of Heat and Mass Transfer*, vol. 50, pp. 3718-3727, 2007.
- [11] J. Y. San and M. D. Lai, Optimum Jet-To-Jet Spacing of Heat Transfer for Staggered Arrays of Impinging Air Jets, *International Journal of Heat and Mass Transfer*, vol. 44, pp. 3997-4007, 2001.
- [12] C. Nuntadusit, M. Wae-hayee, A. Bunyajitradulya, and S. Eiamsa-ard, Heat Transfer Enhancement by Multiple Swirling Impinging Jets with Twisted-Tape Swirl Generators, *International Communication in Heat and Mass Transfer*, vol. 39, pp. 102-107, 2012.
- [13] C. Nuntadusit, M. Wae-hayee, P. Tekasakul, and S. Eiamsa-ard, Local Heat Transfer Characteristics of Array Impinging Jets from Elongated Orifices, *International Communication in Heat and Mass Transfer*, vol. 39, pp. 1154-1164, 2012.
- [14] N. Zuckerman and N. Lion, Jet Impingement Heat Transfer: Physics, Correlations, Numerical Modeling, *Advances in Heat Transfer*, 39, pp. 565-631, 2006.
- [15] T.T. Chandratilleke, D. Jagannatha, and R., Narayanaswamy, Heat Transfer Enhancement in Microchannels with Cross-Flow Synthetic Jets, *International*

Journal of Thermal Sciences, vol. 49, pp. 504-513, 2010.

- [16] S. Ashforth-Frost, K. Jambunathan, and C. F. Whitney, Velocity and Turbulence Characteristics of a Semiconfined Orthogonally Impinging Slot Jet, Experimental Thermal and Fluid Science, vol. 14, pp. 60-67, 1997.
- [17] S. Ashforth-Frost and K. Jambunathan, Effect of Nozzle Geometry and Semi-Confinement on the Potential Core of a Turbulent Axisymmetric Free Jet, International Communication in Heat and Mass Transfer, vol. 23, pp. 155-162, 1996.
- [18] S. Ashforth-Frost, K. Jambunathan, and C. F. Whitney, Velocity and Turbulence Characteristics of a Semi Confined Orthogonally Impinging Slot Jet, Experimental Thermal and Fluid Science, vol. 14, pp. 60-67, 1997.

Appendix B3

Journal Paper

M. Wae-hayee, P. Tekasakul, and C. Nuntadusit, “Heat Transfer Enhancement on a Surface of a Row of Jet Impingements by Elongated Orifice under Cross-flow, Part 1: Parallel Orifice Configuration”, **This manuscript is being drafted.**

**Heat Transfer Enhancement on a Surface of a Row of Jet Impingements
by Elongated Orifice under Cross-flow,
Part 1: Parallel Orifice Configuration**

Makatar Wae-hayee, Perapong Tekasakul, Chayut Nuntadusit*

Energy Technology Research Center and Department of Mechanical Engineering,
Faculty of Engineering Prince of Songkla University,
Hat Yai, Songkhla 90112, Thailand

*Corresponding author, E-mail: chayut@me.psu.ac.th

Abstract

The aim of this research is to enhance heat transfer on a surface of row of impinging jets by elongated orifices under cross-flow. 4 jets with inline arrangement discharging from orifices impinge normally on inner surface of wind tunnel with simulated cross-flow. The elongated orifice with aspect ratio of its length to its width in the range of $AR=1$ (round orifice), 4 and 8 under the same cross-section area were experimentally and numerically examined. Attacking angles, defined as the major axis of the elongated orifice to the cross-flow direction, in the range of $\theta=0^\circ$ to $\theta=45^\circ$ were arranged in parallel configurations. A jet-to-plate distance (H) and jet-to-jet distance (S) were fixed at $H=2D_E$ and $S=3D_E$, respectively (where D_E is the equivalent diameter). The jet velocity was fixed corresponding to $Re_E=13,400$, and cross-flow velocity was varied corresponding to velocity ratios (jet velocity/cross-flow velocity) $VR=3, 5$ and 7 . Temperature distributions on the impingement surface were measured using Thermochromic Liquid Crystal sheet (TLCs). Flow characteristics on the impingement surface were visualized using the oil film technique. Numerical simulation employed to gain insight into the fluid flow was via computational fluid dynamics (CFD). The results indicate that the heat transfer rate of jet from elongated orifice with $\theta=0^\circ$ is higher than those conventional round orifice. The heat transfer rate is conspicuously increased when attacking angle increases from $\theta=0^\circ$ to $\theta=15^\circ$ for the case of $AR=4$ at $VR=3$, and it is abruptly decreased again when attackig angle becomes $\theta \geq 30^\circ$.

Keywords: Heat transfer enhancement, Impinging jets, Elongated orifice, Cross-flow

1. Introduction

Impinging jet is widely employed in many thermal industries applications and gas turbine components due to its high heat transfer rate under impingement region. To suffice heat transfer rate at a large heat transfer area, multiple impinging jets or jet impingement array, generally, are applied. Flow characteristics of jet impingement array

under confined channel, an accumulation of jets after impingement, called a cross-flow, moves toward channel exit. Downstream jets, subsequently, tend to cross-flow path line resulting decreasing its momentum before impingement on a target surface and its heat transfer rate [1-5].

An effort to increase the heat transfer rate of jet impingement array, drilling of effusion holes, on the upper surface (nozzle

plate) [6, 7], and at the lower surface (impingement surface) [8], in confined channel to eliminate the cross-flow has been attempted. Elongated orifices, which were replaced to conventional round orifices to reduce the effect of cross-flow on the jet impingement array, have been investigated [9]. It was found that the heat transfer rate of impinging jets issuing from these substituted orifices is more uniform and higher than those from conventional orifices.

Generally, to identify the interactions between multiple impinging jets and an inherent cross-flow are a difficult task. To clarify these interactions, the investigations are usually performed applying simulated cross-flow through a single impinging jet in wind tunnel [10-13]. In addition, an interaction between adjacent jets of an impingement array play important roles on flow and heat transfer characteristics. In this work, the effect of cross-flow velocity on multiple jet impingements from elongated orifice, applied by Nuntadusit et al. [9], is concerned under simulated cross-flow.

The aim of this research is to experimentally and numerically study the effect of cross-flow velocity on flow and heat transfer of a jet impingement row with elongated orifices to enhance heat transfer rate. The velocity ratio (cross-flow velocity/jet velocity), the aspect ratio of elongated orifice (orifice length/orifice width), and attacking angle, defined as the major axis of elongated orifice to the cross-flow direction, were investigated. The local temperature distribution on the impinged surface was measured using a Thermochromic Liquid Crystal sheet (TLCs), and the local heat transfer coefficient was evaluated using an image

processing method. The oil film technique was used to visualize the flow patterns on the impingement surface. The numerical simulation was employed to gain insight into the fluid flow.

2. Experimental method and parameters

The experimental model is shown in Fig.1. A row of 4 jets with inline arrangement impinges on the surface in a wind tunnel with rectangular cross-section under a cross-flow. The cross-flow was stimulated by introducing air through the test section crosses perpendicularly to the impinging jets. An origin of the Cartesian coordinates was located on the impinged surface. The X-, Y- and Z-axes are cross-flow streamwise, vertical, and spanwise coordinates, respectively. In order to compare the results, both middle jets were considered within area that indicate by dash line in Fig.1(b).

Elongated orifices with aspect ratio of its length to its width, $AR=1$ (round orifice), 4 and 8, having the same exit area of 136.8 mm^2 , and each orifice had an equivalent diameter (D_E) of 13.2 mm as shown in Fig.2 [9]. The attacking angle defined an angle between the major axis of the elongated round orifice to the cross-flow direction (X-axis) was varied from $\theta=0^\circ$, 15° , 30° and 45° as also shown in Fig.2. The jet-to-plate (wind tunnel height) and jet-to-jet distances were fixed at $H=2D_E$ and $S=3D_E$, respectively. The jet velocity was fixed corresponding to $Re_E=13,400$, and cross-flow velocity was varied corresponding to velocity ratios (jet velocity/cross-flow velocity) $VR=3, 5$ and 7 .

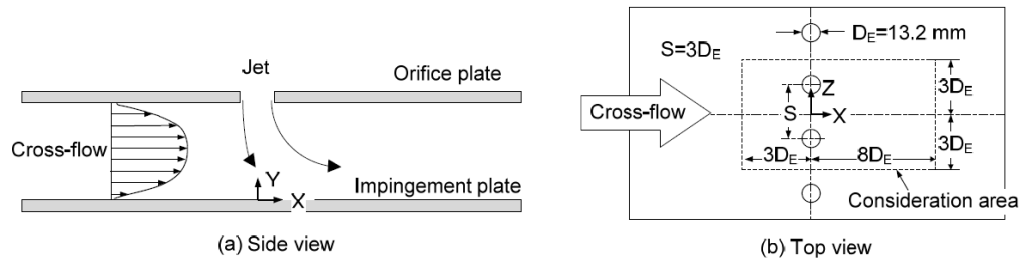


Fig. 1. Experimental model of row of impinging jets.

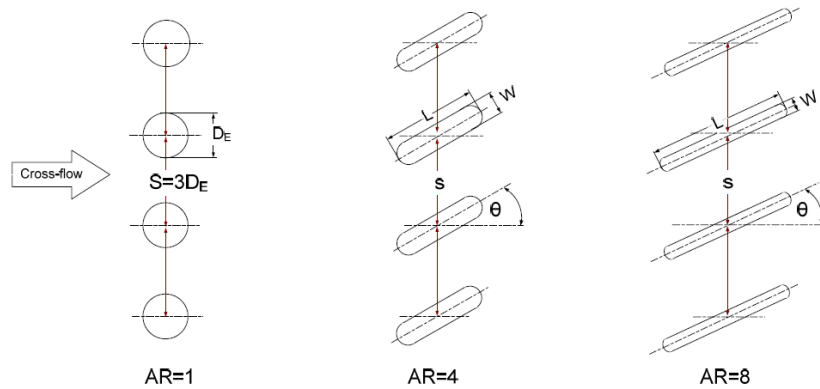


Fig. 2. Configuration of jet arrangement.

3. Experimental setup and method

3.1 Experimental apparatus

The experimental setup was assembled in two parts; jet and cross-flow supplies as shown in Fig.3. The impinging jet was generated by introducing air through a temperature controlled chamber equipped with a heater, a calibrated orifice flow meter, a jet chamber and a jet orifice before entering the test section. The jet chamber having constant cross-section of 360-mm \times 360-mm and a height of 850-mm was equipped with two layers of perforated plates and two layers of mesh plates to achieve an uniform flow field approaching the orifice plate.

The simulated cross-flow was produced by introducing air through the inlet chamber, flow straightener, two layers of mesh plates, the test section and a chamber outlet by using another blower. The cross-section of wind tunnel was rectangular with height of 26.4 mm ($2D_E$) and width of 300 mm. The length of calming section of wind tunnel was 200 cm which is sufficient to achieve fully developed flow in the test section as indicated in Fig.3.

A Pitot-static tube was located upstream of the test section to measure a cross-flow velocity at the center of channel. For all experiments, the inlet temperatures of impinging jets and cross-flow were kept constant at 27.6 $^{\circ}$ C by a temperature and power controller.

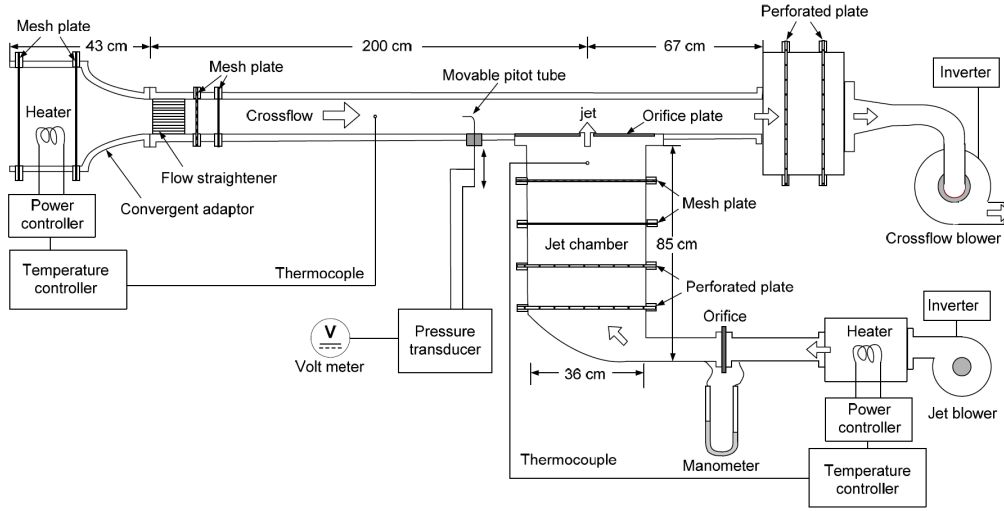


Fig. 3. Schematic diagram of the experimental setup.

3.2 Heat transfer measurement and data reduction

The test section for heat transfer measurement was directly mounted to the jet chamber as shown in Fig.4. The air jets with constant temperature discharging from the orifice plate were impinged on the heated surface for cooling. The wall temperature (T_w) on the impingement surface was measured by using TLC sheet (Omega, LCS-95, USA) that attached on the rear of this surface as shown particularly in Fig. 4. The heat transfer surface made of stainless steel foil which having thickness of 30- μm was installed between a pair of copper bus bars. The heat transfer surface was heated by DC power supply through copper bus bars. An electrical energy dissipated in the stainless steel foil can be determined from

$$\dot{q}_{input} = \frac{I^2 \cdot R}{A} \quad (1)$$

where I is the electrical current, R and A are the electrical resistance and the area of the stainless steel foil.

The local heat transfer coefficient by forced convection of the impinging jets, h , can be evaluated from

$$h = \frac{\dot{q}_{input} - \dot{q}_r - \dot{q}_c}{T_w - T_j} \quad (2)$$

where $\dot{q}_r = \sigma \varepsilon_{TLC} (\overline{T_w}^4 - T_s^4)$ and $\dot{q}_c = \overline{h}_c (\overline{T_w} - T_s)$ are the heat losses to the environment by radiation and convection from rear side of impinged surface, respectively; $\overline{T_w}$ and T_j are the average wall temperature and jet temperature; σ is the Stefan-Boltzman constant; ε_{TLC} is the emissive coefficient of the TLC sheet; T_s is the surrounding temperature; and \overline{h}_c is the average natural heat transfer coefficient calculated from natural convective heat transfer from the heat transfer surface to the surrounding.

The CCD camera was used to capture color patterns on TLC sheet. The images of color pattern were subsequently converted from the RGB (red, green and blue) color system to the HSI (Hue, Saturation and Intensity) color system. The Hue (H) value was used to correlate the color of TLC to their temperature in range of 28-40°C via a calibration. The local Nusselt number was calculated

$$Nu = \frac{h D_E}{k} \quad (3)$$

here, D_E is the equivalent diameter of the orifice and k is a thermal conductivity of an air jet [9, 14].

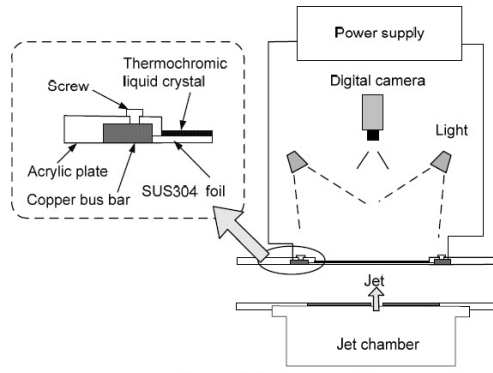


Fig. 4. Test section of heat transfer measurement.

3.3 Flow visualization on the impinged surface

The flow pattern on the impinged surface was visualized by using oil film technique. The oil was mixed with 7 g of liquid paraffin, 3.5 g of titanium dioxide and 1.8 g of oleic acid. The transparent plastic plate

uniformly coated with the oil under the same film thickness was employed to represent the impinged surface. During the experiment, the oil film behavior on the impinged surface was recorded using video camera [9 and 14].

3.4 Numerical simulation

A 3-D numerical simulation with the ANSYS Fluent 13.0 was employed to visualize the flow characteristics of the jets and the cross-flow. The calculation based on finite volume method was adopted to solve governing differential equations with boundary conditions. A numerical model was identically created to the experimental model. A turbulence model with SST was applied due to high accurate prediction in impingement problems and moderate computational cost [12, 15 and 16]. This turbulent model has also been employed to accurately predict a flow and heat transfer characteristics of impinging jet under the cross-flow [13 and 16].

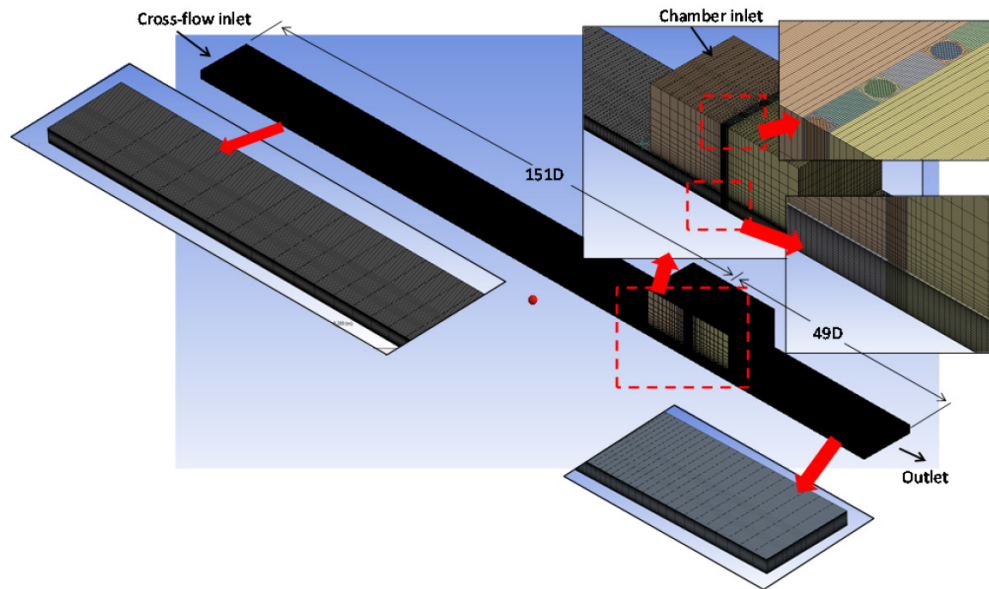


Fig. 5. Numerical model and generated grid.

The generated grid system was even rectangular as shown in Fig.5. The elements were concentrated near the wall of wind tunnel and mixing region. The boundary conditions were identically specified to experimental conditions. The outlet pressure was kept constant at 1 atm. A solution

method was based on SIMPLE algorithm with second order upwind for all spatial discretization. The solution was considered to be converged when the normalized residual of the algebraic equation was less than a prescribed value of $1.0E-5$ [13 and 17].

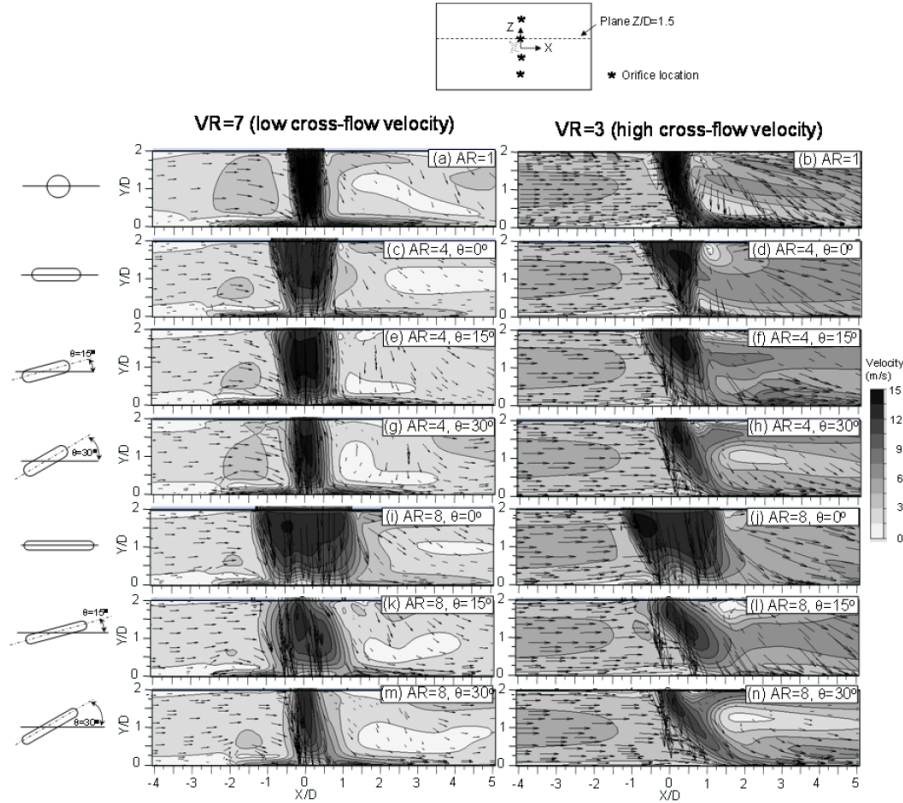


Fig. 6. Vectors and contours of velocity in X-Y plane at $Z/D=1.5$.

4. Results and discussions

4.1 Flow characteristics of jets and cross-flow

Flow characteristics of the jet interacted with the cross-flow using CFD technique are shown in Fig.6-8. Velocity vectors and velocity contours in X-Y plane comparing between low cross-flow velocity (left side) and high cross-flow velocity (right side) at $Z/D=1.5$ and 0 are shown in Fig.6 and 7, respectively. In the case of $VR=7$ as shown

in Fig.6 (right side), the jet impingements are slightly deflected to downstream direction due to low cross-flow velocity. The deflection of jets is comparable throughout the orifice configurations and the attacking angles.

In the case of high cross-flow velocity, $VR=3$, as shown in Fig.6 (left side), the deflection of jets is larger than those the low cross-flow velocity. This deflection is greater when attacking angle becomes larger. The deflections of jets with $AR=8$, moreover, are

prominently greater than those $AR=4$ under the same attacking angle. The greatest deflection of jet is from two factors; strong momentum of cross-flow striking on the jet

flow due to the high cross-flow velocity; and larger interaction area between cross-flow and jet flow due to the increasing of attacking angle.

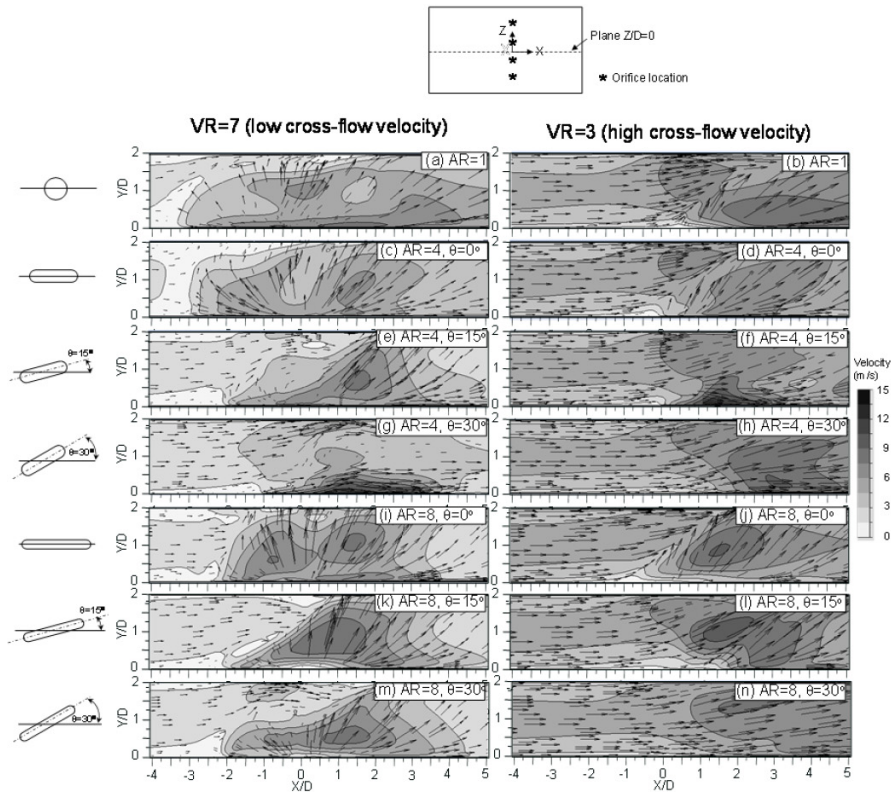


Fig. 7. Vectors and contours of velocity in X-Y plane at $Z/D=0$.

When compare flow characteristics in the case of $AR=4$ and 8 with $\theta = 0^\circ$ at $VR=3$ (Fig.6(d) and (j)) to the case of $AR=1$ (Fig.6(b)), it is found that the deflection of jet from elongated round orifice is smaller than those conventional one. This can be explained that the jet discharge from elongated orifice without attacking angle is more penetrate into the cross-flow than those the conventional orifice. This is important key that why heat transfer rate of impinging jet array from elongated orifice associated with coherent cross-flow is higher than those conventional orifices by Nuntadusit et al. [9].

Flow characteristics through jet interval are shown in Fig.7. This figure can be seen that the interaction between adjacent wall jets flow from lower surface to upper surface for the case of low cross-flow velocity (left side of this figure). The wall jets tend to downstream direction when the attacking angle increases. The deflection of wall jets is more tend to downstream direction when the cross-flow velocity increase (right side of figure). For the case of large attacking angle, $\theta=30^\circ$ and 45° , as shown in Fig.7(h) and (n), the wall jets are completely blown by the high cross-flow velocity.

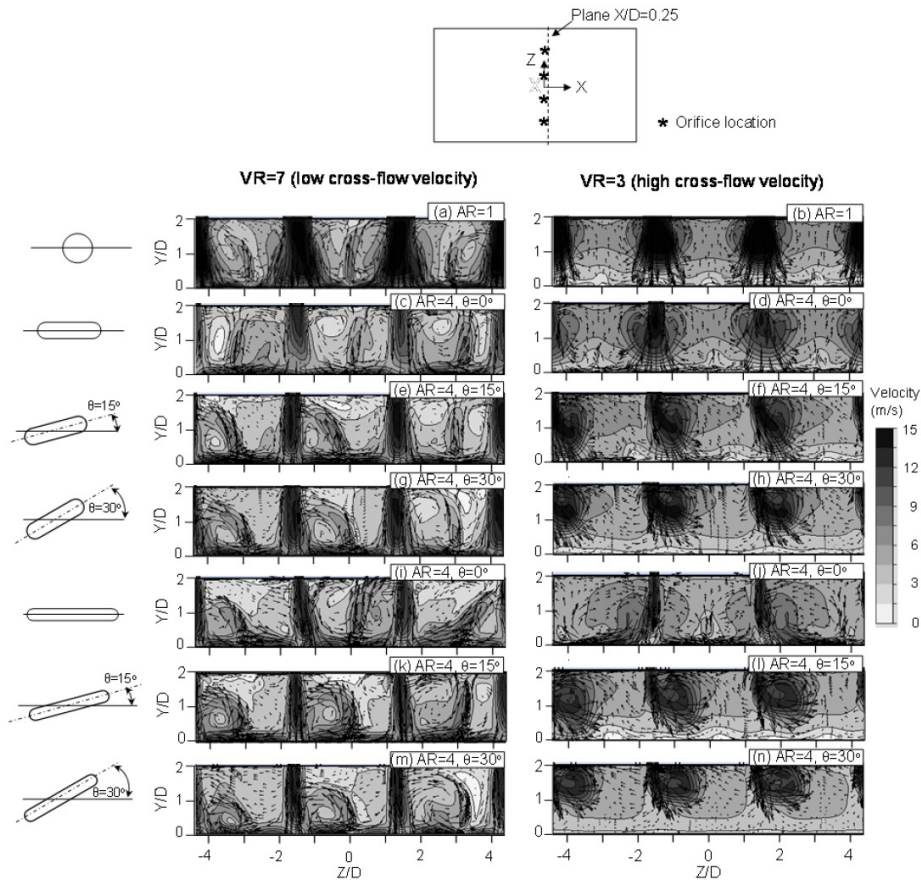


Fig. 8. Vectors and contours of velocity in Y-Z plane at $X/D=0.25$.

A comparison of flow characteristics in Y-Z plane at $X/D=0.25$ are shown Fig. 8. For the case of high cross-flow velocity as shown right side in Fig.8, the deflection of jets tends to +Z-axis when attacking angle is larger. For the case of low crossflow velocity as shown in left side of this figure, the deflection of jets to +Z-axis is smaller because of less significant effect of cross-flow. This section obviously shows that the effect of high cross-flow velocity on attacking angle is more prominent than those the low cross-flow velocity.

4.2 Flow characteristics above the impingement surface

Flow patterns of impinging jets on the impingement surface using the oil film technique are shown in Fig.9. The black and white regions represent the areas where the oil film is completely remove called impingement region and the area with original oil film coating, respectively. The impingement regions of $AR=1$ are more shifted to downstream directions when cross-flow velocity increases. This flow patterns correspond to those flow characteristics of downstream impinging jets in impingement array that the cross-flow velocity increases in this region [14]. For the case of $AR=4$ and 8 with $\theta=0^\circ$ as shown in Fig.9(d)-(f) and (m)-(o), the shifting of impingement regions to downstream direction at high cross-flow

velocity are minimized when compare with the case of $AR=1$. This is due to jets from elongated orifice can more penetrate into the cross-flow as discussed in previous CDF results. This flow characteristics correspond also to those impingement array system that employ elongated orifice [9]. In addition, the

impingement regions are obliquely shifted to $+Z$ axis provided by the larger attacking angle. This is due to inclination sticking of cross-flow on jet impingement flow corresponding to direction of orifice arrangement.

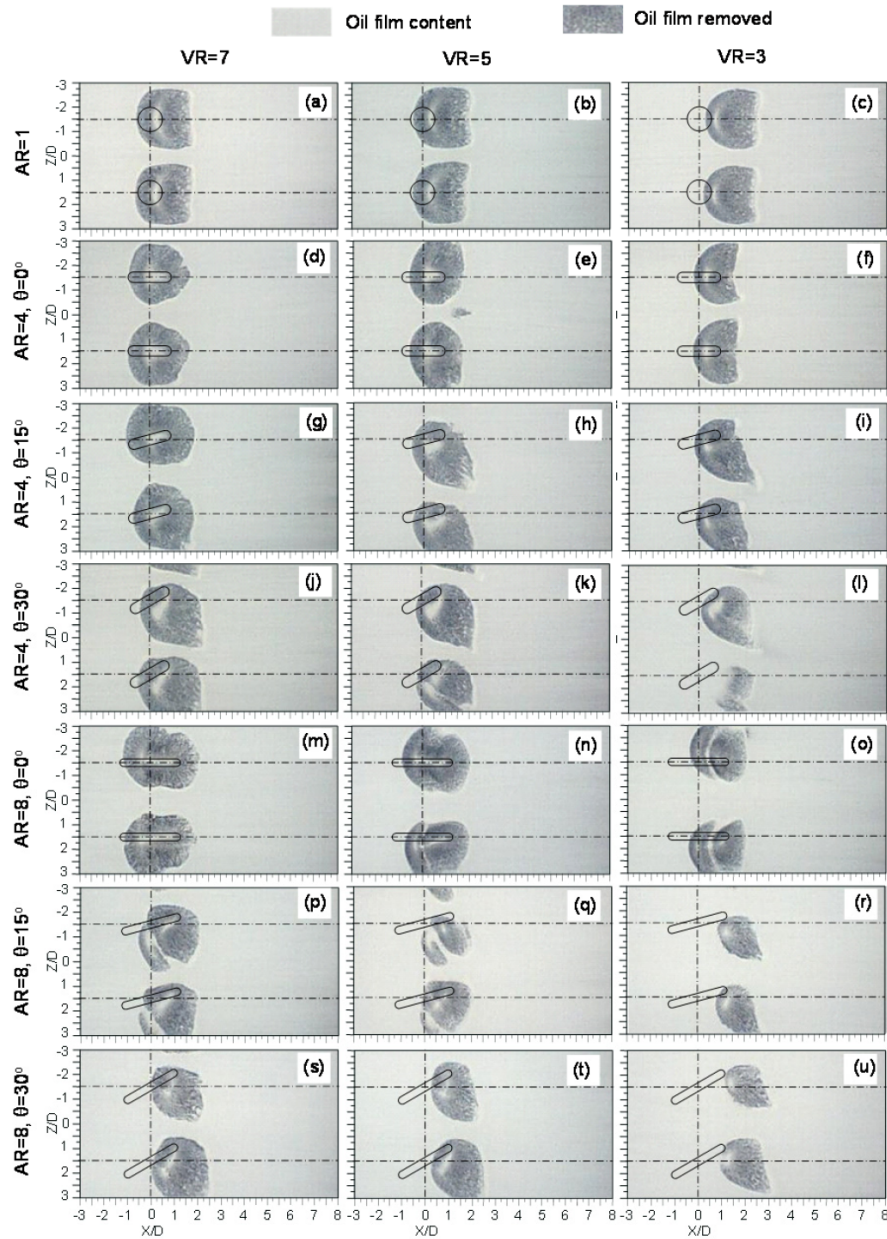


Fig. 9. Flow patterns on the impinging surface (Experimental results).

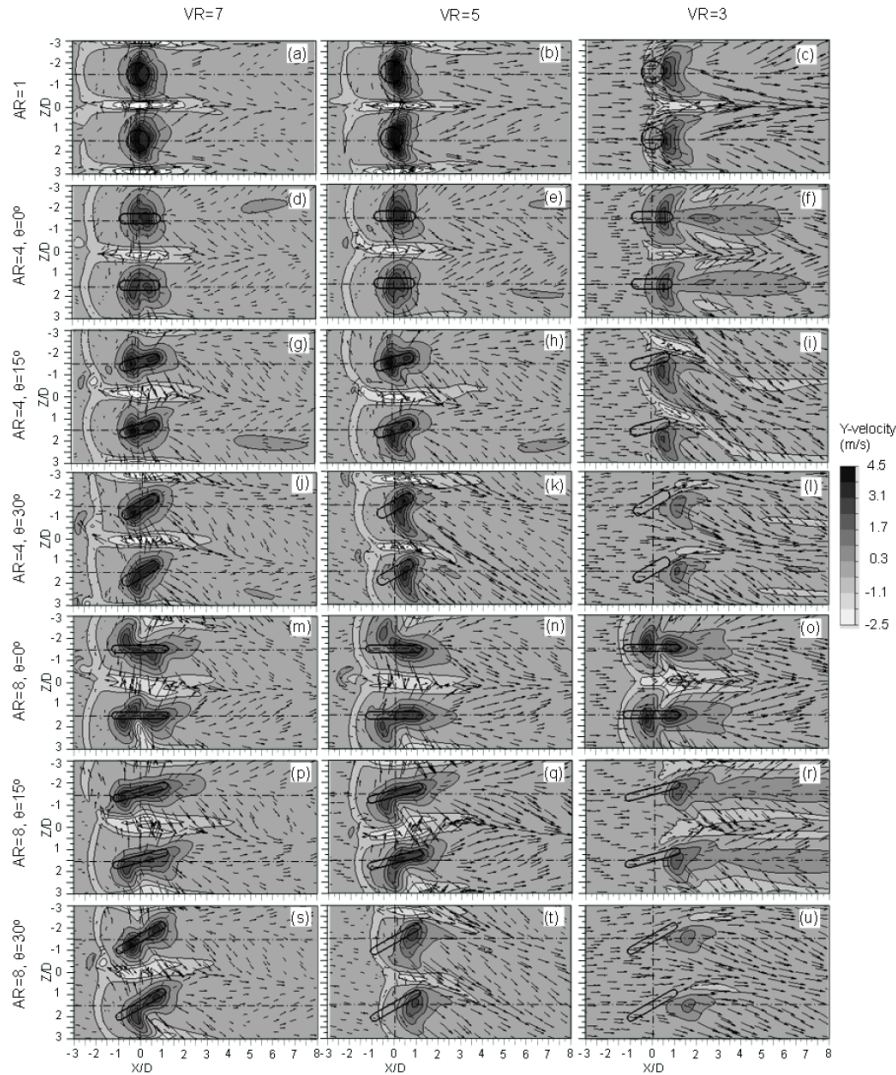


Fig. 10. Velocity vectors and Y-component velocity contours on X-Z plane (CFD results and above from target surface of 1-mm).

The sizes of impingement regions for $AR=8$ at $\theta=15^\circ$ and 30° (Fig.9(p)-(u)) are smaller when compare with the same conditions of $AR=4$ (Fig.9(g)-(l)). The smaller size of this regions for $AR=8$ is from larger interaction area between jet and cross-flow provided by larger attacking angle and longer orifice length ($AR=8$). Moreover, the sizes of impingement regions are getting smaller when cross-flow velocity becomes higher as shown in Fig.9(r) and (u). For the case of without attacking angle, $\theta=0^\circ$, the

sizes of impingement regions for $AR=4$ and 8 are comparable under the same VR as shown in Fig.9(d)-(f) and (m)-(o) even though cross-flow velocity becomes higher.

The velocity vector and contour in the Y-axis on Z-X plane near the impingement surface (1 mm above the surface) from CFD results are shown in Fig.10. This position above from surface is chosen to represent the plane sufficiently near the surface due to the condition at the surface is no-slip. The Y-component velocity represents the velocity in

the direction normal to the impingement surface. The positive direction is towards the direction of the jet that impinges on the target surface. Area of high Y-component velocity contour indicates the impingement region corresponding to removed oil film

region as shown earlier in Fig. 9, and this CFD results agree very well with the flow patterns of oil film technique. With the good agreement, clarification of heat transfer behavior in the next section can refer to the flow characteristics from this CFD results.

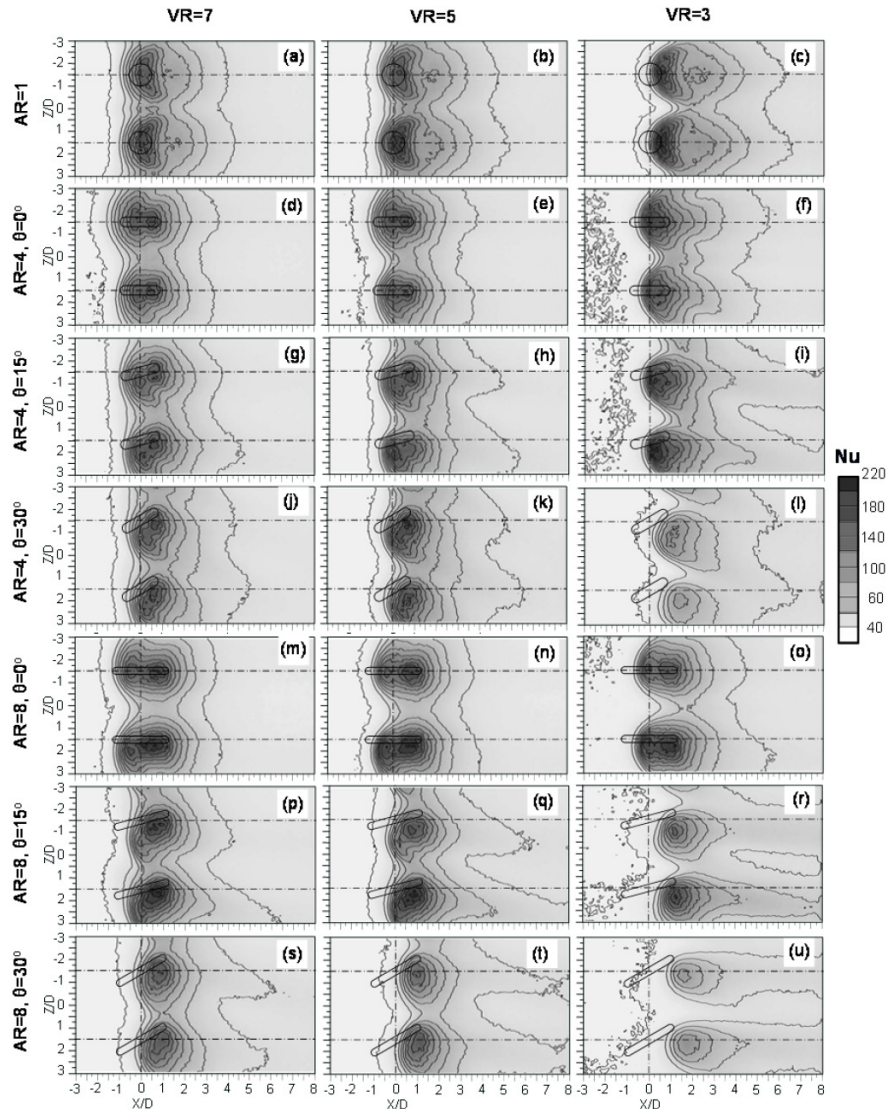


Fig. 11. Nusselt number distributions on the impinged surface (Experimental results, $T_j=27^\circ\text{C}$).

It, in addition, is found that some of the areas of high Y-component velocity of elongated orifice are separated into two "spots", especially for the case of $AR=8$ at

$\theta=0^\circ$ for $VR=3$ as shown in Fig.10(o). This flow characteristic agrees well with the flow pattern on the impingement surface under the same condition as shown in Fig. 9(o). With

the associated cross-section shape of the jet discharged from the elongated orifices, the high jet velocity immediately decays at the center of its cross-section, resulted from a mixing with the surrounding flow. Consequently, the high velocity area is separated into two parts.

4.3 Local Nusselt number on the impinged surface

Nusselt number distributions on impingement surface from experiment are shown in Fig.11. These contours of Nusselt

number correspond to the oil film patterns on the impingement surface as shown in Fig. 9 as well as the contours of Y-component velocity near the impingement surface as shown in Fig.10. Generally, the Nusselt number is high at impingement regions and low at upstream regions. These areas of high Nusselt number are more contracted along upstream direction (-X axis) and more extended along downstream one (X axis) when the cross-flow velocity increases. The areas of high Nusselt number, in addition, are more obliquely extended along +Z axis when the attacking angle is larger.

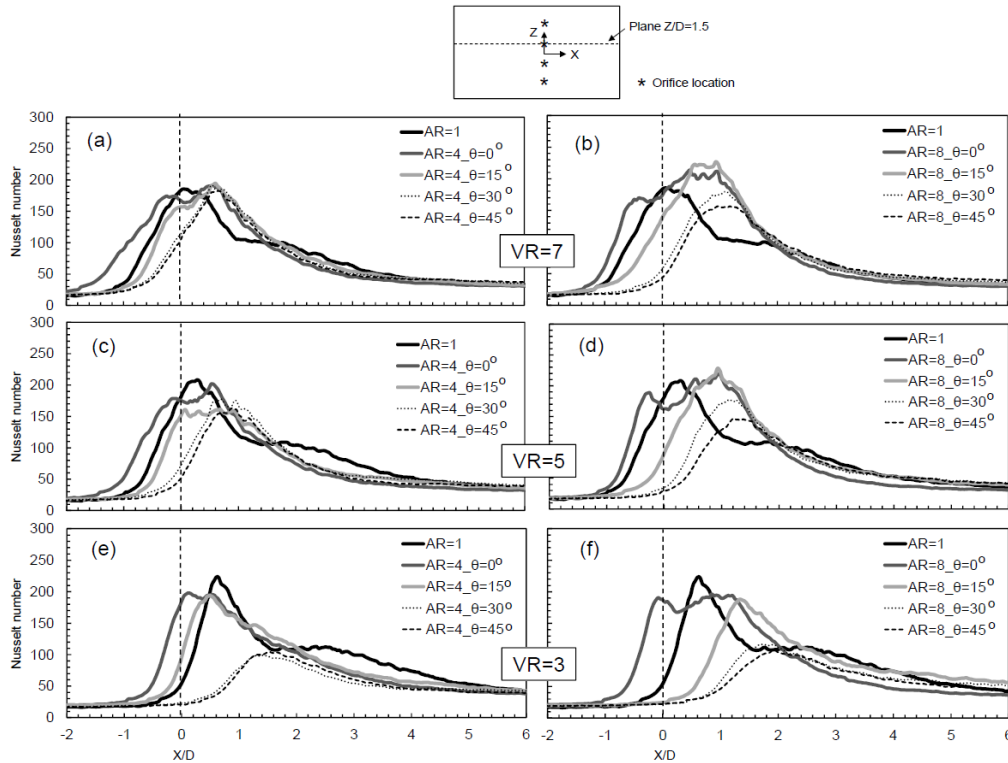


Fig. 12. Nusselt number distribution along downstream direction at $Z/D=1.5$ (Centerline jet, experimental results).

The extension area of high Nusselt number along upstream direction of $AR=4$ and 8 at $\theta=0^\circ$ (Fig.11(d)-(f) and (m)-(o)) are larger than those $AR=1$ (Fig.11(a)-(c)) under the same VR . These results show that the jet discharging from elongated orifice with $\theta=0^\circ$

can minimize the cross-flow effect. This corresponds to the higher heat transfer of impingement array using elongated orifices that has been reported by Nuntadusit et al. [9]. However, for the case of $\theta>0^\circ$, these area of high Nusselt number along upstream

direction are contracted, especially, for the case of large attacking angle and high cross-flow velocity as shown in Fig.11(l) and (u).

Nusselt number distributions along downstream direction at orifice centerline ($Z/D=1.5$) and orifice interval ($Z/D=0$) are shown in Fig.12 and 13, respectively. The results are obviously found to appear that the Nusselt number along upstream direction are lower when attacking angle becomes larger. The Nusselt number along this upstream direction of $AR=4$ and 8 at $\theta=0^\circ$ is higher than those $AR=1$ throughout VR .

The Nusselt number peak tend to decrease when the attacking angle becomes larger and cross-flow velocity is higher. Abruptly decreasing of this peak value for the case of large attacking angle, $\theta=30^\circ$ and 45° , at $VR=3$ is large striking area of significant cross-flow on jet impingement flow. For $VR=3$ as shown in Fig.12(e) and (f), the highest peak value takes place for $AR=1$, and it is sharpe distribution. The peak value of $AR=4$ and 8 at $\theta=15^\circ$, however, lower than those $AR=1$ but the area of peak value larger than those $AR=1$.

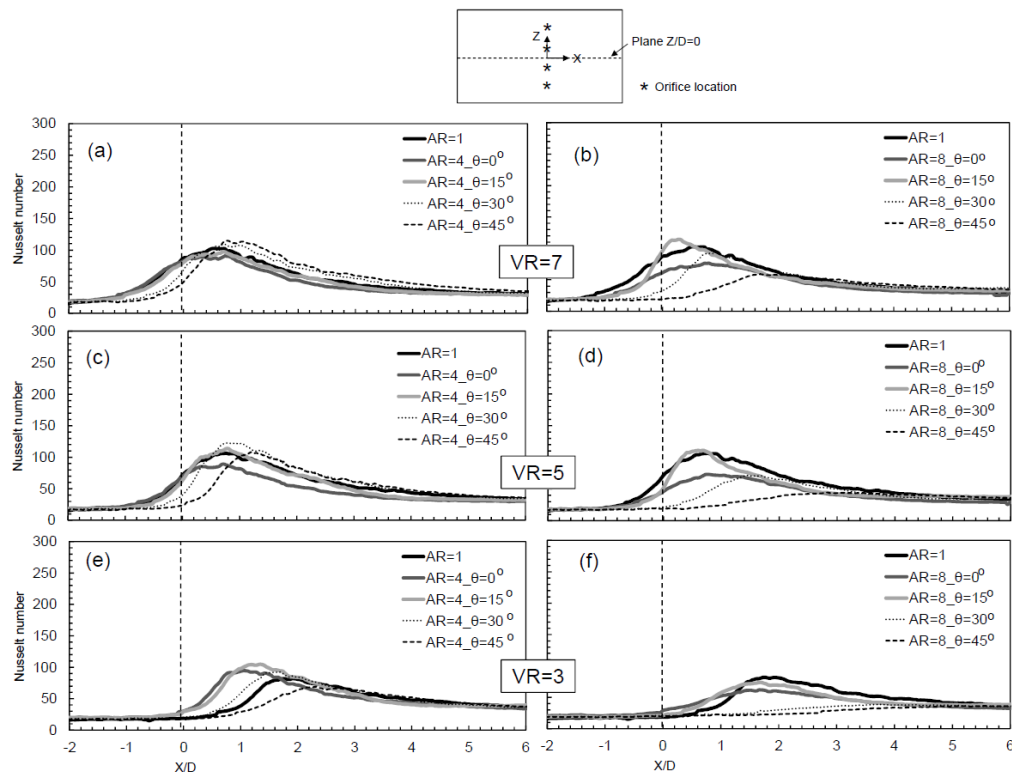


Fig. 13. Nusselt number distribution along downstream direction at $Z/D=0$ (interval jets, experimental results)

Fig.13, Nusselt number distribution along jet interval ($Z/D=0$) show that the peak values of each condition shift to downstream direction when the cross-flow velocity increases. For the case of $AR=4$ at $\theta=30^\circ$ and 45° with $VR=5$ and 7 as shown in Fig.13(a) and (c), Nusselt number distributions along

downstream direction ($X/D>1$) are higher than the others under the same VR . This is due to the shifting impingement region (area of high heat transfer) of jet located at $Z/D=-1.5$ to the orifice interval location ($Z/D=0$) of these conditions. For the case of $AR=8$ with $VR=3$ as shown in Fig.13(f), Nusselt number

distributions of each case are rather flat, especially, for the case of $AR=8$ at $\theta=30^\circ$ and 45° . This Nusselt number distributions correspond to the flow characteristics as

shown previously in Fig.7(j), (l) and (n) that the wall jet is rather completely blown by the high cross-flow velocity, especially, for the case of large attacking angle.

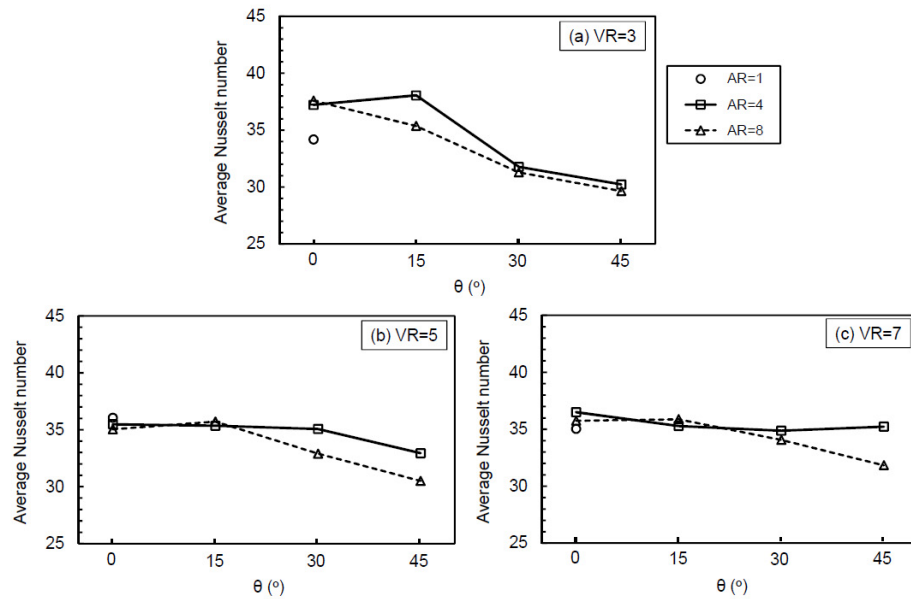


Fig. 14. Average Nusselt number versus attacking angle.

4.4 Average Nusselt number

The average Nusselt number on the impingement surface calculated from the average local wall temperature in area of $-3 < X/D < 8$ and $-3 < Z/D < 3$ versus the attacking angle are shown in Fig 14. Almost all of average Nusselt number of $AR=8$ tend to decrease when the attacking angle increases. For the case of $AR=4$, the average values at $VR=3$ are conspicuously increased when attacking angle increases from $\theta=0^\circ$ to $\theta=15^\circ$. This average values are abruptly decreased again when attackig angle becomes $\theta \geq 30^\circ$.

For the case of $AR=8$ at $VR=3$, the Nusselt number versus the attacking angle are rather consistent. This results can be noted that the effect of attacking angle is slightly significant effect on heat transfer in rate for the case of low cross-flow velocity, $VR=7$. However, for the case of high cross-

flow velocity, $VR=3$, the heat transfer rate is abruptly decreased when the attacking angle becomes larger.

5. Conclusions

The effect of cross-flow velocity on flow and heat transfer characteristics of jet impingement row discharging through elongated orifice with different attacking angle was experimentally and numerically studied. The main results can be summarized as follows;

1. Impinging jets discharging from both elongated orifice at $\theta=0^\circ$ can minimize the cross-flow effect. The deflection of jets toward cross-flow direction of elongated orifices is smaller than those conventional orifice. However, its deflection is more larger when the attacking angle become larger. This affects directly to heat transfer

rate on impingement surface that the impinging jets from both elongated orifice with $\theta=0^\circ$ can increase the heat transfer rate higher than those conventional orifice except the case of for $VR=5$. Almost all heat transfer rate of elongated orifice with $\theta \geq 30^\circ$ are lower than those conventional orifice.

2. The impingement regions (areas of high Nusselt number) are extended in the X-axis and obliquely extended in the +Z-axis when the attacking angle becomes larger. The extension of impingement regions in the X-axis is from the effect of cross-flow, and the oblique extension of these regions in the +Z-axis is from the effect of attacking angle.

3. The heat transfer rate is conspicuously increased when attacking angle increases from $\theta=0^\circ$ to $\theta=15^\circ$ for the case of $AR=4$ at $VR=3$, and it is abruptly decreased again when attacking angle becomes $\theta \geq 30^\circ$.

Acknowledgments

This research was supported by grants from Thailand Energy Policy and Planning Office, Ministry of Energy, the Graduate School and Faculty of Engineering, Prince of Songkla University.

References

- [1] R. Viskanta, Heat transfer to impinging isothermal gas and flame jets, *Exp. Therm. Fluid Sci.* 6 (1993) 111-134.
- [2] L.-E. Brizzi, A. Bernard, J.-L. Bousgarbies, E. Dorignac, J.-J. Vullierme, Study of several impinging jets, *J. Thermal Science* 9 (2000) 217-223.
- [3] B.P.E. Dano, J.A. Liburdy, Structure detection and analysis of non-circular impinging jets in a semi-confined array configuration, *Exp. Therm. Fluid Sci.* 31 (2007) 991-1003.
- [4] L.W. Florschuetz, C.R. Truman, D.E. Metzger, Streamwise flow and heat transfer distributions for jet array impingement with crossflow, *J. Heat Transfer-Trans. ASME.* 103 (1981) 337-342.
- [5] V. Katti, S.V. Prabhu, Influence of spanwise pitch local heat transfer distribution for in-line arrays of circular jets with air flow in two opposite, *Exp. Therm. Fluid Sci.* 14 (2008) 84-95.
- [6] D.-H. Rhee, P.-H. Yoon, H.H. Cho, Local heat/mass transfer and flow characteristics of array impinging jets with effusion holes ejecting spent air, *Int. J. Heat Mass Transfer* 46 (2003) 1049-1061.
- [7] T.B. Hoberg, A.J. Onstad, J.K. Eaton, Heat transfer measurements for jet impingement arrays with local extraction, *Int. J. Heat Fluid Flow* 31 (2010) 406-467.
- [8] H.-C. Chiu, J.-H. Jang, W.-M. Yan, Experimental study on the heat transfer under impinging elliptic jet array along a film hole surface using liquid crystal thermograph, *Int. J. Heat Mass Transfer* 52 (2009) 4435-4448.
- [9] C. Nuntadusit, M. Wae-hayee, P. Tekasakul, S. Eiamsa-ard, Local heat transfer characteristics of array impinging jets from elongated orifices, *Int. Commun. Heat Mass Transfer* 39 (2012) 1154-1164.
- [10] J.-P. Bouchez, R.J. Goldstein, Impingement cooling from a circular jet in a cross flow, *Int. J. Heat Mass Transfer* 18 (1975) 719-730.
- [11] R. J. Goldstein, I. Behbahan, Impingement of a circular jet with and without cross flow, *Int. J. Heat Mass Transfer* 25 (1982) 1377-1382.
- [12] Y. Shi, M.B. Ray, A.S. Mujumdar, Numerical study on the effect of cross-

- flow on turbulent flow and heat transfer characteristics under normal and oblique semi-confined impinging slot jets, *Drying Technology* 21 (2003) 1923-1939.
- [13] M-W. Heo, K.-D. Lee, K.-Y. Kim, Optimization of an inclined elliptic impinging jet with cross flow for enhancing heat transfer, *Heat Mass Transfer* 47 (2011) 731-742.
- [14] M. Wae-hayee, P. Tekasakul, C. Nuntadusit, Influence of nozzle arrangement on flow and heat transfer characteristics of arrays of circular impinging jets, *Songklanakarin J. Sci. Technol.* xx (2013) xxx-xxx.
- [15] N. Zuckerman, N. Lion, Jet impingement heat transfer: physics, correlations, Numerical modeling, *Advances Heat Transfer* 39 (2006) 565-631.
- [16] T.T. Chandratilleke, D. Jagannatha, R. Narayanaswamy, Heat transfer enhancement in microchannels with cross-flow synthetic jets, *Int. J. Therm. Scie.* 49 (2010) 504-513.
- [17] Y.-T. Yang, Y.-X. Wang, Three-dimensional numerical simulations of an inclined jet with cross-flow, *Int. J. Heat Mass Transfer* 48 (2005) 4019-4027.

Appendix B4

Journal Paper

M. Wae-hayee, P. Tekasakul, and C. Nuntadusit, "Heat Transfer Enhancement on a Surface of a Row of Jet Impingements by Elongated Orifice under Cross-flow, Part 2: Counter Orifice Configuration", **This manuscript is being drafted.**

**Heat Transfer Enhancement on a Surface of a Row of Jet Impingements
by Elongated Orifice under Cross-flow,
Part 2: Counter Orifice Configuration**

Makatar Wae-hayee, Perapong Tekasakul, Chayut Nuntadusit*

Energy Technology Research Center and Department of Mechanical Engineering,
Faculty of Engineering Prince of Songkla University,
Hat Yai, Songkhla 90112, Thailand

*Corresponding author, E-mail: chayut@me.psu.ac.th

Abstract

The objective of this research is to enhance heat transfer on a surface of jet impingement row by elongated orifices which have aspect ratio of orifice length to orifice width $AR=4$ and 8 . The row of 4 jets with inline arrangement impinges perpendicularly on inner surface of wind tunnel with rectangular cross-section under simulated cross-flow. Two differences of counter orifice arrangements with convergent and divergent configurations were focused. Attacking angles, defined as the major axis of the elongated orifice to the cross-flow direction, in the range of $\theta=0^\circ$ to $\theta=45^\circ$, and velocity ratios (jet velocity/cross-flow velocity) in the range of $VR=3, 5$ and 7 were experimentally and numerically studied. A jet-to-plate distance (H) and jet-to-jet distance (S) were fixed at $H=2D_E$ and $S=3D_E$, respectively (where D_E is the equivalent diameter). Temperature distributions on the impingement surface were measured using Thermochromic Liquid Crystal sheet (TLCs). Flow patterns on the impingement surface were visualized using the oil film technique. Flow characteristics of jets and cross-flow were studied by numerical simulation method. The results show that the effects of attacking angle with divergent orifice configuration can increase the heat transfer rate on impingement surface, and it was higher than that convergent orifice configuration.

Keywords: Heat transfer enhancement, Impinging jets, Elongated orifice, Cross-flow

1. Introduction

Jet impingement is widely used in various industrial applications such as tempering of glass, drying of paper, cooling of turbine blade and electronic component. Usually, the multiple impinging jets are applied to attain high and uniform heat transfer on a large application surface. An important factor that directly influences on multiple impingement jets under confined channel is a cross-flow. The cross-flow is

generated by accumulation of spent jet moving toward channel exit. Flow rate or velocity of cross-flow, subsequently, increase corresponding to summation of spent jet from upstream jets to downstream jets and so on. So, the downstream jets tend to cross-flow streamwise resulting decreasing momentum of jet before impingement and decreasing heat transfer rate on impinged surface [1-5].

Heat transfer rate on a surface of single impinging jet, generally, is high at jet-to-

plate distance in the ranges of 4 to 6 times of jet diameter [1]. It gets lower distance (lower than two times of jet diameter) for the case of multiple jet impingements to maintain high heat transfer rate due to impinging jets against cross-flow effect [5]. Efforts to minimize the cross-flow effect in some works have been attempted [6-8]. Nuntadusit et al. [9] used elongated orifices to reduce the cross-flow effect on the jet impingement array. They found that the heat transfer rate of impinging jets issuing from elongated orifices is more uniform and higher than those from conventional orifices.

Wae-hayee et al. [10] studied the impinging jet row from elongated orifices under simulated cross-flow to clarify the effect of cross-flow velocity on jet impingement flow. Their study was also focused on the effects of attacking angle with parallel orifice configurations. In this work, the effect of attacking angle with counter orifice configurations that are same experimental model, apparatus and methods with the work of Wae-hayee et al. [10] was attempted.

The aim of this research is to enhance heat transfer rate on impingement surface of row of impinging jets from elongated orifices

under simulated cross-flow. Two differences of counter orifice arrangements with convergent and divergent configurations as shown in Fig.1 were experimentally and numerically investigated. The velocity ratio (cross-flow velocity/jet velocity), the aspect ratio of elongated orifice (orifice length/orifice width), and attacking angle, defined as the major axis of elongated orifice to the cross-flow direction, were examined.

2. Experimental method and parameters

An experimental model of a row of 4 jets discharging from orifices and impinging normal to the opposite surface in the wind tunnel with rectangular cross-section under simulated cross-flow has been employed in our work [10]. The jets configured with inline arrangement, and a centerline through center of each orifice is normal to cross-flow streamwise. The cross-flow with fully developed flow was introduced through jet impingements in the test section. An origin of the Cartesian coordinates was located on the impinged surface. The X-, Y- and Z-axes are cross-flow streamwise, vertical, and spanwise coordinates, respectively.

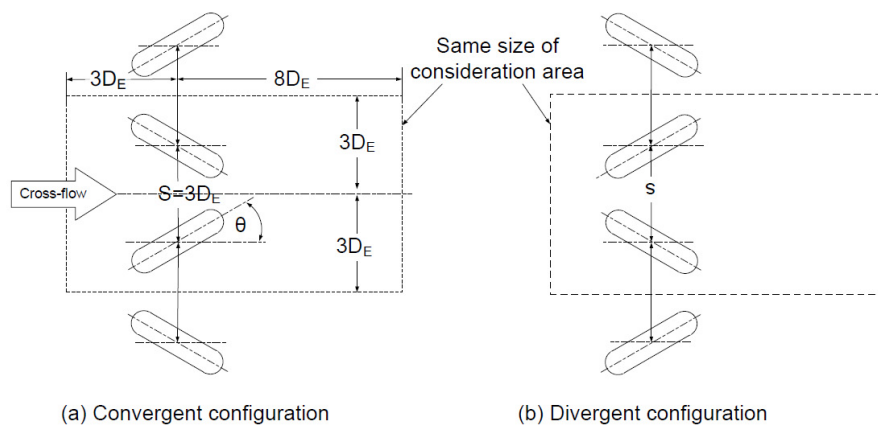


Fig. 1. Configuration of jet arrangements ($D_E=13.2$ mm).

Elongated orifices with aspect ratio of its length to its width, $AR=1$ (round orifice), 4 and 8, and each orifice having the same exit area of 136.8 mm^2 , and an equivalent diameter (D_E) of 13.2 mm were employed [9, 10]. The attacking angle defined an angle between the major axis of the elongated orifice to the cross-flow direction (X-axis) was varied in the ranges $\theta=0^\circ, 15^\circ, 30^\circ$ and 45° . Orifice arrangements with convergent and divergent configurations as shown in Fig.1 were examined. The jet-to-plate (wind tunnel height) and jet-to-jet distances were fixed at $H=2D_E$ and $S=3D_E$, respectively. The jet velocity was fixed corresponding to $Re_E=13,400$, and cross-flow velocity was varied corresponding to velocity ratios (jet velocity/cross-flow velocity) $VR=3, 5$ and 7 .

3. Experimental setup and method

3.1 Experimental apparatus

The experimental setup used here was same in our work [10]. It was composed two parts; jet and cross-flow supplies. The compressed air was forced by blower through a temperature controlled chamber, a calibrated orifice flow meter, a jet chamber and a jet orifice before entering the test section. The jet chamber having constant cross-section was equipped with two layers of perforated plates and two layers of mesh plates to achieve an uniform flow field approaching the orifice plate.

The simulated cross-flow was sucked by another blower through wind tunnel which having height of 26.4 mm ($2D_E$) and width of 300 mm. The length of calming section of wind tunnel was sufficient to achieve fully developed flow before entering the test section. A Pitot-static tube was located upstream of the test section to measure a cross-flow velocity at the center of channel. For all experiments, the inlet temperatures of

impinging jets and cross-flow were kept constant at $27.6 \text{ }^\circ\text{C}$.

3.2 Heat transfer measurement and data reduction

The air jets with constant temperature discharging from the orifice plate were impinged on the heated surface for cooling. The wall temperature on the impingement surface was measured by using the TLC sheet attached on the rear of this surface. The CCD camera was used to capture color patterns on the TLC sheet, and the images of the color patterns were subsequently translated into temperatures via a calibration.

The local Nusselt number was calculated from:

$$Nu = \frac{hD_E}{k} \quad (1)$$

where, h is the local heat transfer coefficient, D_E is the equivalent diameter of the orifice, and k is a thermal conductivity of the air jet [9-11].

3.3 Flow visualization on the impinged surface

The oil film technique was employed to visualize the flow pattern on the impinged surface. The mixer of oil film was liquid paraffin, titanium dioxide and oleic acid. The transparent plastic plate being impingement surface was uniformly coated by oil under the same film thickness. During the experiment, removing of oil film behavior on this surface was recorded using video camera [9-11].

3.4 Numerical simulation

A 3-D numerical simulation with the ANSYS Fluent 13.0 was adopted to visualize the flow characteristics of the jets and the cross-flow. A numerical model was identically created to the experimental

model. The generated grid system was even rectangular, and it was concentrated near the wall of wind tunnel and mixing region. A turbulence model with SST was applied due to high accurate prediction in impingement

problems and moderate computational cost [12-14]. The boundary conditions were identically specified to experimental conditions. The details of numerical method have been specified in our work [10].

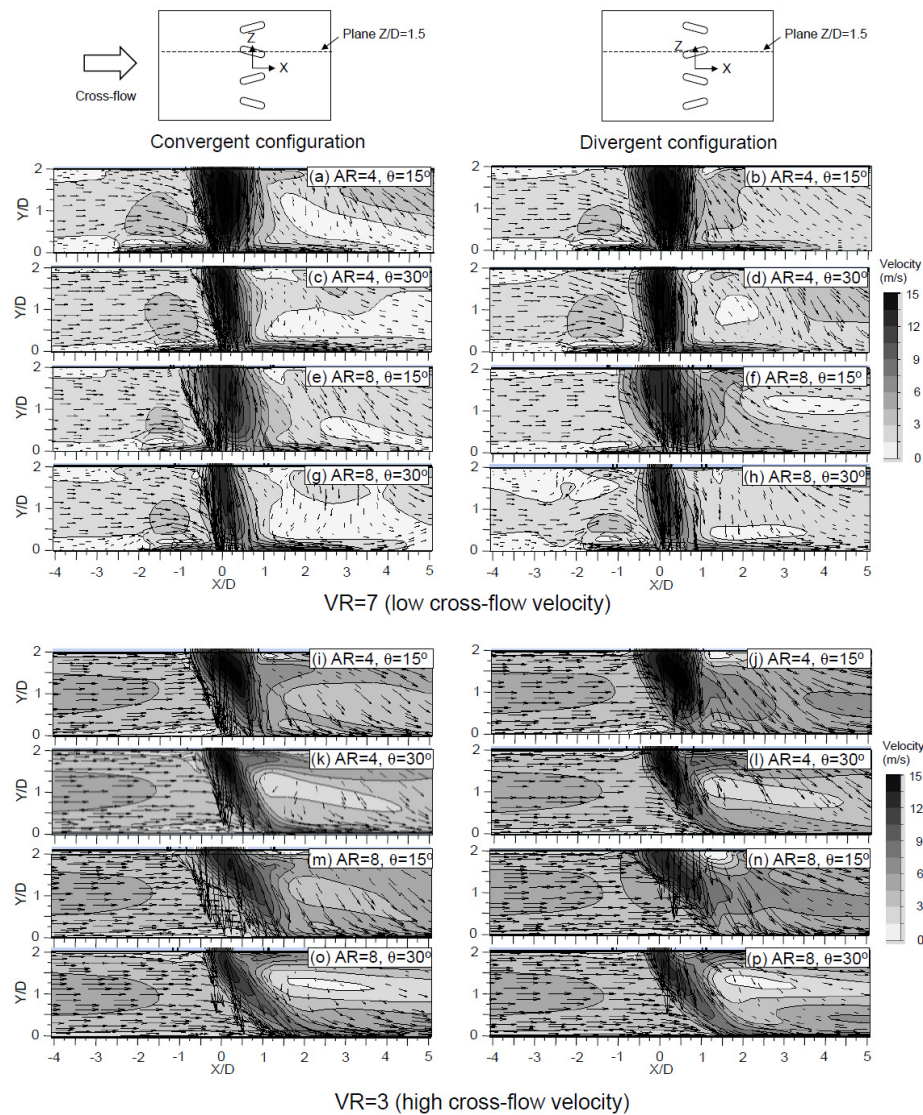


Fig. 2. Vectors and contours of velocity in X-Y plane at $Z/D=1.5$: left side for convergent orifice configuration and right side for divergent orifice configuration (CFD result).

4. Results and discussions

4.1 Flow characteristics of jets and cross-flow

Flow characteristics of the jet interacted with the cross-flow using CFD technique are shown in Fig.2-4. Velocity vectors and velocity contours in X-Y plane comparing

between convergent (left side) and divergent (right side) orifice configurations at $Z/D=1.5$ are shown in Fig.2. The flow characteristics of impinging jet is similar when compare between convergent (left side) and divergent (right side) orifice configurations. The deflections of jet in the case of $VR=3$ (lower

figure group) are greater than those $VR=7$ (upper figure group) due to higher cross-flow velocity. The deflections of jet with $AR=8$ for the case of $VR=3$ (Fig.2(m)-(p)) seem to be greater than those with $AR=4$ (Fig.2(i)-(l)) due to larger interaction area with the high cross-flow velocity.

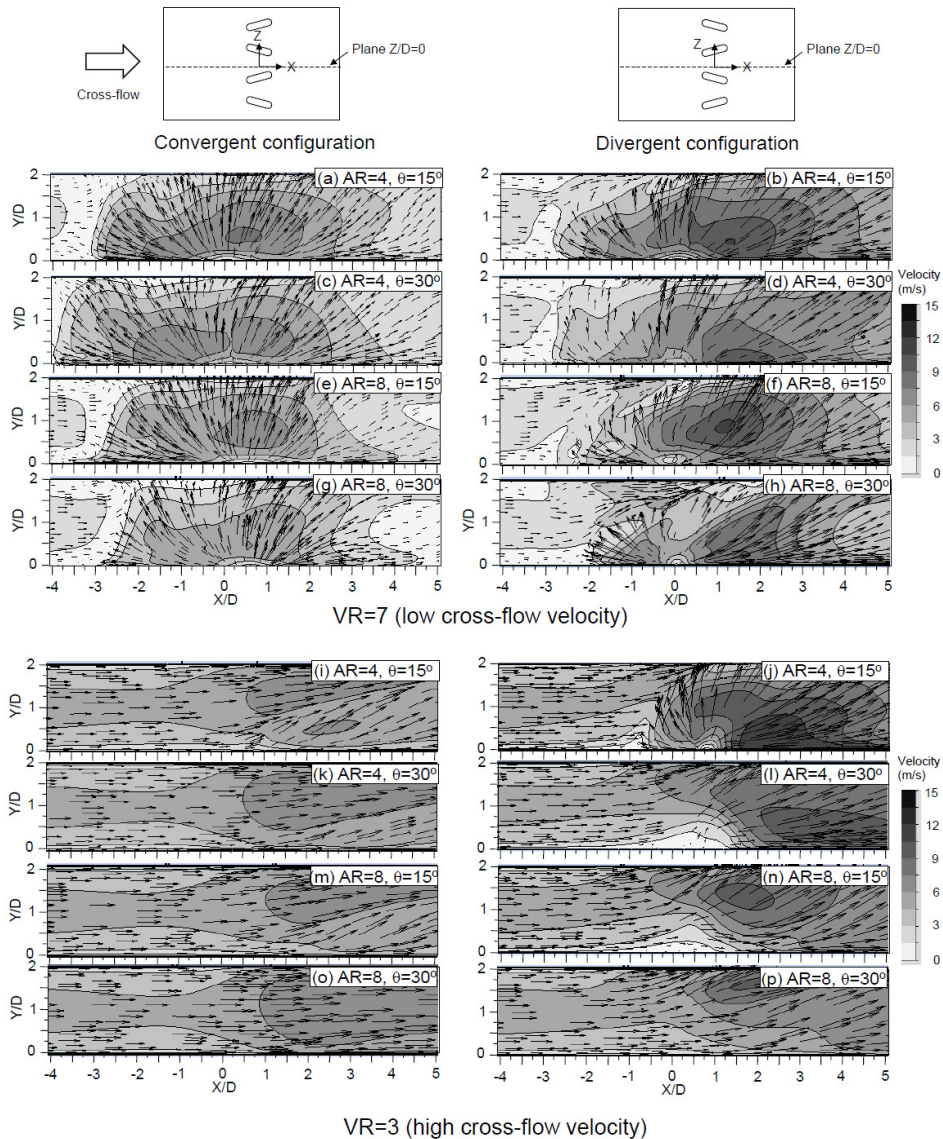


Fig. 3. Vectors and contours of velocity in X-Y plane at $Z/D=0$: left side for convergent orifice configuration and right side for divergent orifice configuration (CFD result).

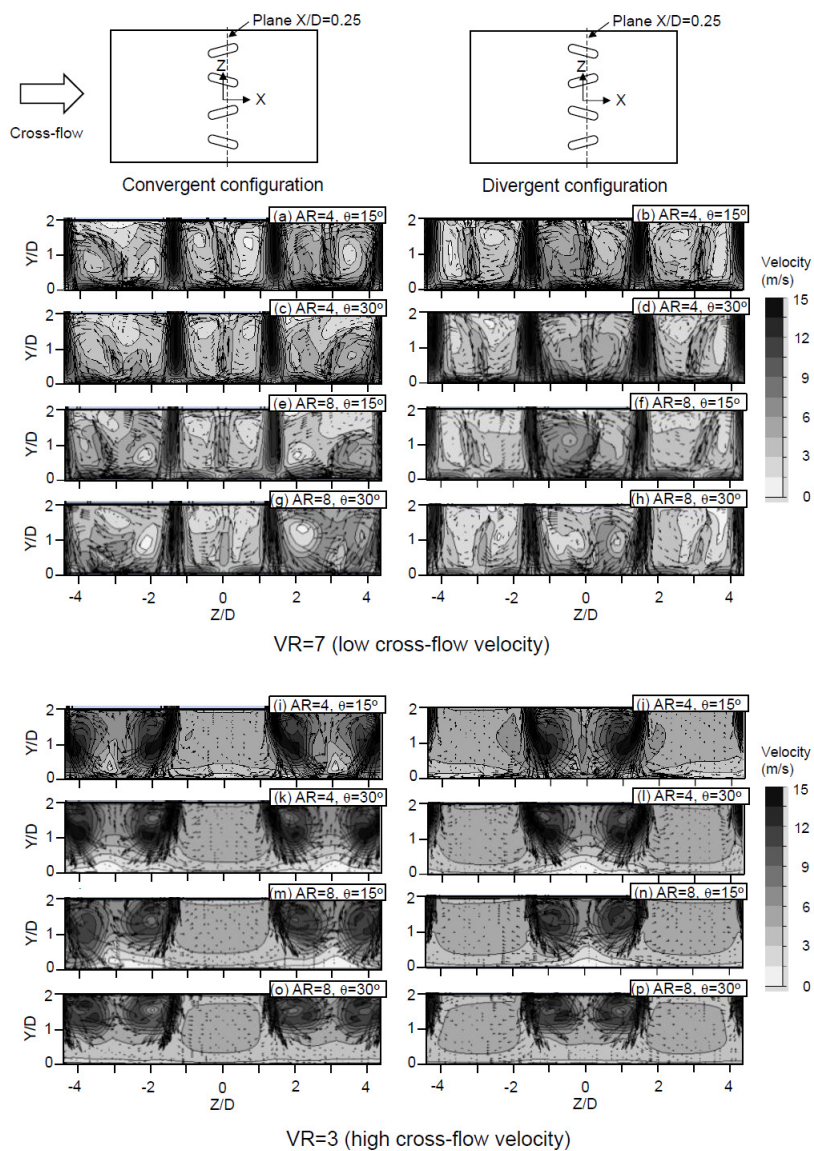


Fig. 4. Vectors and contours of velocity in Y-Z plane at $X/D=0.25$: left side for convergent orifice configuration and right side for divergent orifice configuration (CFD result).

Velocity vectors and velocity contours in X-Y plane comparing between convergent (left side) and divergent (right side) orifice configurations at $Z/D=0$ are shown in Fig.3. The effects of orifice configuration on flow characteristics of this jet interval plane seem to be greater than those the jet centerline plane. For the case of $VR=7$ (upper figure group), wall jets reflect from lower surface to

upper surface. This reflection of wall jets with divergent orifice configurations (right side) tends to downstream direction, and it is larger than those with convergent case (left side). For the case of $VR=3$ (lower figure group), the wall jets are rather completely blown by significant cross-flow except for the case of $AR=4$ at $\theta=15^\circ$ with divergent orifice configuration as shown in Fig.3(j).

When compare between two different orifice configurations (compare between left side and right side of figures), it is found that the wall jets with convergent orifice configurations (left side) are blown by the

cross-flow greater than those with divergent case (right side). This can be seen that the effect of orifice arrangement has significantly effect on flow thought jet interval

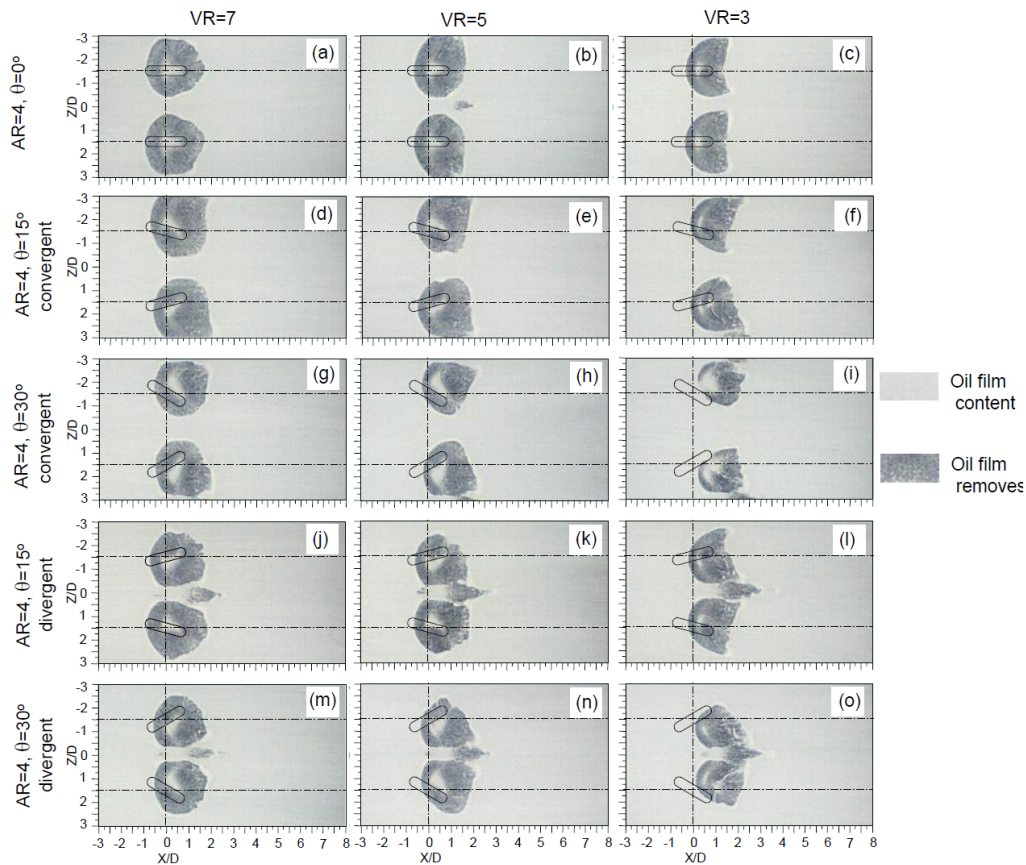


Fig. 5. Flow patterns on the impingement surface for $AR=4$ (Experimental result).

A comparison of flow characteristics in Y-Z plane at $X/D=0.25$ are shown Fig.4. For the case of low cross-flow velocity (upper group), the jets after impingement on the target surface reflect to the upper wall. The deflections of jet slightly tend to spanwise direction corresponding to the direction of attacking angle of orifice configurations. For the case of high cross-flow velocity (lower group), the deflections of jet are obviously expressed due to significant effect of cross-flow velocity. The deflections of both middle jets for convergent orifice configurations

(left side) prefer to both the side walls, and the ones with divergent orifice configurations (right side) prefer inversely to middle regions ($Z/D=0$). This corresponds to the direction of attacking angle between convergent and divergent orifice configurations. In addition, the deflection of jet with $AR=8$ (Fig.4(m)-(p)) seem to be larger than those with $AR=4$ (Fig.4(i)-(l)), and it becomes also larger when compare between the large attacking angle, $\theta=30^\circ$, to the small attacking angle, $\theta=15^\circ$ under the same AR conditions.

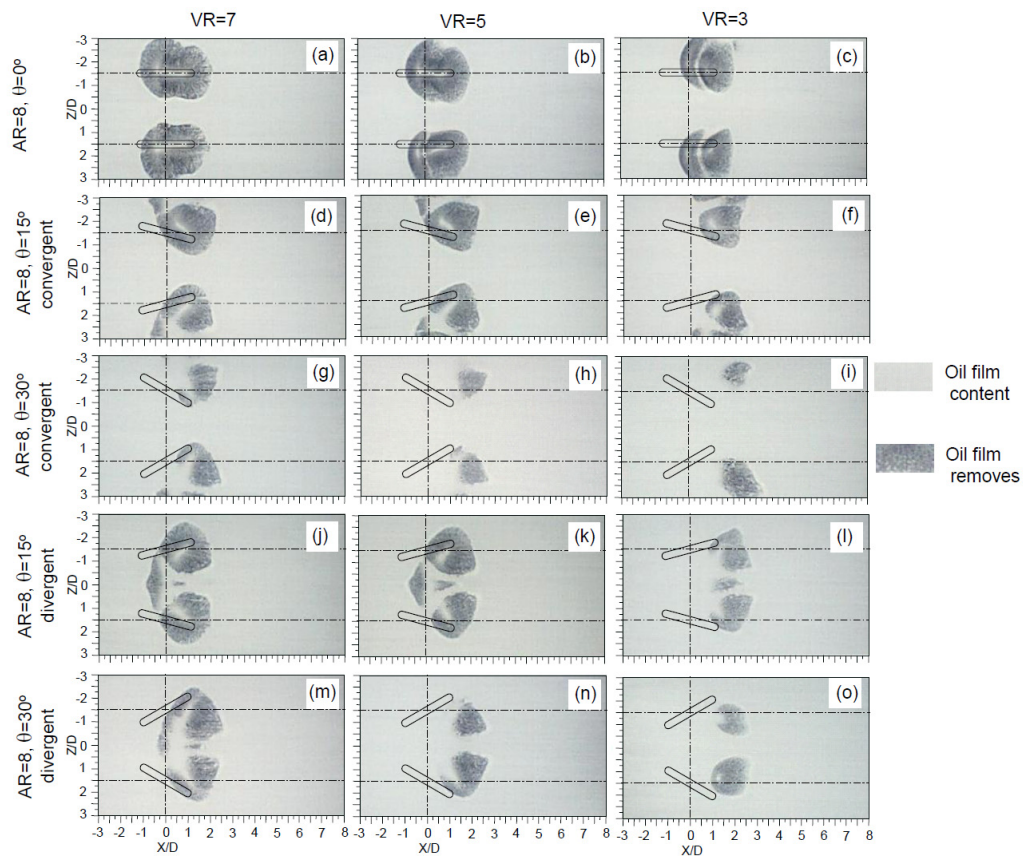


Fig. 6. Flow patterns on the impingement surface for $AR=8$ (Experimental result).

4.2 Flow characteristics above the impingement surface

Flow patterns of impinging jets on the impingement surface using the oil film technique are shown in Fig.5 and 6. The black and white regions represent the areas where the oil film is completely removed called impingement region and the area with original oil film coating, respectively.

The impingement regions are contracted in the upstream direction and extended in the downstream one when the cross-flow velocity increases. Characteristics of extension of impingement regions in the

downstream direction depend on cross-flow velocity and orifice configurations. In the case of $AR=4$ with divergent orifice configuration as shown in Fig.5(d)-(i), the impingement regions of jet located at $Z/D=-1.5$ are extended along $-Z$ axis, and the same way, the ones located at $Z/D=1.5$ are extended along $+Z$ axis. This flow characteristics are similar to the case of $AR=8$ as shown in Fig.6(d)-(i). Here, the areas of impingement regions for $AR=8$ at $\theta=30^\circ$ are smaller as shown in Fig.6(g)-(i) due to larger attacking area between the jet and the cross-flow.

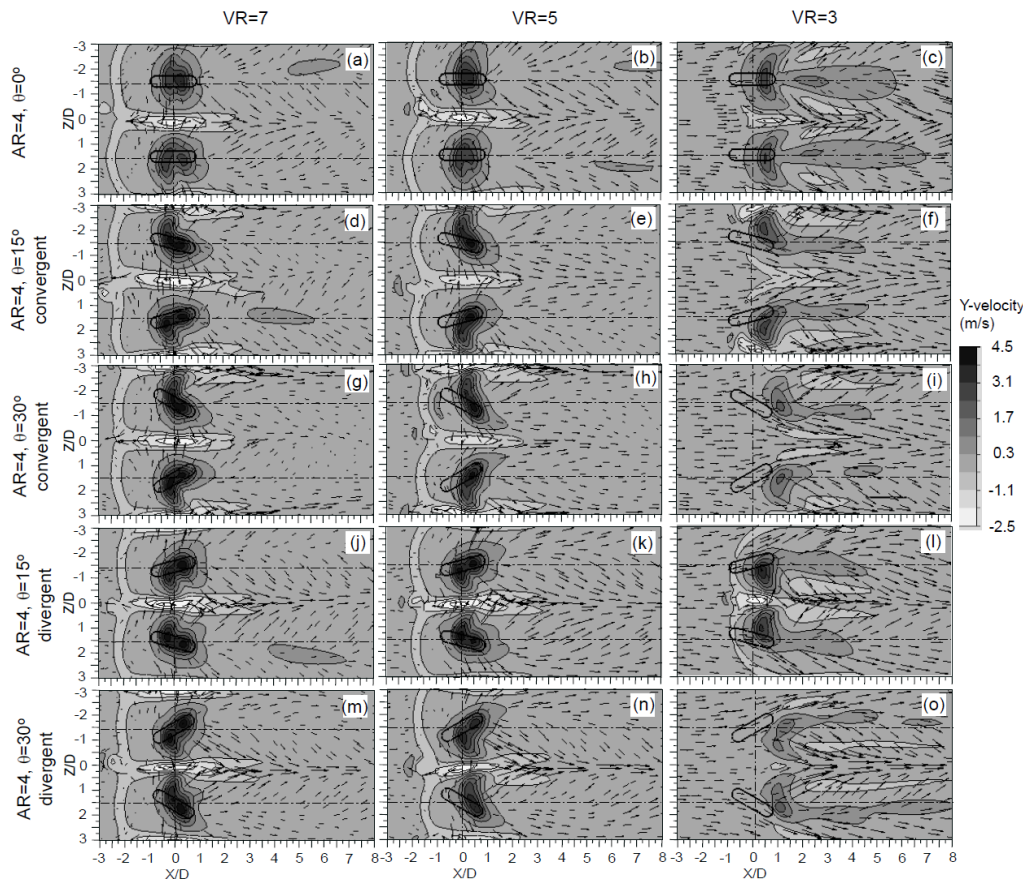


Fig. 7. Flow characteristics of impinging jets on X-Z plane at 1 mm above the impingement surface for $AR=4$ (CFD result).

For the case of divergent orifice configuration as shown in Fig.5(j)-(o) for $AR=4$ and Fig.6(j)-(o) for $AR=8$, the extension direction of impingement regions is inverse when compare with the case of convergent orifice configuration as shown previously in Fig.5(d)-(i) for $AR=4$ and Fig.6(d)-(i) for $AR=8$. This characteristics of flow pattern corresponds to CFD result as earlier shown in Fig.4.

Also in this divergent case as shown in Fig.5(j)-(o) for $AR=4$ and Fig.6(j)-(o), both locations of impingement regions on

individual surfaces are closer when the attacking angle is larger. In addition, the areas of removed oil film are appeared at orifice interval for some cases. This can be attributed that the flow in this region was accelerated to the cross-flow streamwise due to inclination interaction between adjacent wall jets along this orifice interval. These areas of removed oil film are not found to appear for the case of convergent orifice configuration and the case of without attacking angle, $\theta=0^\circ$.

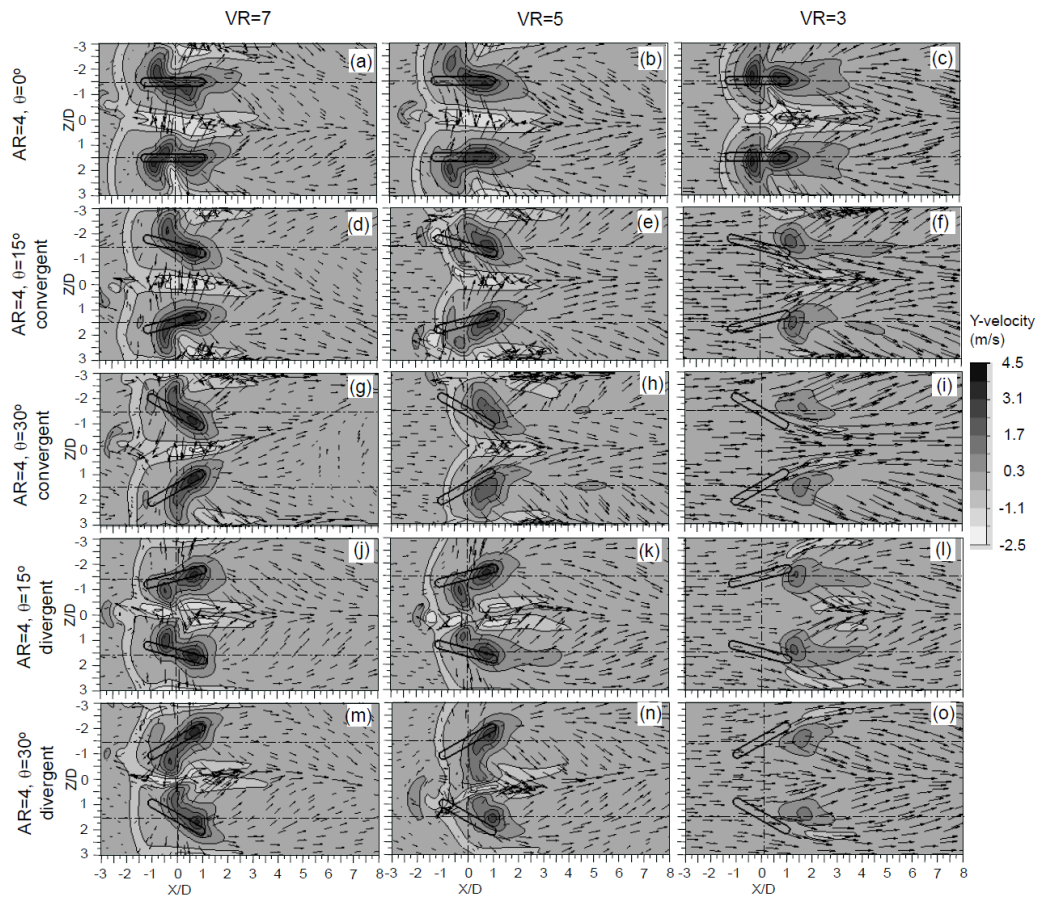


Fig. 8. Flow characteristics of impinging jets on X-Z plane at 1 mm above the impingement surface for $AR=8$ (CFD result).

The velocity vector and contour in the Y-axis on Z-X plane near the impingement surface (1 mm above the surface) from CFD results are shown in Fig.7 and 8. The Y-component velocity represents the velocity in the direction normal to the impingement surface. The positive direction is towards the downstream of the jet that impinges on the wall. Area of high Y-component velocity contour indicates the impingement region. These velocity contours agree very well with the flow patterns on the impingement surface as shown previously in Fig.5 and 6. With the good agreement, clarification of heat transfer behavior in the next section can refer to the flow characteristics from CFD results [10].

4.3 Local Nusselt number on the impinged surface

Nusselt number distributions on impingement surface from experiment are shown in Fig.9 and 10. These contours of Nusselt number correspond to the oil film patterns on the impingement surface in Fig.5 and 6 as well as the contours of Y-component velocity near the impingement surface in Fig.7 and 8. Areas of high Nusselt number, indicated the impingement region, are shifted to downstream direction due to effect of high cross-flow velocity and large attacking angle [10].

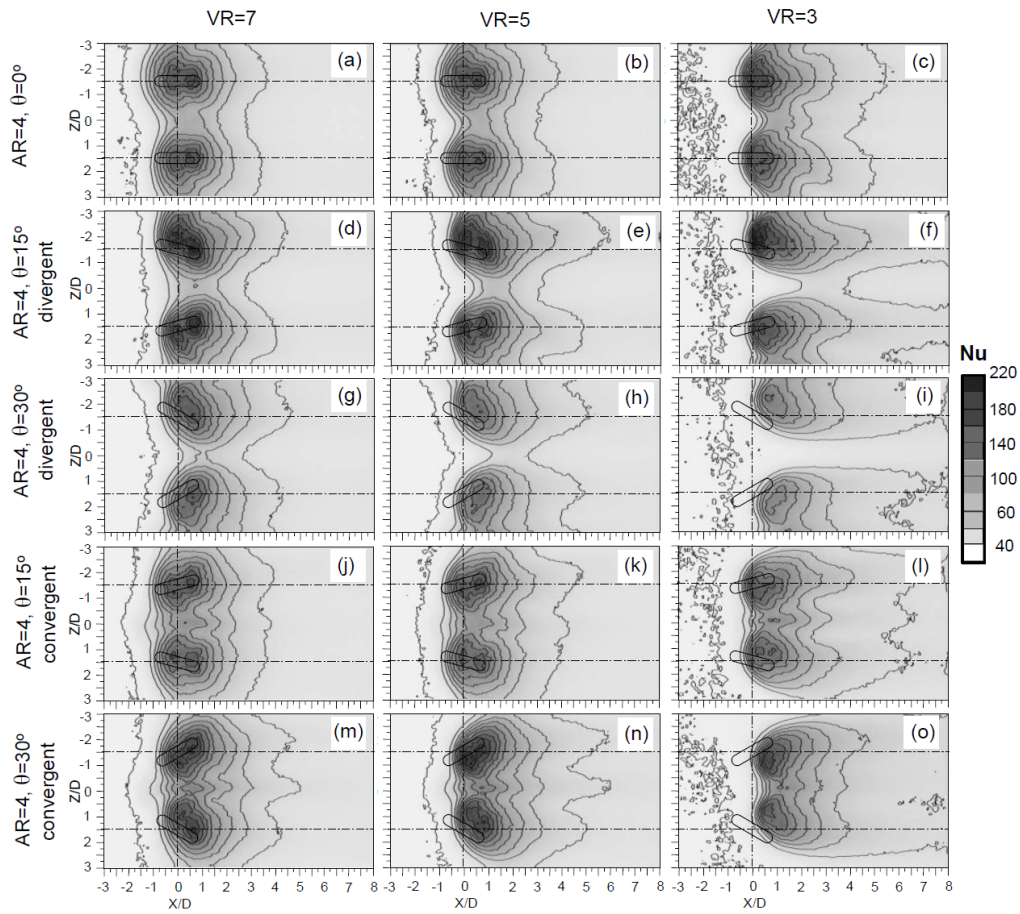


Fig. 9. Nusselt number distributions on the impingement surface for $AR=4$ (Experimental result, $T_j=27^\circ\text{C}$).

For the case of $AR=4$ with divergent orifice configurations as shown in Fig.9(d)-(i), the areas of high Nusselt number are extended along both lateral directions, $+Z$ and $-Z$ axes. The positions of high value areas are more separated when the cross-flow velocity increases and the attacking angle is larger. With the higher cross-flow velocity and the larger attacking angle, the low value areas are clearly seen along this orifice interval, especially for the case of $VR=3$ and $\theta=30^\circ$ as shown in Fig.9(i). This apparent low value area along this orifice interval is seen to be larger when the orifice aspect ratio becomes $AR=8$ as shown in Fig.10(i).

For the case of divergent orifice configuration as shown in Fig.9(j)-(o) for $AR=4$ and Fig.10(j)-(o) for $AR=8$, the characteristics of Nusselt number distributions are apparently different with those the convergent orifice configurations earlier shown in Fig.9(d)-(i) for $AR=4$ and Fig.10(d)-(i) for $AR=8$. The areas of high Nusselt number of divergent orifice configuration are combined together. Its locations of both peak areas are closer when the cross-flow velocity increases and the attacking angle becomes larger. In addition, Nusselt number are enhanced along orifice interval for this divergent case. This location of enhancing Nusselt number corresponds to

those flow pattern on impinged surface with removed oil film as discussed previously.

Nusselt number distributions along downstream direction at orifice centerline ($Z/D=1.5$) for $AR=4$ and 8 are shown in Fig.11 and 12, respectively. The Nusselt number distributions in upstream direction ($-X$ axis) become lower corresponding to the increasing attacking angle. The Nusselt number distributions, however, are comparable in downstream direction at $X/D>2$. The contraction of high value area in

this upstream direction corresponds well with the contraction of impingement regions of oil film technique and areas of high Y -component velocity in CFD result.

In the case of $AR=4$, the Nusselt number peak of each attacking angle are comparable for $VR=7$ (Fig.11(a) and (b)), and it seem to be different for $VR=3$ (Fig.11(e) and (f)). For the case of $AR=8$ as shown in Fig.12, this peak values of each attacking angle are quite different with getting lower when the attacking angle is larger for all VR .

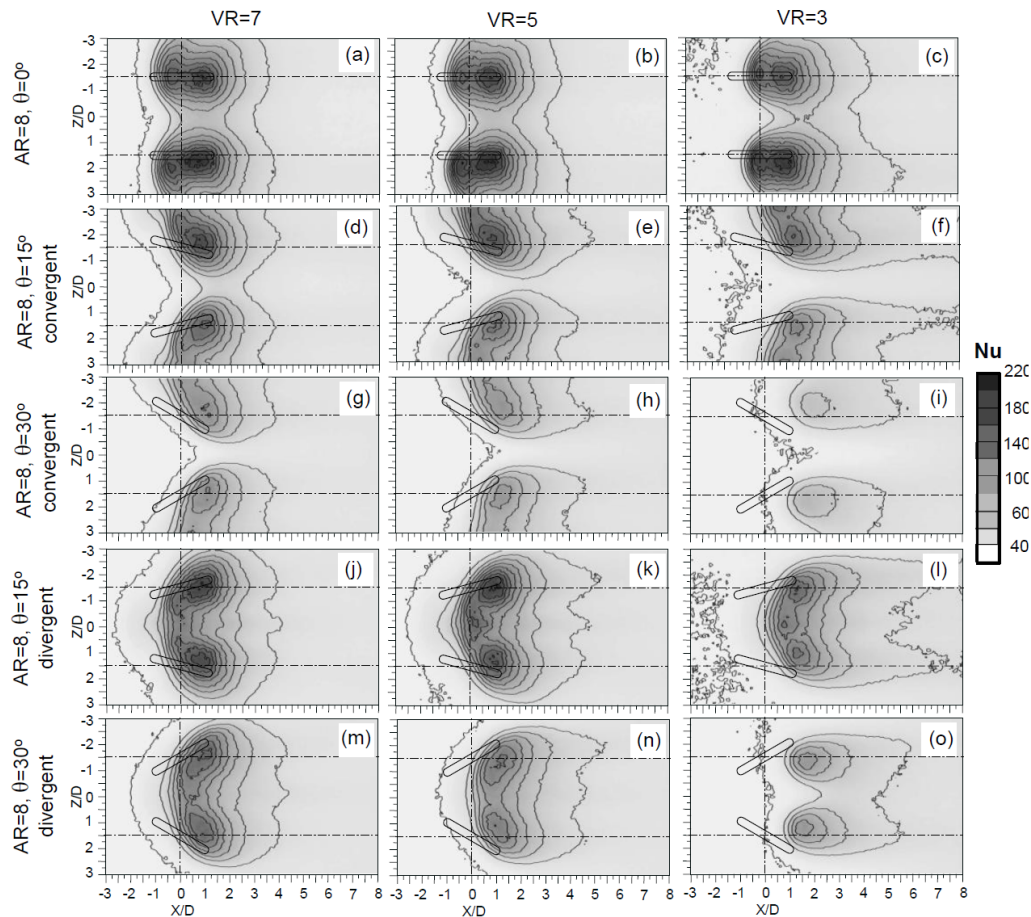


Fig. 10. Nusselt number distributions on the impingement surface for $AR=8$ (Experimental result, $T_j=27$ °C).

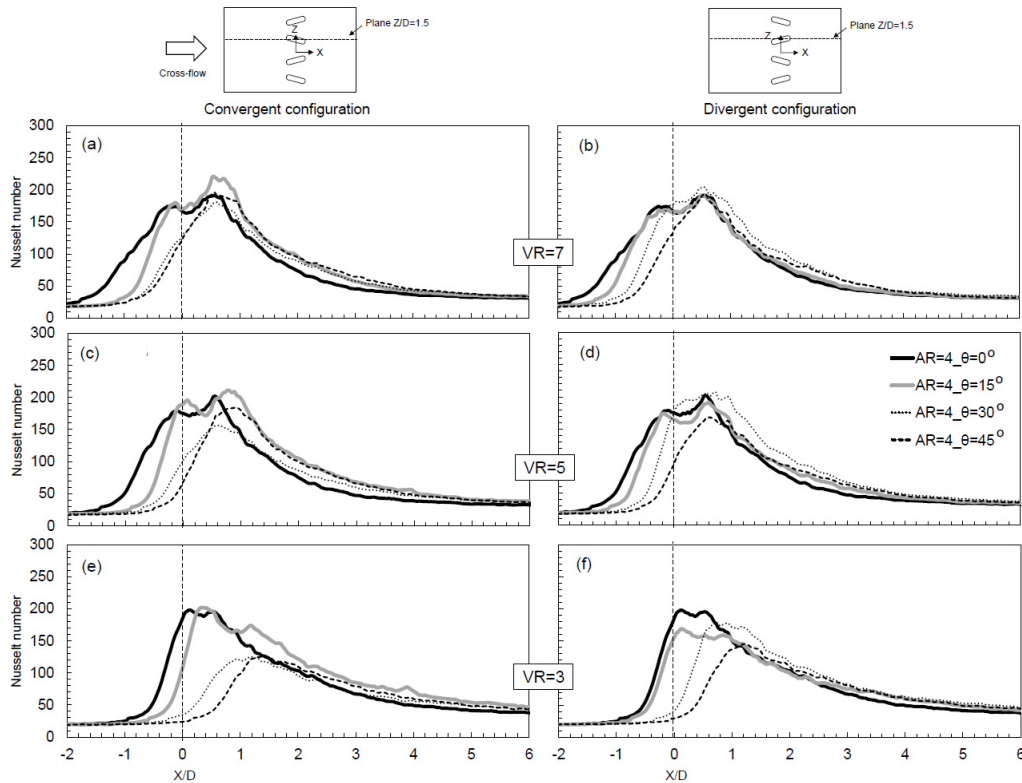


Fig. 11. Nusselt number distribution along downstream direction at $Z/D=1.5$ (Orifice centerline) for $AR=4$: left side for convergent orifice configuration and right side for divergent orifice configuration (Experimental result).

Nusselt number distributions along downstream direction at orifice interval ($Z/D=0$) for $AR=4$ and 8 are shown in Fig.13 and 14, respectively. The effect of orifice arrangement seem to be quite different for this section (compare between left and right figures). The Nusselt number for divergent orifice configuration (right side) is higher than those convergent case (left side). The prominent high values for the case of $AR=8$ at $\theta=15^\circ$ with divergent orifice configuration for $VR=7$ and 5 as shown in Fig.14(f) and (d) correspond to the large area of removed oil film at jet interval as earlier shown in Fig.6(j) and (k).

4.4 Average Nusselt number

The average Nusselt number on the impingement surface calculated from the average local wall temperature in area of $-3 < X/D < 8$ and $-3 < Z/D < 3$ versus the attacking angle are shown in Fig.15. Almost all average values for $AR=4$ is higher than those the case of $AR=8$. For the case of high cross-flow velocity, $VR=3$, the average Nusselt number is decreased when the attacking angle increases. This average values of $AR=4$ with divergent orifice configuration for $VR=5$ and 7 are slightly increased when attacking angle increases from $\theta=15^\circ$ to $\theta=30^\circ$. For the other cases, the average values are decreased when attacking angle increase.

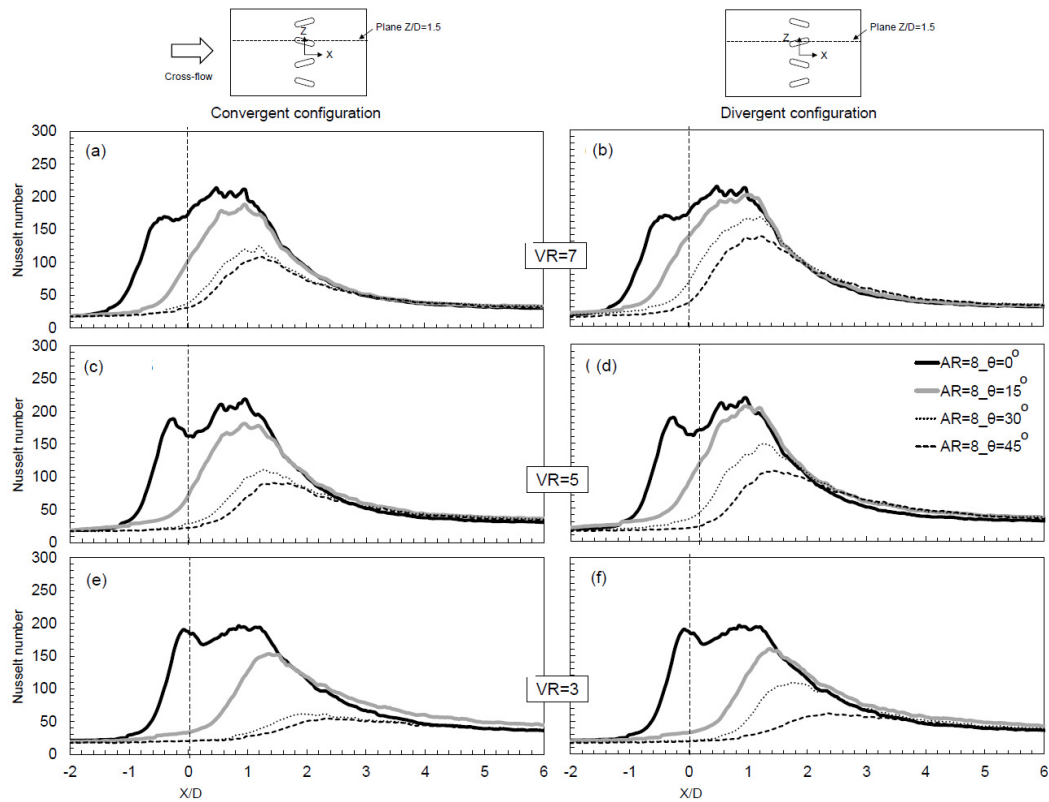


Fig. 12. Nusselt number distribution along downstream direction at $Z/D=1.5$ (Orifice centerline) for $AR=8$: left side for convergent orifice configuration and right side for divergent orifice configuration (Experimental result).

When compare the effect of orifice configurations, almost all average values of divergent orifice configuration is higher than those convergent case. This can be noted that the higher heat transfer for the case of divergent orifice configuration is from enhancement local heat transfer along orifice interval due to inclination interaction of both adjacent wall jets.

5. Conclusions

The effect of orifice arrangements with convergent and divergent configurations on flow and heat transfer characteristics of jet impingement row discharging through elongated orifice with different attacking angle was experimentally and numerically

studied. The main results with varied cross-flow velocity can be summarized as follows;

1. The impingement regions corresponding to high heat transfer areas are separated together for the case of convergent orifice configuration. The distance of separation of these impingement regions (or high heat transfer areas) is larger when cross-flow velocity increases and attacking angle becomes lareger. This is contrast to the case of divergent orifice configuration that the impingement regions (or high heat transfer areas) are combined together. The distance of combination of impingement regions is closer when cross-flow velocity increase and attacking angle becomes lareger.

2. Almost all impingement regions of $AR=4$ are larger than those $AR=8$, and

almost all heat transfer rate of $AR=4$ is also higher than those $AR=8$.

3. Heat transfer enhances prominently along orifice interval for the case of divergent orifice configuration, especially, for the case of $AR=8$ at $\theta=15^\circ$ with low and moderate cross-flow velocity. The locations of this enhancement heat transfer correspond to the removed areas of oil film.

Acknowledgments

This research was supported by grants from Thailand Energy Policy and Planning Office, Ministry of Energy, the Graduate School and Faculty of Engineering, Prince of Songkla University.

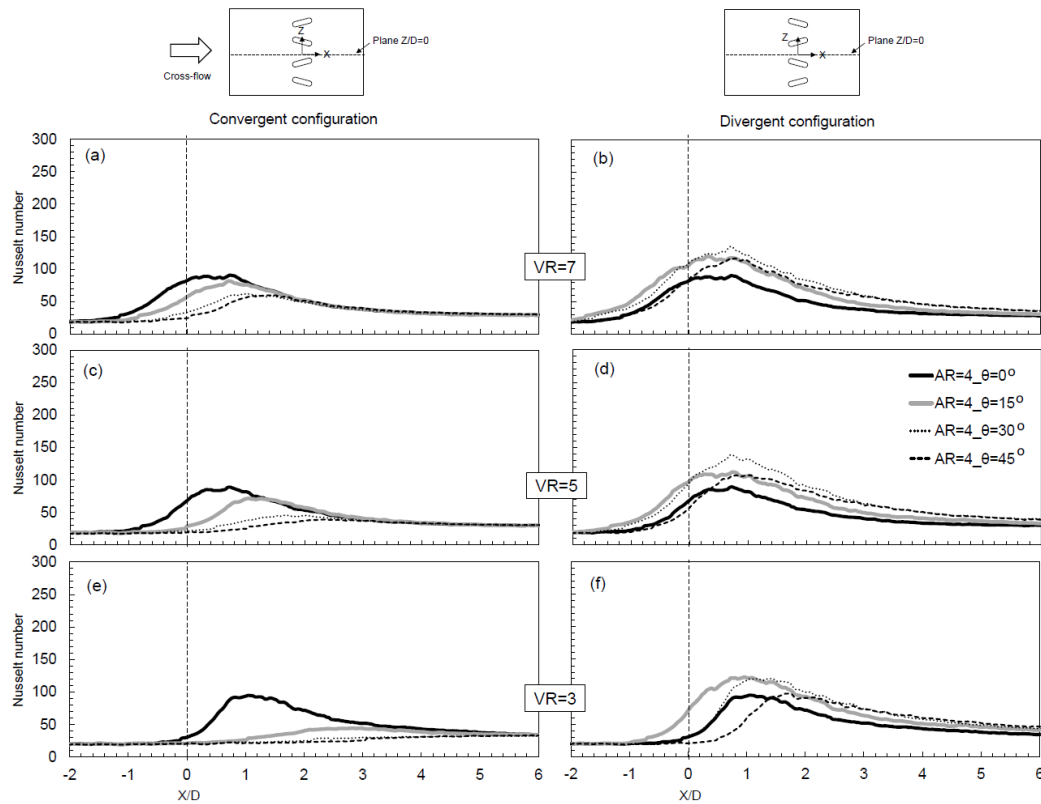


Fig. 13. Nusselt number distribution along downstream direction at $Z/D=0$ (Jet interval) for $AR=4$: left side for convergent orifice configuration and right side for divergent orifice configuration (Experimental result).

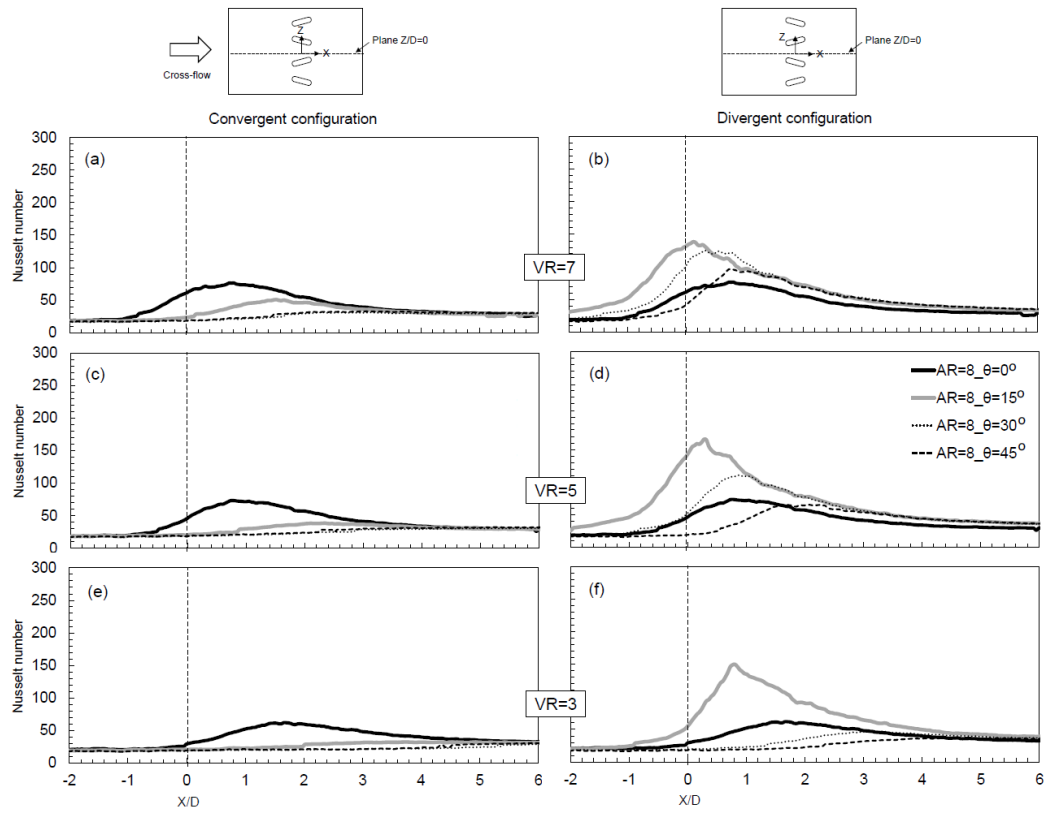


Fig. 14. Nusselt number distribution along downstream direction at $Z/D=0$ (Jet interval) for $AR=8$: left side for convergent orifice configuration and right side for divergent orifice configuration (Experimental result).

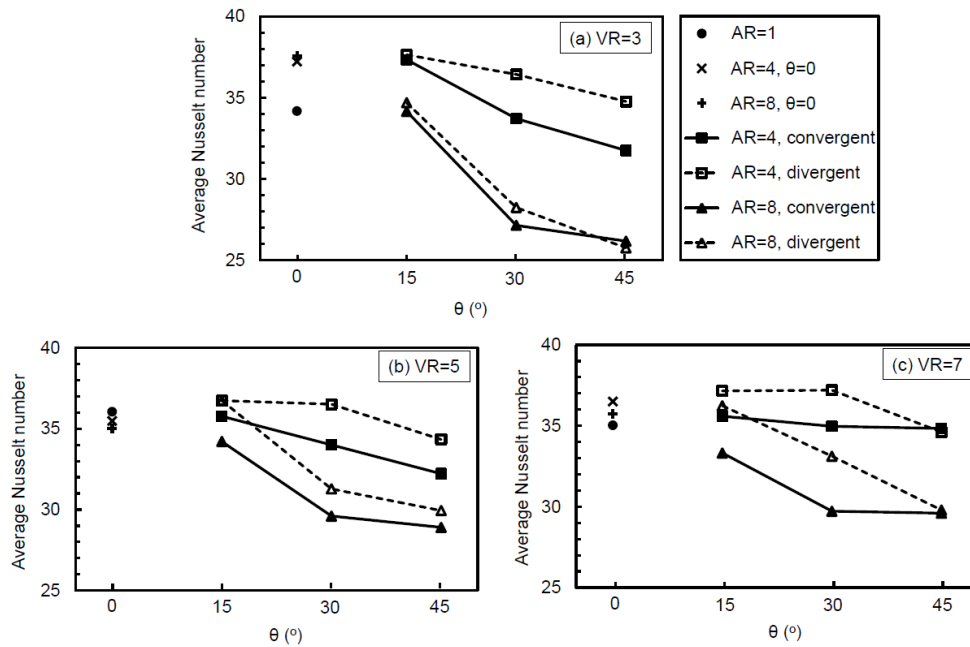


Fig. 15. Average Nusselt number versus attacking angle (Experimental result).

References

- [1] R. Viskanta, Heat transfer to impinging isothermal gas and flame jets, *Exp. Therm. Fluid Sci.* 6 (1993) 111-134.
- [2] L.-E. Brizzi, A. Bernard, J.-L. Bousgarbies, E. Dorignac, J.-J. Vullierme, Study of several impinging jets, *J. Thermal Science* 9 (2000) 217-223.
- [3] B.P.E. Dano, J.A. Liburdy, Structure detection and analysis of non-circular impinging jets in a semi-confined array configuration, *Exp. Therm. Fluid Sci.* 31 (2007) 991-1003.
- [4] L.W. Florschuetz, C.R. Truman, D.E. Metzger, Streamwise flow and heat transfer distributions for jet array impingement with crossflow, *J. Heat Transfer-Trans. ASME.* 103 (1981) 337-342.
- [5] V. Katti, S.V. Prabhu, Influence of spanwise pitch local heat transfer distribution for in-line arrays of circular jets with air flow in two opposite, *Exp. Therm. Fluid Sci.* 14 (2008) 84-95.
- [6] D.-H. Rhee, P.-H. Yoon, H.H. Cho, Local heat/mass transfer and flow characteristics of array impinging jets with effusion holes ejecting spent air, *Int. J. Heat Mass Transfer* 46 (2003) 1049-1061.
- [7] T.B. Hoberg, A.J. Onstad, J.K. Eaton, Heat transfer measurements for jet impingement arrays with local extraction, *Int. J. Heat Fluid Flow* 31 (2010) 406-467.
- [8] H.-C. Chiu, J.-H. Jang, W.-M. Yan, Experimental study on the heat transfer under impinging elliptic jet array along a film hole surface using liquid crystal thermograph, *Int. J. Heat Mass Transfer* 52 (2009) 4435-4448.
- [9] C. Nuntadusit, M. Wae-hayee, P. Tekasakul, S. Eiamsa-ard, Local heat transfer characteristics of array impinging jets from elongated orifices, *Int. Commun. Heat Mass Transfer* 39 (2012) 1154-1164.
- [10] M. Wae-hayee, P. Tekasakul, C. Nuntadusit, Heat transfer enhancement on a surface of a jet impingement row by elongated orifices under cross-flow, Part 1: Parallel jet arrangement.
- [11] M. Wae-hayee, P. Tekasakul, C. Nuntadusit, Influence of nozzle arrangement on flow and heat transfer characteristics of arrays of circular impinging jets, *Songklanakarin J. Sci. Technol.* xx (2013) xxx-xxx.
- [12] M.-W. Heo, K.-D. Lee, K.-Y. Kim, Optimization of an inclined elliptic impinging jet with cross flow for enhancing heat transfer, *Heat Mass Transfer* 47 (2011) 731-742.
- [13] N. Zuckerman, N. Lion, Jet impingement heat transfer: physics, correlations, Numerical modeling, *Advances Heat Transfer* 39 (2006) 565-631.
- [14] T.T. Chandratilleke, D. Jagannatha, R. Narayanaswamy, , Heat transfer enhancement in microchannels with cross-flow synthetic jets, *Int. J. Therm. Sci.* 49 (2010) 504-513.

Appendix C

The publications of array of impinging jets

Appendix C1

Conference Paper

M. Wae-hayee, C. Nuntadusit, and P. Tekasakul “Heat transfer enhancement on a surface under arrays of impinging jets: effect of jet flow arrangement”, The 5th PSU-UNS International Conference on Engineering and Technology (ICET-2011), Phuket, May 2-3,



HEAT TRANSFER ENHANCEMENT ON A SURFACE UNDER ARRAYS OF IMPINGING JETS: EFFECT OF JET FLOW ARRANGEMENT

M. Wae-hayee¹, C. Nuntadusit^{1*}, P. Tekasakul¹

1. Department of Mechanical Engineering, Faculty of Engineering,
 Prince of Songkla University, Hatyai, Songkhla, Thailand

*Authors to correspondence should be addressed via email: chayut@me.psu.ac.th

Abstract: In this article, the effect of jet arrangement on flow and heat transfer patterns on a surface under multiple impinging jets were studied. An array of impinging jets with in-line and staggered arrangement were considered. The effect of crossflow exit orientations; a single and a double outlet were also investigated. The temperature distribution on an impinging surface was visualized by using thermochromic liquid crystal sheet (TLCs) and Nusselt number distribution was evaluated by using image processing method. The flow characteristic on the impinging surface was visualized by using oil film technique. The results show that an interaction between jet and crossflow can increase heat transfer at stagnation region with appropriated velocity ratios between jet velocity and crossflow velocity. The heat transfer rate of in-line arrangement was higher than the staggered arrangement 3.7 % for the single outlet and 25.7 % for double outlet.

Key Words: Array of impinging jets, Jet arrangement, Heat transfer enhancement, Liquid crystal sheet

1. INTRODUCTION

Impinging jets are widely used in many industries which required high heat transfer rate on surface like cooling of gas turbine blade, electronic device, combustion wall and compact high efficient heat exchanger. However, the heat transfer rate is high only in jet directly impinging region. When the high and uniform heat transfer distribution is required over a wide area for example: drying of film sheet, heating of steel sheet, multiple of impinging jets is usually used instead. An accumulated spent jet flow in a confined channel can be produced a crossflow. The crossflow is defined as the fluid flow in the direction perpendicular to the impingement flow [1].

Brizzi et al [2] illustrated the flow and temperature patterns on the impinged surface of array of jets with an

in-line arrangement. The results of the flow pattern corresponded to the temperature pattern. Katti and Prabhu [1] studied the heat transfer rate of in-line arrangement of the array jet. The results showed the jet-to-jet distance at 4D better than 2D and 6D (D is nozzle diameter) and jet-to-plate distance at 1D and 2D have higher heat transfer rate.

Previous studies have been investigated on impingement heat transfer with the crossflow. They found the crossflow significantly reduced the heat transfer on impingement surface [3, 4 and 5]. In this research, the effect of both the in-line and staggered arrangement and the outlet orientation of spent air were studied. The investigations carried out of the array of jet impingement with jet-to-plate spacing for two times of jet diameter. The characteristics of local heat transfer and flow visualization on the impinged surface were investigated.

2. EXPERIMENTAL MODEL AND PARAMETERS

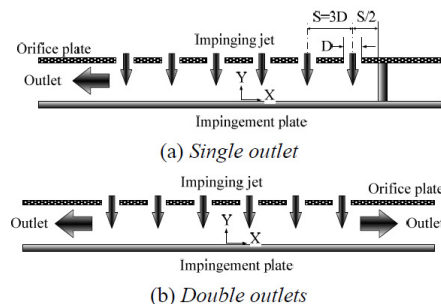


Fig. 1. Sketch of the confined channel with different crossflow exit orientations

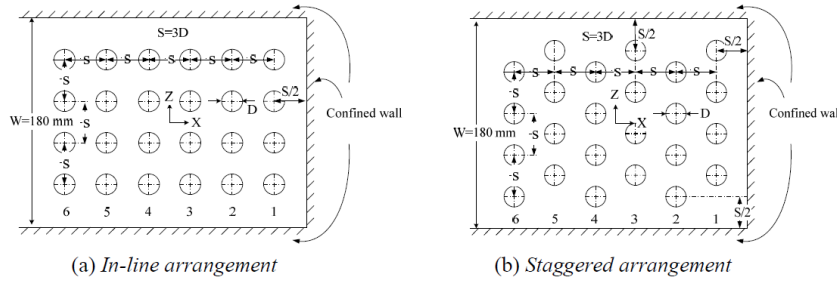


Fig. 2. Experimental model of jet arrangement (Number 1to 6 represente the number of column)

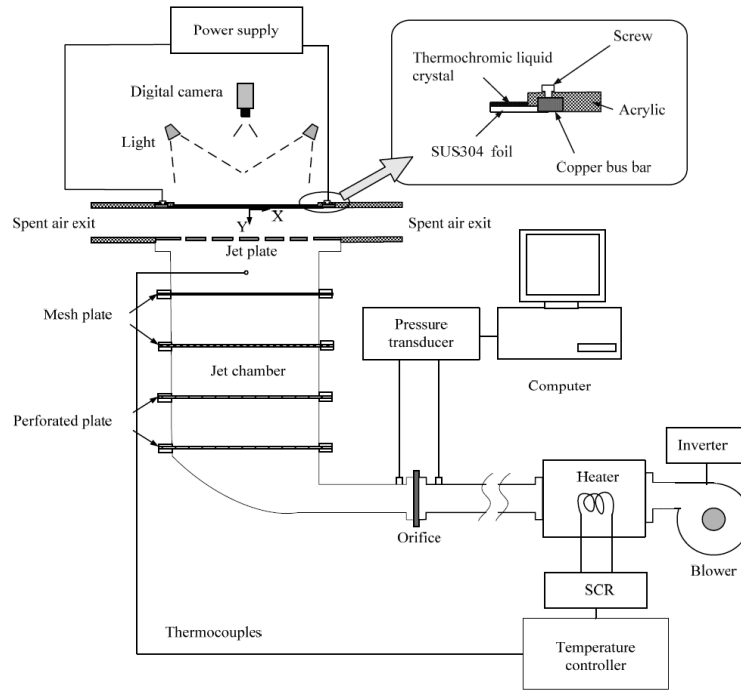


Fig. 3. Schematic view of the experimental setup

The model in this experiment, the jets were discharged from array of circular orifices and then impinged normal to heated surface on opposite surface of rectangular duct. Fig.1 presents the sketch of two different exit orientations; the first is the single outlet (Fig.1 (a)) and the second is the double outlets (Fig.1 (b)). For the single outlet, the spent air was allowed to flow out from the test section with only one direction. For double outlets, the spent air allowed to flow out from the test section with opposite direction. An origin of the Cartesian coordinates was located at the impinged surface as shows in Fig.1. The X, Y and Z-axis are the streamwise, normal to the impinged surface and spanwise direction of duct, respectively.

Fig.2 illustrates the array of jet arrangement are the in-line and staggered arrangement and both arrangement are same number of 6x4 jet holes. A diameter of nozzle was $D=13.2$ mm. The jet-to-jet distance was fixed at

$S=3D$ and jet-to-plate distance was fixed at $H=2D$. All experiments were carried out at constant Reynolds number $Re=12,700$. In case of the staggered arrangement as shows in Fig. 2 (b), the confined wall of the lateral side was given jet-to-wall distance for $S/2$ ($=1.5D$) and this confined wall was given with same dimension for in case of the in-line arrangement as shows in Fig. 2 (a).

3. EXPERIMENTAL SETUP AND METHOD

3.1. Experimental setup

Fig.3 shows schematic view of the experimental apparatus. The blower (3HP) is used for generated the air jet. The air flows through a temperature controlled chamber and towards the orifice flow meter. The air subsequently passes through a jet chamber with constant cross-section 360-mm-wide, 360-mm-long and 850-mm-high. The jet chamber was equipped with two of

perforated plates and two of mesh plates to ensure that uniform flow approached to the nozzle plate. For all experimental conditions, the jet flow was controlled with constant flow rate at $Re = V_j D / \nu = 12,700$ and at constant temperature $T_j = 27^\circ\text{C}$. The test section was mounted upon the jet chamber. In case of single outlet, the test section was mounted by wall with space $1.5D$ ($S/2$) from the column 1 as shows in Fig. 1 (a).

3.2. Heat transfer measurement

Fig. 3 shows the detail of test section for heat transfer measurement. The air with constant temperature was discharged from an orifice plate and impinged upon the heat transfer surface. The heat transfer surface was made of stainless steel foil ($30\text{-}\mu\text{m}$ -thicknesses) which attached with TLC sheet on the rear side of jet impinged surface. The stainless steel foil was stretched between couple of copper bus bars. The heat transfer surface was heated by DC power supply that can supply current up to 40A passes through copper bus bars. An amount of electrical energy is dissipated in the stainless steel foil and it can be calculated from equation

$$\dot{Q}_{input} = I^2 \cdot R \quad (1)$$

where here, I is the electrical current and R is the electric resistance of stainless steel foil.

Then, the heated impinged surface was cooled by impinging jets. Hence, the local values of heat transfer coefficient (h) by force convection of jets can be evaluated from equation

$$h = \frac{\dot{Q}_{input} - \dot{Q}_{losses}}{A(T_w - T_j)} = \frac{\dot{q}_{input} - \dot{q}_r - \dot{q}_c}{T_w - T_j} \quad (2)$$

where $\dot{q}_r = \sigma \varepsilon_{TLC} (T_w - T_s)$ and $\dot{q}_c = h_c (T_w - T_s)$ are the heat loss transferred to the environment by radiation and convection, respectively. The T_w and T_j are the wall and jet temperature, the σ is a Stefan-Boltzman constant, the ε_{TLC} is a emissive coefficient of the black background paint and the TLCs that has been given in [6], T_s is a surrounding temperature and h_c is a natural heat transfer coefficient that was calculated from natural convective heat transfer from the horizontal plate orientation to the surrounding.

The wall temperature (T_w) on the impinged surface was measured by using TLC sheet that attached on the rear side of jet impinged surface. The CCD camera was used to capture colour on TLC sheet. The images of colour pattern on TLC were converted from the RGB (Red, Green and Blue) colour system to the HSI (Hue, Saturation and Intensity) colour system. The Hue (H) value provides a convenient way to correlate the colour of TLC to their temperature in range of $28\text{-}40^\circ\text{C}$. The TLCs was calibrated with same location on the test section to keep all external factors constant. The local Nusselt number was calculated from

$$Nu = \frac{hD}{k} \quad (3)$$

where D is the diameter of orifice and k is a conductivity of air jet. An average Nusselt number was calculated from

$$\overline{Nu} = \frac{\overline{h}D}{k} \quad (4)$$

where here, the average heat transfer coefficient \overline{h} was calculated from Eq.(2) by replacing T_w to $\overline{T_w}$ that is a averaged temperature on the impinged surface.

3.3. Flow visualization on the impinged surface

The flow visualization on the impinged surface was illustrated by using oil film technique. The oil film was mixed by liquid paraffin, titanium dioxide and oleic acid. A transparent plastic plate was coated by oil film and it was replaced to the impinged surface. The CCD camera was captured the oil film flow on the impinged surface at each different time (30 second/frame).

4. RESULTS AND DISCUSSION

4.1 Flow patterns on an impinged surface

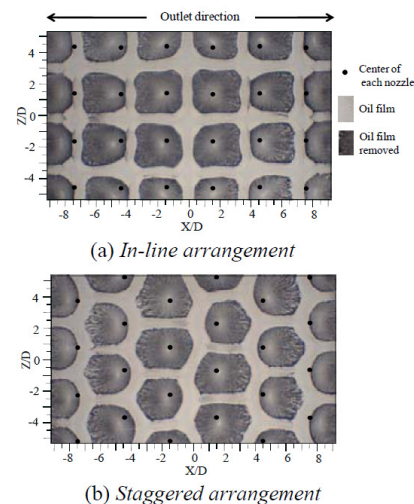


Fig. 4. Flow patterns on the impinged surface in case of double outlet ($Re=12,700$, After jet impinged 1200 second)

Fig. 4 and 5 show the flow visualization on the impinged surface by using oil film technique. The black area and white area represent an oil film completely removed wall region and area of oil film, respectively. The impingement area has a high shear stress on the surface, this effect on the oil film removed from this area. A white point in the middle of black area represents the stagnation point of jet and the black dots are the location of center of each orifice nozzle.

Fig. 4 shows the flow patterns on the impinged surface in case of the double outlet. The flow patterns of both different arrangement illustrate deflection of jet toward the crossflow direction. Deformation of impinged area depend on the location of orifice and jet arrangement.

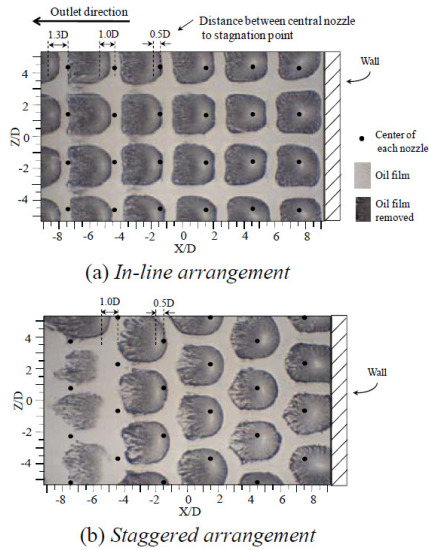


Fig. 5. Flow patterns on the impinged surface in case of single outlet ($Re=12,700$, After jet impinged 1200 second)

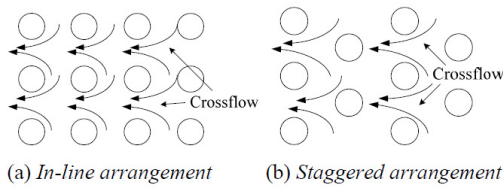


Fig. 6. Illustrate the crossflow passes through the array of jets with different nozzle arrangement

Fig. 5 shows the effect of nozzle arrangement on flow characteristics on the impinged surface in case of the single outlet. The flow pattern in case of in-line arrangement, the stagnation point (Small white point) of jet column 4-6 were shifted to the direction of crossflow. The distance between center of nozzle and stagnation point increased with increasing the number of column. For the column 4, 5 and 6, the shifted distance between center of nozzle to the stagnation point are $0.5D$, $1.0D$ and $1.3D$, respectively as shows in Fig. 5 (a). This deflection of jet can be illustreted the effect of crossflow on the jet flow, especially, the jet which located at last column (Column 6) near the outlet. The stagnation region was shifted far away from the center of jet. Moreover, the jets which located at last column (Column 6) in case of staggered arrangement (Fig.5 (b)), the stagnation region was located at over considered area (disappear on the considered area). The different characteristics of crossflow passes through the jets flow of the in-line and staggered arrangement were illustrate in Fig.6.

4.2 The detail of Nusselt number on the impinged surface

Fig. 7 and 8 show the local Nusselt number distribution on the impinged surface. The heat transfer rate in jet impingement regions of each jets was higher than heat transfer rate in region between jet and around it. The characteristic of heat transfer corresponded to the flow pattern on the impinged surface with same experimental condition. Similarly, the peak of heat transfer occurred at the same location of the jet impinged region as show in Fig. 4 and 5.

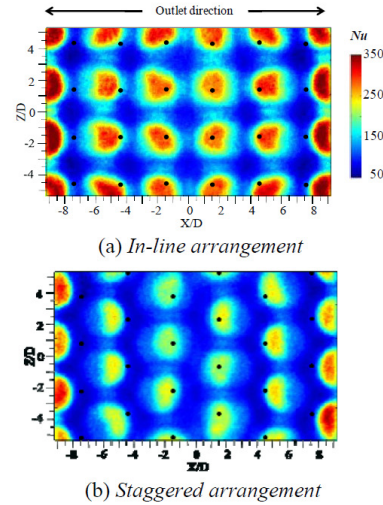


Fig. 7. Nusselt number distribution on the impinged surface in case of double outlet ($T_j=27\text{ }^\circ\text{C}$, $Re=12,700$, black dots represent the center of the orifice jet)

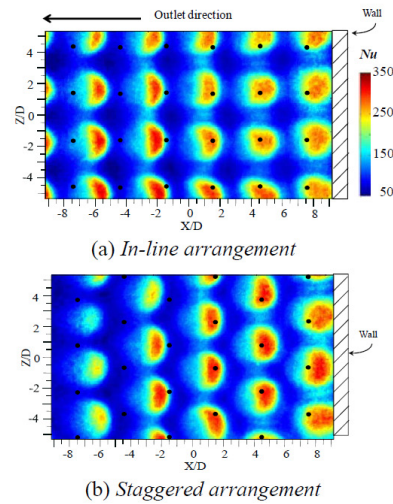


Fig. 8. Nusselt number distribution on the impinged surface in case of single outlet ($T_j=27\text{ }^\circ\text{C}$, $Re=12,700$, black dots represent the center of the orifice jet)

Fig. 9 shows the spanwise averaged Nusselt number. In case of double outlet (Fig. 9 (a)), the peak of heat transfer of in-line arrangement dominated the peak from the staggered arrangement for all location of X-axis.

Otherwise, the location of peak of heat transfer of the single crossflow depended on the jet arrangement as show in Fig. 9 (b). The location of $X > 3D$, the peak of heat transfer of the staggered arrangement dominated the peak from the in-line arrangement. Otherwise, the location of $X < -1D$, the peak of heat transfer of the in-line arrangement dominated the peak from the staggered arrangement.

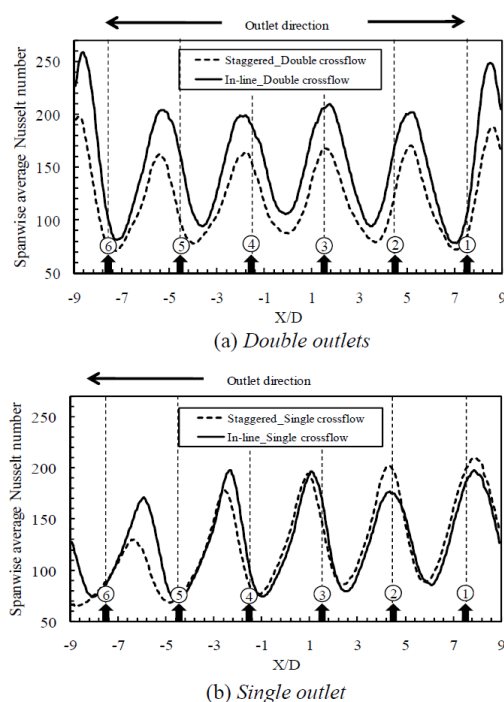


Fig. 9. Spanwise averaged Nusselt number ($T_j = 27^\circ\text{C}$, $Re = 12,700$, Arrow represents the location of nozzle)

Fig.9 (b) shows the effect of crossflow on the impinged heat transfer for single outlet. In case of the in-line arrangement and location of $X < -1D$, an interaction between the jet and the crossflow can be increased heat transfer at each stagnation region with appropriated velocity jet and crossflow. However, increasing of heat transfer will be able only in case of small jet-to-plate distance. This heat transfer behavior corresponded to the results of Katti and Prabhu [1] that showed a range of the jet-to-plate distance $H < 2D$.

However, in case of the staggered arrangement and location of $X < -1D$ as shows in Fig. 9 (b), the flow characteristic of this condition has been shown in Fig. 6 (b). The crossflow with high velocity attacked the jet flow and the jet flow was more deflected toward a downstream of crossflow. Hence, crossflow decreased heat transfer on the impinged surface.

Table 1 shows the variation of averaged Nusselt number on the impinged surface that calculated from the equation (4). The averaged Nusselt number of the in-line arrangement with Double outlet has highest heat transfer than the other parameter. The averaged Nusselt number

shows that the heat transfer rate of the in-line arrangement was higher than the staggered arrangement 3.7 % for the single outlet and 25.7 % for the double outlets.

Table 1. Average Nusselt number

Single crossflow		Double crossflow	
In-line	Staggered	In-line	Staggered
227.7	219.5	273.4	217.5

5. CONCLUSION

In present study, the effects of jet flow arrangement and outlet orientations were experimentally investigated. The main results were shown as follows;

- (1) The flow pattern on the impinged surface was corresponded to the heat transfer characteristic on the impinged surface with same experimental condition.
- (2) The interaction between the jet and the crossflow can increase heat transfer at stagnation region with appropriated velocity ratio between jet and crossflow, otherwise, very high velocity of crossflow can decrease heat transfer in jet impingement region.
- (3) The heat transfer rate of in-line arrangement was higher than the staggered arrangement 3.7 % for single outlet and 25.7 % for double outlets.

ACKNOWLEDGEMENT

This research was sponsored by Faculty of Engineering, Prince of Songkla University through grant No. ENG-53-2-7-02-0070-S.

REFERENCES

- [1] V. Katti and S. V. Prabhu, "Influence of spanwise pitch local heat transfer distribution for in-line arrays of circular jets with air flow in two opposite", *Experimental Thermal and Fluid Science. J.*, 2008, Vol. 33, pp 84-95.
- [2] L.E., Brizzi, A. Bernard, J. L. Bousgarbies, E. Dorignac and J. J. Vullierme "Study of several impinging jet", *Thermal Science, J.*, 2000, Vol. 9, No. 3, pp 217-223.
- [3] J.P. Bouchez and R.J. Goldstein "Impingement cooling from a circular jet in a crossflow", *Heat and Mass Transfer Int. J.*, 1975, Vol. 18, pp. 719-730.
- [4] R. J. Goldstein and I. Behbahan, "Impingement of a circular jet with and without cross flow", *Heat Mass Transfer Int. J.*, Vol. 25, 1982, pp. 1377-1382.
- [5] K. Nakabe, K. Suzuki, K. Inaoka, A. Higashio, J.S. Acton, and W. Chen, "Generation of longitudinal vortices in internal flows with an inclined impinging jet and enhancement of target plate heat transfer", *Heat and Fluid Flow Int J.*, 1998, Vol. 19, pp. 573-581.
- [6] L.F.G. Geers, M.J. Tummers, T.J. Bueninck and K. Hanjalic, "Heat transfer correlation for hexagonal and in-line arrays of impinging jets", *Heat and Mass Transfer Int. J.*, 2008, Vol. 51, pp 5389-5399.

Appendix C2

Conference Paper

M. Wae-hayee, C. Nuntadusit, and P. Tekasakul “Heat Transfer Enhancement on Surface with Jets Impingement from Some Arrays of Elongated Round Orifices”, The 2nd TSME International Conference on Mechanical Engineering (TSME-ICoME 2011), October 19-21, 2011, Krabi, Thailand.



Heat Transfer Enhancement on Surface with Jets Impingement from Some Arrays of Elongated Round Orifices

Makatar Wae-hayee¹, Perapong Tekasakul¹, Chayut Nuntadusit^{*1}

1. Energy Technology Research Center and Department of Mechanical Engineering,
Faculty of Engineering, Prince of Songkla University, Hatyai, Songkhla, Thailand

*Corresponding Author's E-mail: chayut@me.psu.ac.th

Abstract

The aim of this research is to enhance the heat transfer on a target surface of an array of impinging jets by decreasing effect of crossflow. Conventional round orifices (Aspect Ratio, AR=1) were substituted by elongated round orifices with aspect ratio AR=4 and 8 in base on same jet exit area. Two types of orifices arrangement; in-line and staggered arrangement were considered. The experimental investigation was carried out at constant distance from orifice plate to impinged surface $H=2D_E$ (D_E is equivalent diameter of orifice). The heat transfer characteristic was visualized using Thermochromic liquid crystal sheet (TLCs) and Nusselt number distribution was evaluated by image processing techniques. The flow characteristic on the impinged surface was also visualized by oil film technique. The results show that the elongated round orifices with AR=4 can increase average Nusselt number more than case of AR=1 for 6.04% and 12.52% in case of in-line and staggered arrangement, respectively. However, the heat transfer for case of AR=8 was enhanced only for in-line arrangement when compared with the case of AR=1. The results from flow visualization on jets impinged surface show that the jets from elongated round orifices with AR=4 were received crossflow effect smaller than jets from orifices with AR=1 and 8.

Keywords: Impinging jets, Crossflow, Heat transfer enhancement, Elongated round orifice, Orifices arrangement

1. Introduction

Impinging jets are widely used in many industrial applications which required high heat transfer rate on surface such as cooling of gas turbine blade, electronic device or wall of combustion chamber. However, the heat transfer rate is high only in jet directly impinging region. When the high and uniform heat transfer distribution is required over a wide area for

example: drying of film sheet, heating of steel sheet, multiple or array of impinging jets is usually instead. An important parameter that influences on the multiple of jet impingements in a confined space is the crossflow. Here, the crossflow is defined as the fluid flow in the direction perpendicular to the jet impingement flow [1]. The crossflow was produced by



accumulating of spent jets from upstream to downstream of the confined space.

Katti and Prabhu [1] studied the effect of jet-to-jet distance and jet-to-plate distance on heat transfer rate in case of round impinging jets with in-line arrangement. They concluded that the jet-to-jet distance at $S=4D$ give higher heat transfer rate than case of $S=2D$ and $6D$ (D is nozzle diameter). And jet-to-plate distance at $H=1D$ and $2D$ are better than case of $H=3D$.

Brizzi et al. [2] illustrated the flow and temperature patterns on the impinged surface of array of round jets with an in-line arrangement. The results of the flow pattern corresponded to the temperature pattern. And crossflow deforms significantly the impingement area that located at downstream in confined channel.

Previous studies [1-4] have been investigated heat transfer characteristics on jet impingement surface with crossflow. They concluded that the crossflow reduced significantly the heat transfer on impingement surface at downstream [3]. The aim of this research is to increase the heat transfer on the impinged surface by reducing the effect of crossflow in case of low jet-to-plate distance $H=2D_E$. Elongated round orifices with $AR=4$ and 8 were studied compare with conventional round orifices ($AR=1$). The jet Reynolds number for each orifice was kept constant at $Re=13,400$. Two type of jet flow arrangement; an in-line and staggered arrangement were also investigated. The comparisons of flow and heat transfer characteristics on the impinged surface are based on the constant jet mass flow rate.

2. Experimental Model

The experimental model is shown in Fig. 1. The multiple jets are discharged from array of orifices the round orifices, and impinge normal to opposite surface in a confined rectangular duct. The crossflow is then generated by accumulating the jets impinged air at upstream side and finally flow out to exit at one side of the duct. It should be noted that the velocity of crossflow increase as going downstream near the flow exit. The impinging jets in last column near the flow exit affected the strongest cross flow effect. The jet-to-plate distance is $H=2D_E$.

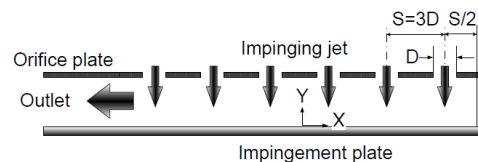
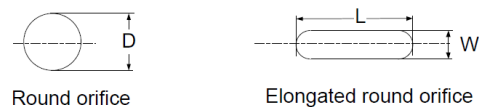


Fig. 1. Experimental model of array of jets impingement

The details of orifice geometry which used in this study are shown in Fig.2. All orifices have same exit area (about 136.8 mm^2). In this study, the equivalent diameter D_E is defined as diameter of round orifice which has same exit area and D_E is equal to 13.2 mm .



	L (mm)	W (mm)
AR=1	13.2	13.2
AR=4	24	6
AR=8	33.6	4.2

Fig. 2. Orifice geometry with identical cross-section area



Fig.3 illustrates the arrangements of array of jets; the in-line and staggered arrangement. Both arrangements have same number of 6x4 jet holes. The jet-to-jet distance was fixed at $S=3D$. The confined walls for each arrangement were fixed at location as shown in Fig. 3.

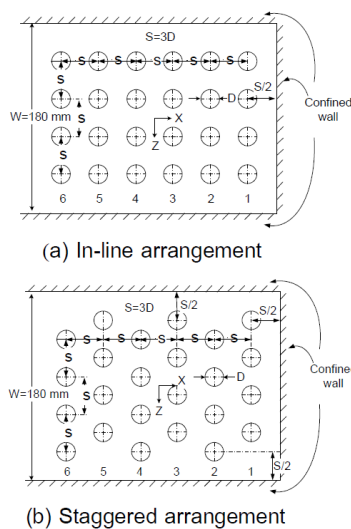


Fig. 3. Jet arrangement (No.1 to 6 represent the number of jets column)

3. Experimental Setup and Method

3.1. Experimental setup

Fig.4 shows schematic diagram of the experimental apparatus. The blower (3HP) was used for generating the air jets. The air flows through a temperature controlled chamber and towards the orifice flow meter. The air subsequently passes through a jet chamber with constant cross-section 360 mm x 360 mm and 850mm in height. The jet chamber was equipped with two of perforated plates and two of mesh plates to ensure uniform flow approached to the orifice plate. For all experimental conditions, the air flow rate was controlled at constant flow. The

Reynolds number of each jet is constant at $Re=V_j D/\nu=13,400$. The jet temperature was measured in jet chamber and controlled at $T_j=27.0^\circ\text{C}$ during experiment.

3.2. Heat transfer measurement

Fig. 4 shows the detail of test section for heat transfer measurement. The test section was mounted upon the jet chamber. The air jets were discharged from orifice plate, and then impinged upon the electrical heated surface for cooling. The heat transfer surface was made of stainless steel foil (30- μm -thickness) which attached with TLC sheet (Omega Engineering, LCS-95) on the rear side of jet impinging surface. The stainless steel foil was stretched between couple of copper bus bars. The heat transfer surface was heated by DC power supply that can supply current up to 50A passes through copper bus bars. An amount of electrical energy is dissipated in the stainless steel foil and is calculated from equation

$$\dot{Q}_{input} = I^2 \cdot R \quad (1)$$

where here, I is the electrical current and R is the electric resistance of stainless steel foil.

The local heat transfer coefficient (h) can be evaluated from equation

$$h = \frac{\dot{Q}_{input} - \dot{Q}_{losses}}{A(T_w - T_j)} = \frac{\dot{q}_{input} - \dot{q}_r - \dot{q}_c}{T_w - T_j} \quad (2)$$

where $\dot{q}_r = \epsilon_{TLC}(\overline{T_w}^4 - T_s^4)$ and $\dot{q}_c = \overline{h}_c(\overline{T_w} - T_s)$ are the heat loss transferred to the environment by radiation and convection, respectively. Here, $\overline{T_w}$ and T_j are average wall temperature and jet temperature, σ is a Stefan-Boltzman constant, ϵ_{TLC} is an emissive coefficient of TLCs (=0.9) [4]. T_s is surrounding temperature and \overline{h}_c is natural heat transfer coefficient for heat loss from the TLC to the surrounding air.



4. Results and Discussions

4.1 Flow patterns on an impinged surface

The flow visualization on the impinged surface is shown in Fig. 5. The black area and white area represent area of oil film removed completely from wall and area of wall with oil film coating, respectively. A white points in the middle of black areas represent the stagnation

point of jet bounded by jet impingement region.

The black dots are the location of center of each orifices. The flow patterns of both in-line and staggered arrangement illustrated that the impingement region at downstream (column No. 4-6) moved to downstream by crossflow. Pattern in jet impingement regions depend on the location on jets and jet arrangement.

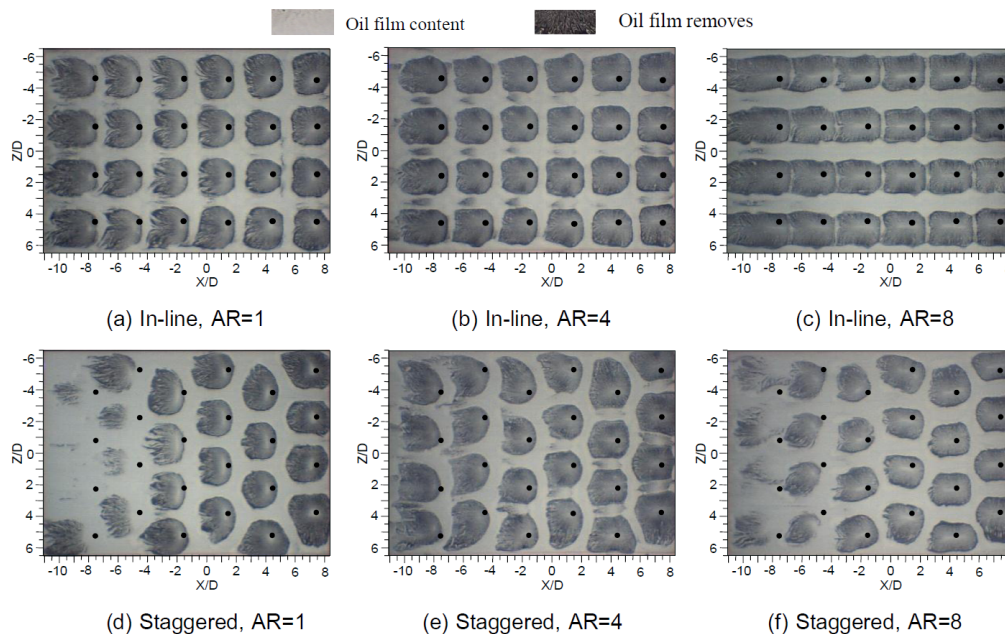


Fig. 5. Flow patterns on the impinged surface ($Re=13,400$, black dot represents the center of each orifice)

In the case of in-line arrangement (Fig. 5. (a)-(c)), the characteristic of stagnation regions are different depending on orifice geometry. The stagnation regions of elongated round orifice jet are more extended to crossflow direction, as increase AR, especially, in case of the AR=8. The stagnation regions for AR=1 (Fig.5 (a)) depends on location of jets, the stagnation regions more moved to the downstream for the jets that located far away from column No.1. However, the movement of

impingement region for elongated round orifices (Fig. 5. (b) and (c)) are smaller than case of AR=1 (Fig. 5. (a)). This means that the elongated round orifices for both AR=4 and 8 can decrease the effect of crossflow to impinging jets.

In case of AR=1 with staggered arrangement (Fig. 5. (d)), the stagnation regions of jets that located in upstream region (column No. 1-3) are more clearly expressed than of the jets that located in downstream region (column



No. 4-6). Due to the confined wall, the impinging jets in downstream area affected the strong crossflow by accumulating spent jets from upstream. So that, the jets that located at downstream region (column No. 4-6) are mixing strongly with crossflow and lose momentum for impinging on target surface. It is contrast from case of in-line arrangement (Fig. 5 (a)). It shows that the stagnation regions are slightly different between upstream and downstream region. Because, the spent jets can pass easily through the channel between the rows of jets. So, the crossflow effect on impinging jets becomes small.

In case of AR=4 with staggered arrangement (Fig. 5. (e)), the stagnation regions

at downstream region (column No. 4-6) are clearer than case of the AR=1 (Fig. 5. (d)). Because, the effect of crossflow on jets from orifices case of AR=4 is weaker than case of AR=1. However, the stagnation regions at downstream region for case of AR=8 are unclear as same as case of AR=1. Since, the orifice with AR=8 is slim and the circumference of this orifice jet which contact with crossflow is larger than case of AR=4, so the mixing between jet and crossflow is more than case of AR=4. The momentum of jet impinging on their target surface is smaller than case of AR=4.

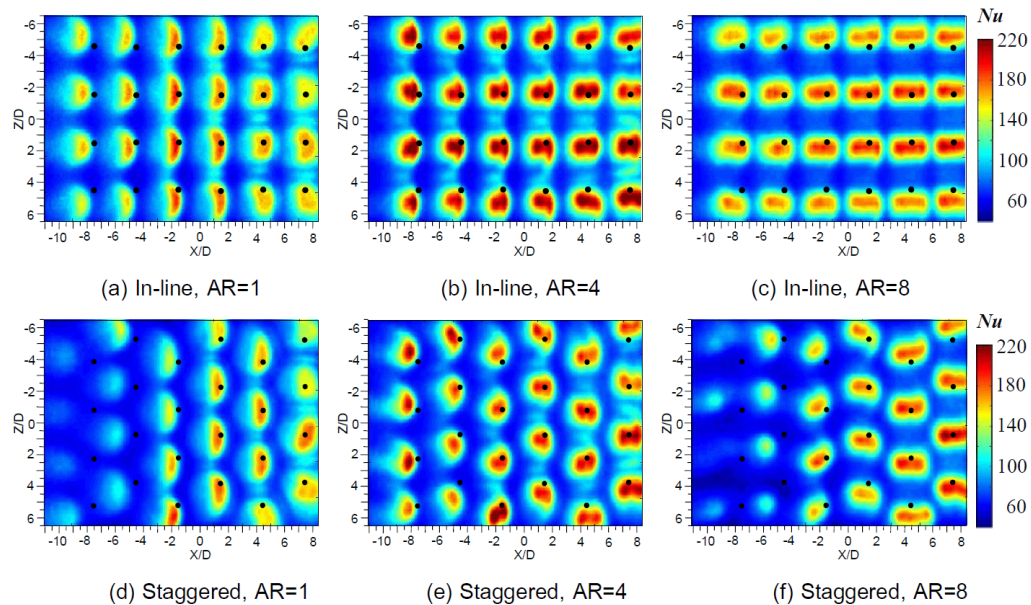


Fig. 6. Nusselt number distribution on the impinging surface ($T_j=27^\circ\text{C}$, $Re=13,400$, black dot represents the center of orifice)



4.2 The local Nusselt number on the impinged surface

The Nusselt number distributions on the impinged surface are shown in Fig. 6. The characteristic of heat transfer corresponded the flow pattern on the impinged surface (Fig.5) with same experimental condition. The Nusselt number in stagnation regions for case of AR=4 and 8 with in-line arrangement is higher than of AR=1. The area of high heat transfer for AR=4 and 8 are extended in crossflow direction corresponding to the orifice geometry.

The Nusselt number characteristic of the staggered arrangement is contrast with case of the in-line arrangement. The Nusselt number in upstream region (column No. 1-3) for case of staggered arrangement is high, but decrease rapidly as going downstream (column No. 4-5). Except for case of AR=4, the Nusselt number decreases gradually when compare with the upstream area of itself. The impinging jets from orifices case of AR=4 can increase heat transfer for both in-line and staggered arrangement. But, the impinging jets from orifices at AR=8 can

increase heat transfer only for in-line arrangement. The reason has been discussed in flow visualization results.

Fig. 7 (a) shows the local Nusselt number distribution along $Z/D=0$ and 1.5 for the in-line arrangement. The results show that impinging jets from orifices at AR=4 give highest peak of Nusselt number. However, it is lower than case of AR=8 in area between the column of jet. The high heat transfer compensate from the stagnation region to area of between the column of jet for case of the AR=8, so the peak of Nusselt number at stagnation region for AR=4 is higher than of AR=8. In addition, the Nusselt number at area of between the rows of jet (dash line) for AR=8 are lowest.

Fig. 7 (b) shows the local Nusselt number distribution along $Z/D=2.25$ for staggered arrangement. The peak of Nusselt number is only high in upstream region (column No. 1-3) and decrease as going downstream (column No. 5). Except for case of AR=4, the peak of Nusselt number is still high in downstream region.

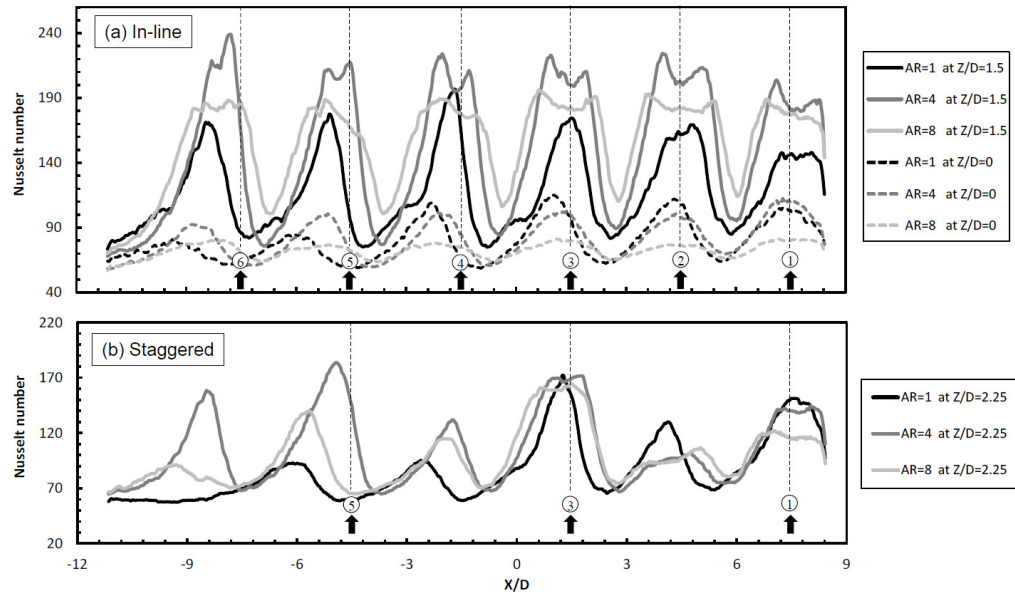


Fig. 7. Local Nusselt number distribution along crossflow direction ($T_j=27^\circ\text{C}$, $Re=13,400$)

4.3 Average Nusselt number

The average Nusselt number on the impinging surface was calculated by using average temperature in area of $-6.5 < Z/D < 6.5$ and $-11.15 < X/D < 8.4$. The results for each orifice geometry and arrangements are compared in Fig. 8. The elongated round orifice can increase heat transfer rate on impingement region. The average Nusselt number of the in-line arrangement is higher than case of staggered arrangement for all of AR. The average Nusselt number for AR=4 with in-line arrangement is highest and slightly higher than case of AR=8. In case of in-line arrangement, the average Nusselt number for both case of AR=4 and 8 are higher 6.04 % and 5.54 % than case of AR=1. However, for the staggered arrangement, only average Nusselt number for case of AR=4 is higher 12.52% than of AR=1, but for case of

AR=8, the average Nusselt number is smaller when compare with case of AR=1.

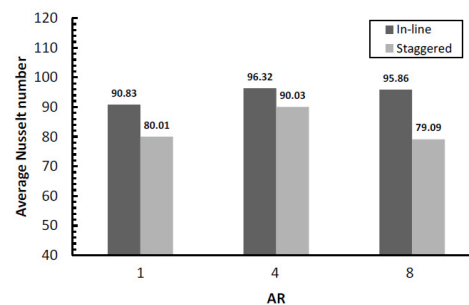


Fig. 8. Average Nusselt number

5. Conclusions

In present study, the effects of orifice geometry and jet flow arrangement were experimentally investigated. The main results were shown as follows;

(1) The impinging jets from elongated round orifices AR=4 can decrease effect of crossflow for both in-line and staggered arrangement, so



the heat transfer rate for both jet arrangement is higher than case of AR=1 and 8.

(2) The AR=8 can increase the heat transfer in stagnation region and area between columns of jet for in-line arrangement, but it is rapidly decrease in downstream region for staggered arrangement.

(3) The average Nusselt number of the in-line arrangement are higher than of staggered arrangement for any AR, and the average Nusselt number for AR=4 is the highest.

Acknowledgement

This research was sponsored by Faculty of Engineering, Prince of Songkla University through grant No. ENG-53-2-7-02-0070-S.

References

- [1] Katti, V. and Prabhu, S. V. (2008), Influence of spanwise pitch local heat transfer distribution for in-line arrays of circular jets with air flow in two opposite, *Experimental Thermal and Fluid Science J.*, vol. 33, pp. 84 – 95.
- [2] Brizzi, L.E., Bernard, A., Bousgarbies, J. L., Dornnac, E. and Vullierme, J. J. (2000), Study of several impinging jet, *Thermal Science J.*, vol. 9 (3), pp. 217 – 223.
- [3] Bouchez, J.P. and Goldstein, R.J. (1975), Impingement cooling from a circular jet in a crossflow, *Heat and Mass Transfer Int. J.*, vol. 18, pp. 719 – 730.
- [4] Geers, L.F.G., Tummers, M.J., Bueninck, T.J. and Hanjalic, K. (2008), Heat transfer correlation for hexagonal and in-line arrays of impinging jets, *Heat and Mass Transfer Int. J.*, vol. 51, pp. 5389 – 5399.

Appendix C3

Journal Paper

M. Wae-hayee, P. Tekasakul and C. Nuntadusit, "Influence of Nozzle Arrangement on Flow and Heat Transfer Characteristics for Arrays of Circular Impinging Jets" Songklanakarin Journal of Science and Technology, 2012, Vol. 35(2), pp.203-212.



Original Article

Influence of nozzle arrangement on flow and heat transfer characteristics of arrays of circular impinging jets

Makatar Wae-hayee, Perapong Tekasakul, and Chayut Nuntadusit*

*Energy Technology Research Center and Department of Mechanical Engineering, Faculty of Engineering,
Prince of Songkla University, Hat Yai, Songkhla, 90112 Thailand.*

Received 31 January 2012; Accepted 1 February 2013

Abstract

The effect of jet arrangements on flow and heat transfer characteristics was experimentally and numerically investigated for arrays of impinging jets. The air jets discharge from round orifices and perpendicularly impinge on a surface within a rectangular duct. Both the in-line and staggered arrangements, which have an array of 6×4 nozzles, were examined. A jet-to-plate distance (H) and jet-to-jet distance (S) were fixed at $H=2D$ and $S=3D$, respectively (where D is the round orifice diameter). The experiments were carried out at jet Reynolds number $Re=5,000, 7,500$ and $13,400$. Temperature distributions on the impingement surface were measured using a Thermochromic Liquid Crystal sheet, and Nusselt number distributions were evaluated using an image processing method. The flow characteristics on the impingement surface were visualized using the oil film technique. The numerical simulation employed to gain insight into the fluid flow of jets between the orifice plate and the impingement wall was via computational fluid dynamics. The results reveal that the effect of crossflow on the impinging jets for the staggered arrangement is stronger than that in the case of in-line arrangement. In the latter case of in-line arrangement, the crossflow could pass throughout the passage between the rows of jets, whereas in the former case the crossflow was hampered by the downstream jets. The average Nusselt number of the in-line arrangement is higher than that of the staggered arrangement by approx. 13-20% in this study.

Keywords: array of impinging jets, in-line and staggered arrangement, crossflow, thermochromic liquid crystal sheet (TLCs), oil film technique, CFD

1. Introduction

Jet impingement is a high-performance technique for heat transfer enhancement in thermal equipment. It has also been used in industrial processes for heating, cooling and drying. Since the heat transfer rate is very high at the area where the jet directly impinges on, it provides rapid cooling or heating on the local heat transfer area (Ashforth-Frost and Jambunathan, 1996; Colucci and Viskanta, 1996). However, many thermal industrial applications have large surface area of heat transfer such as combustor chamber wall and gas

turbine blade cooling, steel and glass quenching, and textile and paper drying. When high and uniform heat transfer rate is required over the entire surfaces, multiple impinging jets or array of impinging jets are applied.

An important factor affecting flow and heat transfer characteristics of multiple impinging jets in a confined space is the crossflow. Crossflow is defined as fluid flow in the perpendicular direction to the jet impingement flow. It can be formed by either external flow or accumulating spent jet flow. In the case of multiple impinging jets in a confined space, the spent jet is accumulated from upstream to the downstream end of the channel. The flow rate, or velocity of the crossflow, is thus increased from upstream to the downstream of the channel. Consequently, the flow and heat transfer of the impinging jets located at downstream of the channel is signi-

* Corresponding author.

Email address: chayut@me.psu.ac.th

ificantly influenced by the crossflow (Viskanta, 1993).

Various previous studies have shown the effects of crossflow on the flow and heat transfer characteristics of multiple impinging jets. Florschuetz *et al.* (1981) investigated the Nusselt number correlation for both the in-line and staggered arrangements in case of jet-to-jet distance of $S > 4D$ (where D is the nozzle diameter). Brizzi *et al.* (2000) illustrated flow and temperature patterns on the impingement surface of an array of jets with in-line arrangement and confirmed that flow patterns correspond to the temperature distributions. Katti and Prabhu (2008) studied heat transfer on an impingement surface under an array of jets, also in an in-line arrangement. Results shown by their study are that the heat transfer rate under jet-to-jet distance in spanwise direction for $S = 4D$ is higher than for either $S = 2D$ or $S = 6D$. However, the optimal jet-to-jet distance in streamwise direction has not been reported.

Not many works have been conducted on the flow characteristics of multiple impinging jets with the effect of crossflow (Carcasci, 1999; Brizzi *et al.*, 2000). It is difficult to identify the interaction between the crossflow and the jet in the case of multiple impingement flows. To illustrate the ratio of jet velocity to the crossflow velocity influencing the flow and heat transfer of impinging jet, a single impinging jet with simulated crossflow was experimentally investigated (Bouchez and Goldstein, 1975; Goldstein and Behbahani, 1982; Nakabe *et al.*, 1998; Barata and Durao, 2004). Recently, a numerical simulation has also been used for a flow field study of a single impinging jet with simulated crossflow (Shi *et al.*, 2003; Yang and Wang, 2005). In order to illustrate the interaction between the jet and the crossflow in case of multiple impingement flows in the present study, numerical simulation has been adopted.

In more recent works it was shown that in order to enhance the heat transfer rate under an array of impinging jets with in-line arrangement, an impingement surface with mounted ribs was applied (Rallabandi *et al.* 2010; Xing *et al.*, 2011; Caliskan and Baskaya, 2012). However, there had been no investigations on staggered arrangement in their works. Hoberg *et al.* (2010) investigated experimentally the impinging jet array together with the use of effusion holes in an effort to enhance the heat transfer rate reduced in the crossflow by a staggered arrangement. Nevertheless, this investigation was observed solely for an average heat transfer without details on its flow characteristics and local heat transfer. A more vigorous study in the work on the flow characteristics and heat transfer to identify and illustrate the effects of crossflow on jet impingement arrays with comparison of in-line and staggered arrangement is thus needed.

The aim of the present study is to investigate the effect of nozzle arrangement for array of impinging jets in case of low jet-to-plate distances. The in-line and staggered arrangement were experimentally and numerically conducted. The temperature distribution on the impingement surface was investigated using a Thermochromic Liquid Crystal sheet (TLCs), and the Nusselt number distribution was evaluated

using an image processing method. The characteristic of the flow on the impingement surface was visualized employing the oil film technique. The numerical simulation employed to gain insight into the fluid flow of multiple impinging jets under crossflow was via a commercial ANSYS ver. 12.0, Fluent software.

2. Experimental Setup and Method

2.1 Experimental model and parameters

An experimental model displaying jets discharging from round orifice and impinging normal to the opposite surface in a confined rectangular duct is shown in Figure 1. Crossflow is generated by accumulation of spent jet (jet after impinging) at the upstream terminal that flows out to the exit at the other end of the duct. A Cartesian coordinate system with its origin allocated at the impingement surface is as shown in Figure 1 and 2. The Y-axis is normal to the target

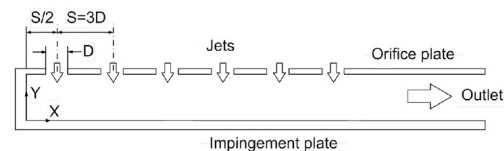


Figure 1. Experimental model of array of impinging jets.

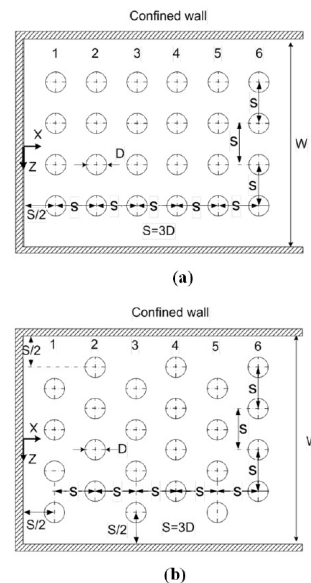


Figure 2. Experimental model of jet arrangement ($D=13.2$ mm, $W=180$ mm): (a) In-line arrangement and (b) staggered arrangement.

surface, while the X- and the Z-axes are along the streamwise and the spanwise directions of the crossflow, respectively.

The arrays of jet arrangements are as shown in Figure 2 which depict the in-line configuration in (a) and the staggered arrangement in (b). The diameter D of each round orifice, having a smooth square-edge nozzle through a plate of 2 mm thickness, is 13.2 mm. Both jet arrangements have the same array of 6×4 jet holes; 6 on the streamwise and 4 on the spanwise direction. Both arrangements have constant jet-to-jet distance $S=3D$ and jet-to-plate distance $H=2D$. In the case of staggered arrangement, as shown in Figure 2(b), a jet-to-sidewall distance of $S/2 (=1.5D)$ is assigned to the nearest nozzles to the wall. Dimensions of the duct for the staggered arrangement, both height and width, are thus fixed by these requirements. The same sidewall distance is assigned to the in-line arrangement, and hence the same duct dimension is applicable for both configurations. The experiments were carried out at jet Reynolds number of $Re=5,000, 7,500$ and $13,400$ that calculate jet velocity at center of nozzle outlet.

2.2 Experimental setup

The schematic diagram and photographs of the experimental apparatus are shown in Figure 3. A 3-HP blower (Artith Machinery, Av-D1216, Thailand) accelerates the air which flows through a temperature controlled chamber equipped with a 2-kW heater (Sangi Electric, FU-4010, Thailand). The heated air is then forced through a calibrated

orifice flow meter and into a jet chamber having a cross-section of $360 \text{ mm} \times 360 \text{ mm}$ and a height of 850 mm. The jet chamber is equipped with two layers of perforated plates and two layers of mesh plates to ensure a uniform flow field when the air approaches the orifice plate. Finally, the compressed air in the chamber forces through the jet orifice and enters the test section.

The test section is directly mounted on top of the jet chamber, as shown in Figure 3. Under all experimental conditions, the jet temperature was controlled at 27°C by a temperature controller (Shinko, JCS-33A, Japan) and a power controller (Sangi Electric, SCR-1A030, Thailand). In these experiments, temperature variations of the jet can be controlled within 0.2°C .

2.3 Heat transfer measurement

Figure 3 also outlines details of the test section for heat transfer measurement. Air with constant temperature is discharged through the orifice plate and impinges upon the heat transfer surface. The heat transfer surface, made of stainless steel foil ($30 \mu\text{m}$ thick), is attached with the TLCs (Omega, LCS-95, U.S.A.) on the rear side of the impingement surface. The stainless steel foil is stretched between a couple of copper bus bars. The heat transfer surface is heated by a DC power supply (Silicon, WYK-15V50A-H, Thailand) that can supply a current up to 50 A through the copper bus bars. Electrical energy dissipated in the stainless steel foil can be calculated from:

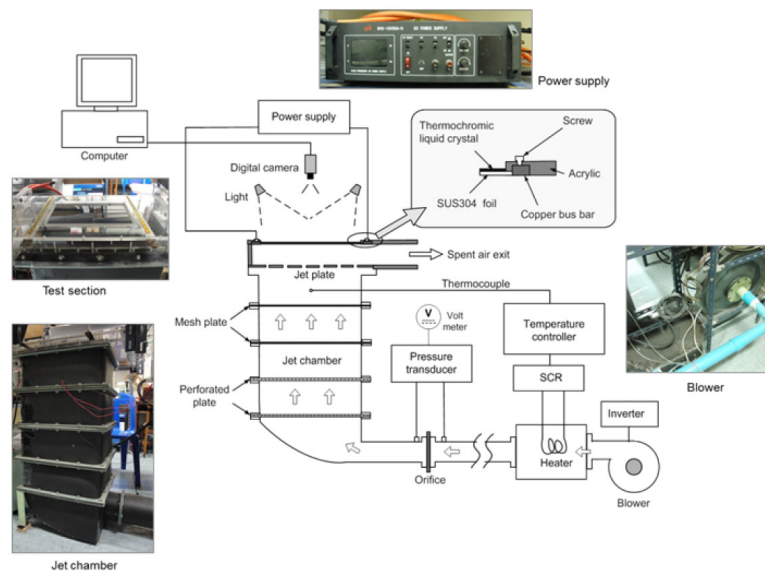


Figure 3. Schematic and photographs of the experimental apparatus.

$$\dot{Q}_{input} = I^2 \cdot R \tag{1}$$

where I is the electrical current, and R is the thermal electrical resistance of the stainless steel foil.

The local heat transfer coefficient by forced convection of the jet, h , can be evaluated from:

$$h = \frac{\dot{Q}_{input} - \dot{Q}_{losses}}{A(T_w - T_j)} = \frac{\dot{q}_{input} - \dot{q}_r - \dot{q}_c}{T_w - T_j} \tag{2}$$

where A is area of stainless steel foil, $\dot{q}_r = \sigma \varepsilon_{TLC} (T_w - T_s)$ and $\dot{q}_c = h_c (T_w - T_s)$ are the heat losses to the environment by radiation and convection, respectively, T_w and T_j are the wall and jet temperatures, σ is the Stefan-Boltzman constant, ε_{TLC} is the emissive coefficient of the TLC sheet (Geers *et al.*, 2008), T_s is the surrounding temperature, and h_c is the natural heat transfer coefficient calculated from natural convective heat transfer from the heat transfer surface to the surrounding.

The wall temperature (T_w) on the impingement surface was measured using the TLCs attached at the rear side of the jet impingement surface. A digital camera (Creative, Live Pro, 1,280×960 pixels, China) was used to capture color on the TLCs under manual brightness mode. Images of color pattern on the TLCs were converted from RGB (Red, Green and Blue) system to HSI (Hue, Saturation, and Intensity) system. The Hue (H) value provides a convenient way to correlate color of the TLCs to the temperature. The TLCs was calibrated under the same conditions of the experimental runs.

The local Nusselt number can be calculated from:

$$Nu = \frac{hD}{k} \tag{3}$$

where D is the round orifice diameter, and k is the jet thermal conductivity.

The average Nusselt number can be calculated from:

$$\bar{Nu} = \frac{\bar{h}D}{k} \tag{4}$$

where \bar{h} is the average heat transfer coefficient, calculated from Equation 2 by replacing T_w with the average temperature on the impingement surface, \bar{T}_w . Details of the heat transfer measurement adopted here have been described in two recent studies, Nuntadusit *et al.* (2012a and b).

2.4 TLCs temperature calibration

Temperature calibration of the TLCs was carried out under similar experimental conditions as that applied to the test section, with same viewing angle and lighting in an effort to keep external factors constant. The calibration rig composes of layers of materials and equipment, respectively, a 75×105 mm acrylic back-plate (10 mm thick, acting as thermal insulator), a thin coil heater (Kyohritsu, 80 Ω, 12 VDC, Japan), an aluminum plate (3 mm thick), four thermocouples, and the TLC sheet to be calibrated, as schematically shown in Figure 4, left view. A DC current was constantly applied to the thin coil heater by a DC power supply (KBM Engineering, PS-3002, Thailand). The maximum average temperature of close to 40°C is measured via four wires of the thermocouples

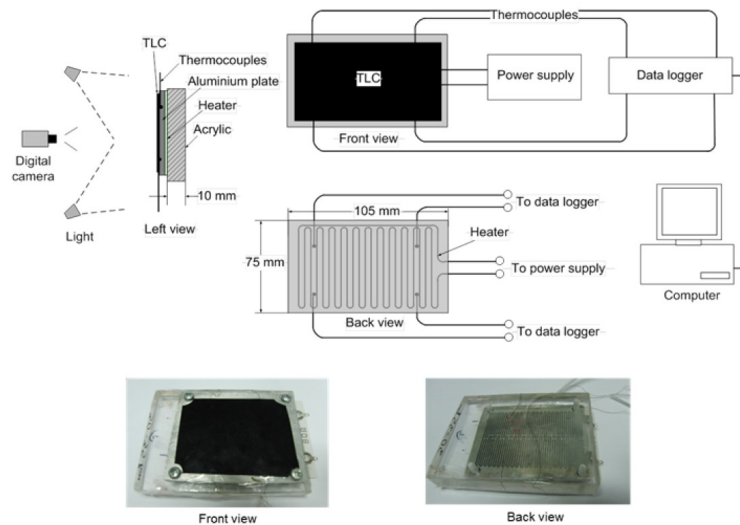


Figure 4. Schematic and photographs of the calibration rig.

mounted at assigned locations on the aluminum plate. Colors on the TLCs and temperatures were simultaneously recorded when an average temperature becomes steady. The electrical current thereafter was gradually decreased to yield lower temperatures. Calibration data were recorded in 0.2°C decremented steps as average temperature until it approached 27°C. Calibration was carried out on five different locations on the calibration rig positioned on the impingement surface. Relationship of the recorded temperature versus the normalized hue value from the color change observations is plotted in Figure 5 for all calibration positions.

2.5 Flow visualization on the impinging surface

Flow visualization on the impingement surface was carried out using the oil film technique. The oil mixture was prepared by mixing 20 g of liquid paraffin with 8.5 g of titanium dioxide and 3.5 g of oleic acid. A transparent plastic plate was used as the jet impingement wall and was uniformly painted coated by the oil. The same camera that has been employed throughout was used to record oil film patterns on the impingement surface at a 30-second time interval. The oil film image was captured in RGB system, as that employed in capturing the TLCs image.

2.6 Numerical simulation

Flow characteristics of the impinging jet in the confined channel were numerically simulated using the computational fluid dynamics (CFD) technique. Commercial package ANSYS (ver. 12.0) was used in this present study. The numerical model was identical to the experimental model schematically shown in Figure 6. Computations were conducted by solving continuity and Navier-stokes equations under existing boundary conditions. This k-ε turbulence model with general wall-function mode has been used in solving many numerical simulation problems (Shi *et al.*, 2003;

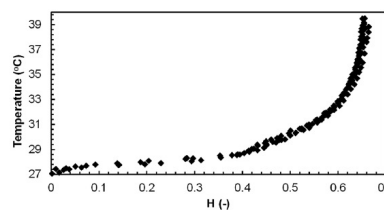


Figure 5. Temperature versus normalized hue value of TLCs calibration.

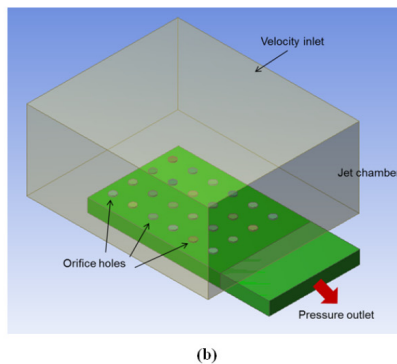
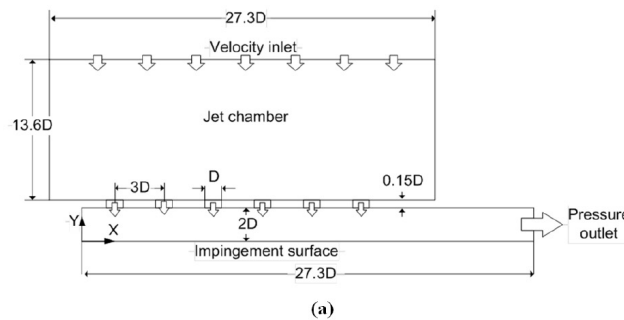


Figure 6. Domain of numerical simulation: (a) Schematic of domain and (b) 3-D numerical domain.

Yang and Wang, 2005).

Figure 7 details the internal grid used in this computation domain. The non-uniform grid system was finely generated for regions near the orifice holes and the impingement surface. A wall inflation function was used to concentrate the elements near the impingement surface. The impact of grid size on the static pressure on the impingement surface is shown in Figure 8. It can be noticed that the trend of static pressure having 1,603,186 and 1,934,306 cells exhibits less discrepancy than most others. The node with 1,603,186 cells was chosen for further simulations to minimize computation costs.

All boundary conditions applied were identical to those specified in experimental conditions. The inlet was regulated to give a constant inlet velocity of 0.36 m/s to maintain an average Reynolds number of the jets at $Re=13,400$. The outlet pressure was kept constant at 1 atm. The solution method was based on SIMPLE algorithm with second order upwind for all spatial discretizations (Versteeg and Malalasekera, 1995). Solutions were considered converged when the normalized residual of all algebraic equations is less than the prescribed value of 1×10^{-4} .

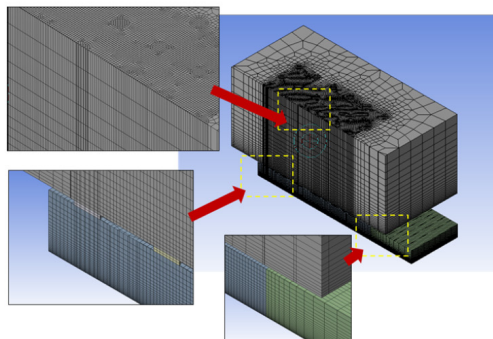


Figure 7. Internal grid system of in-line arrangement.

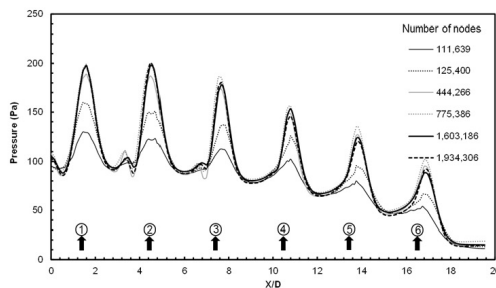


Figure 8. Effect of grid dependence on static pressure on the impingement surface for in-line arrangement (vertical arrows indicate the locations of column jets).

3. Results and Discussions

3.1 Flow characteristics

Flow characteristics derived from an array of impinging jets calculated using the CFD technique at $Re=13,400$ for the in-line and the staggered arrangements are shown in Figure 9 and 10, respectively. Velocity vectors and velocity contours of the flow field in the X-Y plane and the Y-Z plane are shown at major cross sections in the flow channel. In the case of in-line arrangement, the crossflow accumulated from the surface jets meanders between the rows of the jets to the

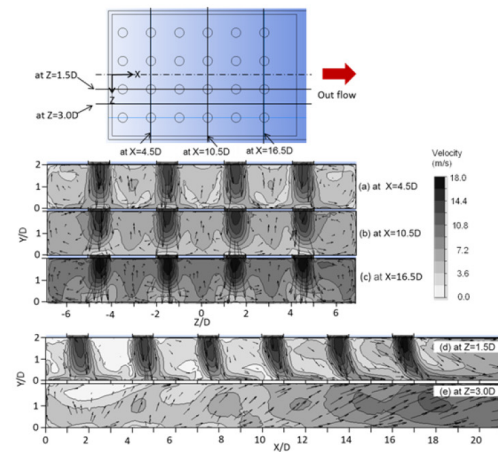


Figure 9. Flow characteristics in the case of in-line arrangement at $Re=13,400$.

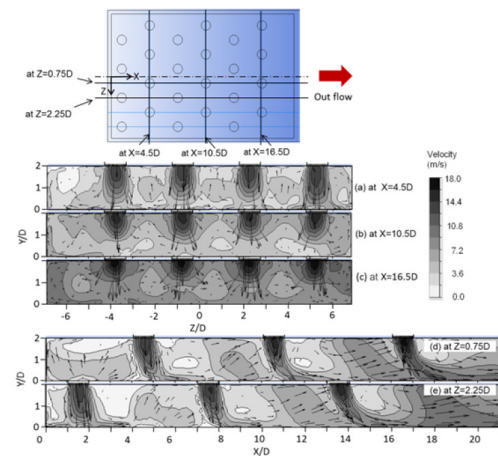


Figure 10. Flow characteristics in the case of staggered arrangement at $Re=13,400$.

channel exit. The crossflow velocity increases along the downstream direction to the channel exit, as notably shown in Figure 9(e). In Figure 9(d), due to the higher crossflow velocity further down the downstream region, deflection of the downstream impinging jets (streamwise nozzles No. 4-6) is larger than that of the upstream impinging jets (streamwise nozzles No. 1-3). When the combined Figure 10(d) and (e), respectively for streamwise nozzles No. 2, 4, 6 and streamwise nozzles No. 1, 3, 5, are compared to Figure 9(d) for streamwise in-line nozzles No. 1-6, deflection of the impinging jets for the staggered jet arrangement in Figure 10 is noticeably larger than the case for the in-line jet arrangement. The most prominent deflection appears for the impinging jets at the last nozzle of the staggered configuration (streamwise nozzle at columns No.6).

The flow characteristics of impinging jets on Z-X plane near the impinged wall (1 mm above the wall) for $Re=13,400$ are shown in Figure 11. The velocity vector and contour in the Y-axis are shown along the location of each orifice. The Y-component velocity represents the velocity in the direction normal to the impingement surface. Its positive direction is towards the downstream of the jet that impinges on the wall. The velocity in the region near each center of impingement is high; impingement regions having velocity higher than 0.5 m/s are clearly seen around the centers of impingement. The impingement surface positioned below the jet having the maximum Y-component velocity in each cell is designated the stagnation point.

The impingement regions in the case of in-line arrangement, shown in Figure 11(a), are clearly shifted towards the downstream direction due to the effect of crossflow. The displacement of each stagnation region (the distance from the centerline of each orifice to the stagnation point of each cell) increases along the downstream direction. These deflections are, however, larger for the case of staggered arrangement as shown in Figure 11(b). Moreover, the stagnation regions of the downstream impinging jets (in column No. 5 and 6) for the staggered arrangement cannot be identified due to strong collision of the crossflow on the jets before impingement.

Flow visualization of jets on the impingement surface using the oil film technique is shown in Figure 12. The black

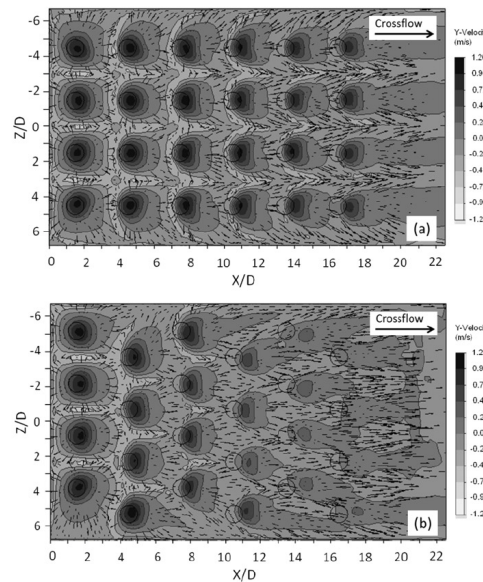


Figure 11. Flow characteristics on Z-X plane near the impinged wall (1 mm above the wall) for $Re=13,400$: (a) In-line arrangement and (b) staggered arrangement.

and white regions represent the areas where the oil film is completely blown off and the area with original oil film coating, respectively. The cluster of white spots in the middle of the black area in each impinging cell represents the stagnation point of the impinging jet bounded in the jet impingement region. The flow patterns of both the in-line and staggered arrangements agree well with the contours of velocity in the Y-component near the impingement surface shown earlier in Figure 11.

The impingement region of each cell expands in the downstream direction and contracts in the upstream direction for the case of the in-line arrangement, as shown in Figure 12(a). Expansions of impingement regions in the downstream direction are more obvious further downstream to the

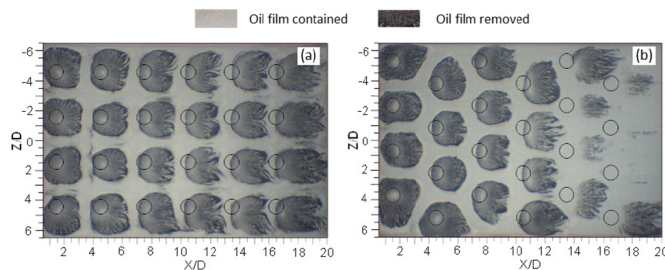


Figure 12. Flow patterns on the impingement surface with oil film technique for $Re=13,400$: (a) In-line arrangement and (b) staggered arrangement.

channel exit. This characteristic of the flow pattern agrees with the flow visualization study of multiple jets investigated by Brizzi *et al.* (2000).

The impingement regions of the in-line arrangement in Figure 12(a) obviously express themselves throughout all orifice locations while they express indistinctly especially for columns No. 5 and 6 in the case of staggered arrangement as shown in Figure 12(b). This is due to strong deflection of the jets before impingement in the location of jet columns No. 5 and 6 as previously shown in Figure 10(d) and (e).

The effect of crossflow on jet impingements for the staggered arrangement is stronger than the case for the in-line arrangement. Schematic outlines of the flow patterns of crossflow that meander through the jets for the in-line and staggered arrangements are shown in Figure 13. The crossflow passes easily through channels between the rows of jets in the case of in-line arrangement, whereas crossflow from a former column of impinging jets strongly exerts impact on the downstream impinging jets in the case of staggered arrangement.

3.2 Heat transfer characteristics on impingement surface

The contours of local Nusselt number on the impingement surface for $Re=13,400$ are shown in Figure 14, and the local Nusselt number distributions along X-axis at different Z/D are shown in Figure 15. The contours of Nusselt number in Figure 14 correspond to the flow patterns on the impingement surface in Figure 12, as well as the contours of velocity in Y-component near the impingement surface in Figure 11.

In the case of in-line arrangement shown in Figure 14(a) the Nusselt number is higher at the inner impingement region and becomes lower around the outer region. The area of high Nusselt number in each impingement cell shifts to the downstream direction (X-axis direction) and tends to contract in the spanwise direction (Z-axis direction); the further along downstream to the channel exit, the more. Figure 15 shows the plots of Nusselt number versus X/D for both jet arrangements but at different Z/D indicated dash line in Figure 14. The peak Nusselt number at each impingement region increases continuously from column No. 1 to column No. 4

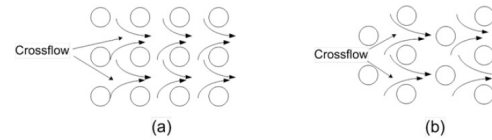


Figure 13. Schematic outlines of crossflow characteristics through difference of jet arrangement: (a) in-line arrangement and (b) staggered arrangement.

for the in-line case at $Z/D=1.5$ (note the black bold solid line peaks in the figure). The highest peak Nusselt number, approx. $Nu=190$, takes place at column No. 4 and the peak decreases again for columns No. 5 and 6. This characteristic of peak Nusselt number at stagnation regions agrees with the result of Katti and Prabhu (2008) in the case of jet-to-plate distance $H < 2D$.

This result can be explained by the effect of crossflow velocity on the jet impingement flow. The Nusselt number at the stagnation point in the case of in-line arrangement is increased by the interaction of crossflow with moderate velocity on jet impingement. It can be attributed that turbulent intensity of the jet is increased by the moderate velocity of crossflow. However, in the case of high crossflow velocity, the jet is deflected downstream, so the peak Nusselt number at stagnation region decreases due to low momentum of jet impinging on the surface. This takes place at columns No. 5 and 6.

The Nusselt number distributions in the upstream regions (from columns No. 1 to No. 3) for the staggered arrangement (Figure 14(b)) are not much different when compared to the case of the in-line arrangement (Figure 14(a)) at same locations. However, the Nusselt number decreases rapidly for the downstream regions (from columns No. 4 to No. 6) of the staggered arrangement because of direct collision of high crossflow velocity with the downstream jets. So, the jets are strongly deflected downstream without impingement as previously mentioned. This results in apparently no stagnation region in the last column of flow visualization in Figure 11(b) and 12(b).

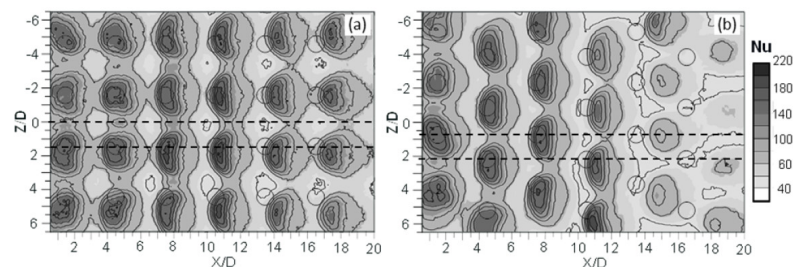


Figure 14. Nusselt number distributions on the impingement surface for $Re=13,400$ ($T_j=27^\circ\text{C}$): (a) in-line arrangement and (b) staggered arrangement.

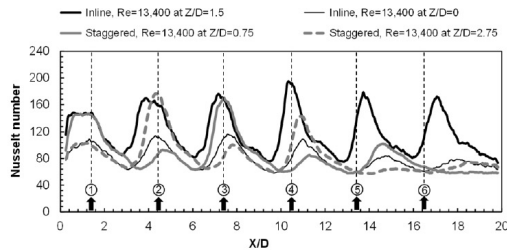


Figure 15. Local Nusselt number distributions along streamwise direction at different Z/D (from dash line in Figure 14 and each arrow indicates the location of orifice).

Figure 16 shows the distributions of spanwise average Nusselt number for the case of $Re=5,000, 7,500$ and $13,400$. This average number is calculated by averaging all local wall temperatures in the Z -axis at a particular X/D . Results show that the spanwise average Nusselt number of the in-line arrangement is generally larger than that in the case of staggered arrangement for all Reynolds number, and certainly for region $X/D > 7$. The peak spanwise average Nusselt number for each impingement region decreases monotonically along the downstream direction in the case of staggered arrangement, whereas for the case of in-line arrangement it tends to increase from jet column No. 1 to No. 3 and then decrease monotonically along the downstream direction to the channel exit. This result corresponds to the local heat transfer enhancement in the impingement region for jets at column No. 3 of the in-line arrangement.

3.3 Average Nusselt number

Variations of the average Nusselt number on the impingement surface calculated from the average local wall temperature for the entire surface versus the Reynolds number are shown in Figure 17. The average Nusselt number of both the in-line and staggered arrangements increases as the Reynolds number increases. The average Nusselt number of the in-line arrangement is higher than that of the staggered arrangement throughout all Reynolds numbers. It has been worked out that the average Nusselt number in the case of in-line arrangement is larger than the case of staggered arrangement by approx. 13-20% in the 5,000-13,400 Reynolds number range in this study.

4. Conclusions

In this study, the effects of jet arrangement on the flow and heat transfer characteristics on a surface under two arrays of jet impingement have been experimentally and numerically investigated. The main results for the in-line and staggered arrangements are as follows:

1. The flow characteristics on the impingement surface from the experiment agree well with numerical results:

the area of high velocity in the Y -component corresponds to its impingement region, and the area of peak velocity in the Y -component corresponds to the stagnation point of each impinging jet. The impingement region in each cell extends more with further distance towards the downstream direction and contracts more with distance towards the upstream. This flow pattern of impinging jets coincides with the local Nusselt number distribution on the impingement surface.

2. The effect of crossflow on the jet in the staggered arrangement is stronger than that for the in-line arrangement. Crossflow can easily pass through the gaps between the rows of in-line jets, whereas it appears to be directly blocked by the downstream jet in the case of staggered arrangement. The last column of the staggered jets is most affected by the high crossflow velocity and deflects more to the downstream direction.

3. Moderate crossflow velocity can increase the peak heat transfer of jet impingement. This heat transfer behavior is attributed to the interaction of moderate crossflow velocity that collides with the jet and increases the turbulent intensity of the jet before impingement. However, in the case of high crossflow velocity, the peak heat transfer decreases due to the low momentum of the jet before impingement.

4. The average Nusselt number of the in-line arrangement is approximately 13-20% higher than that of the staggered arrangement in the 5,000-13,400 Reynolds number range.

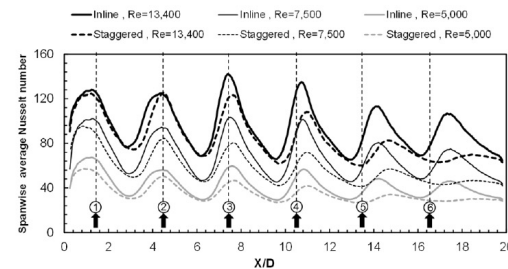


Figure 16. Spanwise average Nusselt number (vertical arrows indicate the locations of column jets).

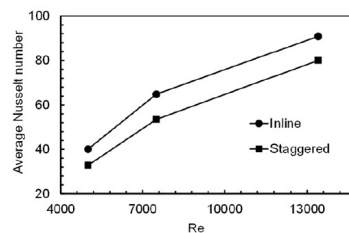


Figure 17. Average Nusselt number for overall impingement surface.

Acknowledgments

This research is co-supported by grants from the Thailand Energy Policy and Planning Office, Ministry of Energy, the Graduate School of the Prince of Songkla University (PSU), and the PSU Faculty of Engineering.

References

- Ashforth-Frost, S. and Jambunathan, K. 1996. Effect of nozzle geometry and semi-confinement on the potential core of a turbulent axisymmetric free jet. *International Communications in Heat and Mass Transfer*. 23(2), 155-162.
- Barata, J.M.M. and Durao, D.F.G. 2004. Laser-Doppler measurements of impinging jet flows through a cross-flow. *Experiments in Fluids*. 36(6), 665-674.
- Bouchez, J.-P. and Goldstein, R.J. 1975. Impingement cooling from a circular jet in a cross flow. *International Journal of Heat and Mass Transfer*. 18(6), 719-730.
- Brizzi, L.-E., Bernard, A., Bousgarbics, J.-L., Dorignac, E. and Vullierme, J.-J. 2000. Study of several impinging jets. *Journal of Thermal Science*. 9(3), 217-223.
- Carcasci, C. 1999. An experimental investigation on air impinging jets using visualization methods. *International Journal of Thermal Sciences*. 38(9), 808-818.
- Caliskan, S. and Baskaya, S. 2012. Experimental investigation of impinging jet array heat transfer from a surface with V-shaped and convergent-divergent ribs. *International Journal of Thermal Sciences*. 59, 234-246.
- Colucci, D.W. and Viskanta, R. 1996. Effect of nozzle geometry on local convective heat transfer to a confined impinging air jet. *Experimental Thermal and Fluid Science*. 13(1), 71-80.
- Florschuetz, L.W., Truman, C.R. and Metzger, D.E. 1981. Streamwise flow and heat transfer distributions for jet array impingement with crossflow. *ASME Journal of Heat Transfer*. 103, 337-342.
- Geers, L.F.G., Tummers, M.J., Bueninck, T.J. and Hanjalic, K. 2008. Heat transfer correlation for hexagonal and in-line arrays of impinging jets. *International Journal of Heat and Mass Transfer*. 51, 5389-5399.
- Goldstein, R.J. and Behbahani, A.I. 1982. Impingement of a circular jet with and without crossflow. *International Journal of Heat and Mass Transfer*. 25(9), 1377-1382.
- Hoberg, T.B., Onstad, A.J. and Eaton, J.K. 2010. Heat transfer measurements for jet impingement arrays with local extraction. *International Journal of Heat and Fluid Flow*. 31, 406-467.
- Katti, V. and Prabhu, S.V. 2008. Influence of spanwise pitch on local heat transfer distribution for in-line arrays of circular jets with spent air flow in two opposite directions. *Experimental Thermal and Fluid Science*. 33(1), 84-95.
- Nakabe, K., Suzuki, K., Inaoka, K., Higashio, A., Acton, J.S. and Chen, W. 1998. Generation of longitudinal vortices in internal flows with an inclined impinging jet and enhancement of target plate heat transfer. *International Journal of Heat and Fluid Flow*. 19(5), 573-581.
- Nuntadusit, C., Wae-hayee, M., Bunyajitradulya, A. and Eiamsa-ard, S. 2012a. Heat transfer enhancement by multiple swirling impinging jets with twisted-tape swirl generators. *International Communications in Heat and Mass Transfer*. 39(1), 102-107.
- Nuntadusit, C., Wae-hayee, M., Tekasakul, P. and Eiamsa-ard, S. 2012b. Local heat transfer characteristics of array impinging jets from elongated orifices. *International Communications in Heat and Mass Transfer*. 39(8), 1154-1164.
- Rallabandi, A.P., Rhee, D.-H., Gao, Z. and Han, J.-C. 2010. Heat transfer enhancement in rectangular channels with axial ribs or porous foam under through flow and impinging jet conditions. *International Journal of Heat and Mass Transfer*. 53(9), 4663-4671.
- Shi, Y., Ray, M.B. and Mujumdar, A.S. 2003. Numerical study on the effect of crossflow on turbulent flow and heat transfer characteristics under normal and oblique semi-confined impinging slot jets. *Drying Technology*. 21(10), 1923-1939.
- Versteeg, H.K. and Malalasekera, W. 1995. An introduction to computational fluid dynamics: The finite volume method. Longman Scientific & Technical, England. 133-155.
- Viskanta, R. 1993. Heat transfer to impinging isothermal gas and flame jets. *Experimental Thermal and Fluid Science*. 6(2), 111-134.
- Xing, Y., Spring, S. and Weigand, B. 2011. Experimental and numerical investigation of impingement heat transfer on a flat and micro-rib roughened plate with different crossflow schemes. *International Journal of Thermal Sciences*. 50(7), 1293-1307.
- Yang, Y.-T. and Wang, Y.-X. 2005. Three-dimensional numerical simulation of an inclined jet with cross-flow. *International Journal of Heat and Mass Transfer*. 48, 4019-4027.

Appendix C4

Journal Paper

Chayut Nuntadusit, Makatar Wae-hayee, Perapong Tekasakul and Smith Eiamsa-ard, Local heat transfer characteristics of array impinging jets from elongated orifices, *International Communications in Heat and Mass Transfer*, Volume 39, Issue 8, October 2012, Pages 1154-1164



Contents lists available at SciVerse ScienceDirect

International Communications in Heat and Mass Transfer

journal homepage: www.elsevier.com/locate/ichmtLocal heat transfer characteristics of array impinging jets from elongated orifices[☆]C. Nuntadusit^{a,*}, M. Wae-hayee^a, P. Tekasakul^a, S. Eiamsa-ard^b^a Energy Technology Research Center and Department of Mechanical Engineering, Faculty of Engineering, Prince of Songkla University, Hat Yai, Songkhla 90112, Thailand^b Department of Mechanical Engineering, Faculty of Engineering, Mahanakorn University of Technology, Bangkok 10530, Thailand

ARTICLE INFO

Available online 18 June 2012

Keywords:

Impinging jets

Cross-flow

Heat transfer enhancement

Elongated orifice

Orifices arrangement

ABSTRACT

The aim of this research is to enhance the heat transfer on an impinging surface under an impinging jet array by minimizing a cross-flow effect. Conventional round orifices (aspect ratio, $AR=1$) are substituted by the elongated orifices with aspect ratio $AR=4$ and 8 with the same jet exit area. Two types of orifice arrangements; in-line and staggered arrays are compared. The experimental investigation was carried out at constant distance from orifice plate to impinged surface $H=2D_E$ (D_E is equivalent diameter of orifice). The heat transfer characteristic was visualized using thermochromic liquid crystal sheet (TLCs) and the Nusselt number distribution was evaluated by an image processing technique. The flow characteristic on the impinged surface was also visualized by oil film technique. The results show that the cross-flow in a case of the jets issued from the orifices with $AR=4$ is considerably less significant than that in cases of the ones delivered from the orifices with $AR=1$ and 8 . At Reynolds number of 13,400, the Nusselt numbers for the jet arrays issued from the elongated orifices with $AR=4$ with in-line and staggered arrangements are respectively 6.04% and 12.52% higher than those for the case of $AR=1$.

© 2012 Elsevier Ltd. All rights reserved.

1. Introduction

Impinging jets are widely used in many industrial applications which required high heat transfer rate on surface such as cooling of gas turbine blade, electronic device or wall of combustion chamber. A typical impinging jet induces an extremely high heat transfer in a stagnation region. However, the heat transfer rate abruptly decreases further away from the region. When the high and uniform heat transfer distribution is required over a wide area for example: drying of film sheet, heating of steel sheet, multiple or array of impinging jets is usually instead. An important parameter that influences on the multiple of jet impingements in a confined space is the cross-flow. Here, the cross-flow is defined as the fluid flow in the direction perpendicular to the jet impingement flow [1]. The cross-flow is formed by the spent air from the impinging jet which is finally exhausted. The cross-flow effect causes an adverse effect on heat transfer on an impinged surface. In order to achieve an efficient heat transfer, the cross-flow effect must be minimized.

Katti and Prabhu [1] investigated the influence of jet-to-jet distance and jet-to-plate distance on heat transfer characteristics of round impinging jets with in-line arrangement on heat transfer. Their results revealed that the maximum heat transfer rate was achieved at $S=4D$ and $H=D$. Brizzi et al. [2] visualized the flow and temperature patterns on the impinged surface of round jet arrays in a cross-flow. They suggested that the cross-flow significantly deforms the impingement

area that located at downstream in confined channel. Bouchez and Goldstein [3] evaluated the local impingement cooling effectiveness and heat transfer coefficients over the interaction area of an air jet impinging on a wall and subjected to a cross-flow of air. It was reported that an impingement cooling effectiveness decreases with the blowing rate especially near the stagnation point. Geers et al. [4] studied the heat transfer in hexagonal and in-line arrays of impinging jets using liquid crystal thermography. Effects of the distance between the impingement plate and the nozzle exit plane on the heat transfer were described. Nuntadusit et al. [5] investigated the effect of the multiple swirling impinging jets on the flow and heat transfer characteristics with different jet-to-jet distances. The flow patterns on an impinged surface were visualized using oil film technique while the distributions of temperature field and Nusselt number on impinged surface were evaluated via a thermochromic liquid crystal sheet coupled with image processing technique. Rhee et al. [6] reported the effects of spent air flows with and without effusion holes on heat/mass transfer on a target plate for array impinging jets. It was found that at small gap distances, the flow without effusion holes caused significantly non-uniform heat/mass transfer coefficients distribution due to the strong effects of a cross-flow and re-entrainments of spent air. When the effusion holes were employed, the uniformity of the distribution was improved. On the other hand, at large gap distances, the effect of cross-flow was weak and the distributions and levels of heat/mass transfer coefficients were similar for both cases. Yan et al. [7] examined the heat transfer on a flat surface under arrays of impinging elliptic jets with different aspect ratios and exit flow conditions using a transient liquid crystal technique. They observed that both aspect ratio and cross-flow significantly

[☆] Communicated by W.J. Minkowycz.

* Corresponding author.

E-mail address: chayut@me.psu.ac.th (C. Nuntadusit).

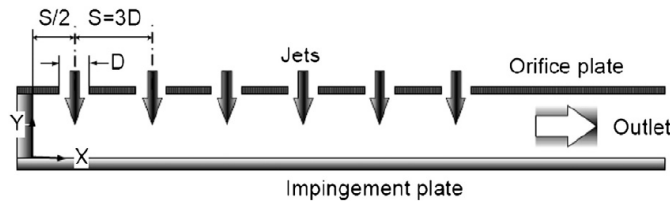


Fig. 1. Experimental model of array of jets impingement.

influenced the axial shift of the impingement/touchdown locations. Yan and Mei [8] reported the heat transfer coefficient distributions over a ribbed surface (broken V-shaped-rib configurations with different exit flow orientations) under impingement of elliptic jet arrays using a liquid crystal thermograph technique. They found that the surface with continuous ribs provides a better impingement heat transfer than that with broken ribs downstream peaks were diminished for increasing cross-flow effect. Chiu et al. [9] investigated the influence of the jet geometries including the aspect ratio (AR) of elliptical jet and jet-to-target spacing on the impinging heat transfer. For the range of AR considered (0.25, 0.5, 1.0, 2.0 and 4.0), the optimum heat transfer performance was achieved at AR = 1.

The heat transfer enhancements by impinging jets with several styles have been numerically investigated. Heo et al. [10] studied the characteristics of the fluid flow and heat transfer of staggered inclined impinging jets on a concave surface using the shear stress transport turbulence model. The effects of the inclination angle of the staggered jet nozzles and the distance between the jet nozzles on the heat transfer performance was also described. Jefferson-Loveday and Tucker [11] used Numerical large-eddy simulation (NLES) to analyze the flow and heat transfer for a round jet impinging on a flat surface at different jet diameters. Rahman et al. [12] investigated the heat transfer characteristics of a free liquid jet discharging from a slot nozzle and impinging vertically on a curved cylindrical shaped plate of finite thickness. They found that the local heat transfer coefficient increased with decreasing nozzle width. Demircan and Turkoglu [13] analyzed the flow and heat transfer characteristics of oscillating air jets impinging on a flat surface. They found that Nusselt number associated with oscillated jets moderately higher than that associated with steady jets. De Lemos and Fischer [14] performed the thermal analysis of an impinging jet on a plate with and without a porous layer. Heat transfer enhancement by the use of the plate with porous layer as compared to that in the case without a porous layer, was achieved only for certain range of values of layer thickness, porosity, and thermal conductivity ratio. Rahman et al. [15] studied the convective heat transfer during free

liquid jet impingement on a hemispherical solid plate of finite thickness. They found that the uniformity of temperature distribution at the solid–fluid interface was improved as thermal conductivity plate materials increased. Rahman and Lallave [16] reported the transient conjugate heat transfer characterization of a free liquid jet impinging on a rotating solid disk of finite thickness and radius. Their results revealed that the duration of the transient increased with disk thickness and decreased with Reynolds number and thermal conductivity ratio.

According to the previously published works [1–4,6–9], cross-flow significantly influences heat transfer characteristics on jet impingement surface. The aim of this research is to improve heat transfer on the impinged surface by optimizing the cross-flow behaviours at low jet-to-plate distance ($H = 2D_e$). Elongated orifices at AR = 4 and 8 with in-line and staggered arrangements, were employed for the purpose and their results were subjected to benchmark with those of the conventional round orifice (AR = 1). The tests were conducted at three different jet Reynolds numbers of 5000, 7500 and 13,400. The heat transfer evaluation criterion is based on a constant jet mass flow rate.

2. Experimental model

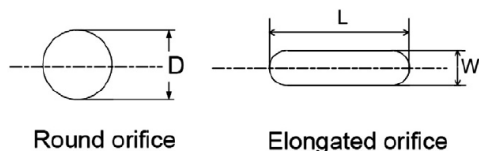
The experimental model is shown in Fig. 1. The multiple jets were discharged from the orifices to impinge on the opposite surface in a confined rectangular duct. The cross-flow is formed by the spent air from the impinging jet which is finally exhausted at one end of the confined area. The jet-to-plate distance was fixed at $H = 2D_e$. The details of orifice geometry used in the present study are shown in Fig. 2. All orifices had the same exit area of 136.8 mm² and each round orifice had an equivalent diameter (D_e) of 13.2 mm. Fig. 3 demonstrates the in-line and staggered arrangements of jet array. Each array consisted of 24 jet holes distributed in 6 columns and 4 rows (6 × 4 jet holes) with constant jet-to-jet distance (S) of 3D. The patterns of the in-line and staggered jet arrays are shown in Fig. 3.

3. Experimental setup and method

3.1. Heat transfer experimental setup and data reduction

Fig. 4 shows schematic diagram of the experimental apparatus. Air jets were generated by the blower (3 hp) and then directed through the temperature controlled chamber with a dimension of 360 mm × 360 mm × 850 mm and the orifice flow meter, respectively. To achieve a uniform air flow approaching to the orifice plate, the jet chamber was equipped with two perforated plates and two mesh plates. The jet chamber temperature referred as inlet temperature (T_i) of test section was kept constant 27 °C. The Reynolds number of a jet was varied at 5000, 7500 and 13,400.

The air jets discharged from the orifice plate, were impinged on the electrical heated surface for cooling. The heat transfer surface was made of stainless steel foil (30-µm-thickness) attached with TLC sheet (Omega Engineering, LCS-95) on the rear of the impinged surface. The stainless steel foil was installed between a pair of copper



Round orifice Elongated orifice

AR=1	D = 13.2 mm	
AR=4	L = 24 mm	W = 6 mm
AR=8	L = 33.6 mm	W = 4.2 mm

Fig. 2. Orifice geometries with identical cross-section area.

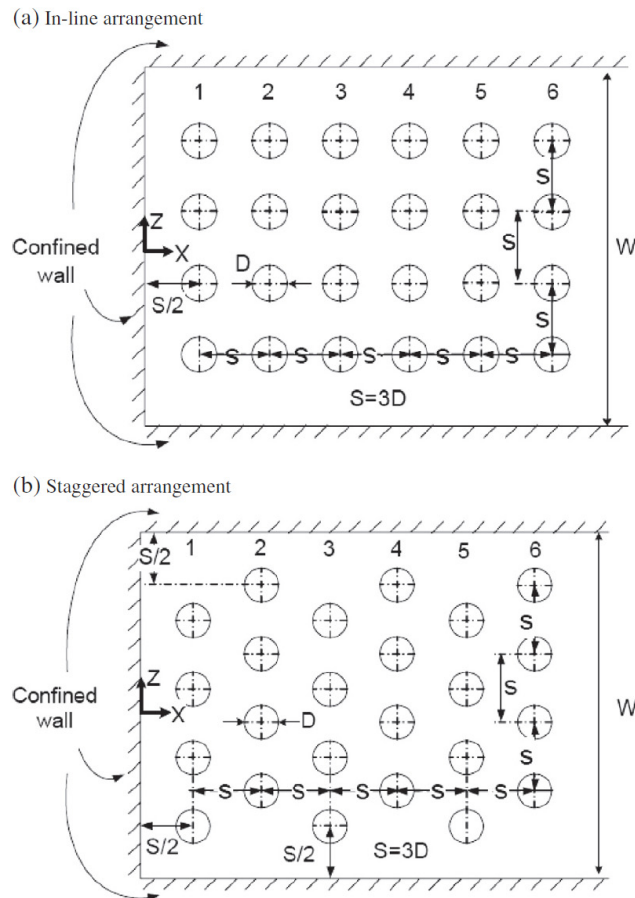


Fig. 3. Jet arrangement (Nos. 1 to 6 represent the number of jets column): (a) in-line arrangement and (b) staggered arrangement.

bus bars. The heat transfer surface was heated by DC power supply that can supply current up to 50 A through copper bus bars. An electrical energy dissipated in the stainless steel foil can be calculated from

$$\dot{Q}_{input} = I^2 \cdot R \quad (1)$$

where here, I is the electrical current and R is the electric resistance of stainless steel foil.

The local heat transfer coefficient (h) can be evaluated from

$$h = \frac{\dot{Q}_{input} - \dot{Q}_{losses}}{A(T_w - T_j)} = \frac{\dot{q}_{input} - \dot{q}_r - \dot{q}_c}{T_w - T_j} \quad (2)$$

where $\dot{q}_r = \sigma \epsilon_{TLC} (\overline{T_w}^4 - T_s^4)$ and $\dot{q}_c = \overline{h}_c (\overline{T_w} - T_s)$ are the heat loss transferred to the environment by radiation and convection. Here, $\overline{T_w}$ and T_j are average wall temperature and a jet temperature, σ is a Stefan-Boltzman constant, ϵ_{TLC} is an emissive coefficient of TLCs ($=0.9$) [4]. T_s is a surrounding temperature and \overline{h}_c is a natural heat

transfer coefficient for the heat loss from the TLC to the surrounding air.

The wall temperature (T_w) on the impinged surface was measured by using TLC sheet that attached on the rear of the impinged surface. The CCD camera was used to capture color patterns on TLC sheet. The images of color pattern were subsequently converted from the RGB (Red, Green and Blue) color system to the HSI (Hue, Saturation and Intensity) color system. The Hue (H) value was used to correlate the color of TLC to their temperature in range of 28–40 °C via a calibration. The local Nusselt number was calculated from

$$Nu = hD_E/k \quad (3)$$

where, D_E is the equivalent diameter of an orifice and k is a conductivity of an air jet.

An average Nusselt number was calculated from

$$\overline{Nu} = \frac{\overline{h}D_E}{k} \quad (4)$$

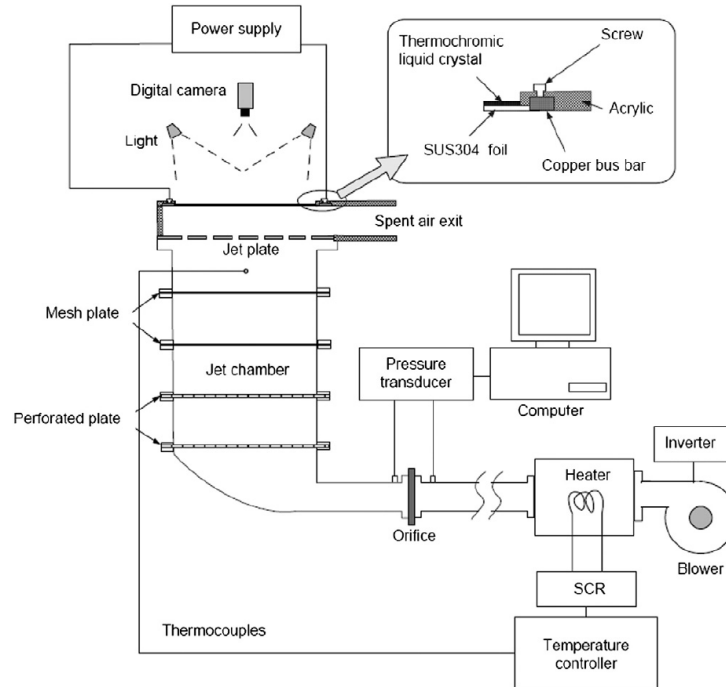


Fig. 4. Schematic diagram of the experimental setup.

where here, the average heat transfer coefficient \bar{h} was calculated from Eq. (2) by replacing T_w with \bar{T}_w .

3.2. Flow visualization on the impinged surface

The flow visualization on the impinged surface was performed using oil film technique. The oil film was prepared by mixing liquid paraffin with titanium dioxide and oleic acid. The transparent plastic plate uniformly painted with oil film was employed to represent the impinged surface. During the experiment, the oil film behavior on the impinged surface was recorded using a CCD camera every 30 seconds.

4. Results and discussions

4.1. Flow patterns on impinged surface

The flow visualization on the impinged surface by oil film technique is shown in Fig. 5(a–f) at $Re = 13,400$. The black area is an impinged surface where an oil film removed while the white area corresponds to remaining oil film. A white points in the middle of black areas represent a stagnation point of jet bounded by jet impingement region. The circles or smooth rectangles marked on the impinged plate are the positions of the orifices. For all cases, the effect of a cross-flow becomes more significant as the axial distance of the cross-flow increases due to the accumulation of an upstream spent air. The effect is notified by the shifting of a center of an impingement jet downstream of the position of an orifice as well as an uneven shape of the impinged jets because the jets are carried along the axial direction by the cross-flow. In addition, the momentum of impinging jet on a impinged surface is weakened as transferred axially

by the effect of the cross-flow. Obviously, the characteristics of impinged surface depend strongly on the geometry and arrangement of jet. The influence of the cross-flow on the impinged jets with an in-line arrangement is less prominent than that on the ones with a staggered arrangement. These results are related to their geometries as the downstream jets with an in-line arrangement are partly concealed from the cross-flow by the upstream ones while the downstream jets with a staggered arrangement are directly exposed to the cross-flow.

For both in-line and staggered jet arrays, the downstream jets issued from round orifices ($AR = 1$) are more significantly affected by the cross-flow than those at higher AR . Especially for the staggered jet array, some of impinging jets in the last column (column No. 6) are almost completely cancelled (Fig. 5(d)), because the large space between jets in an axial direction allows the cross-flow moves more thoroughly. With $AR = 4$, downstream jets seem to be better concealed from the cross-flow especially for the in-line jet array notified by a larger impinged area as well as a more uniform impinging pattern on the impinged surface. However, at $AR = 8$, each jet possesses a large contact between its circumference and the cross-flow along an axial direction, results an increase of a cross-flow effect as compared to that at $AR = 4$, but the effect seems to be less significant than that at $AR = 1$. Therefore for the present range, it can be justified that the cross-flow effect is minimized by the use of the jets with in-line arrangement at AR of 4.

4.2. Local Nusselt number on impinged surface

The Nusselt number distributions on impinged surfaces at $Re = 13,400$, 7500 and 5000 are shown in Figs. 6, 7 and 8. In general, with

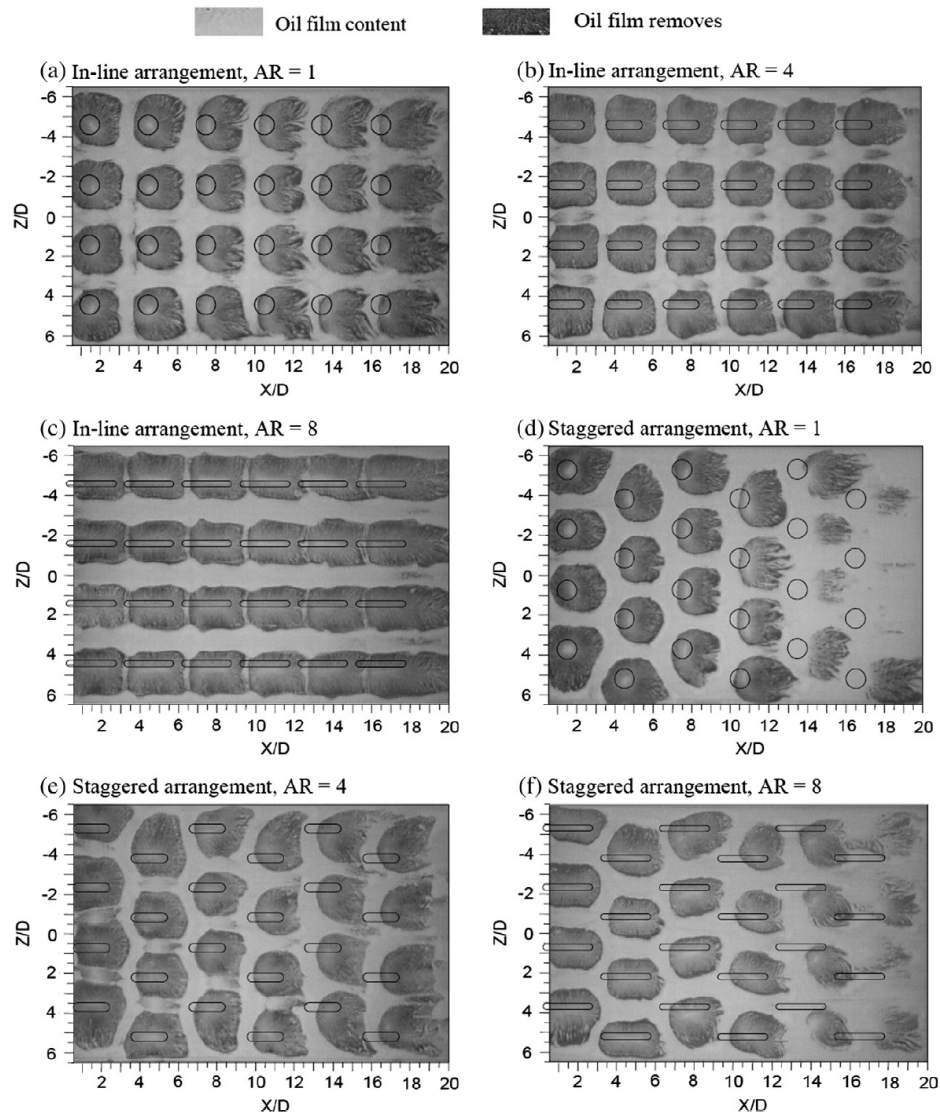


Fig. 5. Flow patterns on the impinging surface ($Re = 13,400$): (a) in-line arrangement, $AR = 1$, (b) in-line arrangement, $AR = 4$, (c) in-line arrangement, $AR = 8$, (d) staggered arrangement, $AR = 1$, (e) staggered arrangement, $AR = 4$ and (f) staggered arrangement, $AR = 8$.

increasing Reynolds number, Nusselt number increases while the Nusselt number distribution pattern slightly changes. The characteristic of heat transfer accords with the flow pattern on the impinging surface shown in Fig. 5. Apparently, Nusselt number associated by the jets with an in-line arrangement are less significantly affected by the cross-flow than those with staggered arrangement indicated by a more uniform Nusselt number distribution on the impinging surface. For the in-line jet arrays at all ARs, Nusselt number of downstream jets is just slightly decreased compared to those of the upstream ones.

On the other hand, for the staggered jet arrays with $AR = 1$ and 8 , Nusselt number is dramatically changed with increasing axial distance (X/D). Only at $AR = 4$, Nusselt number is gradually decreased along the axial direction.

Fig. 9(a–c) shows the local Nusselt number distribution at $Z/D = 0$ and 1.5 for the in-line jet arrays. At $Z/D = 1.5$, the profiles of Nusselt number distributions are similar to the shapes of the orifices producing impinging jets and the width of peak is corresponded to the diameter of round orifices or the length of the elongated ones. Obviously,

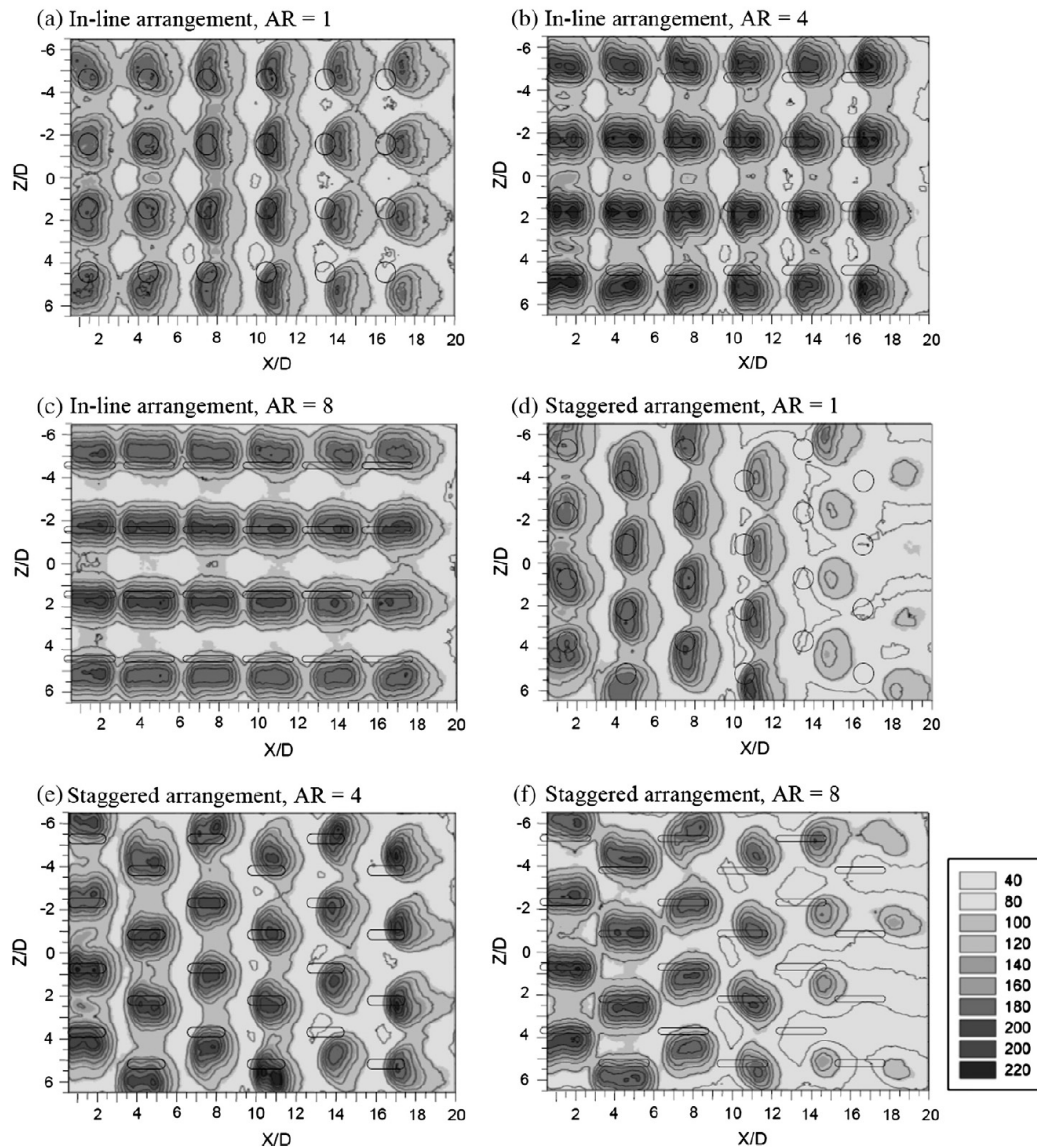


Fig. 6. Nusselt number distribution on the impinging surface in the case of $Re = 13,400$ ($T_f = 27^\circ\text{C}$): (a) in-line arrangement, $AR = 1$, (b) in-line arrangement, $AR = 4$, (c) in-line arrangement, $AR = 8$, (d) staggered arrangement, $AR = 1$, (e) staggered arrangement, $AR = 4$ and (f) staggered arrangement, $AR = 8$.

the jets at $AR = 4$ provide the highest peak as a result of the minimum cross-flow effect as mentioned above. At $Z/D = 0$ (interval between rows of orifices), the profiles for the cases of $AR = 1$ and 4 are in a typical shape with small heights while that for the case of $AR = 8$ is rather flatten since the position is far from the circumferences of jets.

The local Nusselt number distributions at $Z/D = 2.25$ for the staggered jet arrays are demonstrated in Fig. 9(d-f). In general, the change

of Nusselt number distribution for staggered jet arrays is considerably more obvious than that found for in-line jet arrays. Particularly the cases of $AR = 1$ and 8 , in which Nusselt number abruptly decrease along a cross-flow direction resulting in rather flatten peaks beyond X/D of 10 . A decaying of Nusselt number and a shifting of the peak as a result of cross-flow effect, are also found in the case of the staggered jet arrays with $AR = 4$, however, the changes are less significant than other two cases.

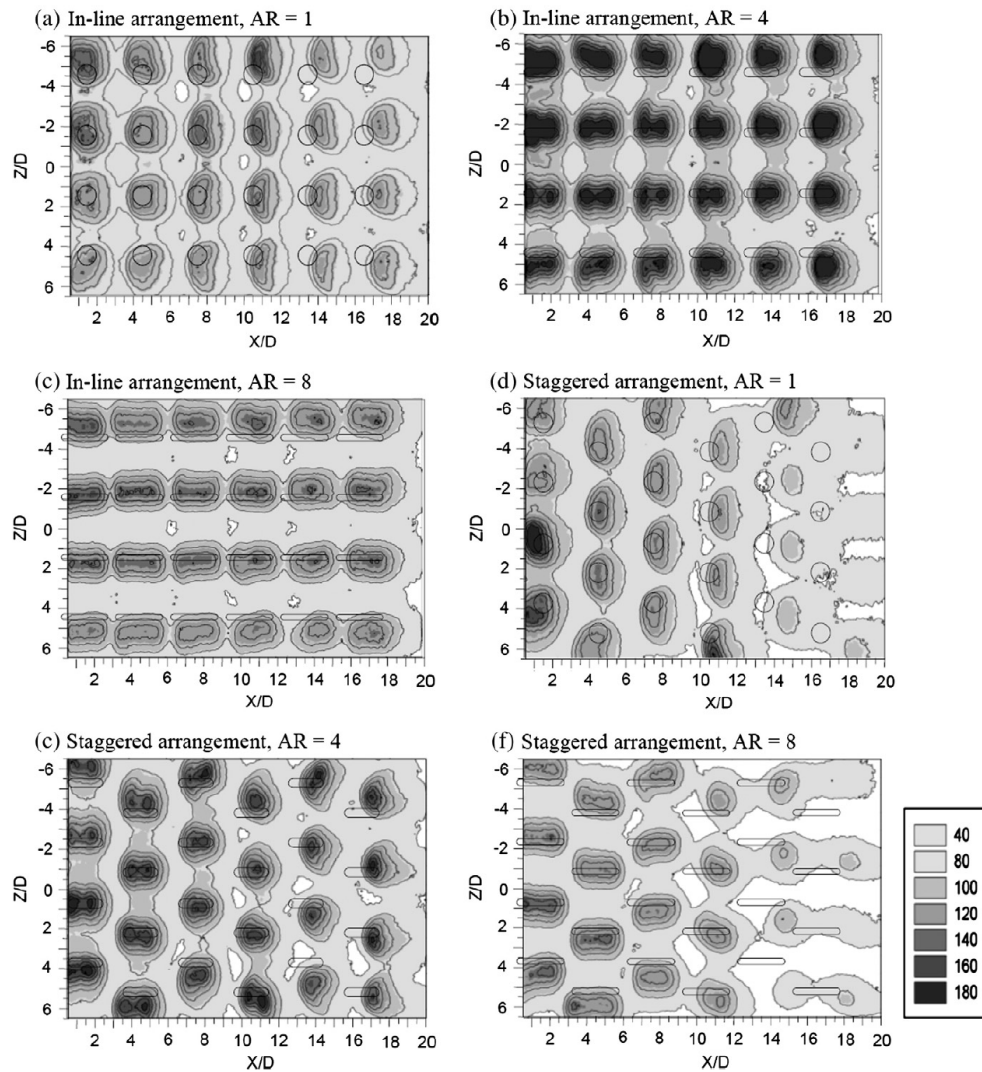


Fig. 7. Nusselt number distribution on the impinging surface in the case of $Re = 7,500$ ($T_j = 27^\circ\text{C}$): (a) in-line arrangement, $AR = 1$, (b) in-line arrangement, $AR = 4$, (c) in-line arrangement, $AR = 8$, (d) staggered arrangement, $AR = 1$, (e) staggered arrangement, $AR = 4$ and (f) staggered arrangement, $AR = 8$.

Fig. 10(a–c) presented the spanwise average Nusselt number for all cases. It can be observed that for the in-line jet array at $AR = 1$ for $Re = 7,500$ and $13,400$ Nusselt number peak of the jet of column No.3 is higher than others. This can be a result of an extra turbulence around the position caused by a moderate cross-flow effect. Beyond column No.3, the cross-flow effect is significant, thus momentum is mainly transfer in a cross-flow direction leading to a weakened momentum on the impinging surface. At low Reynolds number ($Re = 5,000$), the height of Nusselt number peak is comparable for all in-line jet arrays because the jet with a low flow rate produces insignificant cross-flow effect. For staggered jet arrays at $AR = 1$ and 8 , Nusselt number

peak monotonically and substantially decreases due to a significant cross-flow effect. This results in remarkable difference between an upstream Nusselt number and downstream ones. For both in-line and staggered arrays at $AR = 4$, Nusselt number peaks are found to be slightly decreased due to the low cross-flow effect as mentioned previously.

4.3. Average Nusselt number on impinging surface

The average Nusselt number on the impinging surface was calculated using average temperature in area of $-6.5 < Z/D < 6.5$ and $0.5 < X/D < 20$. The results for all cases are compared in Fig. 11. At similar conditions,

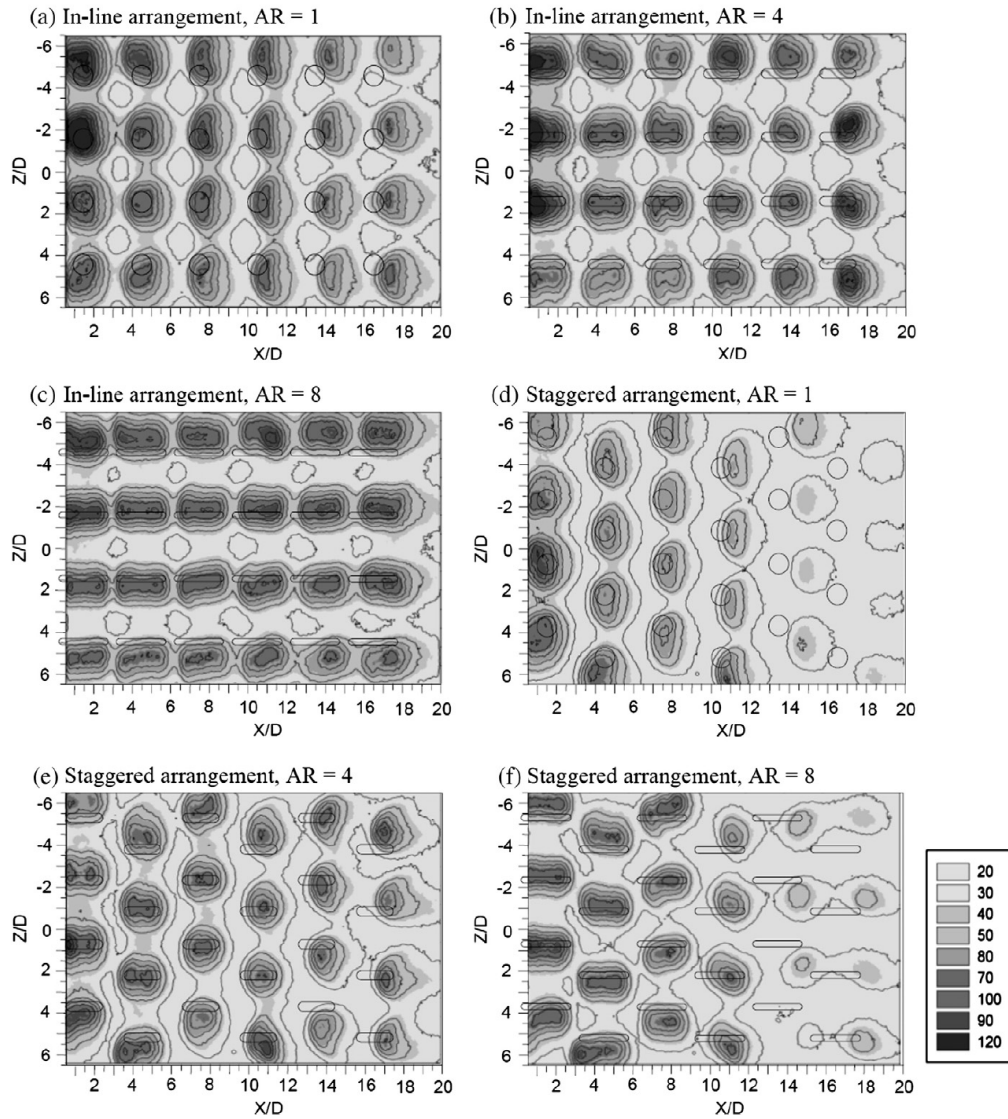


Fig. 8. Nusselt number distribution on the impinging surface in the case of $Re = 5000$ ($T_j = 27^\circ\text{C}$): (a) in-line arrangement, $AR = 1$, (b) in-line arrangement, $AR = 4$, (c) in-line arrangement, $AR = 8$, (d) staggered arrangement, $AR = 1$, (e) staggered arrangement, $AR = 4$ and (f) staggered arrangement, $AR = 8$.

Nusselt number associated with the use of in-line jet array is consistently higher than that by the use of staggered one. Among the cases determined, the in-line jet array with $AR = 4$ offer the highest Nusselt number which is comparable to that with $AR = 8$ at some Reynolds numbers. On the other hand, the staggered arrays at $AR = 1$ and

8 give comparable Nusselt numbers which are considerably lower than those of the other cases, due to the severe cross-flow effect. In case of in-line arrangement, the average Nusselt numbers for the jet arrays issued from the elongated orifices with $AR = 4$ and 8 are respectively 6.04% and 5.54% higher than that for the case of $AR = 1$ (the

typically round orifices). However, for the staggered arrangement, Nusselt number for the jet array delivered from the elongated orifices with AR=4 is 12.52% higher while that obtained from the orifices with AR=8 is 1.15% lower than that for the case of AR=1.

5. Conclusions

In the present study, the effects of the orifice geometry and jet flow arrangement have been experimentally investigated. The results of elongated orifices with aspect ratio (AR)=4 and 8 are compared with those of the ones with AR=1 (the typically round orifices). The jet arrangements determined are in-line and staggered arrays. The main findings are shown as follows;

1. The cross-flow in a case of the jets issued from the orifices with AR=4 is considerably less significant than that in cases of the ones delivered from the orifices with AR=1 and 8.
2. The influence of the cross-flow on the impinging jets with an in-line arrangement is less prominent than that on the ones with a staggered arrangement.
3. Among the cases examined, the in-line jet array at AR=4 gives the most efficient heat transfer on the impinging surface corresponding to the minimum cross-flow effect.

Acknowledgment

This research was supported by grants from Thailand Energy Policy and Planning Office, Ministry of Energy, the Graduate School and Faculty of Engineering, Prince of Songkla University.

References

- [1] V. Katti, S.V. Prabhu, Influence of spanwise pitch local heat transfer distribution for in-line arrays of circular jets with air flow in two opposite, *Experimental Thermal and Fluid Science* 33 (2008) 84–95.
- [2] L.E. Brizzi, A. Bernard, J.L. Bousgarbies, E. Dorignac, J.J. Vullierme, Study of several impinging jet, *Journal of Thermal Science* 9 (2000) 217–223.
- [3] J.P. Bouchez, R.J. Goldstein, Impingement cooling from a circular jet in a cross-flow, *International Journal of Heat and Mass Transfer* 18 (1975) 719–730.
- [4] L.F.G. Geers, M.J. Tummers, T.J. Bueningk, K. Hanjalic, Heat transfer correlation for hexagonal and in-line arrays of impinging jets, *International Journal of Heat and Mass Transfer* 51 (2008) 5389–5399.
- [5] C. Nuntadusit, M. Wae-hayee, A. Bunyajitradulya, S. Eiamsa-ard, Heat transfer enhancement by multiple swirling impinging jets with twisted-tape swirl generators, *International Communication in Heat and Mass Transfer* 39 (2012) 202–207.
- [6] D.H. Rhee, P.H. Yoon, H.H. Cho, Local heat/mass transfer and flow characteristics of array impinging jets with effusion holes ejecting spent air, *International Journal of Heat and Mass Transfer* 46 (2003) 1049–1061.
- [7] W.M. Yan, S.C. Mei, H.C. Liu, C.Y. Soong, W.J. Yang, Measurement of detailed heat transfer on a surface under arrays of impinging elliptic jets by a transient liquid crystal technique, *International Journal of Heat and Mass Transfer* 47 (2004) 5235–5245.
- [8] W.M. Yan, S.C. Mei, Measurement of detailed heat transfer along rib-roughened surface under arrays of impinging elliptic jets, *International Journal of Heat and Mass Transfer* 49 (2006) 159–170.
- [9] H.C. Chiu, J.H. Jang, W.M. Yan, Experimental study on the heat transfer under impinging elliptic jet array along a film hole surface using liquid crystal thermograph, *International Journal of Heat and Mass Transfer* 52 (2009) 4435–4448.
- [10] M.W. Heo, K.D. Lee, K.Y. Kim, Parametric study and optimization of staggered inclined impinging jets on a concave surface for heat transfer augmentation, *Numerical Heat Transfer, Part A: Applications* 61 (2012) 442–462.
- [11] R.J. Jefferson-Loveday, P.G. Tucker, Wall-resolved les and zonal les of round jet impingement heat transfer on a flat plate, *Numerical Heat Transfer, Part B: Fundamentals* 59 (2011) 190–208.
- [12] M.M. Rahman, C.F. Hernandez, J.C. Lallave, Free liquid jet impingement from a slot nozzle to a curved plate, *Numerical Heat Transfer, Part A: Applications* 57 (2010) 799–821.

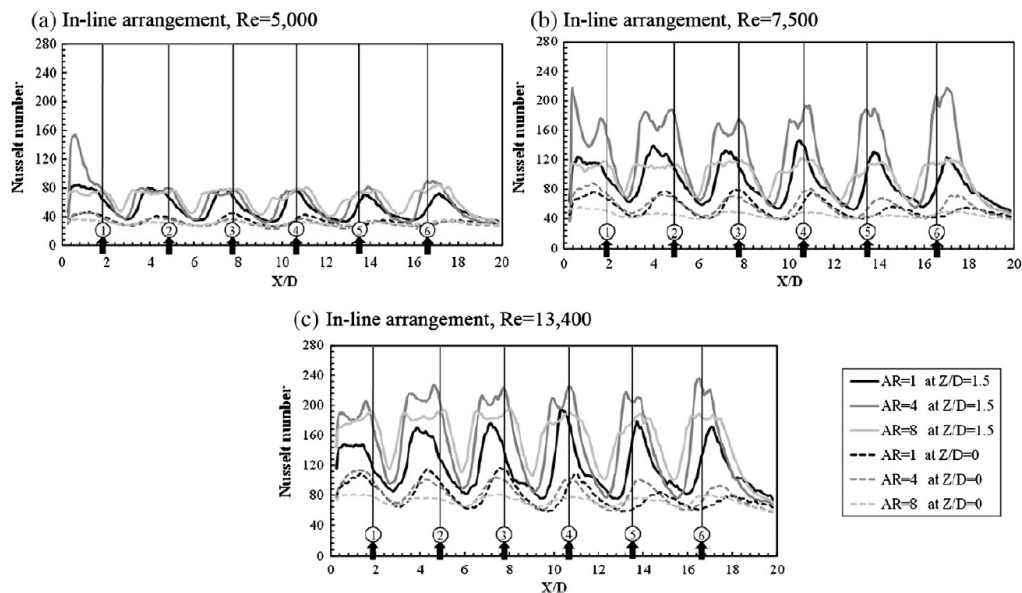


Fig. 9. Local Nusselt number distribution along cross-flow direction ($T_j = 27^\circ\text{C}$): (a) $Re = 5000$, in-line arrangement, (b) $Re = 7500$, in-line arrangement, (c) $Re = 13,400$, in-line arrangement, (d) $Re = 5000$, staggered arrangement, (e) $Re = 7500$, staggered arrangement and (f) $Re = 13,400$, staggered arrangement.

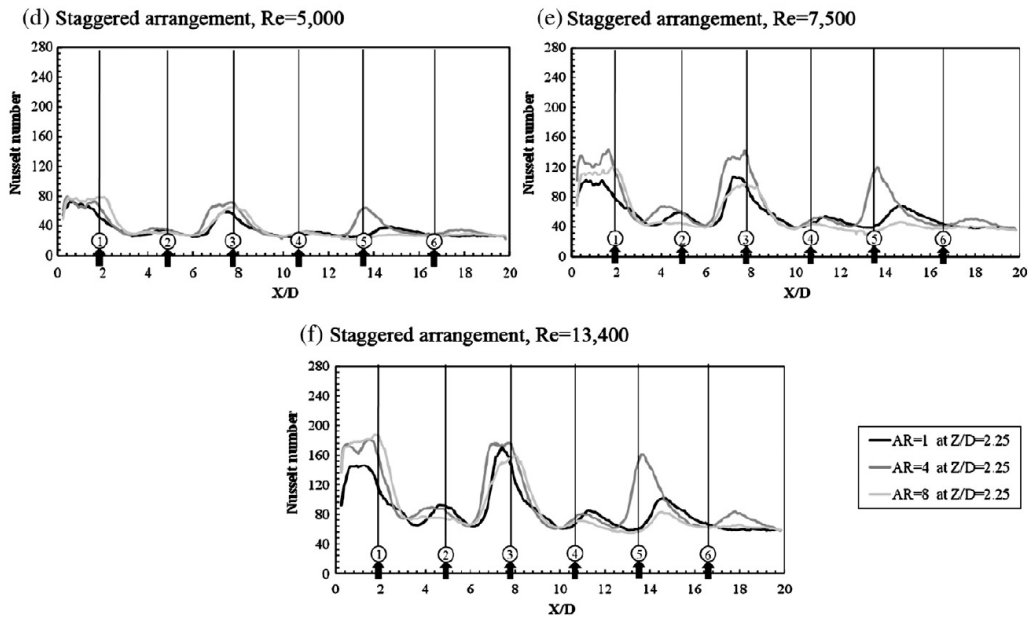


Fig. 9. (continued).

[13] T. Demircan, H. Turkoglu, The numerical analysis of oscillating rectangular impinging jets, *Numerical Heat Transfer, Part A: Applications* 58 (2010) 146–161.
 [14] M.J.S. De Lemos, C. Fischer, Thermal analysis of an impinging jet on a plate with and without a porous layer, *Numerical Heat Transfer, Part A: Applications* 54 (2008) 1022–1041.

[15] M.M. Rahman, J.C. Lallave, C.F. Hernandez, Convective heat transfer from a thick hemispherical plate during free liquid jet impingement, *Numerical Heat Transfer, Part A: Applications* 54 (2008) 581–602.
 [16] M.M. Rahman, J.C. Lallave, Transient conjugate heat transfer during free liquid jet impingement on a rotating solid disk, *Numerical Heat Transfer, Part A: Applications* 55 (2009) 229–251.

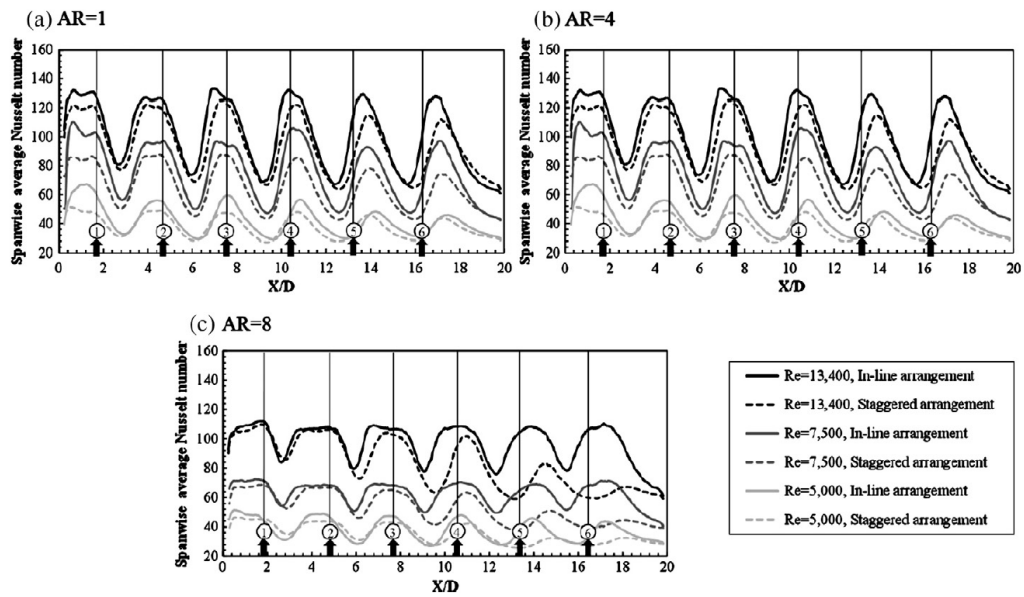


Fig. 10. Spanwise average Nusselt number: (a) AR=1, (b) AR=4 and (c) AR=8.

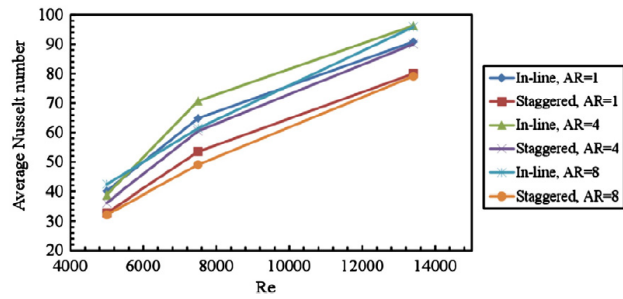


Fig. 11. Average Nusselt number.

Appendix C5

Journal Paper

M. Wae-hayee, P. Tekasakul, and C. Nuntadusit, “Effect of Attacking Angle of Elongated Orifice on the Flow and Heat Transfer Characteristics of Jet Impingement Array”, **This manuscript is being drafted.**

Effect of Attacking Angle of Elongated Orifice on the Flow and Heat Transfer Characteristics of Jet Impingement Array

Makatar Wae-hayee, Perapong Tekasakul and Chayut Nuntadusit*
Energy Technology Research Center and Department of Mechanical Engineering,
Faculty of Engineering, Prince of Songkla University, Hat Yai, Songkhla, 90112 Thailand.

E-mail: chayut@me.psu.ac.th*

Abstract

The objective of this research is to study the attacking angle effect of elongated orifice with $AR = 4$ and 8 on the flow and heat transfer characteristics of jet impingement array. Both the inline and staggered arrangements, having arrays of 6×4 nozzles and attacking angles in the range of $\theta = 0^\circ$ to $\theta = 45^\circ$ were examined. The jet-to-plate distance (H) and the jet-to-jet distance (S) were fixed at $H = 2D_E$ and $S = 3D_E$, respectively (where D_E is the equivalent diameter). The experiments were carried out under jet Reynolds number in the range of $Re = 5,000$ to $Re = 13,400$. Temperature distributions on the impingement surface were measured using Thermo-chromic Liquid Crystal sheet (TLCs). Flow characteristics on the impingement surface were visualized using the oil film technique. Numerical simulation employed to gain insight into the fluid flow was via computational fluid dynamics (CFD). The results indicate that the average heat transfer on the impingement surface tends to decrease when the attacking angle becomes larger. However, local heat transfers at impingement regions in the upstream channel with larger attacking angles, $\theta = 30^\circ$ and 45° , are higher than those at $\theta = 0^\circ$ and 15° , especially in the case of staggered arrangement.

Keywords: Impinging jet array, Heat transfer enhancement, Cross-flow, Thermo-chromic Liquid Crystal sheet (TLCs), Oil film technique, CFD

1. Introduction

Impinging jets are widely used in thermal industrial processes to efficiently enhance heat transfer rate on an impingement surface. Their applications include cooling in gas turbine blades and electronic components, textiles and paper drying, glass and metal sheet quenching, and solar air heater system [1-4]. Many previous works have been devoted to the study of flow and heat transfer characteristics of multiple impinging jets in a confined space [5-7]. Flow and heat transfer characteristics of multiple impinging jets are influenced by

interaction between adjacent jets before impingement on the surface and the wall jets formed by the adjacent jets colliding on the target surface [8]. One other factor that influences multiple impinging jets in a confined space is the cross-flow, defined as the fluid flow in the direction perpendicular to the jet impingement flow. Cross-flow has been found to significantly reduce the heat transfer of downstream impinging jets [9-11]. In more recent works, drilling of effusion holes, on the upper surface (nozzle plate) [12, 13], and at the lower surface (impingement surface) [14], in confined

channel to eliminate the cross-flow has been attempted to enhance the heat transfer rate.

Nuntadusit et al. [15] have replaced conventional round orifices with elongated orifices to reduce the effect of cross-flow on the jet impingement array. They have found that the heat transfer rate using impinging jets issuing from these substituted orifices is more uniform and higher than those from conventional orifices. Another approach to enhance the heat transfer rate is to produce longitudinal vortices near the inclined rectangular blocks mounted on a smooth surface [16, 17]. To apply the inclination interaction between the cross-flow and the jet issuing from the elongated orifice, the attacking angle, defined as the major axis of the elongated orifice to the cross-flow direction, should be examined.

The aim of the present study is to investigate the heat transfer enhancement due to the attacking angle effect of the elongated orifice. The inline and staggered arrangement were experimentally and numerically investigated. The temperature distribution on the impingement surface was measured using a Thermo-chromic Liquid Crystal sheet (TLCs), and the Nusselt number distribution was evaluated using an image processing method. The oil film technique was used to visualize the characteristic of the flow on the impingement surface. The numerical simulation employed to gain insight into the fluid flow was via a commercial ANSYS ver. 13.0, Fluent software.

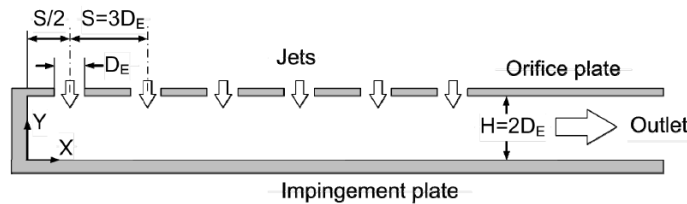


Fig. 1. Experimental model

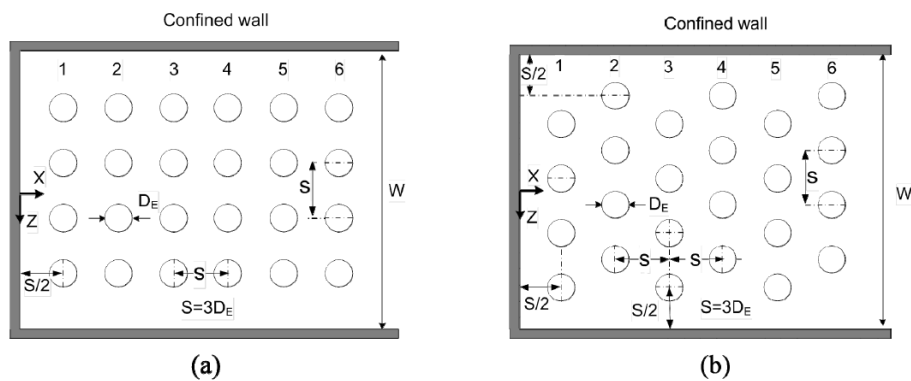


Fig. 2. Jet arrangement (Number 1 to 6 are the jet column) : (a) inline arrangement and (b) staggered arrangement

2. Experimental setup and method

2.1 Experimental model and parameters

An experimental model of jets discharging from orifices and impinging normal to the opposite surface in a confined

rectangular duct is shown in Fig.1. The spent jet flowing parallel to the channel exit, called cross-flow, is exhausted at one end of the duct. The origin of the Cartesian coordinate system was located at the impingement

surface. The Y-axis is normal to the target surface, while the X- and the Z-axes are, respectively, along the streamwise and the spanwise directions of the cross-flow.

AR=1	$D_E=13.2$ mm	
AR=4	L= 24 mm	W= 6 mm
AR=4	L= 33.6 mm	W= 4.2 mm
Attacking angle	$\theta=0^\circ, 15^\circ, 30^\circ$ and 45°	

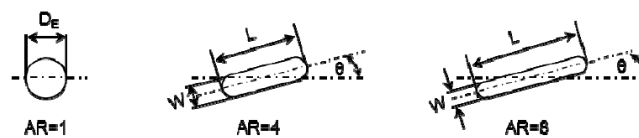


Fig. 3. The details of orifice geometries with identical cross-section area and attacking angle.

The arrays of jet configuration, both for the inline and staggered arrangements, consist of 24 jet holes distributed in 6 columns and 4 rows as shown in Fig.2. All orifices having $AR=1, 4$ and 8 have the same exit area of 136.8 mm^2 , and each round orifice has an equivalent diameter (D_E) of 13.2 mm, as shown in Fig.3. The attacking angle, defined as the angle between the major axis of the elongated orifice to the cross-flow direction (X-axis), was varied as $\theta=0^\circ, 15^\circ, 30^\circ$ and 45° , shown also in Fig.3. The jet-to-plate distance was fixed at $H=2D_E$, and both arrangements have constant jet-to-jet distance of $S=3D_E$. The experiments were carried out at jet Reynolds number, based on the average velocity and D_E , of $Re=5,000, 7,500$ and $13,400$. More details regarding the experimental model have been described in the recent sequential works [15, 18].

2.2 Experimental setup

The schematic diagram of this experimental apparatus is shown in Fig.4 [15, 18]. Heated air was forced through a calibrated orifice flow meter and into the jet

chamber. To ensure a uniform flow field approaching the orifice plate, the jet chamber is equipped with two layers of perforated plates and two layers of mesh plates. The jet temperature, referred to as the inlet temperature (T_j) of the test section, was kept at $27.0^\circ\text{C}, \pm 0.2^\circ\text{C}$.

2.3 Heat transfer measurement and data reduction

The air jets with constant temperature discharging from the orifice plate were impinged on the heated surface for cooling. The wall temperature on the impingement surface was measured by using the TLC sheet attached on the rear of this surface. The CCD camera was used to capture color patterns on the TLC sheet, and the images of the color patterns were subsequently translated into temperatures via a calibration [15, 18].

The local Nusselt number was calculated from:

$$Nu = \frac{hD_E}{k} \quad (1)$$

where, D_E is the equivalent diameter of the orifice and k is a thermal conductivity of the air jet.

An average Nusselt number was calculated from:

$$\overline{Nu} = \frac{\overline{h}D_E}{k} \quad (2)$$

where \overline{h} was the average heat transfer coefficient.

2.4 Flow visualization on the impinged surface

Flow visualization on the impingement surface was carried out using the oil film technique. The oil mixture was prepared from liquid paraffin, titanium dioxide and oleic acid. A transparent plastic plate was used as the jet impingement wall and was uniformly coated by the oil. A video camera was used to record oil film patterns on the impingement surface.

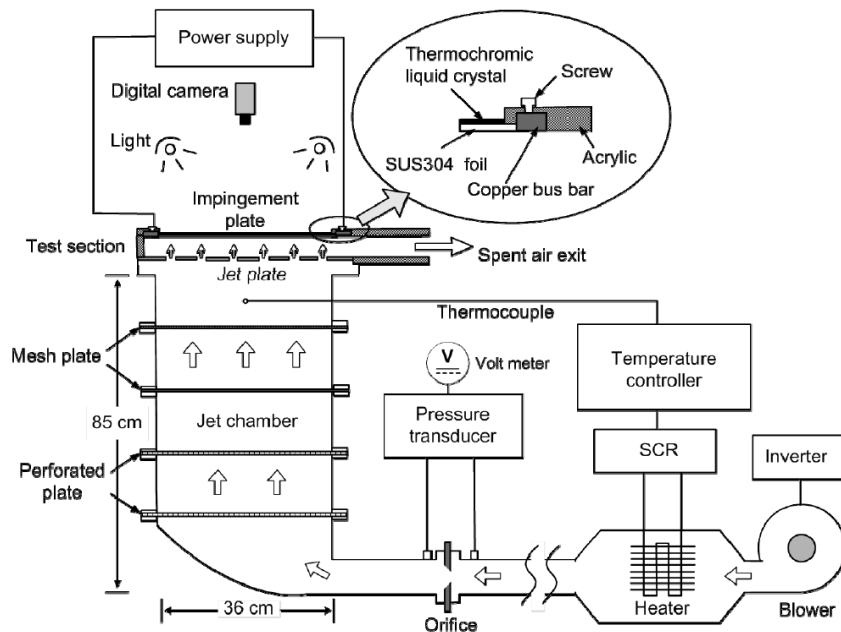


Fig. 4. Schematic of the experimental setup

2.5 Numerical simulation

Flow characteristics of the impinging jets in the confined channel were visualized by computational fluid dynamics (CFD) technique. The commercial package ANSYS (ver.13.0) was used in this present study. The numerical model was identical to the experimental model in its geometries, dimensions, and jet Reynolds number. Computations were conducted by solving continuity and Navier-stokes equations under

existing boundary conditions with SST turbulence model. This turbulence model has been adopted in solving many numerical simulations of jet impingement problems [19, 20].

The non-uniform grid system was finely generated for regions near the orifice holes and the impingement surface. The number of generated grid was varied to achieve an accurate solution with low computation cost. All boundary conditions applied were identical to those specified in the

experimental conditions. Solutions were considered to be convergent when the normalized residual of all algebraic equations is less than the prescribed value of

1×10^{-4} . Details of numerical techniques employed in this article have been described in Wae-hayee M., et al. [18].

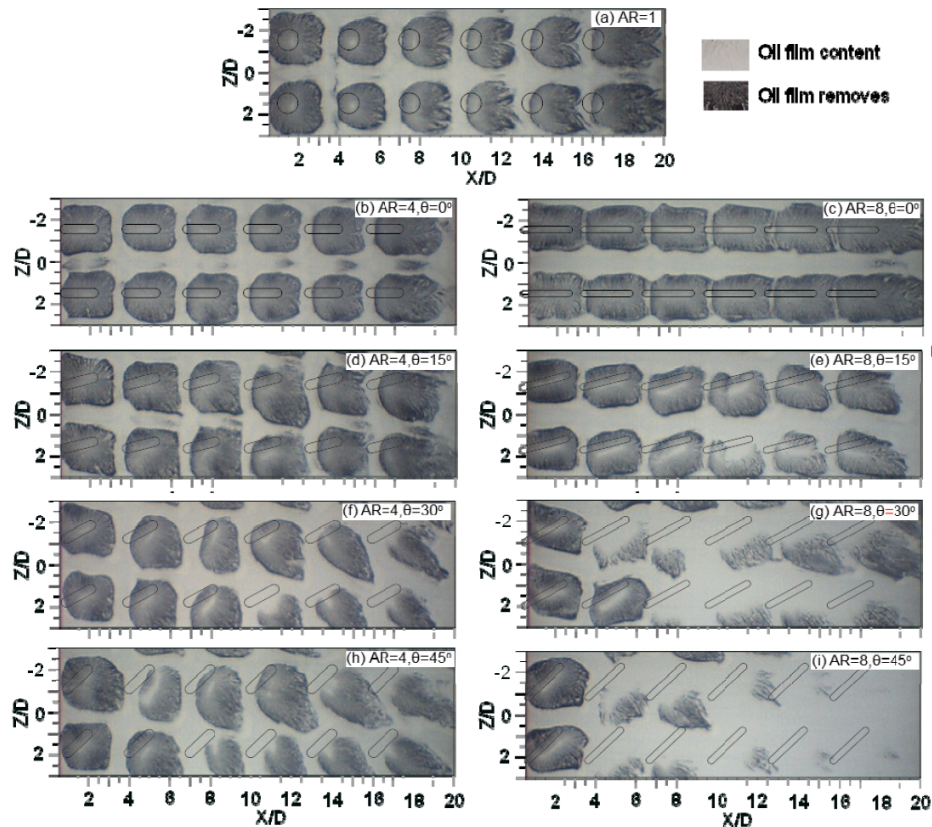


Fig. 5. Flow patterns on the impingement surface with oil film technique for the inline arrangement and $Re=13,400$ (Experimental results).

3. Results and discussions

3.1 Flow characteristics

Flow patterns of impinging jets on the impingement surface using the oil film technique are shown in Fig.5 and 6. The black regions represent the impingement areas where the oil film has been completely removed, and the white regions represent those with original oil film coating. The flow patterns on the impingement surface with $AR=1$, $AR=4$ and $AR=8$ with $\theta=0^\circ$ as shown in Fig.5(a)-(c) for the inline arrangement and

(a)-(c) for the staggered arrangement, are taken from [15] for comparison with results from the present study.

The velocity vector and contour in the Y-axis on Z-X plane near the impingement surface (1 mm above the surface) are shown for the inline arrangement in Fig.7 and for the staggered arrangement in Fig.8. Because the condition at the surface is no-slip, this position is chosen to represent the plane sufficiently near the surface. The Y-component velocity represents the velocity in the direction normal to the impingement

surface, with positive direction towards the downstream of the jet that impinges on the wall. Area of high Y-component velocity contour identifies the impingement region of each cell. These velocity contours of both jet arrangements agree well with the flow patterns on the impingement surface as

shown earlier in Fig.5 and 6 by notifying area of high Y-component velocity of CFD corresponding to the black area of oil film. This good agreement can be correspondingly used to explain the characteristics of jets flow from the CFD results on the heat transfer behavior in the next section

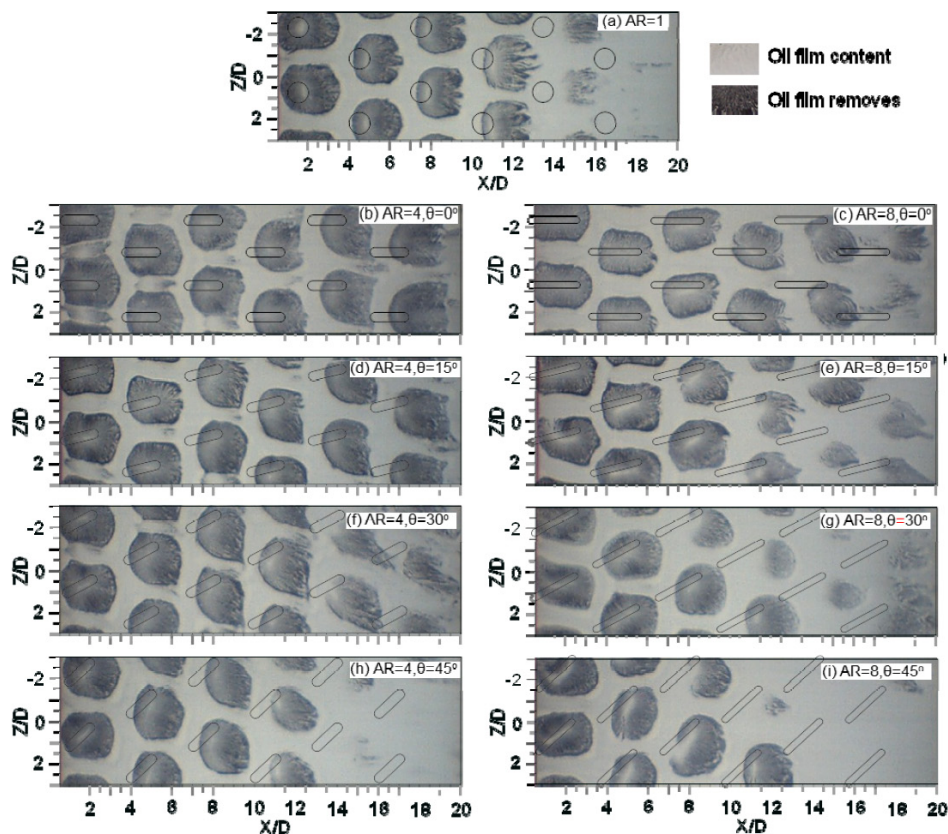


Fig. 6. Flow patterns on the impingement surface with oil film technique for the staggered arrangement and $Re=13,400$ (Experimental results).

For both inline and staggered arrangements of $AR=1$ as shown in Fig.6(a) and Fig.7(a), the impingement area of each cell are shifted to downstream direction due to the effect of cross-flow. This cross-flow effect on jet impingements with inline arrangement is less significant than on the ones with the staggered arrangement by notifying cancellation of the impingements at downstream region ($13 < X/D < 20$). This flow

characteristic can be explained that the cross-flow can easily pass through space between rows of inline jets, whereas it was blocked by downstream jets in the case of staggered arrangement [18]. It can be seen that there are no impingement regions (Black areas) at the last jet column in Fig.6(a) and no areas of high Y-component velocity contour at the same jet column as shown in Fig.8(a). It can also be observed that the deflection of

downstream impinging jets with staggered arrangement as shown in Fig.9(a) is stronger than those with the inline one as shown in Fig.10(a).

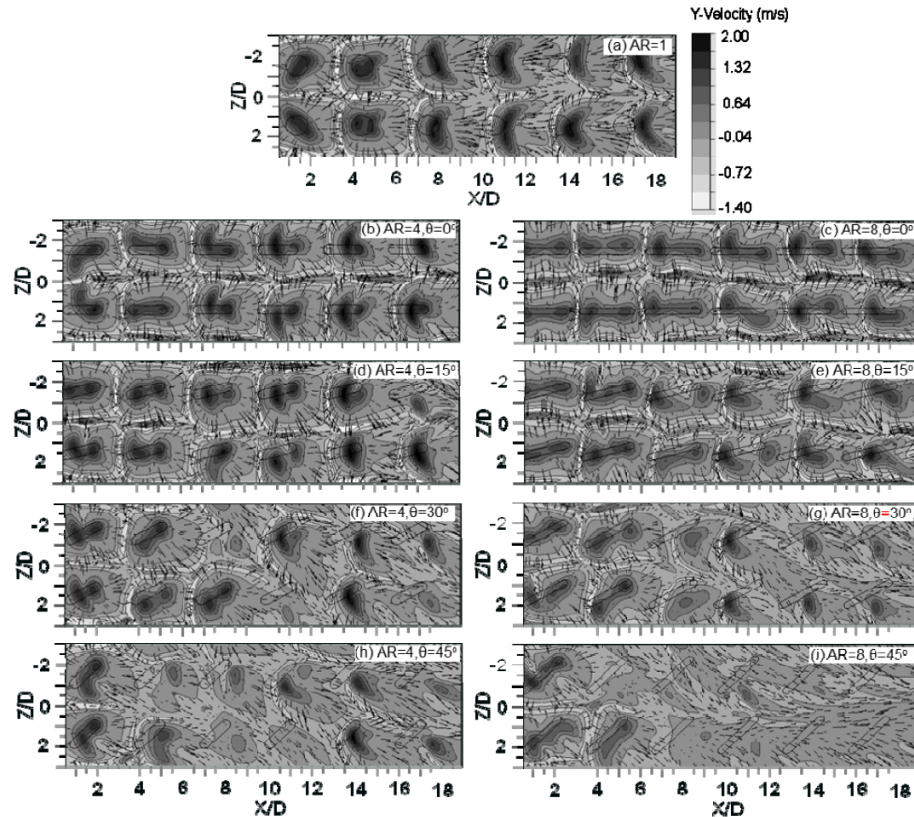


Fig. 7. Flow characteristic of impinging jets on X- Z plane above the impingement surface of 1 mm for the in-line arrangement and $Re=13,400$ (CFD results).

In the case of orifice with $AR=4$ and 8 at $\theta=0^\circ$, it is found that the cross-flow effect can be minimized by these elongated orifices for the inline arrangement, notified by getting the larger impingement region (Black area) of $AR=4$ and 8 (Fig.5(b) and (c)) than those the $AR=1$ (Fig.5(a)). For the case of staggered arrangement, the impingement region (Black areas) at downstream region ($10 < X/D < 20$) of $AR=8$ (Fig.6(c)) is larger than that $AR=1$ (Fig.6(a)), but it seem to be smaller comparing to those $AR=4$ (Fig.6(b)). This is due to the jet issuing from elongated orifice with $AR=8$ producing the longer circumference as well as increasing contact area to mix with the cross-flow. It can also

be observed that the Y-component velocity areas at the downstream direction of $AR=8$ (Fig.8(c)) are smaller than that the $AR=4$ (Fig.8(b)) and larger than those $AR=1$ (Fig.8(a)). Corresponding to preceding paragraph, with the case of $\theta=0^\circ$, the use of jet with $AR=4$ and inline arrangement can be minimized the cross-flow effect. More details of this section have been intensely discussed in [15].

In the case of $AR=4$ with $\theta=15^\circ$ for the inline arrangement as shown in Fig.5(d), the impingement region of each cell is directly extended in the X-axis and obliquely extended in the Z-axis. In addition, each impingement cell is more obliquely extended

in the +Z-axis and contracted in the -Z-axis when the attacking angle becomes larger, at $\theta=30^\circ$ and 45° as shown in Fig. 5(f) and (h). This is different from those with $AR=4$ at

$\theta=0^\circ$, that the impingement regions are particularly extended in the X-axis (without extending into the +Z-axis) as shown in Fig.5(b).

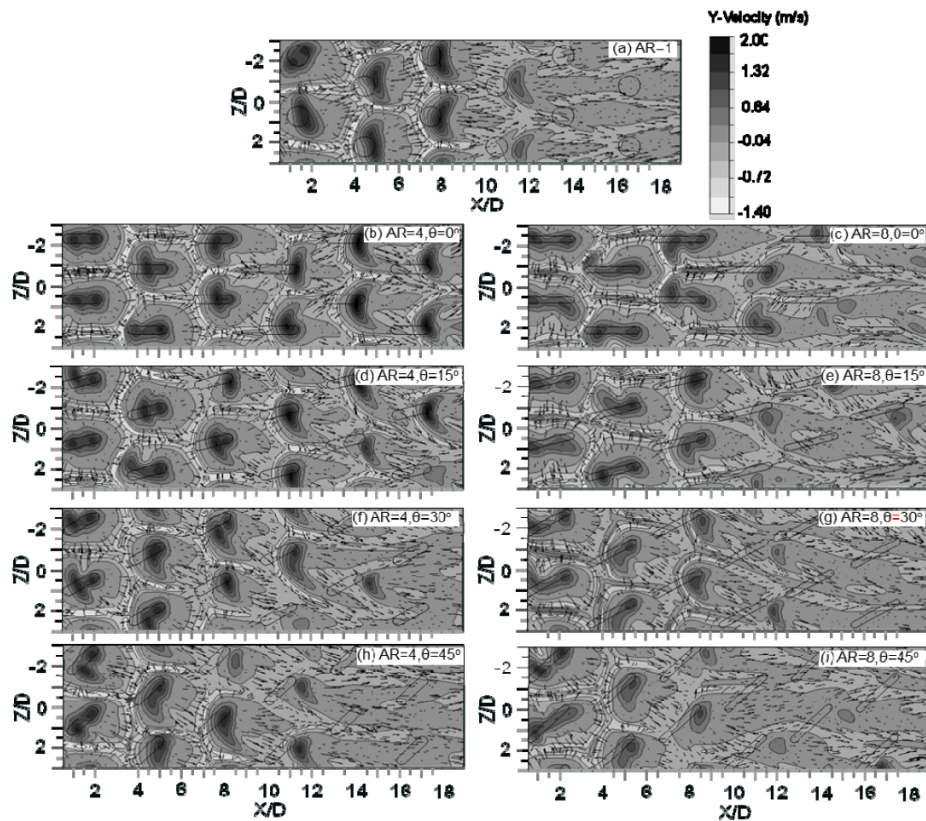


Fig. 8. Flow characteristic of impinging jets on X- Z plane above the impingement surface of 1 mm for the staggered arrangement and $Re=13,400$ (CFD results).

The extension of the impingement regions to the downstream direction is from the cross-flow effect. It can be observed from Fig.9 and 10 that the downstream impinging jet (jet columns No.4 to 6) are more deflect to cross-flow parthline than that the upstream jets(jet columns No.1 to 3). The oblique extension of impingement region to the +Z direction is from the attacking angle effect as shown in Fig.11. The jets are deflected in the +Z direction along the orifice configurations. This deflection is stronger when location of jets is far from the first jet column. Moreover, the deflection of jets with

staggered arrangement is larger than the one with inline that will be discussed in the next section.

For the case with $AR=8$ at $\theta=15^\circ$ with the inline arrangement as shown in Fig. 5(e), the characteristics of flow patterns of the jets is similar to the case with $AR=4$ under the same attacking angle mentioned above. However, when the attacking angle becomes $\theta=30^\circ$ and 45° , the impingement regions at $4 < X/D < 20$ seem to be getting smaller as shown in Fig. 5(g) and (i). For the case of the largest attacking angle, $\theta=45^\circ$, particularly, there is no impingement area in the downstream

region ($13 < X/D < 20$) because the high cross-flow velocity strikes on the jet flow with the large attacking area. This can be observed in Fig.9(e) for the case of $AR=8$ at $\theta=45^\circ$ that the downstream impinging jets (columns 5 and 6) tend to cross-flow part line with slightly impinging on the target surface.

When the in-line and staggered arrangements are compared, it is found that the impingement regions for the in-line arrangement can be seen throughout the streamwise direction (except for the case of $AR=8$ at $\theta=30^\circ$ and 45°). This flow characteristics are similar to the case of staggered arrangement for $AR=4$ at $\theta=0^\circ$, $\theta=15^\circ$, $\theta=30^\circ$ (Fig.6(b), (d) and (f)) and $AR=8$ at $\theta=0^\circ$ (Fig.6(c)). However, for the others, they are unclearly expressed at the downstream area ($10 < X/D < 20$). The absence of the impingement regions corresponds to

the stronger deflection of the downstream jet with staggered arrangement as compared at the same conditions between Fig.9. and 10.

Results show that the attacking angle has significant effects on the impinging jet array of the elongated orifice as schematically sketched in Fig. 12. For the case of attacking angle $\theta=0^\circ$, the cross-flow strikes on the jet issuing from the elongated orifice with the small attacking area as depicted in Fig. 12(a). This attacking area becomes larger when the attacking angle is increased, as shown in Fig. 12(b) and (c). Moreover, the attacking angle effect for the case of $AR=8$ is more prominent than for the case of $AR=4$ due to the longer perimeter of $AR=8$. Consequently, the deflection of jet from the orifice with $AR=8$ is larger than the case of $AR=4$ as mentioned above.

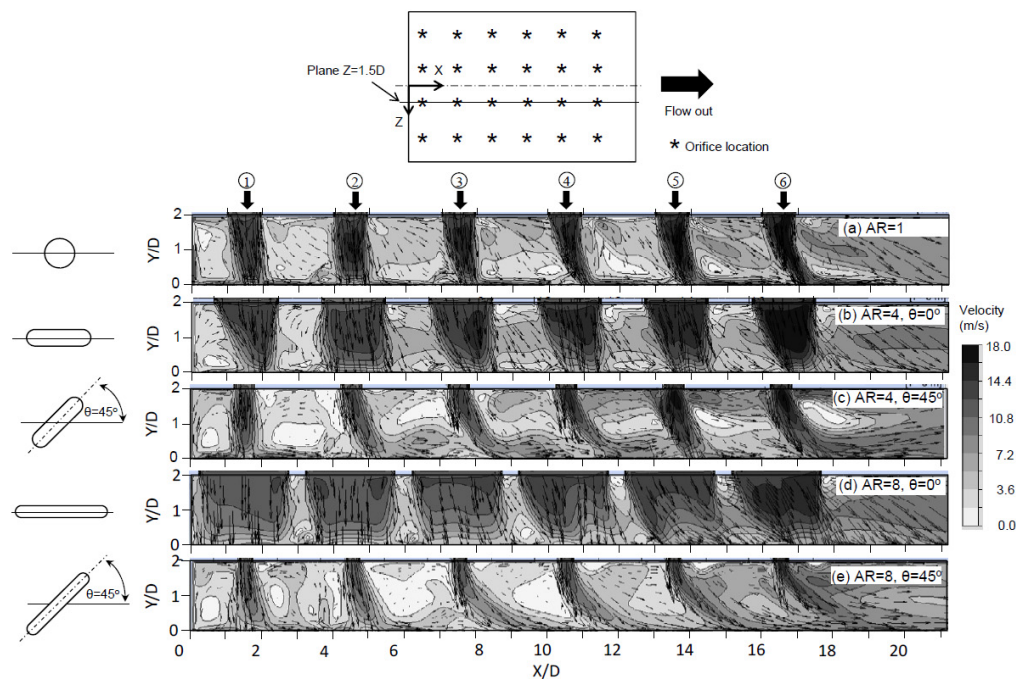


Fig. 9. Flow characteristic of impinging jets on X-Y plane at $Z=1.5D_E$ for the in-line arrangement and $Re=13,400$ (CFD results, Numbers in marked circle indicate the jet column order).

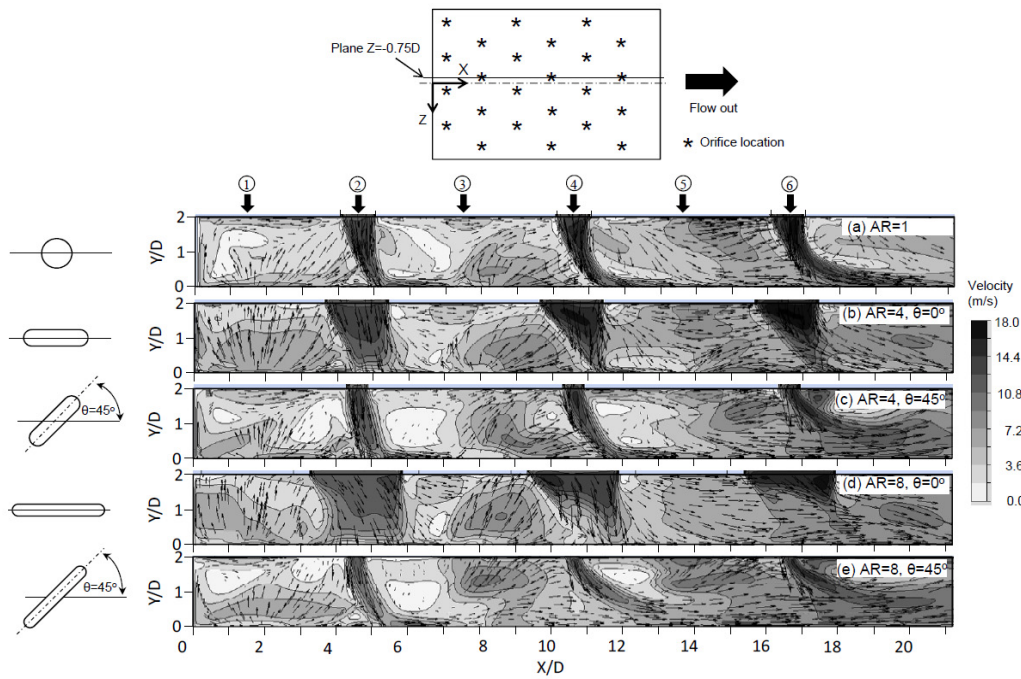


Fig. 10. Flow characteristic of impinging jets on X-Y plane at $Z=-0.75D_E$ for the staggered arrangement and $Re=13,400$ (CFD results, Numbers in marked circle indicate the jet column order).

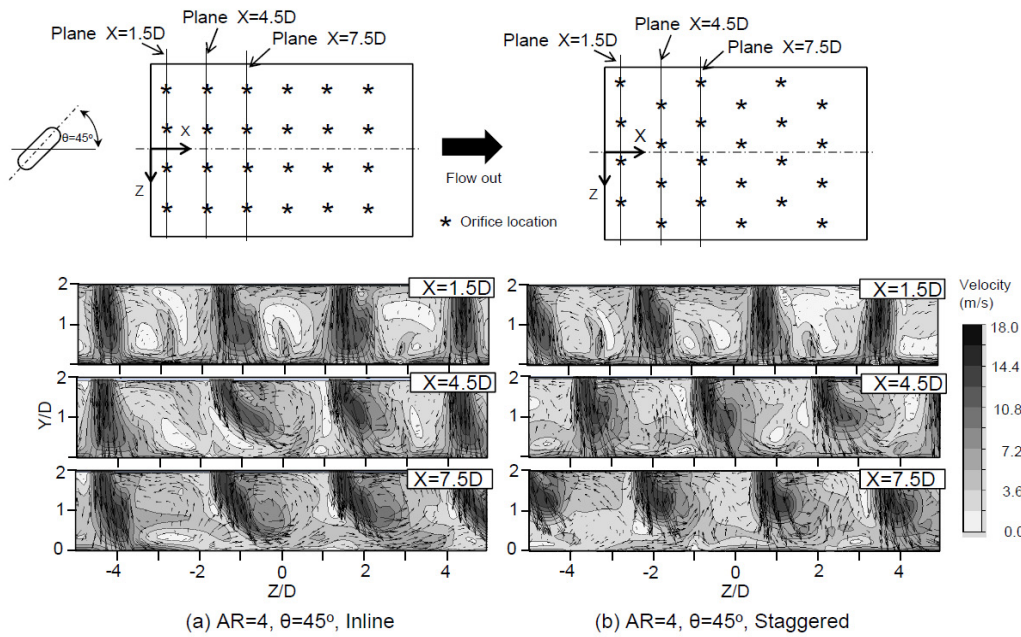


Fig. 11. Flow characteristic of impinging jets on Y-Z plane for $AR=4, \theta=45^\circ$, and $Re=13,400$ (CFD results).

In line with the above observations, the areas of high Y-component velocity, as defined in the impingement regions for the case of staggered arrangement, $AR=4$ and 8 at $\theta=30^\circ$ and 45° when $0 < X/D < 10$ (Fig. 8(f), (g), (h) and (i)), are more clearly seen than those the inline one under the same conditions (Fig. 7(f), (g), (h) and (i)). These flow characteristics can be explained, that the staggered configuration elongated orifice allows the downstream wall jets of each impingement cell to pass through the downstream jet intervals, as depicted in Fig. 13(b), whereas those arranged with the inline configuration are blocked by the downstream jets, as depicted in Fig. 12(a). It should be noted that this different flow characteristics between the inline arrangement and the staggered arrangement appear particularly for the case of large attacking angles, $\theta=30^\circ$ and 45° where $0 < X/D < 10$, and there are also significant effects on the heat transfer characteristics, illustrated and discussed in the next section.

3.2 Heat transfer characteristics on the impingement surface

Contours of local Nusselt number on the impingement surface for $Re=13,400$ for both jet arrangements are shown in Fig. 14 and 15. These contours correspond to the oil film patterns on the impingement surface in Fig. 5 and 6, as well as the contours of Y-component velocity near the impingement surface in Fig 7 and 8. Areas of high Nusselt number ($Nu > 180$) are impingement regions that relate to the black area of flow patterns and high Y-component velocity in flow fields. Generally, the heat transfer rates of impinging jets for $AR=4$ and 8 at $\theta=0^\circ$ are higher than those for $AR=1$, as compared and depicted in Fig. 14(a)-(c) and 15(a)-(c), and the areas of high heat transfer are shifted further downstream as previously discussed in [15].

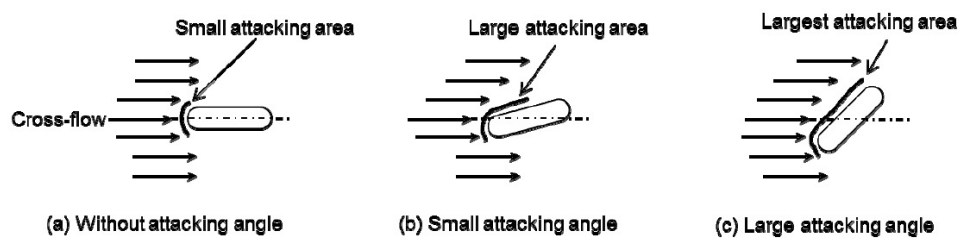


Fig. 12. Sketch of flow characteristics of the cross-flow through difference of attacking angle.

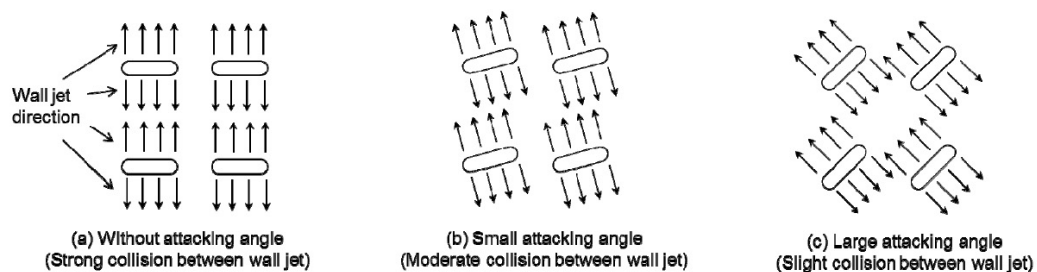


Fig. 13. Sketch of attacking angle effect on the wall jet at upstream region.

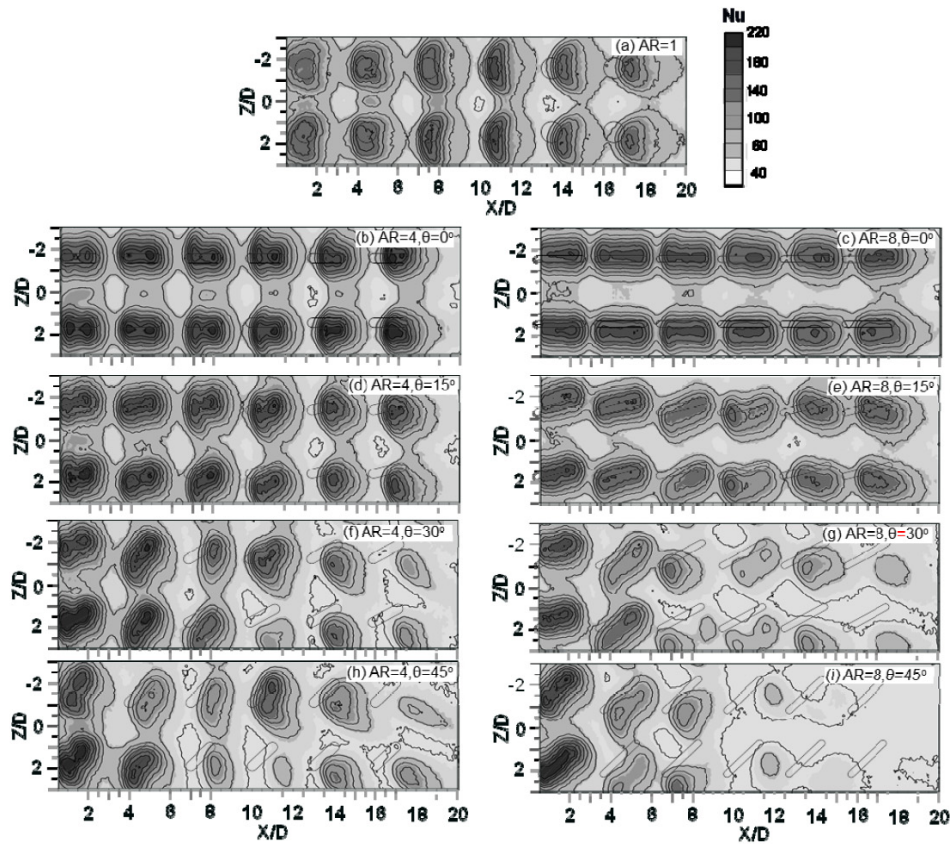


Fig. 14. Nusselt number distributions on the impingement surface for the inline arrangement and $Re=13,400$ (Experimental results, $T_j=27^\circ\text{C}$).

The characteristics of Nusselt number distributions for the case of a small attacking angle, $\theta=15^\circ$, is comparable to those with the attacking angle of $\theta=0^\circ$, but is quite different from the case of large attacking angles at $\theta=30^\circ$ and 45° . The Nusselt number in the downstream region ($10 < X/D < 20$) of both jet arrangements abruptly decreases when the attacking angle is larger due to increasing attacking area between the cross-flow and the impinging jets, as discussed earlier on the jet flow characteristics.

Indeed, the areas of high Nusselt number ($Nu > 180$) in each impingement cell are extended in the X-axis and obliquely extended in the +Z-axis when the attacking angle is larger. This corresponds well to those impingement regions on the surface as

shown before in Fig. 5 and 6 by the oil film technique, and in Fig. 7 and 8 by the CFD. The extension of these high value areas in the X-axis is from the effect of cross-flow shown earlier in Fig. 9 and 10, and the oblique extension of these areas in the +Z-axis is from the effect of attacking angle as previously illustrated in Fig. 11.

From Fig. 14, the area of high Nusselt number (corresponding to impingement regions) of each impingement cell for inline arrangement with $AR=4$ and 8 at $\theta=0^\circ$ and 15° is rather uniformly distributed from upstream to downstream direction. These areas become smaller when the attacking angle become larger to be $\theta=30^\circ$ and 45° . Especially for the case of $AR=8$ and $\theta=45^\circ$, there are no impingement region for the last

jet column as shown in Fig.14(i). This is due to large blocked area from the long circumference of orifice with $AR=8$ and the large attacking angle at significant cross-flow effect at downstream direction as earlier discussion in flow characteristics. These area becoming smaller at downstream direction is clearly seen for the case of staggered

arrangement as shown in Fig.15 accept for $AR=4$ with $\theta=0^\circ$ and 15° as shown in Fig.15(b) and (d). The distribution of area of high Nusselt number is rather consistent from upstream to downstream direction. This is shown that the jet from $AR=4$ can be minimized the effect of cross-flow batter than that $AR=8$.

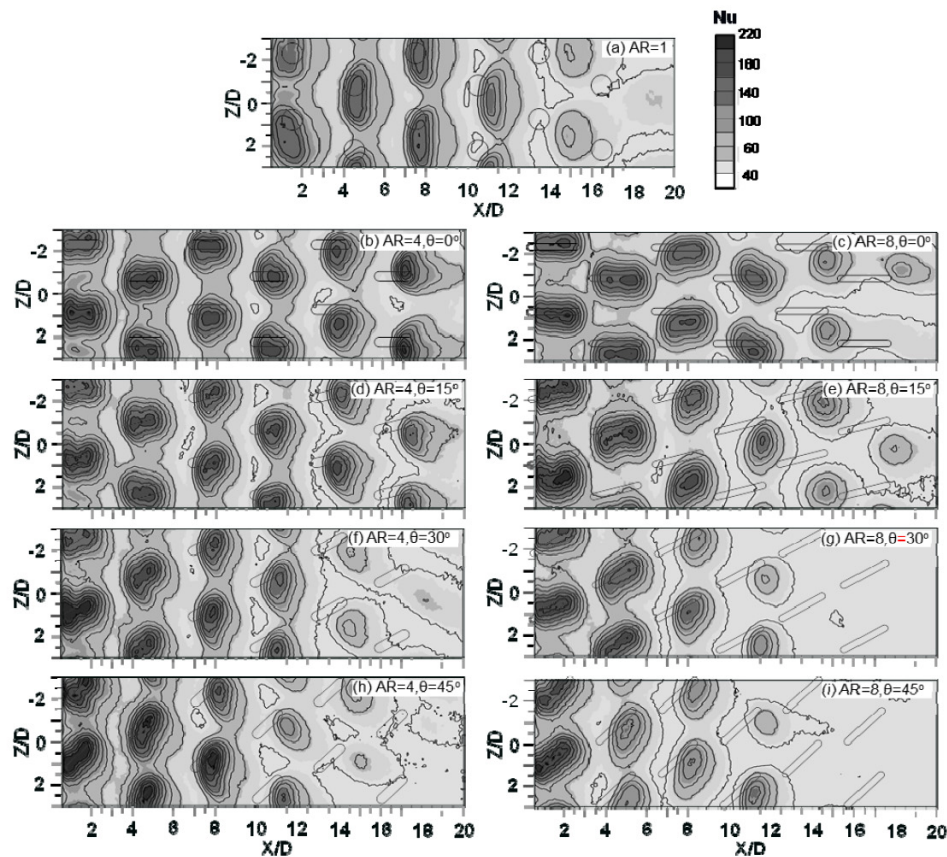


Fig. 15. Nusselt number distributions on the impingement surface for the staggered arrangement and $Re=13,400$ (Experimental results, $T_j=27^\circ\text{C}$).

3.3 Spanwise average Nusselt number

Distributions of the spanwise average Nusselt number along the downstream direction for the case of $Re=5,000$, $7,500$ and $13,400$ are shown in Fig. 16. Each value in this case is calculated from the local heat transfer coefficient, which in turn is dependent on the average local wall

temperatures taken in the range of $-3 < Z/D < 3$. Generally, decreasing Reynolds number, the value gets smaller while its distribution characteristics slightly change. Each distribution and its peak value at a particular X/D location for the case of attacking angle at $\theta=0^\circ$ and $\theta=15^\circ$ is quite similar and consistent compared to other spanwise locations, as shown in Fig.16(b)-(e). But, the

peak value seems to be dramatically decreased when the attacking angle becomes larger at $\theta=30^\circ$ and 45° towards the downstream region ($10 < X/D < 20$), as shown in Fig. 16(f)-(i). In the particular case of $AR=8$ at $\theta=45^\circ$ (Fig.16 (i)), the distributions

in this region become rather flat, especially for $Re=7,500$ and $5,000$ for both jet arrangements. This relates to those the cancellation of impingement of downstream jets as early shown in Fig 10(e).

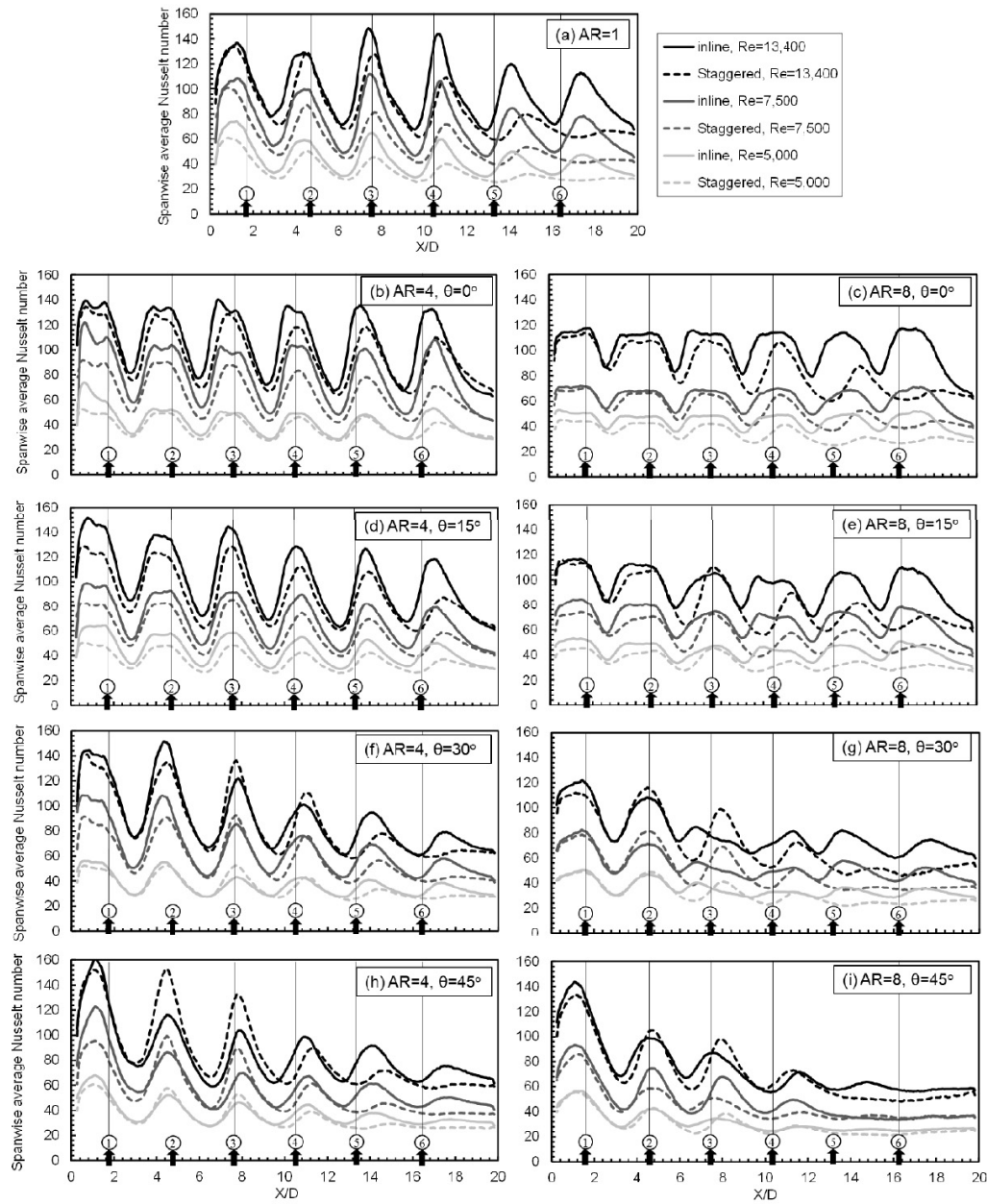


Fig. 16. Spanwise average Nusselt number distribution along the cross-flow direction (Experimental results, $T_j = 26.7^\circ\text{C}$ and numbers in marked circle indicate the jet column order).

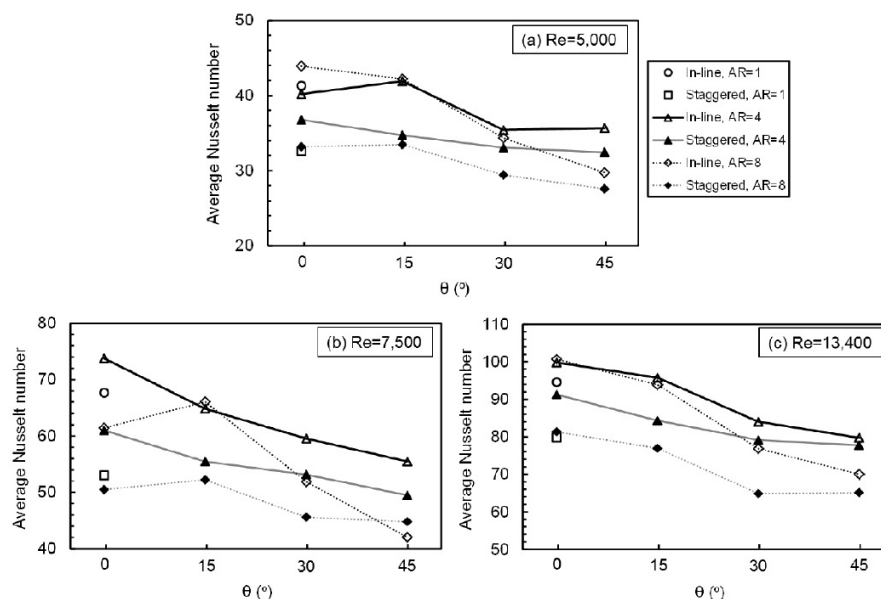


Fig. 17. Average Nusselt number (Experimental results).

Almost all of the spanwise average Nusselt number for the inline arrangement is higher than those of the staggered arrangement except their peak values at jet column 3 and 4 for $AR=4$ at $\theta=30^\circ$ (Fig. 16(f)); and jet column 2 and 3 for $AR=8$ at $\theta=30^\circ$ (Fig. 16(g)), and $AR=4$ and 8 at $\theta=45^\circ$ (Fig. 16(h) and (i)). This is due to the high local Nusselt number at their impingement regions resulting from the effects of jet arrangement and attacking angle on the wall jet that had been explained in Fig.13.

3.4 Average Nusselt number

The average Nusselt number on the impingement surface calculated from the average local wall temperature in area of $0.5 < X/D < 20$ and $-3 < Z/D < 3$ versus the attacking angle are shown in Fig.17. From this figure, the effect of every parameter on the overall heat transfer can be summararily seen. The effects of jet arrangement are revealed that the average values from inline configuration is almost higher than those the staggered one, and the values from $AR=4$ is

almost higher than those the $AR=1$ and 8, due to less significant cross-flow effect of inline arrangement and appropriation of width and length of $AR=4$ comparing with the case of $AR=8$.

Almost all of the average Nusselt number tends to decrease when the attacking angle is increased. However, as shown in Fig. 17 (b), for the case of $AR=8$ with $Re=7,500$ in both jet arrangements, the average value at $\theta=15^\circ$ is higher than that at $\theta=0^\circ$, but is still lower than that for the case of $AR=1$.

For the case of $AR=4$, $Re=13,400$ with the inline arrangement (Fig. 17(c)), and $AR=8$, $Re=5,000$ with the staggered arrangement (Fig. 17(a)), the corresponding average Nusselt number in the case of $\theta=15^\circ$ is slightly higher than that for $AR=1$, but is still lower than that at $\theta=0^\circ$. From these results, the effect of attacking angle is not very significant in increasing the heat transfer on the overall impingement surface. It can, however, increase local heat transfer in the upstream region, the area with minor cross-flow effect.

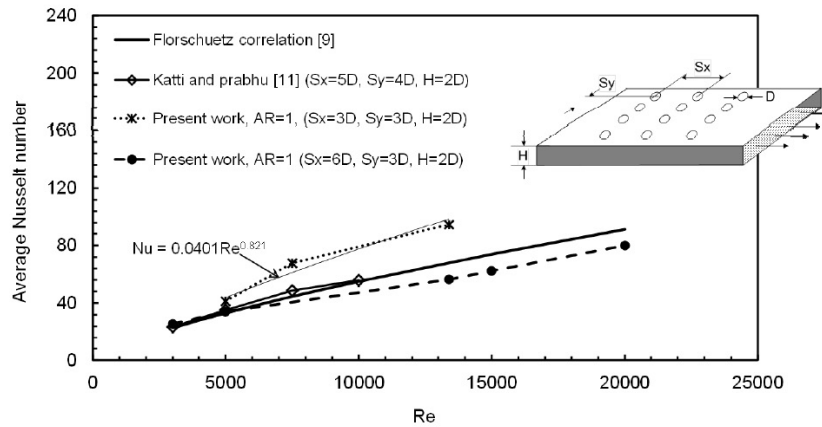


Fig. 18. Average Nusselt number (Experimental results).

Table 1. Correlation equations for $5,000 \leq Re \leq 13,400$

Orifice geometry	Inline	Staggered
AR=1	$0.0401Re^{0.8216}$	$0.0167Re^{0.895}$
AR=4, $\theta=0^\circ$	$0.0215Re^{0.8949}$	$0.0171Re^{0.9066}$
AR=4, $\theta=15^\circ$	$0.0381Re^{0.8267}$	$0.0188Re^{0.8879}$
AR=4, $\theta=30^\circ$	$0.0255Re^{0.857}$	$0.0207Re^{0.8715}$
AR=4, $\theta=45^\circ$	$0.0398Re^{0.8031}$	$0.0186Re^{0.8791}$
AR=8, $\theta=0^\circ$	$0.0336Re^{0.8949}$	$0.0154Re^{0.9034}$
AR=8, $\theta=15^\circ$	$0.05Re^{0.7965}$	$0.029Re^{0.8323}$
AR=8, $\theta=30^\circ$	$0.0336Re^{0.8076}$	$0.0373Re^{0.7883}$
AR=8, $\theta=45^\circ$	$0.018Re^{0.8695}$	$0.0198Re^{0.85597}$

Fig.18 is shown an example of plotting the average Nusselt number versus Reynolds number for $AR=1$ with inline arrangement to predict an empirical correlation. Table.1 is shown the power correlation equation that obtained from all experimental results. It should be noted that these correlation equations can be adopted for the Reynolds number in the range of $5,000 \leq Re \leq 13,400$, the jet-to-plate distance of $H=2D_E$ and the jet-to-jet distance of both streamwise and spanwise direction of $S=3D_E$. In addition, the well-known correlation for impingement heat transfer with cross-flow of Froshuetz et al. [9] and results of Katti and Prabhu [11]

are added in Fig.18. It is difficult to find the jet-to-jet spacing in previous work that be same with the present study. The modified jet-to-jet spacing in streamwise direction, $S_x=6D$, in this work is provisionally plotted due to simple modification of the test section. The slight discrepancy of plotting for this and those studies is from small different jet-to-jet spacing. This is exactly known that the small different jet-to-jet spacing results slightly different heat transfer on target surface.

4. Conclusions

The main focus of this study is to examine the attacking angle effect from air jets discharging through elongated orifice with $AR=4$ and 8 on the flow and heat transfer characteristics of different jet impingement arrays, inline and staggered arrangements, by experimental and numerical investigation. The main results are as follows:

1. The jet issuing from elongated orifice with $AR=4$ can minimize the cross-flow effect, and the aspect ratio of this orifice shouldn't more than $AR=8$.

2. The effect of small attacking angle ($\theta=15^\circ$) from elongated orifice on the flow and heat transfer of impinging jet array are rather similar to the case of attacking angle at $\theta=0^\circ$. It is, however, quite different when the attacking angles become larger at $\theta=30^\circ$ and 45° . At downstream regions, especially, heat transfer rapidly decreases and deflection of the jets veers towards the downstream direction without actual impingement. The decrease in heat transfer and deflection of the jets around these downstream regions for staggered arrangement is more prominent than those of the inline one.

3. Generally, heat transfer on the impingement surface decreases greater when the attacking angle becomes larger. However, when specific area on this surface is considered, local heat transfer at the upstream region for large attacking angles $\theta=30^\circ$ and 45° is found to be higher than those for attacking angles $\theta=0^\circ$ and 15° , especially in the case of staggered arrangement. These results are also confirmed by flow visualization on the region with larger impingement area.

Acknowledgments

This research is supported by grants from the Thailand Energy Policy and Planning Office,

Ministry of Energy, the Graduate School of the Prince of Songkla University (PSU), and the PSU Faculty of Engineering.

References

- [1] R. Viskanta, Heat transfer to impinging isothermal gas and flame jets, *Exp. Therm. Fluid Sci.* 6 (1993) 111-134.
- [2] P. Brevet, C. Dejeu, E. Dorignac, M. Jolly, J.J. Vullierme, Heat transfer to a row of impinging jets in consideration of optimization, *Int. J. Heat Mass Transfer* 45 (2002) 4191-4200.
- [3] S.W. Chang, S.F. Chiou, S.F. Chang, Heat transfer of impinging jet array over concave-dimpled surface with applications to cooling of electronic chipsets, *Exp. Therm. Fluid Sci.* 31 (2007) 625-640.
- [4] R. Chauhan, N.S. Thakur, Heat transfer and friction factor correlations for impinging jet solar air heater, *Exp. Therm. Fluid Sci.* 44 (2013) 760-767.
- [5] L.-E. Brizzi, A. Bernard, J.-L. Bousgarbies, E. Dorignac, J.-J. Vullierme, Study of several impinging jets, *J. Thermal Science* 9 (2000) 217-223.
- [6] B.P.E. Dano, J.A. Liburdy, Structure detection and analysis of non-circular impinging jets in a semi-confined array configuration, *Exp. Therm. Fluid Sci.* 31 (2007) 991-1003.
- [7] L.F.G. Geers, M.J. Tummers, T.J. Bueningk, K. Hanjalic, Heat transfer correlation for hexagonal and in-line arrays of impinging jets, *Int. J. Heat Mass Transfer* 51 (2008) 5389-5399.
- [8] J.Y. San, M.D. Lai, Optimum jet-to-jet spacing of heat transfer for staggered arrays of impinging air jets, *Int. J. Heat Mass Transfer* 44 (2001) 3997-4007.
- [9] L.W. Florschuetz, C.R. Truman, D.E. Metzger, Streamwise flow and heat transfer distributions for jet array impingement with

- crossflow, *J. Heat Transfer-Trans. ASME.* 103 (1981) 337-342.
- [10] B.P.E. Dano, J.A. Liburdya, K. Kanokjaruvijit, Flow characteristics and heat transfer performances of a semi-confined impinging array of jets: effect of nozzle geometry, *Int. J. Heat Mass Transfer* 48 (2005) 691-701.
- [11] V. Katti, S.V. Prabhu, Influence of spanwise pitch local heat transfer distribution for in-line arrays of circular jets with air flow in two opposite, *Exp. Therm. Fluid Sci.* 14 (2008) 84-95.
- [12] D.-H. Rhee, P.-H. Yoon, H.H. Cho, Local heat/mass transfer and flow characteristics of array impinging jets with effusion holes ejecting spent air, *Int. J. Heat Mass Transfer* 46 (2003) 1049-1061.
- [13] T.B. Hoberg, A.J. Onstad, J.K. Eaton, Heat transfer measurements for jet impingement arrays with local extraction, *Int. J. Heat Fluid Flow* 31 (2010) 406-467.
- [14] H.-C. Chiu, J.-H. Jang, W.-M. Yan, Experimental study on the heat transfer under impinging elliptic jet array along a film hole surface using liquid crystal thermograph, *Int. J. Heat Mass Transfer* 52 (2009) 4435-4448.
- [15] C. Nuntadusit, M. Wae-hayee, P. Tekasakul, S. Eiamsa-ard, Local heat transfer characteristics of array impinging jets from elongated orifices. *Int. Commun. Heat Mass Transfer* 39 (2012) 1154-1164.
- [16] G. Biswas, K. Torii, D. Fujii, K. Nishino, Numerical and experimental determination of flow structure and heat transfer effects of longitudinal vortices in a channel flow, *Int. J. Heat Mass Transfer* 39 (1996) 3441-3451.
- [17] L.-T. Tian, Y.-L. He, Y.-G. Lei, W.-Q. Tao, Numerical study of fluid flow and heat transfer in a flat-plate channel with longitudinal vortex generators by applying field synergy principle analysis. *Int. Commun. Heat Mass Transfer* 36 (2009) 111-120.
- [18] M. Wae-hayee, P. Tekasakul, C. Nuntadusit, Influence of nozzle arrangement on flow and heat transfer characteristics of arrays of circular impinging jets, *Songklanakarin J. Sci. Technol.* 32 (2013) 203-212.
- [19] T.T. Chandratilleke, D. Jagannatha, R. Narayanaswamy, Heat transfer enhancement in microchannels with cross-flow synthetic jets, *Int. J. Therm. Sci.* 49 (2010) 504-513.
- [20] M.-W. Heo, K.-D. Lee, K.-Y. Kim, Optimization of an inclined elliptic impinging jet with cross flow for enhancing heat transfer, *Heat Mass Transfer* 47 (2011) 731-742.

VITAE

Name Mr. Makatar Wae-hayee

Student ID 5210130016

Educational Attainment

Degree	Name of Institution	Year of Graduation
Bachelor of Industrial Technology in Mechanical Technology	Rajamangala University of Technology Srivijaya	2007
Master of Engineering in Mechanical Engineering	Prince of Songkla University	2009

Scholarship Awards during Enrolment

1. Research assistant scholarship, Engineering faculty, Prince of Songkla University, 2007-2009
2. Graduate school scholarship, Graduate school, Prince of Songkla University, 2009-2011

List of Publication and Proceedings

Journal Publication

C. Nuntadusit, M. Wae-hayee, A. Bunyajitradulya, S. Eiamsa-ard, "Heat transfer enhancement by multiple swirling impinging jets with twisted-tape swirl generators", International Communications in Heat and Mass Transfer, 2012, Vol. 39, pp.102-107.

C. Nuntadusit, M. Wae-hayee, A. Bunyajitradulya, S. Eiamsa-ard, "Thermal visualization on surface with a transverse perforated rib", International Communications in Heat and Mass Transfer, 2012, Vol. 39(5), pp.634-639.

C. Nuntadusit, M. Wae-hayee, A. Bunyajitradulya, S. Eiamsa-ard, "Visualization of flow and heat transfer characteristics for swirling impinging jet", International Communications in Heat and Mass Transfer, 2012, Vol. 39(5), pp.640-648.

C. Nuntadusit, M. Wae-hayee, P. Tekasakul, S. Eiamsa-ard, "Local heat transfer characteristics of array impinging jets from elongated orifices", International Communications in Heat and Mass Transfer, 2012, Vol. 39(8), pp.1154-1164.

M. Wae-hayee, P. Tekasakul and C. Nuntadusit, "Influence of Nozzle Arrangement on Flow and Heat Transfer Characteristics for Arrays of Circular Impinging Jets" *Songklanakarin Journal of Science and Technology*, 2012, Vol. 35(2), pp.203-212.

International Conference

C. Nuntadusit, M. Waehahyee, A. Bunyajitradulya and T. Shakouchi, "Heat transfer enhancement for a swirling jet impingement" *The ISFV14 - 14th International Symposium on Flow Visualization*, June 21-24, 2010, EXCO Daegu, Korea.

M. Wae-hayee, C. Nuntadusit, and P. Tekasakul "Effect of velocity ratio on flow and heat transfer characteristics of an impinging jet in crossflow", *The 5th PSU-UNS International Conference on Engineering and Technology (ICET-2011)*, Phuket, May 2-3, 2011 Prince of Songkla University, Faculty of Engineering Hat Yai, Songkhla, Thailand.

M. Wae-hayee, C. Nuntadusit, and P. Tekasakul "Heat transfer enhancement on a surface under arrays of impinging jets: effect of jet flow arrangement", *The 5th PSU-UNS International Conference on Engineering and Technology (ICET-2011)*, Phuket, May 2-3, 2011, Prince of Songkla University, Faculty of Engineering Hat Yai, Songkhla, Thailand.

M. Wae-hayee, C. Nuntadusit, and P. Tekasakul "Heat Transfer Enhancement on Surface with Jets Impingement from Some Arrays of Elongated Round Orifices", *The 2nd TSME International Conference on Mechanical Engineering (TSME-ICoME 2011)*, October 19-21, 2011, Krabi, Thailand.

M. Wae-hayee and C. Nuntadusit, "Flow and Heat transfer Characteristics of Non-circular Impinging jet in Crossflow" *The 8th International Conference on Flow Dynamics (ICFD2011)*, November 9-11, 2011, Sendai, Miyagi, Japan.

M. Wae-hayee C. Nuntadusit, and P. Tekasakul, "Heat Transfer Enhancement of an Impinging Jet in Crossflow by Elongated Round Orifice" *The 10th International Gas Turbine Congress 2011 Osaka (IGTC'11)*, November 13-18, 2011, Osaka, Japan.

B. Kaewkraikrong, M. Wae-hayee, T. Leevijit and C. Nuntadusit, "Study on Heat Transfer Characteristics of Impinging Jet with Delta Tabs Attachment at Pipe Exit", *The 10th International PSU Engineering Conference*, May 14-15, 2012, Songkhla, Thailand.

K. Songkaor, M. Wae-hayee, T. Leevijit and C. Nuntadusit, "Effect of Nozzle Geometry on Flow Characteristic of Jet from Expansion Pipe Nozzle", *The 10th International PSU Engineering Conference*, May 14-15, 2012, Songkhla, Thailand.

C. Nuntadusit and M. Wae-hayee, "Drying of Rubber Sheet Using Impingement of Multiple Hot Air Jets" The First Asia Pacific Rubber Conference (ARPC2013), September 5-6, 2013, Prince of Songkla University, Thailand.

C. Nuntadusit and M. Wae-hayee, "Flow and Heat Transfer Characteristics of Row of Jet Impingement from Elongated Orifice under Cross-flow" The 4th International Conference on Jets, Wakes and Separated Flows (ICJWSF2013), September 17-21, 2013, Nagoya, Japan.

National Conference

M. Wae-hayee and C. Nuntadusit, "A Study Flow and Heat Transfer Characteristics on a Surface with Air Jet Impingement", The 6th PSU Engineering Conference (PEC-6), May 8-9, 2008, Prince of Songkla University, Thailand.

M. Wae-hayee, C. Nuntadusit and A. Bunyajitradulya, "Heat Transfer Enhancement on Surface Using Array of Impingement Swirl Jets", The 22th Conference of the Mechanical Engineering Network of Thailand (ME-NETT-22), October 15-17, 2008, Thammasat University, Thailand.

M. Wae-hayee and C. Nuntadusit, "Study of Flow Behaviors of Swirling Jet Impinging on a Wall Using Visualization Method", The 7th PSU Engineering Conference (PEC-7), May 21-22, 2009, Prince of Songkla University, Thailand.

M. Wae-hayee and C. Nuntadusit, "Study of Flow Behaviors of Swirling Jet Impinging on a Wall Using Visualization Method", The 7th PSU Engineering Conference (PEC-7), May 21-22, 2009, Prince of Songkla University, Thailand.

M. Wae-hayee and C. Nuntadusit, "Wall Heat Transfer Measurement Technique Using Thermochromic Liquid Crystal Sheet", The 23th Conference of the Mechanical Engineering Network of Thailand (ME-NETT-23), November 4-7, 2009, Chiang Mai University, Thailand.

M. Wae-hayee and C. Nuntadusit, "Drying of Rubber Sheet Using Impingement of Multiple Hot Air Jets", The 23th Conference of the Mechanical Engineering Network of Thailand (ME-NETT-23), November 4-7, 2009, Chiang Mai University, Thailand.

M. Wae-hayee, B. Jring-jit, P. Smithmaitrie and C. Nuntadusit, "A Study of Heat Transfer Characteristic on a Surface of a Piezoelectric Fan", The 8th PSU Engineering Conference (PEC-8), April 22-23, 2010, Prince of Songkla University, Thailand.

M. Wae-hayee and C. Nuntadusit, "Measurement of Heat Transfer Coefficient on a Surface Using Thermochromic Liquid Crystal with Transient Technique",

The 8th PSU Engineering Conference (PEC-8), April 22-23, 2010, Prince of Songkla University, Thailand.

P. Phanit, M. Wae-hayee and C. Nuntadusit, “Drying of Rubber Sheet Using Impingement of Multiple Hot Air Jets”, The 23th Conference of the Mechanical Engineering Network of Thailand (ME-NETT-23), November 4-7, 2009, Chiang Mai University, Thailand.

N. Suwanmala, M. Wae-hayee, S. Sea-ung and C. Nuntadusit, “A Study of Heat Transfer on a Surface for Impinging Flame Jet”, The 24th Conference of the Mechanical Engineering Network of Thailand (ME-NETT-24), October 20-22, 2010, Ubon Ratchathani University, Thailand.

M. Wae-hayee, P. Smithmaitrie and C. Nuntadusit, “Flow and Heat Transfer on a Surface of Air Jets from Couple of Piezoelectric Fans”, The 24th Conference of the Mechanical Engineering Network of Thailand (ME-NETT-24), October 20-22, 2010, Ubon Ratchathani University, Thailand.

M. Wae-hayee and C. Nuntadusit, “Heat Transfer of An Impinging Jet in Crossflow : Effect of Velocity Ratio Between Crossflow and Jet Flow”, The 24th Conference of the Mechanical Engineering Network of Thailand (ME-NETT-24), October 20-22, 2010, Ubon Ratchathani University, Thailand.